The Effect of Hip Muscle Contraction on Stress Response of the Lower Extremities during the Normal Walking

By:

Mahdi Hossaeini Marashi

Submitted as part of the requirement for the degree of Doctor of Philosophy

Supervised by:
Professor Ibrahim Esat
Dr Bin Wang

College of Engineering, Design and Physical Sciences

Department of Mechanical and Aerospace Engineering

Brunel University London
August 2019

Abstract

There is a growing concern to determine the essential characteristics of mechanical coupling between muscles and bone tissue during the normal walking cycle undertaken as a common daily activity.

The physiological and biomechanical aspects of the musculoskeletal model propose that muscle contraction induce mechanical stimuli to muscle attachment sites, thereby creating skeletal movement. However, the main question remains regarding how the muscle contraction affects the femoral bone structure and its stress responses.

This study aimed to determine the influence of muscle contraction on stress distribution and deformation characteristics of the lower limb.

Analytical and numerical approaches were used to provide adequate data and evidence for achieving the goal of the study. For the analytical method, two main studies were defined including a skeletal model (without considering muscle contraction, 3D-No Mus) and a musculoskeletal model (with the effects of muscle contraction, 3D-All Mus). For the numerical method, a skeletal study on hip muscles (i.e. 3D-H Mus) and one on knee muscles (i.e. 3D-K Mus) were added to ensure the results were not achieved randomly. Computed tomography (CT) and magnetic resonance imaging (MRI) was used to obtain an authentic CAD model of the lower extremities of a healthy male. A unique CAD model, including seven major hip and knee joint components and 19 muscle groups were developed for the quasi-static finite element (FE) analysis.

Hip contact force (HCF) was predicted using two-dimensional (2D) and three-dimensional (3D) equilibrium static equations for the single support stance and pre-swing phase of the gait cycle. The estimated HCF in the single support stance was 11% higher than the pre-swing phase of the gait and no considerable variation was identified between 2D and 3D studies. On the other hand, the effect of muscle contraction on the HCF of the musculoskeletal model was approximately two times higher than the estimated HCF for the skeletal model.

An analytical approach was used to predict normal and shear stress for three susceptible regions of the femur including femoral head, head-neck and mid-plane diaphysis. The results demonstrated that the muscle contraction increased both normal and shear stresses on the femoral head of the 3D-All Mus model by 230% compared to the skeletal model without any muscles (3D-No Mus) in the single support stance. Furthermore, the muscle contraction

in the 3D-All Mus increased the shear stress on the femoral neck region in the single support stance and pre-swing phase of the gait cycle on average 228% and 218%, respectively, compared to the shear stress in the skeletal model (3D-No Mus). In the single support stance, muscle contraction in a human musculoskeletal (3D-All Mus) model increased the normal and shear stress on the femoral diaphysis on average 229% and 236%, respectively, compared with the skeletal model (3D-No Mus).

Muscle contraction significantly enhanced the stress response of muscle attachment sites as well as the overall stress of the femur using FE analysis. This study indicated that muscle contraction increased normal stress at the single support and swing stance of the gait cycle by 190% and 143%, respectively. However, the observed results for shear stress presented a lower increase. The effect of muscle contraction on the stress response of the meniscus was also examined. It was observed that the effect of knee muscle contraction increased the maximum principal stress on the meniscus by 800% compared with the study where muscles were excluded during the gait cycle. Additionally, the obtained stress distribution on the femur and menisci demonstrated that the effect of muscles significantly eliminated the risk of stress concentration occurrence.

Furthermore, in the pre-swing phase of the gait cycle, the normal stress predicted by the analytical method was 30% greater than the normal stress estimated by FE analysis. However, for normal stress in the single support stance, the results of FE analysis had a high correspondence with the analytical approach and improved the existing assumption about the effect of muscle contraction on the stress behaviour of the femur. In conclusion, the outcome of this thesis presents a new paradigm where muscle contractions on the musculoskeletal model significantly increased stress characteristics on the femur and other lower extremities during normal walking.

Keywords:

Hip Contact Force, Muscle Contraction, Stress Configuration, Stress Distribution, Finite Element Analysis, Analytical Approach.

In addition, We wanted to confer favour upon those who were oppressed in the land, and make them leaders, and make them inheritors.

(Qur'an, AL-QASAS, 5)

To My

Twelfth Imam **(*peace be upon him*)**

A**cknowledgments**

I would like to express my appreciation to Professor Ibrahim Esat and Dr Bin Wang for their supervision and advice throughout this project. Their limitless support guided me through the previous four years, which were very trying at times. They advised and guided me in the right direction towards the end of my PhD, helping me to achieve significant outcomes. I particularly acknowledge Professor Ibrahim Esat for giving me the opportunity to work on his assumption and idea.

Throughout the analytical approach process of this research, I received significant support and assistance. I wish to thank Dr Gholam Reza Abbaszadeh Mosayebi, whose expertise was invaluable, and gave me the idea to determine the formula for the susceptible regions of the femur in particular.

On a personal note, I wish to thank my family: my twin cousins, Mohammad Reza and Mohammad Javad, and particularly my wife, Maryam, for their continued support throughout this research, and without whom this would have been a much less enjoyable process.

In addition, I wish to express my gratitude to my father and mother for their wise counsel, endless support throughout my life, and for always being available to lend a sympathetic ear. I also wish to express my appreciation to my lovely brothers and sisters, Mojgan, Nasrin, Sara, Ali, and Mohammad, who have always been supportive of me.

Finally, I thank my colleagues, managers, and senior lecturers at Uxbridge College, who provided useful assistance in terms of relaxation outside of this research.

S. Mahdi .H. Marashi

Statement of Originality

I certify that the content of this thesis is my own work under supervision of Professor Ibrahim Esat, Dr Bin Wang. Any data, images and tables of others, whether published or otherwise, are fully acknowledged in my thesis.

Mahdi Hossaeini Marashi

Table of Contents

List of Figures

List of Tables

Abbreviation

FEA	Finite Element Analysis
3D-CAD	Three-Dimensional Computer-Aided Design
CT	Computed Tomography
THR	Total Hip Replacement
BW	Bodyweight
EMG	Electromyography
HCF	Hip Contact Force
3D-All Mus	Musculoskeletal Model –Including All Hip and Knee Muscles
3D-Hip Mus	Including Hip Muscles
3D-Knee Mus.	Including Knee Muscles
3D-No Mus.	Skeletal Model. No Muscle attached to the FE model
ACL	Anterior cruciate ligament
PCL	Posterior Cruciate Ligament

LCL	Lateral Collateral Ligament
MCL	Medial Collateral Ligament
RASIS	Right Anterior-Superior Iliac Spine
LASIS	Left Anterior-Superior Iliac Spine
RPT	Right Pubic Tubercle (Pelvis)
RPSIS	Right Posterior-Superior Spine
GTROCH	Great Trochanter
MED/LAT-EP	Medial And Lateral of Epicondyle
TIBTUB	The Origin of The Tibia1 Tuberosity
MEDMAL	Medial Projection of Malleolus on Fibula
LATMAL	Lateral Projection of Malleolus on Fibula
HEEL	The Reference Point (Origin) of The Heel Segment
DOFs	Degree of Freedom
ILPSO	Iliopsoas
ADLB , ADM	Adductor Longus Brevis , Adductor Magnus
GMEDA	Anterior Gluteus Medius , Anterior Gluteus Minimus
GMEDP	Posterior Gluteus Medius , Posterior Gluteus Minimus
GMAXM	Medial Gluteus Maximus
GMAXL	Lateral Gluteus Maximus
SAR	Sartorius
GRA	Gracilis
HAMS (ST, SM and BFSL and FSH)	Semimembranosus, Semitendinosus, Biceps Femoris Long-Short Head
RF	Rectus Femoris
VAS (VMO, VL and VIM)	Vastus Medialis Oblique, Vastus Intermedius, And Vastus Lateralis
GAS , SOL	Gastrocnemius , Soleus
PIR	Piriformis
GAS	Gastrocnemius
HU	Hounsfield Unit
STP	Standard Pressure and Temperature
NURBS	Non-Uniform Rational B-Spline
STL	Stereolithographic
RP	Rapid Prototyping
DICOM	Digital Imaging and Communications in Medicine
GT	Great Trochanter

Nomenclature

E	Young's modulus
ρ	Density
e	Strain
H	Origin or Reference Point at the Top of Femur
$F_X^{Mus.}$	Muscular Contact Forces in X-axis
$F_Y^{Mus.}$	Muscular Contact Forces in Y-axis
$F_Z^{Mus.}$	Muscular Contact Forces in Z-axis
${M_Y}^{MUS}$	Total Moments of the Muscular Force in Y-axis
${M_Z}^{MUS}$	Total Moments of the Muscular Force in Z-axis
K_z	Knee Reaction Force in Z-axis
K_y	Knee Reaction Force in Y-axis
R_z	Hip Reaction Force in Z-axis
R_y	Hip Reaction Force in Y-axis
L_f	Length of Femur
R_X^{α}	Reaction Force in X-axis at pre-swing phase (i.e. 50%) of the Gait
R_y^{α}	Reaction Force in Y-axis at pre-swing phase (i.e. 50%) of the Gait
R_Z^{α}	Reaction Force in Z-axis at pre-swing phase (i.e. 50%) of the Gait
Sqrt.	Square Root
M_x^{BW}	Moment of Bodyweight in X-Direction (reference point is H)
m_1	Mass of Femur in Z-Direction
m_2	Mass of Tibia in Z-Direction
M_x^{m1}	Moment of Mass of Femur in X-Direction
M_Y^{m1}	Moment of Mass of Femur in Y-Direction
M_x^{m2}	Moment of Mass of Tibia in X-Direction
M_Y^{m2}	Moment of Mass of Tibia in Y-Direction
$M_X^{Re.Knee}$	Moment of Knee Reaction in X-Direction
$M_Y^{Re.Knee}$	Moment of Knee Reaction in Y-Direction
$M_Z^{Re.Knee}$	Moment of Knee Reaction in Z-Direction
σ^2	Variance
X_i	Observed Value
μ	Mean Value
σ_N^h	Normal Stress on Head of Femur
σ_T^h	Shear Stress on Head of Femur
σ_N^{h-n}	Normal Stress on Head-Neck of Femur
σ_T^{h-n}	Shear Stress on Head-Neck of Femur
σ_N^d	Normal Stress on Diaphysis of Femur
σ_{T-X}^d	Shear Stress on Diaphysis of Femur anteriorly
σ_{T-Y}^d	Shear Stress on Diaphysis of Femur laterally
σ_B^d	Bending Moment stress on Diaphysis of Femur
I	Moment of Inertia
y	Vertical Distance from Neutral Axis
${\sigma_N}^{Ave}$	Average Normal Stress
${\sigma_T}^{Ave}$	Average Shear Stress

Chapter 1: Introduction

1.1 Introduction

The hip joint is a type of ball and socket (spheroidal-synovial) joint in which the head of the femur (ball-shaped bone) fits into acetabulum. The femur naturally rotates in all directions with a common centre of a socket, creating a wide range of movements when undertaking daily activities. Hence, the hip joint and its function perform a vigorous role to stabilise and harmonies the lower limb movements.

To comprehend the hip joint mechanism and associated functions of the hip muscles the numerical and analytical techniques were considerably progressed. The main reason to consider virtual techniques are attributed to the restrictions of *in-vivo* methods to analyse the function of human muscles. Within a wide range of non-invasive studies and numerical method, finite element analysis is able to create the compatible virtual environment resembling the human body. However, the reliability and validity of the FEA studies and obtained results are highly reliant upon the applied joint force, boundary conditions, assigned materials properties, and the three-dimensional computer-aided design (3D CAD) models.

However, the outcomes of the computational studies may provide adequate clinical information to enhance the design of implants, reduce complications of hip replacement and improve the surgical procedures. Brekelmans, et al., (1972) and Goel, et al., (1978) studied mechanical behaviour and stress analysis of the lower extremities using simplified models of the pelvis, femur, and employing approximate point loads to find the muscle and joint contact forces.

The development of computational hardware and commercial software, many researchers have recently employed complex 3D geometry using the computed tomography images and applied complex contact force to capture FEA results (Bergmann et al., 1993, 2001; Chen et al., 2014; Damm et al., 2013; Schwachmeyer et al., 2013; Zhang et al., 2015, Bergmann et al., 2016; Ng et al., 2018). Nonetheless, many simplistic assumptions were considered for the muscles simulations and employing compatibility conditions of muscles around the joint. Neglecting the muscle

contraction and its effect around the hip and knee joint may create a large deceptive view from the computational modelling. Several FEA studies have been conducted by considering the simplified boundary conditions to achieve the FEA results, which are, listed as follows (Winter, 1990; Dalstra, et al., 1995; Majumder, et al., 2004; Bachtar, et al., 2006; Silvestri, 2008; Silvestri, et al., 2009; Anderson, et al., 2010, Mo, et al.,2017; Wang, et al., 2017; Li, et al., 2019).

- Replacing muscles with the simple discrete spring.
- Using the basic passive Hill-type model.
- Employing time independent muscles force.
- Considering the point loads contact force.

Although simplifying models and boundary conditions such as employing limited numbers of muscles within the FEA may reduce time and be cost-efficient, the absence of muscles must have affected local stress-strain distribution in a lower limb body and hip joint. In this case, the created local stress may cause to create early failure in Total Hip Replacement (THR) or produce other complications pertaining to the hip joint.

To comprehend the importance of considering muscle contraction within the simulation of the lower extremities, the total number of THR surgery and revision operation were reviewed.

1.2 Motivation of Study

The statistical analysis of the THR and revision operations shows that it is necessary to review the loading condition and stress behaviour of the hip joint compartments.

THR is a standard medical procedure to remove the damaged hip cartilage or its bony part (i.e. head of femur), replaced prosthetic components to release the pain, and improved the hip function. Hip replacement is one of the most successful surgical procedures in the field of orthopaedic surgery for those suffering from health issues like osteoarthritis, congenital deformities, avascular necrosis, rheumatoid arthritis and post-traumatic stress disorder (Parvizi, et al., 2009). Although various reasons can be listed for an unsuccessful THR procedure, the majority of failure cases were reported due to the biomechanical reasons (Pustoc'h, & Cheze, 2009; Elkins, 2013). The biomechanical of failure after hip cementless implementation occurred because of the excessive implant-bone interface stress, which caused to dislocate the hip prosthesis and compromise cementless prosthesis durability (Elkins, 2013).

Furthermore, the lack of stability between the femur and stem due to excessive micro-motion has a strong influence over the cementless arthroplasty. This phenomenon reduces the durability of biological attachment and causes the huge cost and consequences such as femur fracture or loosening of the implant. Despite these aspects, surgical procedure, patient conditions, and design of the hip implant are also important considerations for total hip replacement (Huiskes & Boeklagen, 1988; Viceconti et al., 2001).

Revision surgery is the main element for measuring the success rate of the hip replacement; this is the duration of maintaining time between the first and second surgery. The surgical procedure of THR has shown good progress and success rate in the past few decades due to enhancing the accuracy of THR procedure by up to approximately 10% (Mancuso et al., 1997; Kurtz et al., 2007). Alongside increasing the success rate of THR, the absolute number of failed joint replacements has increased significantly because of the recent rise of incidences (Taylor & Prendergast, 2015). Furthermore, there has been a continuous rise of hip arthroplasty internationally caused by increased numbers of the population, the human ageing phenomenon, and increased high-risk activities. The total number of primary THR is estimated to enhance 174% per year in the United States. For the hip replacement, revision surgery is expected 137% growth between 2005 and 2030 (Kurtz, et al., 2007). Whereas the number of total hip replacement enhanced 285,000 surgeries per year in which from 60% up to 90% of total number categorised in THR cementless technique (Rockville, 2018).

Moreover, the total number of hip injuries and fractures was estimated to exceed beyond 500,000 in the US by the end of 2040 (Cummings, et al., 2002). During the period 1967 to 2013, overall THR operations and surgeries were increased from 6 to 16,330 in Sweden (SHARR, 2013). In Australia, the number of the total hip replacement has increased by 46.50% per year from 2003 (AOANJRR, 2016).While the incidence rate of THR for osteoarthritis is estimated to rise up to 208%, by 2030 (Ackerman et al., 2019).

According to 15th annual report from the National Joint Registry in England, Wales, Northern Ireland and the Isle of Man (2018), 992,218 primary hip operation were performed. While the number of total knee replacement (TKR) recorded 1,087,696 in 2018. Moreover, out of the total joint operations, 27,608 and 28,717 patients requested the hip and knee revision operations respectively, while around 1% of the THR and TKR operations need to be revised more than one time. The most common reasons for revision were dislocation/subluxation (4,663 patients), aseptic

loosening (6,705 patients), adverse soft tissue reaction to particulate debris (4,619 patients), infection (3,872 patients), and pain (4,507 patients). It is reported that the cementless implants are used for THR increased from 16.8% to 42.5%. Whereas the numbers of cemented implants employed for THR decreased from 60.5% to 33.2% over the same period. According to NJR 15th (2018), nearly 3.06 % and 6.29 % of the cemented and uncemented hip implants required revision surgery within a mean of first 10 years after implementation however; it depends on patient health conditions and implant replacement technique.

The outcomes of this study may help to reduce the risk of failure in THR via improving the design of implants and modifying joint replacement procedures.

1.3 Aim and Objective

This study aims to determine the effect of the muscle contraction on stress response, and the mechanical behaviour of the lower extremities within the normal walking process. To accomplish this, the mechanical behaviour and stress response of the femur, as a primary part of the hip joint, was investigated using analytical and numerical analyses. There is a well-established assumption for explaining the bio-function of muscles during human locomotion, as they support the bony parts in completing their movement during daily activity. Nevertheless, the above-mentioned assumption does not explain whether the contraction between muscle and its attachment sites creates any local stress.

The general objective of this thesis is to determine the stress characteristics of the lower limb by considering the local stresses. While the specific objectives are listed as follows

1. To determine the influence of muscle contraction on the stress, stress distribution, strain and, deformation of the hip joint components, particularly the femur, during normal walking.
2. To assess the effect of hip spanning and non-spanning muscles on the stress response of the meniscus and articular cartilage during normal walking.
3. To determine the local stress of muscle attachment sites (i.e. origin and insertion) due to muscle contraction within the normal walking.

1.4 Thesis outline

Following the current introduction, an outline of the thesis is presented for achieving the main aim of this study.

Chapter 2: Anatomical background & Literature review

Chapter 2 reviews the physiological and anatomical characteristics of the hip joints and their relevant soft tissue. The primary knowledge to perform an accurate virtual simulation of the lower limb will be reviewed. Consideration will be given to hip joint function, hip joint segments, hip muscle compartments, and their function within normal walking. This chapter also defines anatomical planes and directions of the human body. In addition, the preceding researches, which relates to the computational study of the bodyweight and stress analysis during the gait cycle will be reviewed and presented in this chapter.

Chapter 3: Hip and Knee Muscles (Anatomical background)

Chapter 3 provides a brief and concise overview of the musculoskeletal system and introduces the relevant anatomical and clinical concepts of hip and knee muscles. In addition, the function of the individual muscles, muscle groups, the anatomical sites of each muscle (i.e. origin and insertion) will be reviewed. This chapter also covers (3D) coordinates system of all the components in the musculoskeletal model. In this chapter, also the gait analysis and its terminology, as well as the correct points for attaching electromyography (EMG) electrodes will be reviewed. The outcomes of this chapter will be applied in a gait analysis chapter to specifically determine placements for markers and sensors in the human body, based on collected kinetic and kinematic data.

Chapter 4: Analytical Analysis to Determine HCF

Chapter 4 predicts the hip joint reaction force at the top of the femoral head using the method of joints. To accomplish the aims of this chapter, two primary case studies are introduced, which include information on hip contact force with muscle contraction, and then without considering any muscle contraction (i.e. HCF All Mus. and HCF No Mus., respectively).

For each study, the HCF will be calculated for the two critical steps of normal walking, called ‘single support stance’ (i.e. 18-30% of gait), and pre-swing phase (i.e. mid-stance at 50% of gait). In addition, 2D and 3D equilibrium static conditions will be considered for all studies to include all aspects of the analytical approach. Hence, eight studies will be defined to determine hip contact force at the top of the femoral head, using equilibrium static equations where the hip joint is located.

The obtained HCF for all 3D studies will provide adequate data for the next chapter, which will aim to determine local stress for specific regions of the femur.

Chapter 5: Stress Analysis using Analytical Approach

Chapter 5 identifies the most susceptible segments of the femur that can lead to the failure or fracture of femur. This will be done by determining their stress behaviour, via the application of a unique analytical method known as 'parallel planes'.

The main aim of this chapter is to determine local stress for inclined and perpendicular faces (i.e. 'planes') according to their susceptible regions of a femur. The predicted HCF from the previous chapter is employed to predict the stress values and their distribution for the selected vulnerable regions. Two primary case studies, HCF-All Mus. and HCF-No Mus., will be employed within single support and pre-swing gait stance. The effect of muscle contraction on local stress will be predicted for three femoral regions and two gait stances. The predicted local stress for the femoral regions will be applied in the following chapter to check the validity of the acquired results from virtual modelling and FEA.

Chapter 6: Definition of Finite Elements Parameters

Chapter 6 defines the essential characteristics of the numerical approach and finite element parameters, including muscle fibre direction, muscle contraction, body weight, and ligament contact force. Four models will be defined according to the main aim of this study, in order to determine the stress-strain configurations and deformation of lower extremities, i.e. the 3D-All Mus., Hip Mus., Knee Mus., and 3D-No Mus. In addition, this chapter provides a comprehensive review about selected parameters of FE modelling. These parameters include model segmentation for creating the CAD model, contact regions for the CAD models, material properties of the lower limb, meshing strategy, and a numerical solver approach. The FE model and its analysis generated a wide range of outcomes in factors including stress, strain, and deformation for selected CAD models, which will be reported and discussed in the next chapter.

Chapter 7: Results and Discussion

Chapter 7 reports the obtained results from the numerical approach, followed by a preliminary discussion based on the bio-functional analysis. This chapter includes two main parts. The first presents non-comparative results to determine whether the acquired results from the developed FE models and applied loading and boundary conditions, can present authenticated evidence and

results. In addition, the obtained results of this study will be compared with existing evidence and data from other studies to establish a degree of result verification. The second part of this chapter includes a comparative analysis of four trials presented in Chapter 6, to determine whether the FE analysis can acquire adequate evidence to support the main assumption of this thesis.

Chapter 8: Summary and Conclusion

Chapter 8 summarises the main conclusions of the study and emphasises the primary contribution of the thesis. The limitations of the current study and recommendations for future research will also beconsidered in this chapter.

Figure1-1 shows the selected research methodologies for this study, including analytical and numerical analysis, and how they are interlinked. The selected approaches are classified as non-invasive and non-experimental methods for examining the impact of muscles on the stress characteristics of the lower extremities.

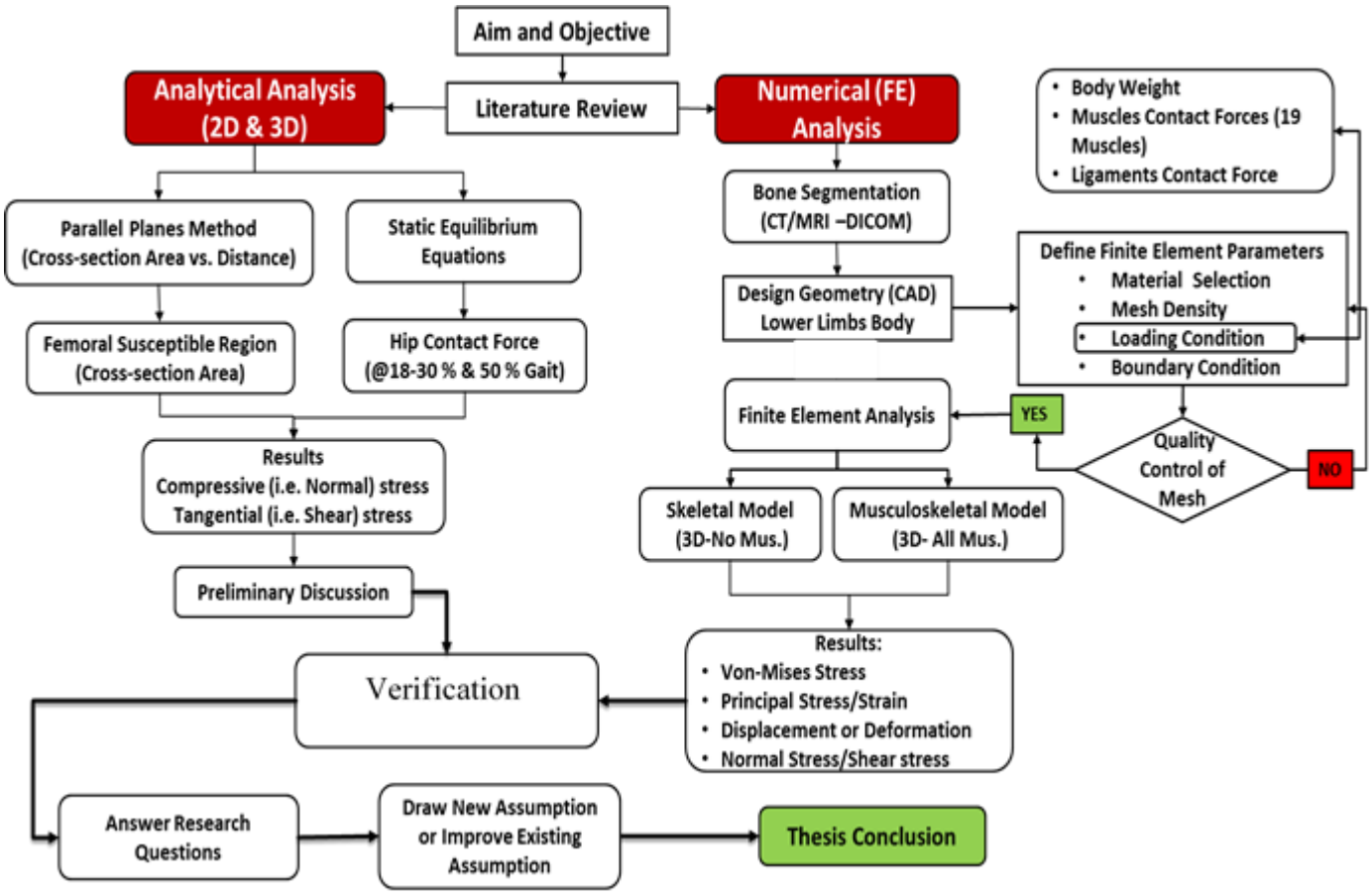

Figure 1-1: Schematic illustration of the research methodology applied for this thesis.

Chapter 2

Anatomical background and Literature review

2.1 Introduction

This chapter reviews the physiological and anatomical characteristics of the hip joints and its relevant soft tissues to comprehend the preliminary knowledge about lower limb body. The anatomical planes and directions are described before outlining the context of lower limb anatomy. In addition, the function of the hip joint, its bony segments, and key spanning muscles around the hip joint are considered. For the bony segments of the hip joint, the anatomy of the femur, its structure and its ligaments will be explained. Finally, the primary procedures of predicting the Hip Contact Force (HCF) within the normal walking cycle are reviewed to produce the reliable literature and input data for the analytical and numerical stress analysis in chapter 7 and 8.

2.1.1 Anatomical planes and directions

To describe the biomechanics and perspective of the lower limbs, it is necessary to study anatomical plans and directions within the human body. In addition, the following essential knowledge is required of the hip joint function and its movement within the normal walking activity to create the preliminary concepts for the computational analysis.

Figure 2-1 shows the different anatomical planes of the human body. The axial or horizontal plane, which is parallel to the ground, is known as the ‘transverse plane’. While, the frontal plane of the human body that is perpendicular to the transverse plane (toward the ground), is called the coronal and separate the human body into the anterior (front) and posterior (back) sections. The sagittal (median) plane divides the human body into the left and right part, and is perpendicular to the transverse and coronal planes. The three human planes can be further understood by considering six different directions of the human. With reference to the midline of the body, the sagittal plane produces the medial (toward the midline) and lateral (away from the midline) directions as shown in figure 2.1. On the coronal plane, the term ‘proximal’ describes the direction towards the origin of the limb (any arbitrary origin), whilst the direction away from the origin of the limbs is known as the ‘distal’. The clinical definition for the proximity directions are ‘superior’ and ‘inferior’ which indicated the upward and downward directions of the body respectively.

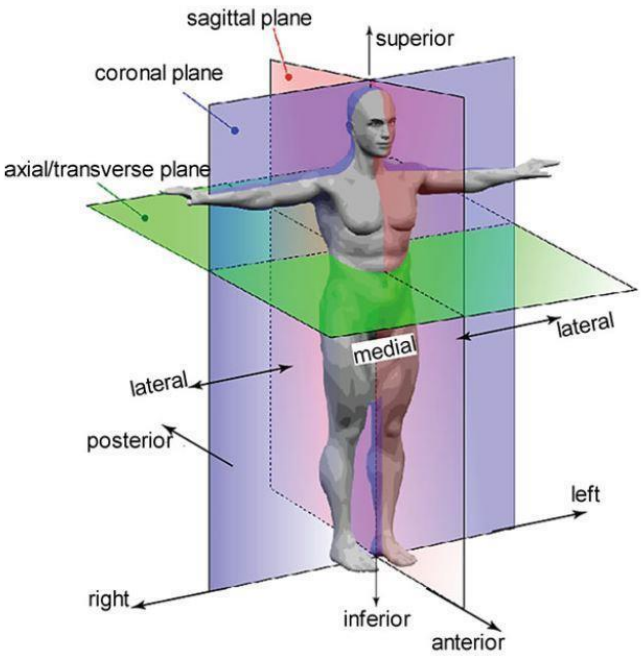

Figure 2-1: Schematic of the anatomical planes and directions of human body (Adapted from Netter, 2019).

2.2 Hip anatomy

The hip joint is formed by the primary connection between the bones of the lower and upper limbs of the human skeletal system, the scientifically term of this is the acetabulofemoral joint. The main function of the hip joint is to support the weight of the body and transfer load from the upper limb to the lower limb. A ball (femoral head) and a hemi-spherical socket (acetabulum) form the main parts of the hip joint as shown in figure 2.2 (a).

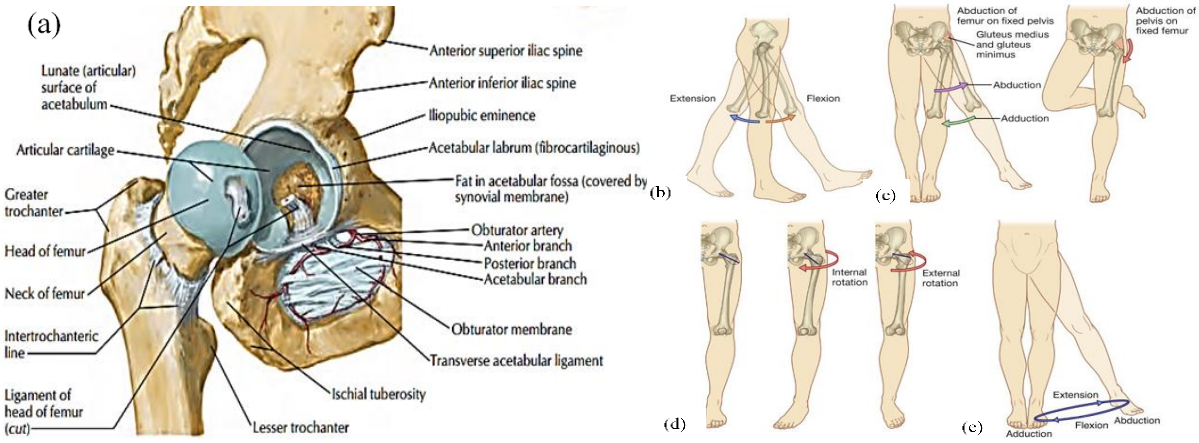

Figure 2-2: (a) The hip joint anatomy (Adapted from Netter, 2019) and hip movements including (b) flexion and extension (c) Abduction and adduction, (d) External and internal rotation, and (e) Circumduction (Basic medical key, 2016).

The head of the femur fits into the acetabulum of the pelvis and is supported by bands of the soft tissue called ligaments (i.e. hip capsule). The hip capsule provides the stability of the joint during its movements. A smooth durable cover named articular cartilage (a protein substance) which cushions at the end of surface bones on the femoral head and pelvis acetabulum facilitates the movement process. In order to provide easy and painless movements, a thin, smooth tissue called the synovial membrane covers all remaining surface of the hip joint.

2.2.1 Hip Movement

Figure 2.2 (b, c, d, and e) show that movement of the hip joint can be considered using three main rotations in three directions: flexion-extension, abduction-adduction and internal and external rotation. Flexion occurs when the leg is raised to the front of the body, thus decreasing the angle between the leg and femur. The extension gesture occurs when the position of the leg is opposed to the flexion position and can be increased to approximately 90°. However, by lifting the knee towards the chest, the knee extension can be increased by up to approximately 150 °. Hip extension increases the angle between the anterior surface of the femur and the body from the anatomical position. The range of hip movement in flexion-extension can vary from approximately 40°, where the knee is in flexion position, up to a maximum extension of 60°, where the knee is moved towards the back (Kingston 1996). Furthermore, if the angle between the midline of the lower limb body and femur increases up to 30°, abduction movement occurs (Kingston 1996). Whereas adduction of the hip is the opposite of abduction and has a similar range of motion. The lateral or external rotation of the hip takes the knee and femur away from the midline of the human body. Whilst the medial or internal motion of the hip brings the frontal thigh and knee joint closer to the midline of the body. The average range of the external and internal rotation is approximately 60° to 30° respectively (Kingston 1 996).

2.3 Soft Tissues

2.3.1 Cartilage and Ligament

Cartilage is a rubber resembling structure that exhibit hyperplastic properties. It acts as a shock absorber and load-bearing surface at the end of the long bones or joint spaces. In addition, the cartilage provides a smooth and polished surface for the body segments, which reduces the friction and assists in their ability to slide or move easily over each other (Martin, et al., 1998). There are three main types of cartilage with various functions and tasks. Elastic cartilage is of yellowish colour with low transparency and better flexibility and is located in the external part of the ear. Fibrocartilage cartilage is found in different areas in the human body, including the pubic symphysis, the intervertebral disks, and in the bony compartments of and certain tendons.

Hyaline cartilage or articular cartilage is the most prevalent type of soft tissue and is associated with different segments of the body including the tracheal rings at the end of the ribs, growth plates, and the bone surface in various type of the joints (Caligaris & Ateshian, 2008). Another soft tissue in the human body is the connective fibrous tissue called the 'ligament' which links bones together via a tough short band. The ligaments usually generate a supportive role in one direction for the joint (Hamill & Knutzen, 2009).

2.3.2 Hip and Knee Ligaments

The joint capsule includes three main ligaments which surrounding the hip joint, creating a watertight and impermeable environment. Figure 2-3 (a) shows the pubofemoral, ischiofemoral and iliofemoral ligaments stabilise the hip joint. In addition, the labrum ligament is placed around the edge of the acetabulum and creates specific structure to aid ball movement in the cup smoothly (Moore & Agur, 2005; Netter, et al., 2019). The anterior cruciate ligament (ACL) is a part of the anterior cruciate ligament, is positioned beneath the knee joint to support knee movements. The ACL located at the end of the femur condyle to the uppermost side of the tibia and connected to one of its ligaments. The collateral and cruciate ligament and their position are shown in Figure 2-3 (a). The ACL protects the tibia from moving progressively in front of the femur and makes a harmonic and relative movement to the femur (Malagelada et al., 2014). The Posterior Cruciate Ligament (PCL) is another part of the cruciate ligament, which is located at the inner area of the kneecap and it can be recognised from posterior side of the knee. The PCL keeps the femur within its location and prevents femoral moving further backward than usual (Malagelada, et al., 2014). The Lateral Collateral Ligament (LCL) stabilises the lateral compartment of the knee joint by controlling the posterolateral rotation of the tibia relative to the femur. It assists the knee flexion at 30˚. The Medial Collateral Ligament (MCL) is one of the four major ligaments, which is strong and located at the inner aspect of the knee and supports the knee joint and its movements. It assists to transfer the external stress through the knee effortlessly within the various types of knee movements. It has one femoral attachment on the medial epicondyle and two tibial attachments as insertions. The insertions points of MCL include the posteromedial crest of tibia and the SM tendon (Malagelada , et al., 2014).

2.4 Femur Bone

The femur is the longest bone in the human body and exhibits the anisotropic mechanical properties. The Young's modulus alongside of the femur axis is approximately 17.4 GPa with an angle of 90˚. While its Young's modulus parallel to the ground plane (i.e. the transverse plane) is predicted approximately 11.7 GPa (Callister, 2000). Figure 2-3 (b) shows the bone

structure of the femoral head. The femur is divided into two different types of bone material including cortical and cancellous bone, which are not homogeneous. The cancellous bone consists of spongy bone and forms the majority of the central part of a femur; the outer shell of the femur bone is made up from cortical. The major component of the epiphyses in the femur consists of the lower density material (i.e. spongy bone). Moreover, trabecular or cancellous bone is placed at the inner part of the femur (i.e. on radial view). It has very close contact with internal tissue, which supplies the blood to the bone. The femur is the longest and strongest bone in the human skeletal system and supports body weight during many activities such as running, jumping, walking, and standing. It consists of two parts; the primary part is diaphysis or called central shaft and two wider and rounded bulges at the end known as epiphyses. The epiphysis is linked to the diaphysis through conical regions known as metaphysis. The diaphysis is generally made from a higher density hard bone cortical, and at the core is composed of cancellous, which is the low-density spongy bone. The epiphyses and metaphysis mostly contains cancellous or spongy bone within a thin shell of cortical bone.

The femoral neck has an irregular cross-section and spheroid on the upper end and is approximately elliptical. The major and minor axes of ellipse has a ratio of 1.6 on the lower end, which is close to the femoral shaft. The upper part of the neck-shaft provides attachment sites for a number of muscles and builds the most tangible part of the femur known as great trochanter. The great trochanter is a large, irregular, and quadrilateral eminence section, situated approximately 10 mm below the head of the femur in the adult and is directed to the lateral and backward. The lesser trochanter is a conical eminence on the medial side of the femur on the other side of the femur (Gray, 1918).

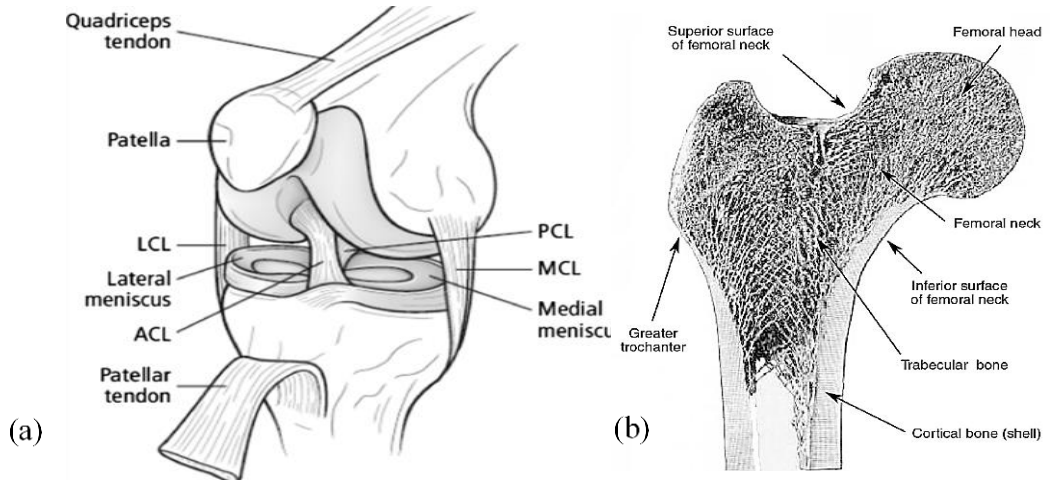

Figure 2-3 (a) The anterior view of the cruciate ligament at the kneecap (Adapted from Harris & Anderson , 2009) and (b)The structure of femur bone including the cortical and trabecular tissues (Adapted from Voo, et al., 2005).

2.4.1 Mechanical Properties of Femur

Cortical bone is also known as compact bone or lamellar bone. Forming the exterior layer of the bones, it is extremely hard, with a density between 1200 kg/m^3 and 2100 kg/m^3 (An & Draughn 2000; Jonkers, et al., 2008; Zioupos, et al., 2008). The cancellous bone, also known as the spongy or trabecular bone, is full of cavities causing a decreased density of up to 50 kg/m^3 (Gibson, 2005). An & Draughn, (2000) reported that the density of the cancellous tissue has a similar type of tiny holes resembling the cortical bone, but this has been disputed by other scholars' contributions (Zioupos, et al. 2008). Lee et al., (2012) reported the diameter of pores of cancellous bone 300-600 (μm) which has 75 – 85 % porosity. Whereas the porosity of the cortical reported 5-10 % and the diameter of pores computed 10-50 (μm).

With increasing age, the density and strength of the bone increased until human maturity (around the age of 35 years old) and then starts decreasing. Nonetheless, the bone has adaptive properties, which can alter and modify its tissue according to its density and maturity. Many studies have proposed a power law correlation between the apparent density and elastic modulus of cortical and cancellous bone as shown in 2-1(Keller, 1994; Rho, et al., 1995; Rice, et al., 1988; Schaffler & Burr, 1988). The value of the power for cortical bone (b = 4 -7.4, Currey, 1988; Schaffler & Burr, 1988) is higher than cancellous bone (b = 1.27 - 2.57, Keller, 1994; Rho, et al., 1995; Rice, et al., 1988) which showing the higher stiffness of the cortical bone tissue.

$$\boldsymbol{E} \alpha\, \boldsymbol{\rho^b} \qquad (2\text{-}1)$$

Where, ρ shows the density of the bone, E presents the Young's modulus of femur, and b is the constant parameter, which shows the stiffness of the bone tissue. Carter and Hayes (1977) formulated the relationship between the modules and density by a cubic equation. Later on, Rice, et al., (1988), computed a better correlation with a squared relationship. However, two other scholars identified the power of ρ to be slightly less (Hodgskinson & Currey 1992; Morgan et al. 2003). Furthermore, Carter and Hayes (1988) found another formula, in which the modulus and density correlation was affected by the strain rate $(\dot{e})$ which shown by equation 2-2.

$$E = 3790\, \dot{e}^{\,0.06} \rho^3 \qquad (2\text{-}2)$$

Where, $\dot{e}$ represents the strain rate of the femur and E represents the Young's modulus.

In general, the mechanical properties of femur such as modulus of elasticity and yield strength influenced by the strain rate of the test as well as the mineral composition of the bone (i.e.

density of the bone). Wright and Hayes, (1976) conducted the uniaxial tensile test on the standard longitudinal 100 samples of the bovine compact bone from the mid-diaphysis. They considered variable strain rate from 5.3×10^{-4} to 237 (1/s) to determine the microstructure and dry density of their specimens. They found significant positive correlation between increasing strain rate and obtained value of the ultimate strength and elastic modulus. For instance, for the lowest strain rate (5.3×10^{-4} 1/s) the ultimate tensile strength and elastic modulus of bovine bone are determined 99.2 ± 4.7 and 17000 ± 0.8 MPa respectively. While, by increasing the strain rate to 237 (1/s) the ultimate tensile strength and elastic modulus are increased up to 271.4 ± 8.4 and 40400 ± 4.0 MPa respectively. Furthermore, Hansen et al., (2008) studied the effect of strain rate from 0.08 up to 30 (1/s) on the compression and tensile properties of the human cortical bone. The femoral bone from the 51 years old male donor was used to make the longitudinal dog-bone shaped specimens. They concluded that young modulus is increased steadily and continuously by increasing the strain rate. In addition, the same propensity has been realised for the ultimate properties including ultimate tensile and compressive stress. Whereas the obtained results of human bone are showing less rise in comparison to the bovine compact bone. Zimmermann, et al., (2016) conducted another study to test the characteristics and behaviour of the restored osseous cell under two physiological strain rates. They considered two various strain rates including 10^{-2} and 10^{-5} (1/s) which produced the displacement rate of 1.0 and 0.001 (mm/s) respectively. The faster strain rate shows the running physiological strain and the slower strain rate represents the quasi-static loading. The femoral cortical specimens (n=15) were loaded in tension and classified in three various group including young (n= 5) and healthy individuals, individuals (n=5) diagnosed with osteoporosis (i.e. osteodensitometry) and bisphosphonate-treated cases (n= 5). Their results exhibited that the plasticity properties for all groups reduced at higher strain rate. While the osteoporosis group was reduced fibrillar deformation at low strain rate as well. In addition, it has been concluded that the restored tissue after osteoporotic is more susceptible to brittle fracture rather than the young and bisphosphonate-treated samples.

Table 2-1 compares the mechanical properties of the cancellous and human cortical bone. Several researchers were examined the human tissue bones experimentally to determine the isotropic and anisotropic properties of the bone tissue (Dong, et al.,2016 ; Homminga et al., 2002; Giesen et al., 2001; Martin et al.,1998; Mirzaali, et al., 2016; Morgan et al., 2018; Painkra et al.,2018; Wang, et al., 2010).

Giesen et al., (2001) examined 47 cylindrical cancellous bone specimens, which obtained from 24 embalmed cadavers under the uniaxial compression tests. The compression test was

performed in two loading directions including axial loading (i.e. longitudinal) and a direction perpendicular to the axial direction called transverse loading. They are concluded that the cancellous bone was in axial loading 2.8 times stronger upon failure and 3.4 times stiffer than in transverse loading.

In addition, Homminga, et al., (2002) used the "equal bone mass subset" specimens in which the subset was included a bone volume fraction less than a standard deviation from the mean of the fracture group. They designed two different groups including the control specimen group with 11 specimens (mean age 80 years, SD 12) and fracture specimen group with 19 samples (mean age 81years, SD 8). Specimens extracted either from female cadavers (control group) or from women who had experienced arthroplasty for neck fractures to make the fracture group. They could determine the compressive yield stress of the cancellous bone in a longitudinal direction around 6.7 ± 2.70 MPa.

Table 2-1: Comparison of the human cancellous and cortical bone

Mechanical properties	Cancellous	Cortical
Tensile yield stress - (Longitudinal direction)-MPa	---	18,160 ± 1,880 [(b)]
Compressive yield stress - (Longitudinal direction)-MPa	6.7 ± 2.70 [(a)]	115.06 ± 16.36 [(b)]
Young's modulus (E) (Compression test), (Longitudinal direction)	431 ± 217 [(c)]	18,160 ± 1,880 [(b)]
Young's modulus (E) (Compression test) (Transverse direction) MPa	127± 92 [(c)]	5,650 ± 1,610 [(d)]
Ultimate compressive stress MPa – (Longitudinal direction)	4.5 ± 1.90 [(c)]	153.59 ± 21.63 [(b)]
Ultimate compressive stress MPa - (Transverse direction)	1.6 ± 1.00 [(c)]	65.2 ± 13.8 [(b)]
Ultimate compressive strain (%) – (Longitudinal direction)	1.65 ± 0.29 [(c)]	1.3 ± 0.30 [(d)]
Ultimate compressive strain (%) - (Transverse direction)	2.11 ± 0.46 [(c)]	2.2 - 4.6% [(e)]

[(a)] Homminga, et al., (2002)
[(b)] Mirzaali, et al., (2016)
[(c)] Giesen, et al., (2001)
[(d)] Dong, et al., (2016)
[(e)] Martin, et al., (1998)

Dong, et al., (2016) evaluated the post-yield behaviour of cortical using a compression loading in a progressive loading protocol to determine the elastic modulus of the cortical bone. They

examined 24 cylindrical specimens from mid-shaft of the femoral of human cadaveric. Samples were obtained from eight middle-aged males (age 51.5±3.3 years old) and tested under compression loading. Dong, et al., (2016) determined that the elastic modulus of the cortical bone in a longitudinal direction (18,160 MPa) is significantly higher than the transverse direction including radial and circumferential directions (5,650 MPa).

Moreover, Mirzaali, et al., (2016) tested 20 female and 19 male from healthy donors with age from 46 to 99 years without any bone diseases. They performed various types of mechanical tests to determine the mechanical properties of the cortical bone including compression, torsion, quasi-static macroscopic tests in tension, and micro indentation test. Their results confirmed that age and small variations in bone mineral composition (i.e. average bone mineralisation) have less effect on the micro indentation properties of human lamellar tissue in elderly donors. In addition, they determined that the ultimate compressive stress in a longitudinal direction is 2.3 times higher than in the transverse direction.

2.5 Review Hip Contact Force

To determine the localised stress, strain, and deformation of hip joint compartments an *in-vivo* study is required to govern the accurate hip contact force during daily activity such as normal walking. This section attempted to review the literature and outcomes of some studies in which the computational approach applied was via musculoskeletal models to determine the joint contact force accurately. Musculoskeletal modelling is one of the most applicable methods to examine joint contact forces through body movement and daily activities. To achieve a high accuracy level of estimation, subject-specific models can be used to extract knee and hip joint contact forces during the normal activity. Twenty-four articles were reviewed to examine the applied computational modelling methods. The obtained outcomes including initial assumptions, musculoskeletal models, applied software, boundary conditions, and validation methods summarised in appendix A.

There is a direct relationship between applied numbers of muscle activation lines, degrees of freedom (DoF) and generic musculoskeletal models. Researchers considered a different number of muscle activation lines for a musculoskeletal model from 11 (Lin et al., 2010) to 163 (Moissenet et al., 2016; Zhang et al., 2015; Chen et al., 2014; Modenese et al., 2011, 2013), while the DoF number varies based on the types of joint and applied analytical assumptions (i.e. static, dynamic, 2D or 3D). For instance, for the patellofemoral (PF) joint, DoF can be considered 0, 1 or 6, while for the tibiofemoral (TF) joint it can be assumed as 1 or 6 and for the hip joint can be 3 or 6.

Alternatively, some researchers modified muscle parameters to simplify calculation steps for joint contact force and muscle contact force (Moissenet et al., 2017; Navacchia et al., 2016; Heller et al., 2005). For instance, they altered a level of muscular redundancy, muscle activation lines, muscle attachment sites on the model and other parameters of muscles.

Moissenet et al. (2016) studied different types of muscles, while Navacchia et al. (2016) and Zhang et al. (2015) examined the effect of muscle geometry, such as muscle path and insertion sites. Conversely, other researchers focused on the parameters of the Hill-type muscle, such as the length of the optimal fibre, and the length of the tendon, pennation angle and other model parameters extracted from electromyography (EMG) (Navacchia et al., 2016; Serrancoli et al., 2016; Manal and Buchanan, 2013).

Some researchers employed musculoskeletal modelling through simulation software to determine contact forces accurately (Chèze et al., 2015; Pandy and Andriacchi, 2010; Erdemir et al., 2007). In this case, they determined hip contact force and tibiofemoral joint force with a high level of accuracy by considering the initial compatibility factors for their virtual musculoskeletal models (Ding et al., 2016; Jung et al., 2016; Kia et al., 2014; Marra et al., 2014; Gerus et al., 2013). Modification of the optimisation problem in the generic musculoskeletal model and computational modelling was carried out to determine the joint-muscles contact force in normal walking. Some scholars altered the optimisation problem by changing the objective function (Knarr and Higginson, 2015; Zhang et al., 2015; Chen et al., 2014; Steele et al., 2012; Modenese et al., 2011), while others modified design parameters like joint contact force, ligaments and bony parts (Moissenet et al., 2014; Modenese et al., 2013).

With the help of an artificial hip joint instrument incorporating sensors, joint contact force was measured *in-vivo*. However, muscle contraction was difficult to measure in the body using this method. Various studies have been completed with inserted sensors to measure the force acting across the hip with the help of implants (Bergmann et al., 2001; Taylor and Walker, 2001; Taylor et al., 1997; Brand et al., 1994; Bergmann et al., 1993; Davy et al., 1988; Rydell, 1966).

Rydell (1966) conducted a study to measure strain during normal walking using strain gauges. He attached several strain gauges to a hip prosthesis and recorded signals by connected wires. The duration of the experiment was restricted as the gauges were removed once the trial was completed after six months of implantation. To acquire better results, other researchers eliminated connected wires and applied various internal batteries (Davy et al., 1988) and external induction coils (Bergmann et al., 2001; Taylor et al., 1997; Bergmann et al., 1993).

Rydell (1966) then used another type of implant to allow the transmission of signals from the body to an external antenna. Hence, transmitting signals wirelessly provided further opportunity to monitor hip contact forces for a longer period. The force acting on the hip was measured throughout the gait cycle. However, the data obtained for gait analysis was presented for peak forces only. Furthermore, there was a different impact for patients depending on their walking style and body type. Adequate steps were considered by normalising the data related to body weight (BW) or multiples of BW (Moissenet et al., 2017).

Brand et al. (1994) predicted the ratio of generated forces during the toe-off over the heel strike within the gait cycle. He stated that the ratio does not always remain constant for the same patient. Davy et al. (1988) conducted a study to examine the effect of partial load-bearing on hip contact forces for three participants using crutches for a normal gait cycle. Bergmann et al. (2001) conducted a different study to record hip contact force. They studied the effects of changing walking speed for their subject up to eight times higher than normal walking speed within the gait cycle. In two cases, the results were shown to be similar (2.79 and 2.75×BW) and for another two patients, different magnitudes were achieved (2.5 and 2.18×BW) for heel strike force. Nevertheless, they were unable to draw a definitive conclusion for the investigation because of the limited number of studies and different conditions applied. Overall, the data obtained for HCF varied from a minimum value of peak force 0.9×BW (for patient VN) in the study by Taylor et al. (2001) up to maximum peak force 4×BW measured by Bergmann et al. (2001) for patient JB.

The average peak of HCF for those participants not using aids during walking was recorded at 2.69 BW during normal walking speed using an instrumented hip replacement (Bergmann et al., 2016; Taylor et al., 2001; Taylor et al., 1997; Brand et al., 1994; Bergmann et al., 1993; Rydell et al., 1966).

Some researchers employed different types of software to attain outcomes including Anybody (Damsgaard et al., 2006) and OpenSim (Delp et al., 2007). Both software packages were used for slightly more than fifty per cent of the studies (13 studies). MATLAB was applied for a quarter of the studies and ADAMS (MSC Software, USA) or custom-made software, SIMM (Motion Analysis Corporation, Musculographics, USA) were applied for the other studies.

Heller et al. (2001) used custom-made software to generate a musculoskeletal model of the hip joint based on VH's project (Ackerman, 1991). They considered DoFs 6, 3, 6 and 3 for the pelvis, hip, TF and ankle, respectively. They developed a lower extremities model with 95 muscle activation lines per leg and used a point load technique to connect the muscle attachment sites. For the validation dataset, they used HIP98 data for the following subjects,

HSR, KWR, PFL and IBL (Bergmann et al., 2001). Additionally, Heller et al. (2005) carried out another study four years later with some differences, including a redundant number of muscles and reported a superior-inferior hip contact force 2.8 - 3.8 ($\pm$ 0.1)×BW.

Fregly et al. (2012) used medical imaging data to investigate the tibiofemoral (knee joint) contact force in medial and lateral directions through various daily activities (e.g. walking) and different forms of walking (e.g. normal, medial trust, bouncy). They employed Horsman et al.'s (2007) model with 163 muscle activation lines for each leg to complete the musculoskeletal model. They applied point load and wrapping-affected surface techniques for a participant with a mass of 78.4 kg and a height of 167 cm. They reported total knee contact force 2600 N, about 3.3×BW of their participant. However, they did not compute the applied stress on the knee compartments, due to employing muscle activation lines and local stress.

Lundberg et al. (2012) conducted a study to develop a musculoskeletal model using MATLAB software. They used Delp's (2009) model, its variants and 15 muscle activation lines directed by point load technique. They considered six DoFs for TF and varus-valgus moment linear function for their model. The validation of datasets was conducted based on the acquired gait data from four persons who had instrumented knee implants according to Mündermann et al.'s (2008) study. Furthermore, they carried out another study in 2013 with some differences, including the number of DoFs, the ratio of medial-lateral contact force and passive stiffness of the joint model. They reported TF contact force 2.8×BW for a female subject with a height of 167 cm and a weight of 78.4 kg.

Dumas et al. (2012) used MATLAB software to create a musculoskeletal model of the tibiofemoral joint. They applied Delp's (2009) model and 43 muscular activation lines per leg. DoFs in this study were 6, 3, 1 and 1 for the pelvis, hip, TF and ankle, respectively. They assumed the point load technique for muscle activation lines and the inverse dynamics-based static optimisation method for force estimation. The objective function was the sum of squared muscle stresses for a male subject weighing 67 kg and at a height of 172 cm. They reported the maximum hip and TF contact forces as 4.5 and 4.3×BW, respectively.

Hast and Piazza (2013) conducted another study on generic musculoskeletal models of the tibiofemoral joint using SIMM software. Delp's (1990) model with DoFs for the pelvis, hip, TF, PF and ankle were 6, 3, 6, 6 and 1, respectively. They assumed 13 muscle activation lines per leg using wrapping surfaces and point load. They considered a rigid body spring for the joint contact model according to Li et al.'s (1997) study. They developed lower extremities based on an 83-year-old subject weighing 67 kg with a height of 172 cm. They computed an average of three trials and reported the maximum TF contact force around $2.9 \pm 0.2 \times$ BW.

Modenese et al. (2011) carried out a study using OpenSim software to generate the musculoskeletal model of a hip joint. They applied Horsman et al.'s (2007) model, its variant and 163 muscle activation lines per leg. They employed DoFs for the pelvis, hip, TF and ankle at 6, 3, 1 and 1, respectively. The wrapping surfaces, point load technique and one-point rigid contact model was used to model the joint contact. They used HIP98 software for the validation process based on the acquired datasets from the subjects HSR, KWR, PFL and IBL, according to Bergmann et al.'s (2001) study. They reported HCF for all subjects from 2.8 to 4.2 × BW.
Manal and Buchanan (2013) conducted a study using SIMM software to generate a musculoskeletal model of a TF joint. They used Delp's (2009) model variants and 12 muscle activation lines per leg to develop their model. They assumed various DoF numbers for their computational model including 6, 3, 3 and 3 for pelvic, hip, TF and ankle joint, respectively. They used a male subject weighing 78.4 kg and a height of 167 cm and reported medial and lateral TF contact forces 1.78×BW and 0.5×BW, respectively.

Lund et al. (2015) used the Anybody software and variation dataset for studying the tibiofemoral joint and its total contact force. They assumed various DoF numbers for their computational model, including six DoFs for the pelvis, three DoFs for the hip, one DoF for the TF, one DoF for the PF and two DoFs for the ankle joint. They applied 159 muscle activation lines per leg for their study. They found minimum and maximum TF contact forces around 1.63 and 4.24×BW, respectively, for the various stances of the gait cycle.

Lerner et al. (2015) conducted another study using OpenSim software to generate a musculoskeletal model to determine TF contact force. They applied Delp's (1990) model with various DoFs for the pelvis, hip, TF, ankle and subtalar (6, 3, 1, 1 and 1, respectively). They assumed 64 muscle activation lines per leg and point load techniques with the assumption of a two-point rigid contact model (Steele et al., 2012). They used an 82-year-old male subject weighing 67 kg and 172 cm in height. They reported the first peak of medial and lateral TF contact force between 1234–1461 N and 319–502 N, respectively. The second peak of TF contact force was reported from 786 to 1244 N on the medial side and 85 to 417 N on the lateral side of TF. Hence, Lerner et al. (2015) concluded that the maximum TF contact force could be 1.8 and 1.52×BW on the medial and lateral side of TF, respectively.

Guess et al. (2014) carried out a study using ADAMS, MATLAB and Simulink software to create a TF joint. They developed 44 muscle activation lines per leg, which was directed by muscle point load technique. The joint contact model was assumed as a deformable contact with viscous damping. They used a male subject with a mass of 64.6 kg and height of 166 cm.

They reported the maximum TF contact force 1.02×BW on the medial side and 1.3×BW on the lateral side of TF.

Serrancoli et al. (2016) conducted a study to determine total knee contact force using Arnold et al.'s (2010) model. Their model had various DoFs, including 6, 3, 6, 6 and 2 for pelvic, hip, TF, PF and ankle joints, respectively. They considered 44 muscle activation lines per leg and wrapping surfaces were used for muscle paths. They used an 88-year-old weighing 65 kg and 166 cm in height to develop the model. They reported the maximum total knee contact force as 2.45×BW.

2.6 Review of the FE analysis of the lower extremities

In this section, the preceding researches and studies related to computing stress analysis, conducting loading conditions and applying boundary conditions for FE models of the lower extremities during the gait cycle were reviewed. Rapperport et al., (1985) conducted a study to obtain the equivalent stress of the femur in hip joint by considering the distributed pressure across the articular surface of femoral head. They estimated a femur stress of 10 MPa by applying load magnitude of 1000 N statically with an angle of 40˚ towards inferior and medial direction. Rapperport et al., (1985), applied static loading condition (1000 N) while according to the realistic condition during the gait cycle the dynamic load should apply. According the conducted literature, the dynamic loading condition can be varied from 2.5 up to 4.5 × BW as a function of the time of walking (Rydell, et al., 1966; Brand, et al., 1994; Taylor, et al., 1997; Taylor, et al., 2001; Bergmann, et al., 1993; Bergmann, et al., 2016). Therefore, their results cannot show the realistic stress characteristics of the femur.

Later on, Lotz et al., (1995) investigated the effect of structural bone by considering the cortical and cancellous material for the femur bone during the gait cycle. They determined the von-Mises stress for the healthy case study at sub-capital of the femur head 11 MPa within a heel strike. While during the standing on one leg, the stress estimated 7.2 MPa. In addition, they predicted equivalent stress 19 MPa for mid-plane of the femoral neck within the single support stance. Their predicted equivalent stress for the mid of femoral neck at a single support stance (19 MPa) is highly matched with the Antonio, et al., (2012)' result.

Antonio, et al., (2012) predicted failure mode of the femur via using different types of materials including isotropic and orthotropic. They applied a complex loading condition including seven major muscles during the gait cycle. They estimated equivalent stress for isotropic and orthotropic materials 16 and 18.05 MPa respectively. In addition, they stated that the magnitude and configuration of maximum principal stress highly matched with the equivalent stress.

Montanini and Filardi (2010) investigated the local stress and strain during the fixation of the femur in cortical bone via experimental and finite element model. They reported that a wide range of stress depends on the attachment sites of the strain gauges and local stress on the surface of the femur. They estimated the equivalent stress from 18 to 42 MPa for the S2 case study. In this case, the implanted sensor has been used to determine the strain and stress.

Jonkers et al., (2008), simulated half of femur bone to investigate stress distribution on proximal femur after total hip replacement. They applied cementless implant, quasi-static loading condition, and considering the muscles' contractions. They reported maximum von-Mises stress 45 MPa for the patients who were examined between three to six months after THR. Jonkers et al., (2008) simplified the hip joint and considered just half of the femur geometry, which were created a significant deviation in their obtained results.

Chethan, et al., (2018) compared the homogeneous and inhomogeneous femur bone to determine the effect of the material structure on the von-Mises stress under static loading condition. They reported a maximum von-Mises 20.7 MPa for static loading 1000 N, while for the 3000 N; the magnitude of von-Mises was estimated up to 57.1 MPa. In addition, Cook et al., (2017) reported a similar von-Mises value for the implanted femur up to 63.01 MPa and for the same loading condition (i.e. 3000 N). Chethan, et al., (2018) and Cook et al., (2017) did not consider any femoral head cartilage and other lower extremities in their hip joint structure or FE model.

Cardiff, et al., (2013) analysed the hip joint numerically at three different phases of the gait cycle including maximum force at the mid-stance, heel strike, and toe-off phase. They studied the effect of muscle contraction of a group of muscles (i.e. abductor muscles) included gluteus medius and gluteus minimus, on stress distribution of the acetabular, femoral head and pelvis using the point load and mapped approaches. They developed a finite volume-based transient structural contact solver technique to analyse the hip joint. For their analysis, the updated Lagrangian mathematical model and linear elastic properties were applied, while inertia and body forces were neglected.

Cardiff et al. (2013) predicted the maximum von Mises stress at 30 MPa for three sites of the hip joint at the mid-stance of the gait cycle, including the ilium directly above the acetabulum, the acetabular roof bone and near the fixed iliosacral joint. The maximum predicted contact pressure was 26 MPa, occurring in the most superior contact region of the hip joint.

They also examined the same contact regions at the toe-off and heel strike of the gait cycle. Three contact regions of the heel strike model experienced the maximum predicted contact

pressure at 26 MPa, where the contact area was 3.83 x 10^{-4} m^2 and the average pressure was 10.1 MPa. In contrast, there were two (rather than three) contact regions in the toe-off model with the contact area at 4.62 x 10^{-4} m^2. The maximum predicted contact pressure for the toe-off model was 23 MPa, while the average pressure was 5.93 MPa.

Furthermore, the maximum contact pressure of the thinner cartilage model (0.48 mm) was 34.58 MPa for a contact area of 2.51 x 10^{-4} m^2. Hence, Cardiff et al. (2013) reported the average contact pressure of 9.30 MPa for the thinner cartilage model and the cartilage model of 0.72 mm with a contact area of 3.59 x 10^{-4} m^2, the maximum predicted contact pressure and the average contact pressure were 21.59 MPa and 6.86 MPa, respectively.

Cardiff et al. (2013) completed the stress analysis of the hip joint using the model with just the abductor muscle group, one-third of the femur, pelvis and their cartilages. Therefore, the effect of other compartments of the lower limbs of the body such as the articular cartilage, meniscus, and tibia has been neglected. In addition, they only considered one muscle group and the effect of muscle contraction of the majority of hip spanning and non-hip spanning muscles was neglected in their model which can create a significant variation on the local stress. Furthermore, they conducted the nonlinear study and developed three different models based on the critical position of the femur of the gait cycle and then applied the static force on their models to determine the stress of the femur. Although the developed approach has saved the cost of finite volume analysis, the effect of residual stress from the prior moment of the three-targeted stances is completely neglected. In addition, the obtained results are restricted merely to the three models and do not produce a clear image of the stress behaviour of the femur during the whole gait cycle.

Several FE software can be applied to analyse the lower extremities numerically including Simulink/Matlab, Simulia Abaqus, Simulia Tosca, Solidworks, and Ansys Workbench (Coquim et al., 2018; Gislason et al., 2015; Guess et al., 2014; Obbink-Huizer, 2020).

For instance, Obbink-Huizer (2020) conducted a study to optimise a hip implant with the objective of minimising the strain energy density of the optimised part. In this study, the femur was modelled in Solidworks and transferred to Simulia Abaqus. Kinematic couplings were assigned to bond the hip contact region, knee region and muscle region to their individual reference points. Furthermore, the BW load in all three directions was applied to the hip and muscle reference points, while the knee reference point was fully constrained with a muscle adhered to the attachment site. They improved the stress result of the optimised model by 35% in comparison to the actual model.

Nevertheless, over the last two decades, many researchers have selected Ansys Workbench to conduct FE analysis of the lower extremities (Coquim et al., 2018; Mughal et al., 2015; Jade et al., 2014; Dash et al., 2013; Maharaj et al., 2013; Mishra et al., 2011; Schulze-Bauer et al., 2007; Senalp et al., 2007; Kayabasi and Erzincanli, 2006).

Senalp et al. (2007) analysed the curvatures of four various stems of a hip prosthesis under static, dynamic and fatigue loading using commercial finite element analysis software. Ansys was applied to examine the stem shapes under static BW load and dynamic walking load. Pro/Engineer software was used to develop CAD modelling of the stem shapes and the models were transferred to Ansys. They assumed two materials, Ti–6Al–4V and cobalt-chromium, to examine the performance of the stem shapes based on the material properties. They concluded that the notched and curved stems could reduce the sliding of the implant in bone-cement and helped the implant stick to the bone-cement surface. In addition, a particular stem geometry (stem 3) made of Ti–6Al–4V demonstrated the best stress response under static and dynamic loading.

Maharaj et al., (2013) studied the curing methods of the fractured bone by using bone plates to join the fractured bone. They are examined various bone plates made of different biomaterials including stainless steel, titanium, alumina, and Nylon to determine the best material for the joining plate application. They modelled femur and fixation plates in Solidworks and transferred models to the Ansys Workbench to complete the static structural analysis.

They concluded that the titanium and stainless steel (316 L) plates were created similar equivalent stress, while the total deformation of the titanium was considerably lower than stainless steel.

Jade et al., (2014) conducted a study to determine the role of curvature geometry in mechanical strength of femoral diaphysis. They modelled the femoral diaphysis as a hollow cylinder then conducted finite element analysis by Ansys Workbench (V.14.0). Subsequently, to verify their obtained results the CT scan analysis was employed. They reported the maximum von-Mises stress via FE software and CT scan 18 and 21 MPa respectively. However, the role of muscles and the effect of muscle contraction on the stress distribution have been neglected.

Mughal et al., (2015) conducted another study to examine the stresses behaviour of the human femur. They developed a CAD model using the 3D scanning of the generic human femur for an individual weighing 70 kg, an average adult weight, as a static loading condition. An inhomogeneous femoral structure with a marrow cavity as a hollow cylinder was developed. The FE analysis was built using solid tetrahedral elements via Ansys Workbench. They identified maximum normal stress on the posterior side of the femur shaft at 24.23 MPa.

Coquim et al. (2018) conducted a study using Ansys Workbench to investigate the biomechanical performance of the metal plate and bone strut technique for fixing recalcitrant non-union of femur mid-shaft defects. FE analysis and experimental tests were applied to examine the femur at 15˚ of adduction at a subclinical hip force of 1 kN and 3 kN, respectively. For FE analysis, the 3 kN load represented about four times the bodyweight of a 75 kg person to examine clinically relevant cases. The loading conditions were applied on the intact femur and eight different models with a combination of a femur and lateral metal plates. The metal plates were modelled as a fixed part alongside the femur length. They concluded that an intact femur experienced the lowest peak of stress at 40 MPa, while the other eight cases experienced stress in the range of 42 to 170 MPa, which made them all the more susceptible to fracture. Nevertheless, the equivalent stress of the intact femur obtained from FE analysis may not represent the realistic stress value because the effect of muscle contraction was been considered.

There are several reasons why Ansys software has been selected as the main platform to conduct FE analysis in this study. The Ansys Workbench enables researchers to analyse complex structures, such as the lower extremities, using different custom materials and various available solvers. Furthermore, it provides a project management area to connect multi-physics analysis effortlessly and conduct parametric studies (Pereira, 2019).

In this case, multiple scenarios and several physics can be analysed under similar boundary conditions, loading conditions, meshing systems and FE solver. Furthermore, to compare the outcomes of various studies in a platform, the project management area helps researchers connect multi-physics and various scenarios whilst for other software packages it is required to use the coding system to compare the acquired results. Ansys Workbench provides a quasi-static platform to analyse large assemblies (e.g. seven compartments of a lower leg) under a function of force-time and achieves the nonlinear results. The Ansys distributed compute services (DCS) aids the researcher to manage the several iterations, design points, and tasks that are spread across networks, clusters, and operating systems (Pereira, 2019).

In this case, the cluster-based analysis helps researcher to apply the nonlinear iterations solver, actual 3D geometries, and various contact regions for the FE models to enhance the accuracy level of stress analysis and achieve valid results. For the meshing system, ANSYS Design-Modeler provides a smart meshing structure to achieve optimal meshing on the parts and assembly for linear and non-linear studies. However, different modules were added to the Ansys software to control and adjust the mesh as needed for the project (Pereira, 2019).

Chapter 3

Hip and Knee Muscles Anatomical background

3.1 Introduction

This chapter provides a brief and concise overview of the musculoskeletal system by introducing the relevant anatomical and clinical concepts of hip and knee muscle including injuries and complications. It is necessary to understand the bio-function and structure of muscles to analyse their performance during the normal walking. In addition, it is essential to determine the coordinate system of the lower limb to predict the muscle contraction and generated moment around the hip joint.

Skeletal muscles creates various types of movement and activity in body segments by generating force or inducing pressure on the human skeleton. Each muscle is attached to the skeleton through two points of body segments called origin and insertion (Hamill & Knutzen, 2009). Within a muscle contraction, the generated tension caused to move the muscle insertion towards the origin site while the origin point of muscle is fixed.

Muscles can be classified into three main groups according to their activities, concentric, eccentric and isometric action. However, each muscle only creates one type of rotation in the joint. A concentric action occurs when a muscle condenses during its activity, thus causing movement in the joint or attached bones by contraction. Several joints movements are created by concentric muscle action, for example, flexion of the knee. On the other hand, the term of eccentric muscle action is applied exclusively to those joints, which are subjected to an external rotation greater than the torque generated by the muscle. The term isometric muscle action is used for muscles that contract and generates tension but where there is no significant change in the joint orientation. For instance, holding an arm statically (Hamill & Knutzen, 2009).

3.2 Musculoskeletal System

Muscles and ligaments are associated with various types of movement in the human skeleton. Ligaments are fibrous tissues, which connect two bones and assisting in muscles to create various types of movement in the human body. Muscles and their attached ligaments control and synchronise any movements within the range of daily activities or high-risk activities (Van

Wynsberghe et al. 1995). Twenty- two muscles cross the hip and knee joint contributed to generate the hip movements. All these muscles have different attachment sites in the skeleton, which allows different actions or muscles functions to take place. The muscle origin point is the fixed site of a muscle compartment where the attachment point remains relatively immobile during its contraction. The insertion site defines the other side of the muscle that attaches to the bone or ligaments and can easily move by muscle contraction. It is noted that a muscle may not always have two specific points to attach; they may attach to the common tendons with other individual muscles (e.g. quadriceps muscles), or cover a wide-ranging area of bones to attach (e.g. quadriceps muscles), or cover a wide range area of bones to attach to (e.g. gluteus maximus) (Molini, et al., 2011). Table 3-1 represents muscle functions and their origin and insertions of the major hip muscles.

Table 3-1:Main functions of hip muscles and their origin and insertion points (adapted from Dowson et al., 1981)

Movement	**Muscle**	**Origin**	**Insertion**
Flexion	Gracilis	Pubic bone	Anterior medial tibial condyle
	Pectineus	Pubic bone	Pectineal line
	Iliopsoas	Iliac fossa, anterior lumber spine	Lesser trochanter
	Sartorius	Anterior superior iliac spine	Anterior medial tibial condyle
	Rectus Femoris	Anterior superior iliac spine	Tibial tuber via patellar tendon
Extension	Gluteus maximus	Posterior ilium, sacrum	Iliotibial band and gluteal tuberosity
	Biceps Femoris	Ischial tuberosity, linea Aspera	Fibular head
	Semitendinosus	Ischial tuberosity	Anterior - medial tibial condyle
	Semimembranosus	Ischial tuberosity	Medial tibial condyle
Abduction	Tensor Fascia Latae	Lateral to Anterior superior iliac spine	Inserts into iliotibial band
	Gluteus medius	Gluteal lines on posterior ilium	Greater trochanter
	Gluteus minimus	Gluteal lines on posterior ilium	Greater trochanter
Adduction	Adductor magnus	Inferior pubis and ischium	Adductor tuberosity, linea aspera
	Adductor longus	Pubic bone	Linea aspera
	Adductor brevis	Pubic bone	Upper linea aspera

3.3 Anatomy of Muscles

Human muscles can be classified according their functions, activities or by their attachment places, therefore muscle classification would be very complicated in a scientific study. Two muscle groups can be identified according to their attachment points, hip & groin muscles group and knee muscles group (Netter, et al., 2019). The current study reviewed the function and force of the 21 individual muscles around hip and knee joints within normal walking. They can be classified in various shape and form, but are mainly involved in lower extremities activities and movements.

3.4 Knee Muscles

3.4.1 Quadriceps Femoris Muscles

According to Kim et al., (2009) the knee muscle is comprised of the quadriceps femoris and hamstring muscle groups. The quadriceps muscles are located on the front side of the femur and includes four muscles; Vastus lateralis (VL), Vastus Intermedius (VIM), Vastus Medialis (VM), and Rectus Femoris (RF). These four muscles extend the knee joint during concentric contraction. The RF and VIM muscles form the intermediate part of muscle whereas the VL is located on the lateral side of the muscle and the VM is situated on the medial side of the femur (Hamill & Knutzen, 2009). Figure 3-1 presents the origin and insertion of quadricep muscles. The RF is the only quadricep muscle, which is attached to two joints and connects the knee joint to the hip joint. It has two origin points on the pelvis and femur (anterior inferior iliac and upper margin of the acetabulum), whilst its insertion point places on the quadriceps tendon (Hamill & Knutzen, 2009). The function of the RF is varied, as it is dependent upon its lever and its different conjunctions. However, it is the only the muscle that assists the hip flexion movement by bending the femur bone and supporting an extension of the knee joint (Thorpe, 2015). The VL is located on the right side of the thighbone on the frontal plane view and is the strongest muscle in the quadriceps femoris muscle. It has two origins from the femur, the linea aspera and great trochanter as well as having one insertion on the lateral condyle of the femur (kenhub-Education, 2013). The VM also has two origins including linea aspera and an intertrochanteric line of the femur. Its insertion is located on the patella implement of the outermost side of the knee junction, helping to extend the entire femur. The origin point of the VIM is located at the front side of the femur near to the great trochanter and the insertion of the VIM is located on the quadriceps tendon. It is hard to study and obtain VIM signals using surface electromyography method due to its deep positioning behind the rectus femoris and leg-bone (Miller & Webb, 2008; Moore & Dalley, 2006).

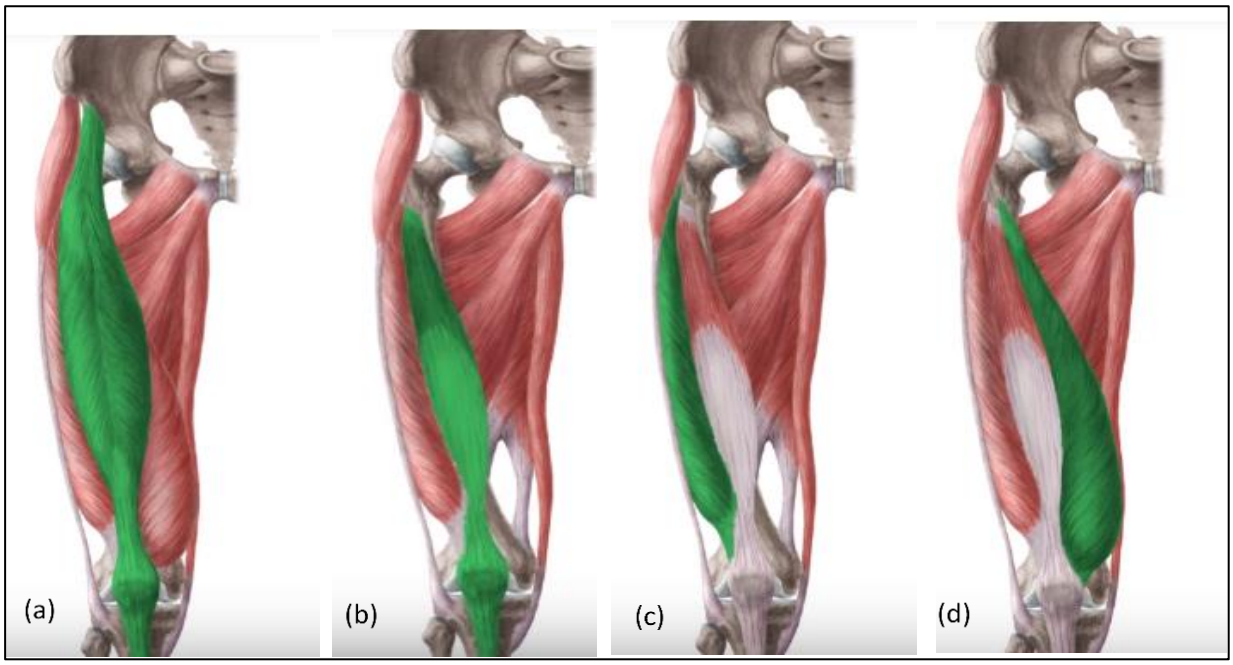

Figure 3-1: The quadriceps femoris muscles attached to the right femur, including (a) RF, (b) VIM, (c) VL and (d) VM (Adapted from ken hub-Education, 2013).

3.4.2 Hamstring Muscles Group

The hamstring muscles group is classified as a knee muscle family and mainly contributes to the knee flexion. (Hamill & Knutzen, 2009). The hamstring muscles consists two components including Semitendinosus (ST) and Semimembranosus (SM) muscles as presented in Figure 3-2. The hamstring is a member of the posterior compartment muscles, which is attached across the knee and hip joint. The main function of the SM and ST is to extend the femur around the hip and is associated with the flexion of the leg in the knee joint. During knee flexion, the biceps femoris externally rotate the leg whereas the SM and ST support internal rotation of the knee joint (Hamill & Knutzen, 2009).

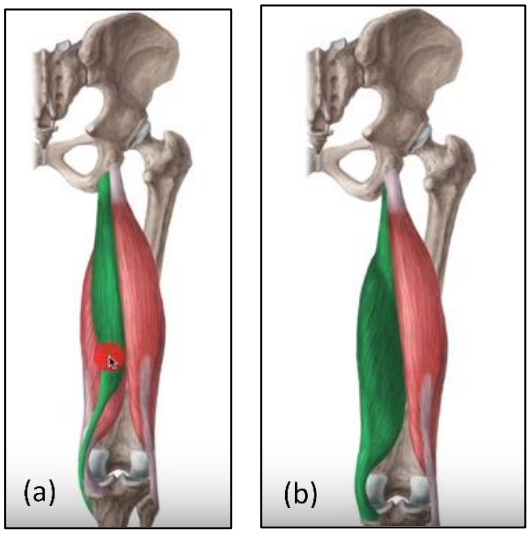

Figure 3-2: The hamstring muscles attached to the right femur, including (a) ST and (b) SM, (Adapted from ken hub-Education, 2013).

3.5 Hip and Groin Muscles

The hip and groin muscles includes four groups of muscles and two individual muscles: the adductor group, the iliopsoas group, the gluteal group, the biceps femoris group, and two single muscles including gastrocnemius and soleus muscles (Netter, et al., 2019; Thorpe, 2015).

3.5.1 Adductor Muscles Group

The adductor muscles support hip adducting-abducting movements. This means they aid body a segment (such as a leg) to move from the outside to the centre of the body, and vice versa. The groin muscles include five main muscles including Pectineus, Adductor Magnus (ADDM), Adductor Longus (ADDL), Adductor Brevis (ADDB), and Gracilis (GR) (Netter, et al., 2019; ken hub-Education, 2013). In addition, one subset muscle named Adductor Minimus (ADDM) is attached to the other adductor muscles. Figure 3-3 shows the origins and insertion of the adductor muscles group. The pectineus is located between the iliopsoas and adductor longus muscles. It is generates very low-level signals of EMG; and therefore, cannot be easily examined its signal using surface electromyography method. In this study, the location of origin and incretion of the pectineus muscle were neglected in the computational model and analysis chapters, for the sake of simplicity. However, its magnitude was considered as part of the adductor group muscles. The Gracilis (GR) muscle is the only muscle, which links the hip and knee joints in this group. The origin point of the GR is located on the external point of the ischiopubic ramus (on the pubic bone) and its insertion extends down to the upper medial shaft of the tibia (Netter, et al., 2019; Thorpe, 2015).

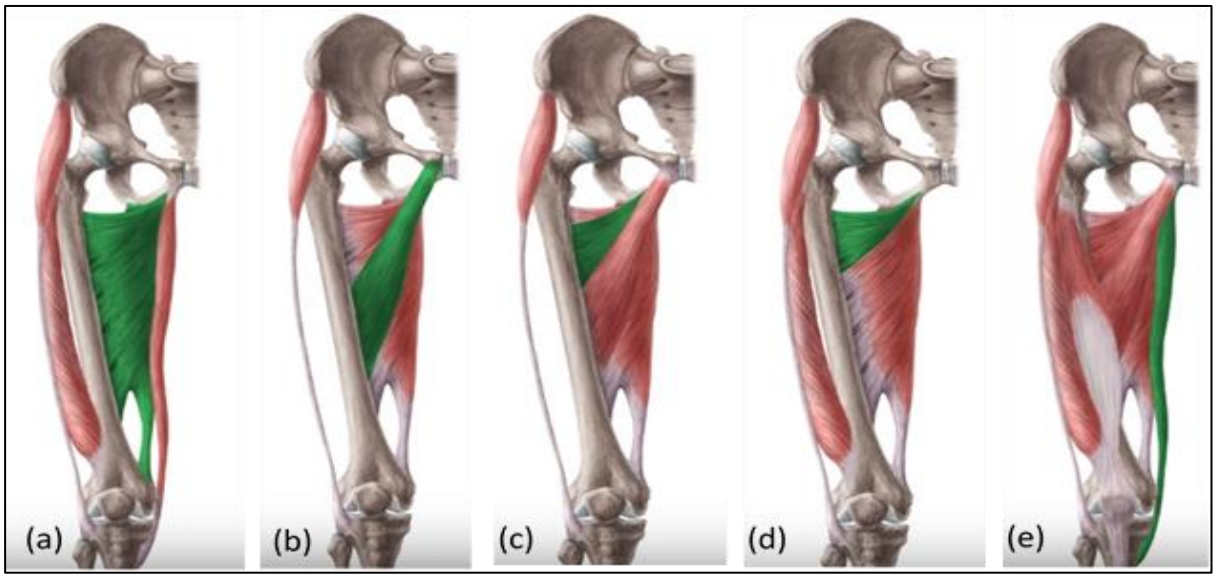

Figure 3-3: The adductor muscles group attached to the right femur. (a) Adductor Magnus, (b) Adductor Longus, (c) Adductor Brevis, (d) Adductor Minimus, and (e) Gracilis (Adapted from ken hub-Education, 2013).

3.5.2 Gluteal Group Muscles

Three main muscles of the gluteal group muscles are shown in figure 3-4. One of the strongest muscles in the human body is the Gluteus Maximus muscle (G-Max), which is located in the buttocks and connects the coccyx to the other surrounding bones in that area. The G-Max is responsible for the movement of the hip joint and femur (Thorpe, 2015). The Gluteus Medius muscle (G-Med) is attached to the great trochanter at the top of the femur and its origin placed on the other end of the ilium of the pelvis bone. The main function of the G-Med is the rotation of the femur from the centre of the body superficially, which stabilises normal walking. Gluteus Minimus muscle (G-Min) inserts into the great trochanter on the top of the femur bone and its origin locates on the ilium of the pelvis. The G-Min muscle surrounds the hip joint and is used as a secondary muscle to support hip extension (Thorpe, 2015).

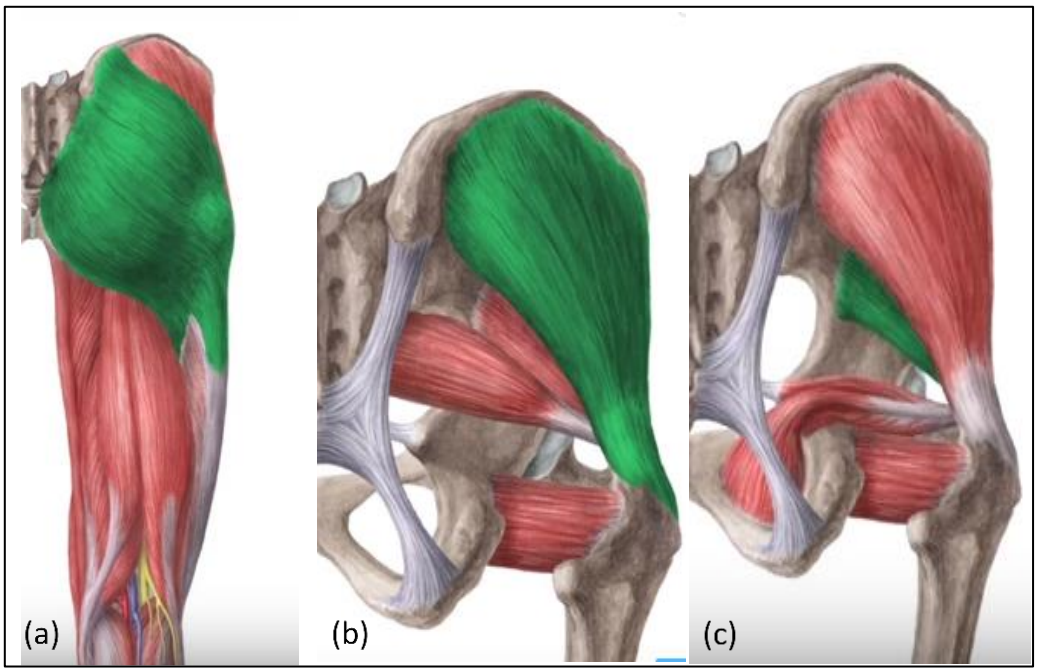

Figure 3-4: The three muscles of gluteal muscles group attached to the hip joint (a) Gluteus maximus, (b) Gluteus medius, and (c) Gluteus minimus (Adapted from ken hub-Education, 2013).

3.5.3 Biceps Femoris and Iliopsoas Group

The Biceps Femoris (BF) includes two muscles named long head (BFLH) and short head (BFSH) muscles. They are jointed together distally in their origin point on the ischial tuberosity of the pelvis. Their primary insertion point of the BF-long head is located on the fibular head but there are two other insertions points named the lateral collateral ligaments and the lateral tibial condyle. Figure 3-5 (a) shows the BF long head muscle while the short head cannot be seen on the posterior view. The BF contributes to support the knee flexion as well as tibia

rotation laterally and hip flexion (Thorpe, 2015). The iliopsoas muscle is spanning around the hip joint and consisting of two muscles with various origin areas. As part of the iliopsoas group, the psoas major and Iliacus muscles are associated with the hip flexion and have an important role during walking. The origin point of iliacus muscle is located on the iliac fossa of the pelvis and its insertion point is placed on the lesser trochanter of the femur with the insertion of the psoas muscle. Figure 3-5 (b) shows the origin and insertion of the iliopsoas muscle (Teitz & Graney, 2003).

3.5.4 Gastrocnemius and Soleus muscles

The plantarflexion supports various foot movements, including toe flexion downward and by increasing the angle between the toe and sole of the leg. This type of movement is required in jumping, walking and running (Teitz & Graney, 2003). The gastrocnemius muscle (GAS) is a powerful and large muscle that is attached to the leg and supports the body segment for plantarflexion and knee flexion. Figure 3-5 (c) shows the insertion and origin points of the GAS and soleus muscles, their insertion points are located on the calcaneal tuberosity and have conjoint areas on the posterior compartment of the leg, whilst their origin points are located in different places of the lower limb segments. The soleus muscle originates from the head of the fibula whereas the GAS muscle origination on the medial and lateral of femur condyle (Teitz & Graney, 2003).

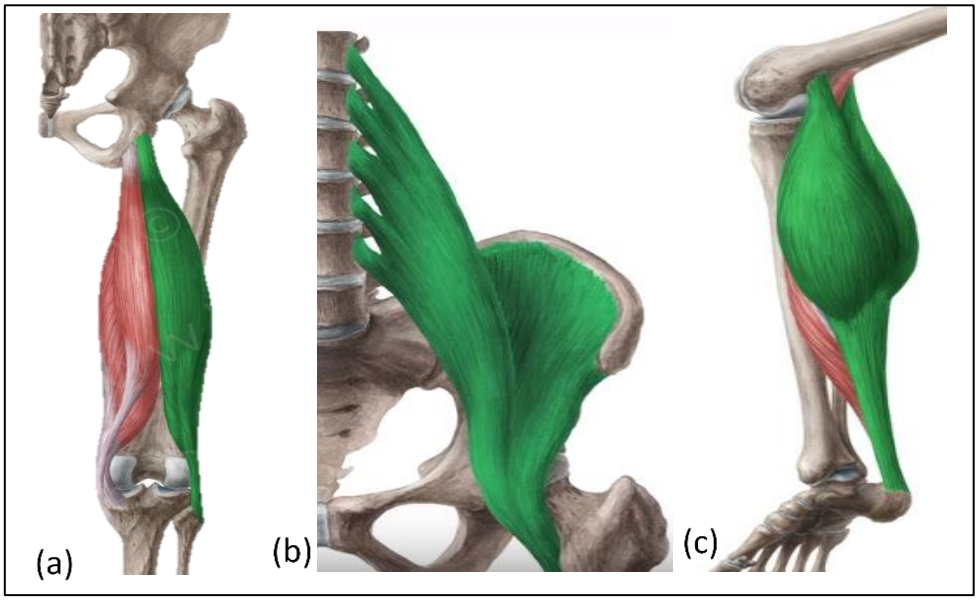

Figure 3-5: Hip Muscle group including (a) Bicep femoris long head, (b) The iliopsoas muscle consists of the psoas major and the iliacus muscles, and (c) Soleus and Gastrocnemius muscles (Adapted from kenhub-Education, 2013).

3.6 Muscle Injury and Remedial

Muscles injury minimises the ability of mobile to produce force and causes restricted muscle function. Any muscle is affected by laceration can cause a change in; its mechanical and biological characteristics; even after the healing process, the lacerated muscle may never return to its original shape and form. Several studies were conducted to find the best methods to recover injured muscles as well as to identify the weakest point of muscle in the body (Kaariainen et al. 1998; Garrett & Duncan 1988; Huard et al. 2002; Meneghini et al. 2006; Malik & Dorr 2007; Crow et al. 2007).

During hip arthroplasty, muscles are separated from their attachment bones and divided from the other muscle group. These operations cause a complicated issue called muscle laceration and reduce the quality of the muscle function (Meneghini et al. 2006). Although muscle lacerations can heal during the remedial time, often, the dense connective scar tissue replaces healthy muscle tissue. This replaced tissue, minimises effective muscle functions. The muscle fibres laceration are the most harmful and detrimental type of laceration for recovery of the muscle, especially when muscle fibres dissect from the blood supply (Garrett & Duncan 1988).

There are three stages of muscle recovery, including turgescence and inflammation, regeneration, and fibrosis (Huard et al. 2002). Scar tissue is only formed during the fibrosis phase, which might be reduce the overall strength of the healed muscle. Generally, this step starts in two to three weeks after muscles injured or damaged and often takes more than six weeks to return to normal function (Malik & Dorr 2007). Kaariainen et al. (1998) conducted a study in rats to determine the recovery process of muscles after its laceration. The injured-healed muscle was tested under the tensile test up to failure mode of the muscle and the obtained results were measured as elongation of the healed muscles. They found a significant variation in results of the damaged leg compared to the undamaged muscle in the non-operated leg. The injured-healed muscle showed a significant reduction in muscle length at the point of failure as well as a maximum load required for failure of the muscle is reduced. While the undamaged muscle in a non-operated leg called ‘contralateral leg’, presented the different results. The failure load of the recovered part of the muscle showed 50% reduction in the contralateral muscle. Furthermore, the elongation of scar tissue, formed on the laceration site, reduced while the scar had a higher elastic modulus (Kaariainen et al. 1998). Crow et al. (2007) examined the effect of the mechanical strength of damaged muscles. They identified that any changes in mechanical strength of the damaged muscle; can affect the biological response of a muscle. (Huard et al., (2002) reviewed different methods that were applied to measure the strength of the muscle and clarified a reduced magnitude force was generated by damaged/repaired muscle.

Garrett and Duncan (1988) conducted a study to find the impact of full and partial laceration on strength and shortening of the muscle. They achieved this by using the extensor digitorum muscle in the New Zealand white rabbit. They suggested that under the same control/boundary conditions, the fully teared muscle recouped 54% of tensile strength. In addition, they identified that muscle shortening is also affected by laceration or strain phenomenon, however, a reduction in muscle tension was greater than a reduction in muscle extension within shortening. Hence, the study stated that the minimisation of strength on injured muscle is not constant over the pressure or force range on muscles, which is why lacerating muscle is unable to recover full strength. Therefore, muscles that get injured or lacerated do not recover their full strength after the healing process. Various factors and causes can be involved to determine the strength of wounded/healed muscle including the way of improvement and the level of damage. During the hip arthroplasty surgery, many of the muscles are divided alongside of the act-line of the muscle fibres rather than lacerated. This will affect the strength of the muscles differently compare to the laceration of muscle across its body. Furthermore, the position of laceration can affect the muscle strength of wounded or healed muscle. It was clearly shown that the healed and cured muscles after THR were not able to reach their original strength and therefore cannot be considered as a normal subject.

3.7 Three - Dimensional Coordinates System of Lower Limb

To define the segment orientation and muscle coordinates, the local right-handed or general orthogonal reference system (LAS) is identified (Brand et al., 1982; Mansour and Pereira, 1987; White, et al., 1989). The local LAS can be defined in various places to identify the accurate segment ordinations based on the nearest LAS. Therefore, it was nescessary to define the three different LASs to recognise the orinationa of origins for each body segments during the gait cycle. Table 3-2 lists the LAS and other important refrence points of the superfecial on lower limb. According to White, at al., (1989), the origins and insertions of each muscle can be located and landmarked by using their developed method, however, for each musculoskeletal component, data and references points should be coordinated accordingly.

Table 3-2: The LASs and local origins of the human body defined (Adapted from White, et al., 1989).

Name of LAS	Location	Explanation
RASIS	Right anterior-superior iliac spine	Point (a) in figure 3-7. The reference point for the pelvis and describes the pelvis orientation segments.
LASIS	Left anterior-superior iliac spine	
RPT	Right pubic tubercle (pelvis)	

RPSIS	Right posterior-superior spine	To locate the RPT when the subject is moved
GTROCH	Great trochanter	Point (b) in figure 3-7. To locate the origin of the femur axis and aid to define the medial-lateral epicondyle reference points.
MED/LAT-EP	Medial and lateral of epicondyle	
TIBTUB	The origin of the tibia1 tuberosity	Point (c) in figure 3-7.
MEDMAL	Medial projection of malleolus on fibula	
LATMAL	Lateral projection of malleolus on fibula	
HEEL	The reference point (origin) of the heel segment	Point (d) in figure 3-7.

Appendix B lists the local origins (a, b, c and d) that represent the mean location of the superficial landmarks on bone segments, as well as the origin and insertion of activated muscle. The obtained data were acquired from a male participant with a height of 1.77 m and mass of 66.5 Kg (White, et al., 1989).

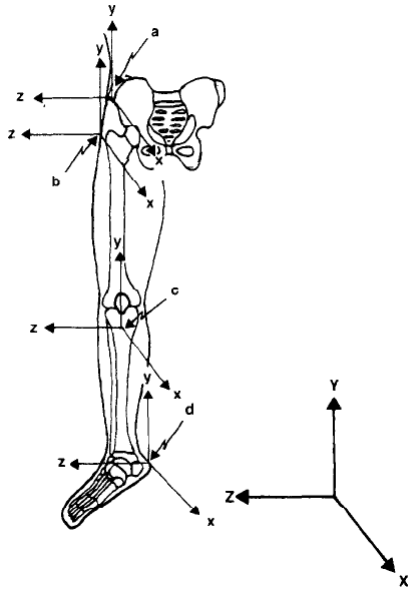

Figure 3-6: The superficial reference points and anatomical local and overall axis systems. a- RASIS, b- GTROCH, c-TIBTUB and d-HEEL (adapted from White, et al., 1989).

3.8 Gait Analysis

The term ‘gait’ refers to the pattern or style of human walking. The gait is a medium to study motion style and locomotion of human body while maintaining its harmony with the help of limbs (Fletcher, 2017). Various types of user data and information can be collected according

to an individual's style and way of walking. The acquired data may apply for recognition or investigation of diseases or select the appropriate recovery methods in treatment process (Crowinshield et al., 1978). For instance, the range of flexion-extension angles can be altered according to femur injuries increased walking speed, or a decrease in human age. Hence, various complications can be identified with the aid of gait-analysis and comparison to healthy samples (Crowinshield et al., 1978).

Various types of recording technologies and facilities are required to analyse human gait accurately. Although the nature of the human gait typically follows common patterns, which can be biphasic or bipedal, nevertheless it may vary from case to case based on the walking style. To capture human motion, kinematic parameters are obtained and kinetic information is recorded (such as ground reaction force). This is done using infrared cameras, which track the subject's position, electronic sensors mounted on the body, and force plates that are embedded in pathway. In this section, the gait analysis and its terminology will be reviewed.

3.8.1 The Gait Cycle

There are two distinctive phases in the gait cycle named as the stance phase and swing phase during the normal walking. Both phases are inter-connected and further divided into eight different sub-steps described in terms of the percentage in each gait cycle (Vaughan et al., 1999).

During the normal walking gait, approximately 60% of the gait cycle occurs in the stance phase, where the foot remains in contact with the ground. The stance phase of the gait cycle begins from the targeted foot where the heel makes contact with the ground. It then comes into flat in contact with the ground before the heel rises. The stance phase is ended by lifting the toe off the ground. The remaining phase is known as the swing phase, which is when the foot moves through the air; this constitutes 40% of the gait cycle. Double support occurs when both feet are in contact with the ground and bear the full body weight (De-la-Herran et al., 2014). Within the targeted leg swing phase, the other leg supports the body. The swing phase ends with the heel contact and the cycle will repeat. Figure 3-8 shows the human gait cycle and related stance phases, whilst Table 3-3 coordinates new terminology with traditional nomenclature it also describing each step of the human gait cycle. For the gait analysis, the speed of normal walking should be specified and normally a specific speed is taken to investigate a human gait, however the subject's self–selected speed is a common practice nowadays. Normal walking is comparatively easy to study because it is an activity, which is performed by all ambulating patients on a regular basis (Morlock et al., 2001).

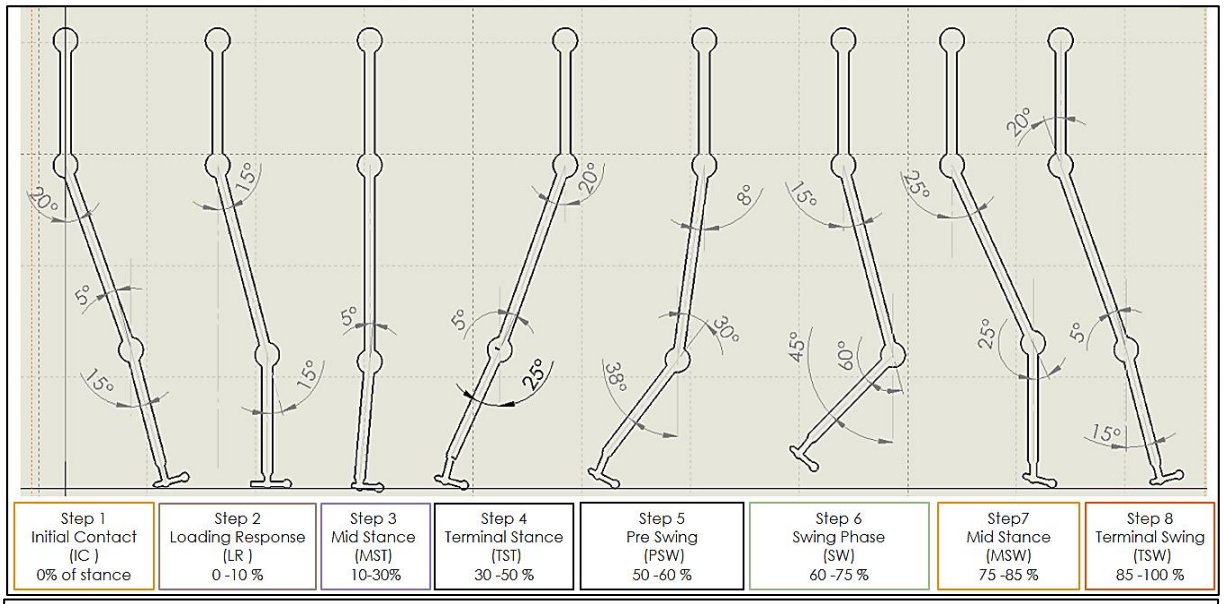

Figure 3-7: The human gait cycle and its new nomenclature. Percentages show the ratio of each stance to the entire cycle. The absolute and relative angles of a knee and hip joint demonstrated for each stance.

Table 3-3**: Definition of the human gait stance phases including old and new terminology.**

Old Terminology	New Terminology	Description
1. Heel strike	Initial contact (IC)	The body's centre of gravity places at lowest position and the human gait initiates at this point.
2. Foot- Flat	Loading Response (LR)	Takes place when a toe and sole of the foot touch the ground simultaneously.
3. Mid-stance	Mid Stance (MST)	The body's centre of gravity places at highest of its position. It happens when the swinging foot passes the stance foot
4. Heel-off	Terminal Stance (TS)	It occurs when the heel loses its contact with the ground.
5. Toe-off	Pre Swing (PSW)	The supportive foot sole still contacts with the ground, but the stance phase terminates because the targeted toe leaves the ground.
The swing phase stage		
6. Acceleration	Swing Phase (SW)	It occurs when an entire foot loses contacts with the ground and hip flexor muscles are able to do forward acceleration.
7. Mid-swing	Mid Stance (MS)	The body centre is placed at the same position of the mid-stance by the other foot. It occurs when the leg passes beneath of your body.
8. Deceleration	Terminal Swing (TS)	Muscles prepares body to stabilise and prepare foot for next heel strike.

3.8.2 Source of Erroneous Gait

The human gait is monitored and measured with the help of cameras and markers mounted on the skin of the subject. Using various raw markers on skin (e.g. retro-reflective or light emitting), can help the infrared cameras to monitor the subject's movements accurately. Nevertheless, using this technique to monitor the gait may produce errors because some markers may be blocked during the gait process (Vaughan et al. 1992). The relative position of a marker on the skin with respect to the limb, which is assumed to obtain data, can be considered as a major source of error. In fact, the markers just measure the skin movements, which move with the respect of the limb and not actual limb movements and therefore measure the relative movement of limb and additional noise (Cappozzo et al., 1996).

3.8.3 Electromyography Signal and Data Processing

Human muscles react during various sequences and events. Therefore, when they are injured this can be identified using Electromyography. This experimental medium provides adequate information about how the muscles will coordinate in such situations. Principally, while implementing electromyography, the electrodes are used to observe the signals from a human's neural systems of muscles (Hug, 2011). There are two various methods can be used to record the signal of muscles, surface EMG and intramuscular EMG. The variation between them depends on the location of electrodes that have been employed. During the surface EMG, the electrodes are attached to human skin, whereas, intramuscular EMG, uses the electrodes in the form of needles that are interested into the muscles of interest. Needle techniques can tear muscle tissues and cause severe pain during the action, the abnormal lead of the movement or action pattern. With the needle electrodes, the volume of muscles, which can be recorded from the signals, is comparatively small and may not represent the total muscle force (Hug, 2011).

In order to reduce the source of errors from soft tissues and skin, a bone landmark and bone raw placement can be used. Some researchers and researchers use bone markers and the needles are mounted to the bone through a drilling process. Bone markers add more stability to their marker position and therefore generate reliable outputs and results (Fuller et al. 1997; Benoit et al. 2006). These types of markers can lead to obtaining accurate results, reducing sources of error, and help to quantify errors effectively. Nonetheless the bones markers cause pain which may affect the normal gait process, limits the movement of bone, and restrict movement other soft skin and tissue (Lundberg 1996). In addition, the bone markers may occasionally cause infection. Fuller et al. (1997) compared the function of the skin marker with the pin (or bone) marker. It was found that the skin markers that are placed up to 20 midstance from the underlying bone have inconsistent errors and therefore cannot be considered as the particular

systematic error. However obtained results from this study show that the fast movement can increase the probabilities of erroneous results.

3.9 Muscles contraction via Experimental Method

In order to investigate the experimental procedure, it is necessary to use the EMG method to obtain the muscle contact forces of lower limbs body. The main aim of this section is to obtain valid input data from preceding studies to apply in analytical and numerical solutions. The muscles contraction can be obtained via various methods including forwarding dynamic optimisation, EMG and experimental muscle activity, static optimisation, or combinations of all (Richards, et al., 2010). Although the forward dynamics and static optimisation can predict the contact force of muscles during the normal walking activity. Outcomes of both methods are restricted to several boundary conditions and kinematic assumptions (Richards, et al., 2010). Several parameters affected by the obtained estimated results (forward dynamic or reverse dynamic methods) including:

- The number of raw marker placements
- The method of employing marker placements
- The calibration and post processing methods
- Degree of freedom (DOFs) of 3D model
- Number of applied muscles in 3D model
- Power of a software

Furthermore, the outcomes of the virtual techniques are not authentic without considering the kinematic and kinetic data, which are usually obtained from experimental EMG (Richards, et al., 2010). The first step of attainting the EMG data is by recording the muscle activation signals during specific daily activity, like normal walking. The second step includes data processing techniques to clear noisy data from interferences by using specific software (e.g. Maths Works, MATLAB-Version: R2015a). The third step of the activity identifies data from EMG for the activation of muscles and final verification.

3.9.1 EMG Pre & Post-Processing

The pre-testing step requires the preparation of skin and removal of skin hair from the placement of electrode. This should be accomplished to improve the adhesion of the electrodes and data conduction. A cleaning process with alcohol removes dead skin and dirt, which helps to minimise the electrical impedance. A coating of gel on the electrodes improves the conduction characteristics and lower impedance. Furthermore, the placement of electrodes on the prepared site is a vital part of the experimental procedure and needs to follow the specific

standard such as the Surface Electromyography for the Non-Invasive Assessment of Muscles (SENIAM), which included the recommended guidelines of the European Union (SENIAM, 1999). There may be invalid signals caused by the high sensitivity of transmitters when external forces cause sudden movement. To prevent or minimise the external interference, transmitters were fixed using straps. Figure 3-8 describes various stages of applying EMG-to-Force technique to obtain the musculoskeletal force (Bogey et al, 2005).

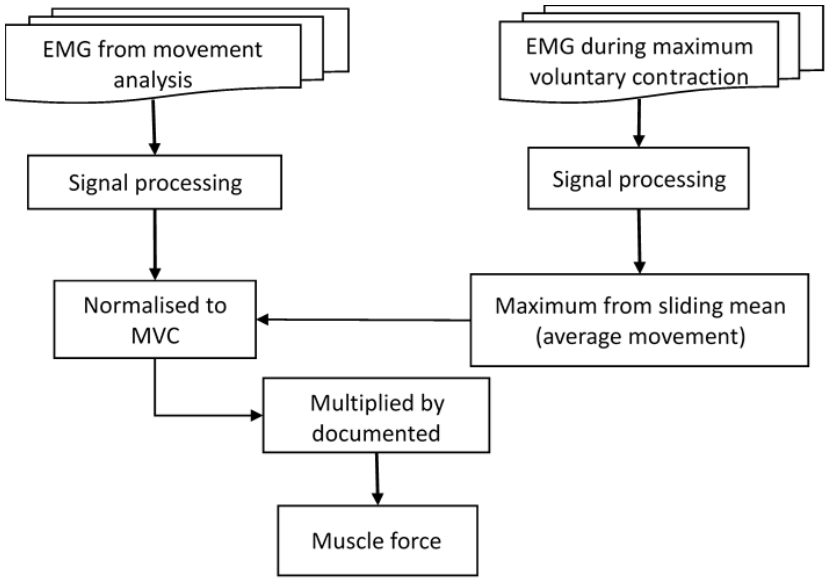

Figure 3-8: Illustration of using EMG-to Force technique applied for the individual muscular force (Adapted from Bogey et. al, 2005).

In this thesis, the Correa, et al., (2010)'s study was used as a reliable source to acquire muscles contraction. They computed the muscle contraction from the obtained EMG databased which was accomplished by Anderson & Pandy (2001) by *in-vivo* experimental method. Anderson and Pandy (2001) examined five healthy adult males, with an average age 26±3 years, height 176±3 cm, and the mass of 70.1±7.8 kg. Prior taking data, each subject underwent a warm-up step by walking four outdoor laps, measuring a total 400 m. During the third lap, the time and steps were counted to compute the frequency of one-step. Subsequently, each subject practiced walking on 11 m walking pad inside the laboratory.

For each subject, the frequency of a footpath step was measured. Retroreflective markers were attached to the lower limb body based on a Helen Hayes marker set. The surface electrodes (i.e. Noraxon Scottsdale, AZ) were also attached to the skin. The above-mentioned process was repeated five times for each subject to collect adequate data. The photosensitive eyes (or infrared cameras) ware triggered during data collections. During each trial, all data and information were recorded using video, force plate, and EMG simultaneously where the subject

walked at a self-speed (1.25 m/s). The video-based system was applied to record the kinematic data by using four-camera and motion analysis software. All channels from the force plate were recorded using an EMG at 1000 Hz, then filtered by using band-pass between the 50Hz and 200Hz and finally rectified. Muscle dynamic activation signals, including excitation and contraction, were modelled using a first-order differential equation to link the rate of the change to the muscle activation signal. The activation level of a muscle can be carried from zero (no contraction) to one (full contraction) and vice versa for the no excitation and full muscle excitation. The outcomes of the muscle activation were represented by the net effect of the motor neuron and stimulation frequency of the muscle (Anderson & Pandy, 2001). The abbreviations of muscle names used in their study and adapted for this thesis are listed in table 3-4. The sample of the recorded EMG of the muscles during the gait was adapted from Anderson & Pandy, (2001), and is presented in appendix C.

Table 3-4 :The abbreviations and lower limb extremity muscles applied in this study

Abbreviation	Name of muscles
ILPSO	Iliopsoas
ADLB , ADM	Adductor longus brevis , Adductor magnus
GMEDA	Anterior gluteus medius and anterior gluteus minimus
GMEDP	Posterior gluteus medius and posterior gluteus minimus
GMAXM	Medial gluteus maximus
GMAXL	Lateral gluteus maximus
SAR	Sartorius
GRA	Gracilis
HAMS (ST, SM and BFSL and FSH)	Semimembranosus, Semitendinosus, Biceps femoris long-short head
RF	Rectus femoris
VAS (VM, VL and VIM)	Vastus medialis, Vastus intermedius, and Vastus lateralis
GAS , SOL	Gastrocnemius , Soleus

3.9.2 Hip Muscles Contraction

According to Bergmann et al., (1993) the human hip joint endures the maximum contact forces up to 4-5 times of body weight (exclusively for one participant) and an average 2-3 times of BW. Several reasons can be attributed to justify the observed variation of the HCF, which explained in section 2.5. Many studies were accomplished to determine the hip joint loading and characteristics of the muscles hip contact forces to aid a THR and other hip complications (Crowninshield et al., 1978; Rohrle et al., 1984; Davy et al., 1988; Bergmann et al., 2001; Heller et al., 2005; Correa, et al., 2010; Adouni, et al., 2012).

Figure 3-10 shows the muscles contraction for the total hip muscles (including the hip spanning muscle and non-hip spanning muscles), centrifugal and gravity force. All forces were applied on the acetabulum of the hip in the body's spatial directions including anterior-posterior, medial-lateral and superior-inferior. The shaded areas demonstrate the total contact force subjected across three coordinate directions.

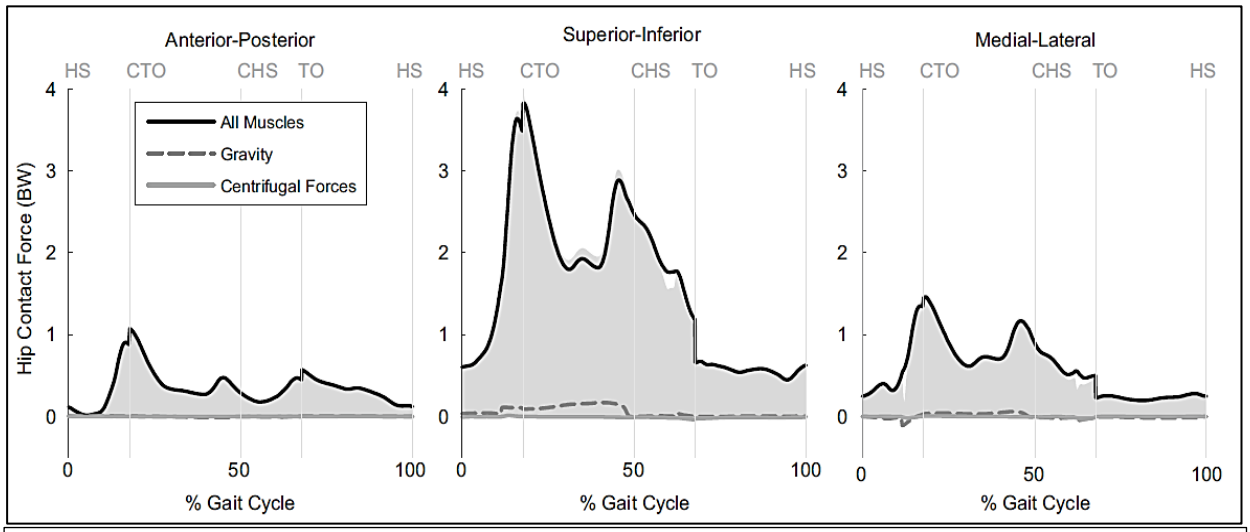

Figure 3-9: The contribution of total muscles contraction of the hip joint during the gait, all forces are normalised by applying the BW of a participant (697 N) (Adapted from, Correa, et al., 2010).

Table 3-5 shows the maximum peak of muscle contraction and figure 3-11 demonstrates the muscle contraction contributes on hip joint loading during the normal walking.

The contact force of all hip-spanning and selected non-hip spanning muscles were calculated according to the EMG recorded data. Four major muscles, including GMED, GMAX, iliopsoas and hamstring, are spanning around the hip joint, which contribute maximal force to all three components of the hip contact forces. Three non-hip spanning muscles that attach alongside the femur bone (including VASTI, soleus, and gastrocnemius) did not contribute adequately to the hip contact force. However, the effect of non-hip spanning muscles cannot be neglected within the stress-strain analysis and finite element analysis of the hip joint during the gait cycle.

Table 3-5: Contributions of selected muscle forces and their components in the peak contact force of hip joint. Including hip spanning and non-spanning muscles (Correa, et al., 2010).

Peak contact force of the hip muscles (x BW)	Anterior	Superior	Medial
Hip-spanning muscles			
Gluteus medius (GMED)	1.1	1.87	0.89
Gluteus maximus (GMAX)	-0.3	1.27	0.39
Hamstrings	-0.2	0.27	0.01
Iliopsoas	0.03	0.02	≤ 0.01

Rectus femoris (RF)	≤ 0.01	0.04	≤ 0.01
Piriformis	-0.03	0.06	0.07
Adductors (ADD)	-0.01	0.06	0.03
Selected non-hip-spanning muscles			
VASTI (Including vastus medialis, vastus intermedius, and vastus lateralis combined)	0.18	0.32	0.09
Soleus	0.01	0.01	≤ 0.01
Gastrocnemius (Including medial and lateral compartments of gastrocnemius)	≤ 0.01	≤ 0.01	≤ 0.01

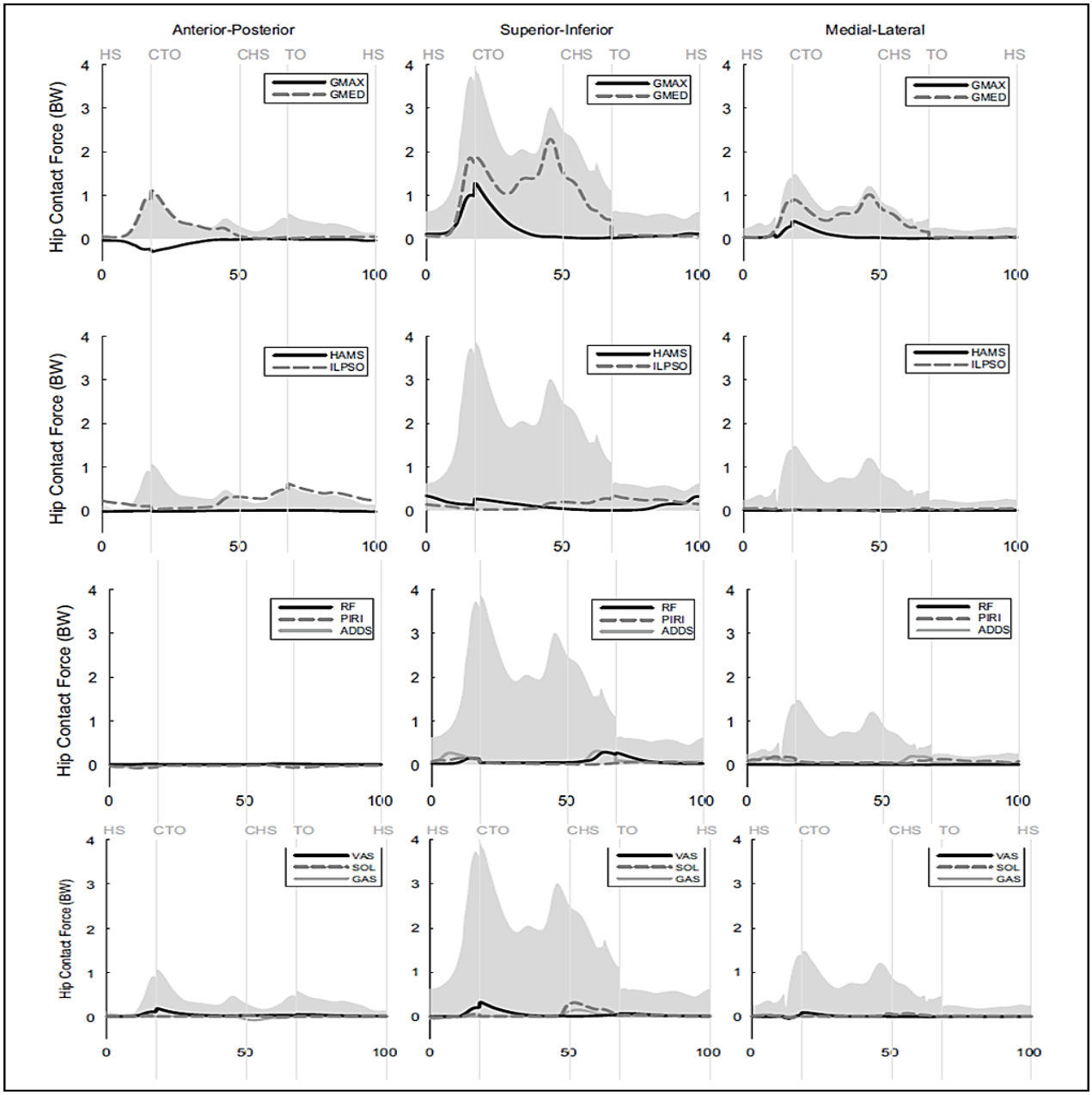

Figure 3-10: Contributions muscle contraction for all hip-spanning and selected non-hip-spanning muscles. The shaded areas demonstrate the total contact forces (Adapted from Correa, et al., 2010).

3.9.3 Knee Muscles contraction

The hip muscles contraction during the normal gait is reported in section 3.9.2. Nevertheless, the quadriceps muscles (i.e. RF, VL, & VM) and the individual hamstring muscle (not total hamstring group) like a ST will be reviewed in this section.

Heintz & Gutierrez-Farewik, (2007), measured the muscle contraction of nine lower limb muscle during the gait analysis. They performed surface EMG technique to record signals of the lower limb muscles of a healthy participant with height 164 cm, weight 59.3 kg and 34 years old. The EMG signals recorded using the surface electrodes (Motion Labs System, Baton Rouge, LA, USA) were placed by an experienced lab-technician according to guidelines and instructions of fine-wire placement in Peretto et al., (1992). In addition, the kinematic data was captured using a six-cameras and a motion analysis system (Vicon, Oxford UK) at 50Hz along a 10 m pathway with the subject's own speed. The kinematic parameters were calculated with a Plug-In-Gait and Vicon (as a common gait model), while the ground reaction force data was collected from double force platforms. The outcomes of the selected knee muscles contraction during the gait cycle are denoted in figure3-12. The dotted line graph represents the muscle contraction using the static optimisations technique. Whilst the continuous line shows the muscles contraction via conducting EMG-to-Force method.

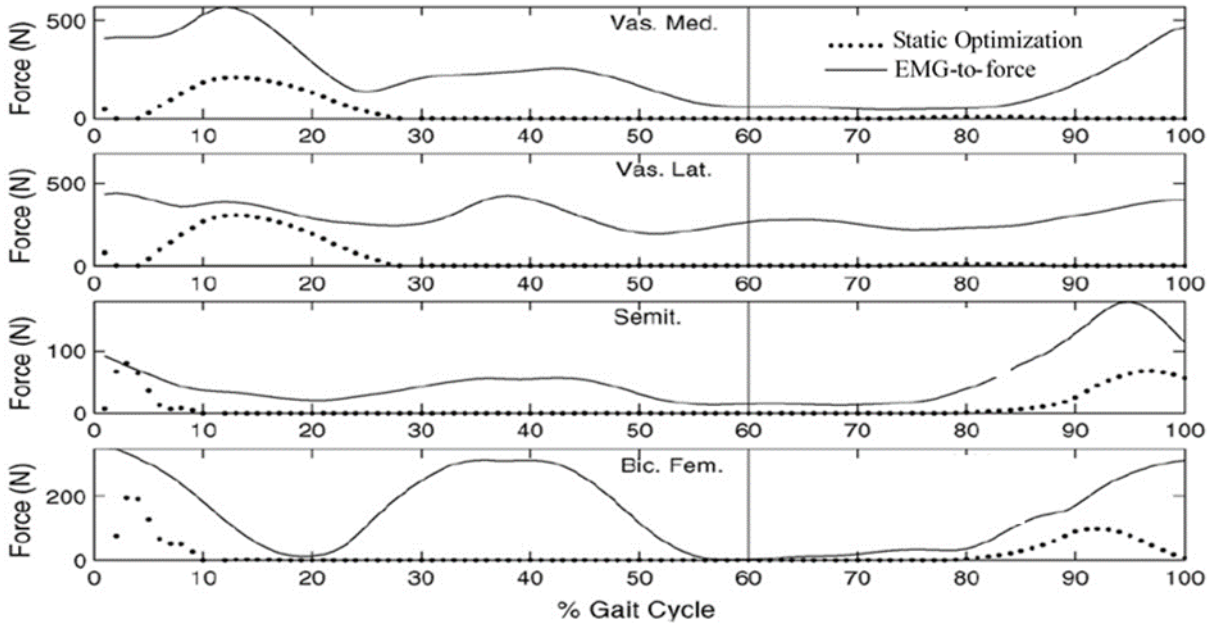

Figure 3-11: Selected knee muscles contraction from static optimisation (dotted line) in comparison to the EMG-to-force method (solid line) during a gait cycle (Adapted from Heintz & Gutierrez-Farewik, 2007)

Chapter 4

Analytical Method to Determine HCF

4.1 Introduction

The analytical approach is applied for the simple geometry and structure to determine the stress, strain or deflection. Nevertheless, application of the superposition principle, a method of section, and method of joints were used to examine the structure and determine the resultant of forces (Erochko, 2015). In comparison, the numerical modelling or FE analysis required moderately extensive computation assets, while analytical models can be produced the results rapidly with a small amount of computation expense and mathematical knowledge (Jarquio, 2007).

In this chapter, the hip joint reaction force at the top of the femoral head will be computed using the method of joints within the gait cycle. To accomplish this within the chapter, two main case studies will be introduced including the hip contact force with muscle contraction and without considering any muscle contraction (i.e. HCF All Mus. and HCF No Mus.). For each study, the HCF will be calculated for two critical stances of the normal walking called single support stance (i.e. 18-30%) and pre-swing phase (i.e.mid-stance at 50%). In addition, 2D and 3D equilibrium static conditions will be considered for all studies to cover each aspect of the analytical approach. Hence, eight various studies determine the hip contact force at the top of the femoral head analytically using the equilibrium static equations. The obtained HCF for all 3D studies will provide adequate data for the next chapter, due to determination of the local stress for the specific regions of the femur.

4.2 Reviewed Related Work

According to Brekelmans et al., (1972) the maximum hip joint force, strain and stress can be estimated using analytical models with little expense, however, there are some restrictions, which limited the mathematical technique. These include:

- Difficulty in giving analytical descriptions of the geometry of skeletal parts due to the inhomogeneous lower limb geometry

- It is complicated to restrict the real load distribution compare to the real conditions.
- Application of the analytical technique cannot represent the real physical characteristics of the bone material (i.e. inhomogeneous anisotropic materials) and mostly the material behaviour is neglected from the estimations.

Determination of the value and angle (i.e. orientation) of the total hip contact force (HCF) are important for various reasons including designing better implants, optimising the THR, and identifying the stress-strain characteristics of the hip joint.

Several researchers identified two peaks of HCF as the crucial stances during the normal walking of human including the single support (i.e.18-30%) and pre-swing (i.e.50 %) of the gait cycle. Hence the analytical approach in this chapter focuses on the analysis of the HCF within these two peaks (Chen et al., 2014; Dumas et al., 2012; Guess et al., 2014; Heller et al., 2001; Hast and Piazza, 2013; Lundberg et al, 2013; Lund et al., 2015; Modenese et al. 2011; Manal and Buchanan, 2013; Serrancoli et al., 2016). The main reason for conducting the analytical methods (i.e. 2D and 3D) in this study is, to determine whether the muscles contraction within the normal walking (i.e. gait) cause the value of HCF to increase or decrease. For instance, Stansfield, et al., (2003) compared the measured and calculated the hip joint contact force of 3D model of the lower limb body during different daily activities such as the normal, slow and fast walking. They reported maximum hip contact forces for the normal walking at a self-selected speed for the subject A and B 2.8 and 3.2×BW respectively.

4.3 Hip Contact Force (Static Equilibrium)

In order to find the effect of the muscles contraction and their corresponding moments during the gait, it was necessary to determine the hip contact force (HCF) for the two following scenarios:

1. HCF **with** contribution of muscle contraction and their created moments
2. HCF **without** contribution of muscle contraction and their created moments

In addition, the HCF was computed through considering two various equilibrium static conditions.

The plane stress (i.e. two-dimensional or 2D) conditions for the lower limb, included:

1) 2D-force of the activated muscles
2) 2D- moments of the activated muscles
3) Two knee reaction force (without any reaction of moment)
4) Two hip reaction forces

Furthermore, another study was conducted with respect to the three dimensional (3D) condition for the same lower limb system to adjust the boundary conditions of the 2D study and determined the HCF more accurately during the gait cycle. For the hip and knee joints, the ball & socket and frictionless pin (i.e. hinged) joints were considered respectively (Boguszewsk, et al., 2016; Fellows et al., 2016; Li 2017). There are three unknown spatial reaction force (e.g. Rx, Ry and Rz) for the ball & socket joint, however, the Rx was neglected to satisfy the plane stress condition. Similarly, for the knee (i.e. hinge) only two reaction forces were considered. There is no reaction moment for the hip joint (i.e. ball & socket joint) based on the function of the hip joint, because it can rotate in all directions without restrictions. According to Winter (2009) because the knee joint is situated at the middle of the lower limb structure and is restricted by another two joints (i.e. ankle and hip joint), two reaction moments (i.e. My and Mz) can be neglected with good tolerance. However, for 3D studies, all assumptions considered are based on the realistic loading conditions and no reactions force and moment were neglected. Figure 4-1 shows the anatomical model and free body diagram of the lower limb within the simple support leg. The mass of the femur and tibia denoted as m_1 and m_2 respectively. The R and K are denoted as a hip reaction force and knee reaction force respectively.

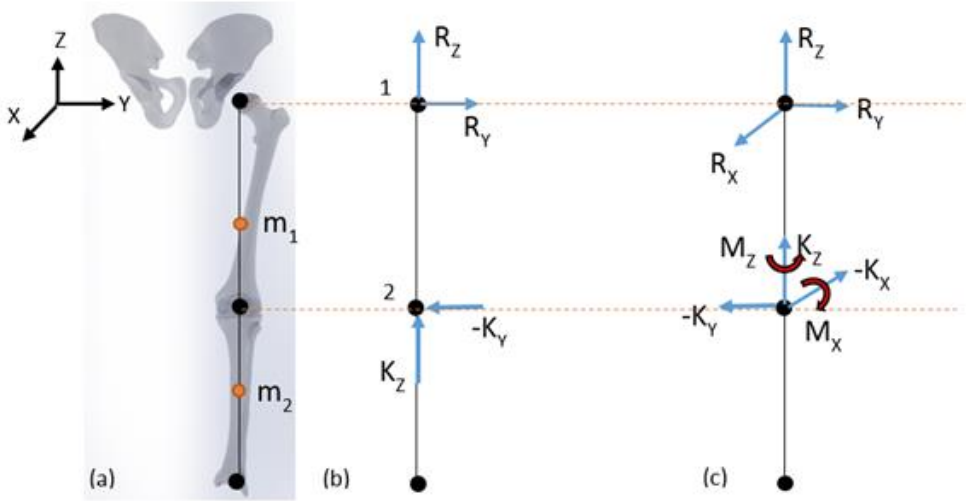

Figure 4-1:(a) The anatomical model of the lower limbs of human body and (b) the 2D link – segment model with the related to studies 2D-All Mus. and 2D-No Mus., and (c) the 3D link – segment model freedom related to studies of 3D-All Mus. and No Mus. The R and K are denoted as a hip and knee reaction force respectively.

Table 4-1: Defined studies and their boundary conditions for the analytical approach.					
Method	Study Name	Muscle contribution	Stance phase of the gait		Other characteristics of 2D and 3D studies.
Analytical Study - Static Equilibrium	2D- All HCF-Mus.	Considering effect of muscles contact force and their created moments during the gait cycle.	18-30 % Standing on one leg (6 major groups of muscles contributed)	50% Pre-swing (7 major groups of muscles contributed)	Figure 4-1 (b) 1) Tibiofemoral angle (i.e. Q angle 0 ˚) 2) Plane stress - strain condition (i.e. 2D) The hip joint at 18-30% and 50% discretized and considered as ball and socket joint. Two reaction forces in Y and Z-directions are replaced and X component was neglected. 3) Knee joint replaced with a hinge. It is considered 2 reaction forces in Y and Z-directions and X component was neglected. No reaction moments considered for the knee joint.
	2D-HCF-No Mus.	The muscles contraction and their moments were not considered during the gait.			
	3D-All HCF- Mus.	Considering effect of muscles contraction (6 major group of muscles contributed) and their created moments during the gait cycle.	18-30 % Standing on one leg	50% Pre-Swing	Figure 4-1 (c) 1) Tibiofemoral angle 9 ˚ for man. 2) 3D study was considered 3) The femur at specific stance of the gait discretized and considered as ball and socket joint with three-reaction force in X, Y and Z-axis. 4) Knee joint replaced with a hinge joint with one degree of freedom (1 rotation in y-axis). It was considered 3 reaction forces in X, Y, and Z-directions and two reaction moments in X and Z- directions.
	3D-HCF-No Mus.	The muscles contraction and their moments were not considered during the gait.			

4.4 HCF in 2D via Analytical study

For the analytical study the healthy male subject (54-year-old, ID: 24759123) with the anthropometric measurements of 81.74 Kg and 182 cm was selected. The lower limb of the participant were converted to the CAD files via the MRI. The dataset of the MRI source was recorded in January 2001 and uploaded to the www.Pcir.org for public used in November 2007 (Pcir, 2007). The unique CAD model was applied for both analytical and numerical study.

For 2D studies, the anterior-posterior component of force was neglected due to the fact that the minimum muscle contraction recorded by EMG process on that direction (see figure 3-11). On the other hand, several researchers report the same phenomenon experimentally (Daniel et al., 2001; Stansfield, et al., 2003; Wang, et al., 2004, Correa, et al., 2010; Bergmann, 2015; Wang, et al., 2017).

Hence, the plane stress conditions were assumed due to demonstrating hip reaction forces for a ball and socket joint and show less complexity in calculations steps. In this case, the x components of the muscles, hip reaction and knee reaction force on the anterior-posterior direction of the body were taken to be zero.

Theoretically, the double support stance during the gait shows to be less critical situation due to the distribution of the BW between two legs. Whilst during the single support stance, whole BW is subjected to the targeted leg. Therefore, the HCF and its reaction force (RHFC) were increased during the simple standing stance (i.e. 18% up to 30%) and hyperextension of the hip (i.e. 50%) within the gait cycle.

Figure 4-2 (C) shows the three various position of the targeted leg including the hip extension, simple support, and hip flexion stances during normal cwalking. The maximum angle of the hip flexion and hip extension were reported as 25° and -20° respectively (Lewis & Sahrmann, 2015). The centre of the femoral head (denoted as H in figure 4 -2 (b)) was considered as a reference point to compute the HCF, its reaction, and muscle moment.

The muscle moment arm was defined as the perpendicular distance between the H and the origin attached point of muscles in the z and y directions. The mechanical axis of the lower limb demonstrated in Figure 4-2 (b), where the ankle, centre of the knee and the centre of the femoral head, were situated in a same location alongside of the z-axis (i.e. superior - inferior) spatially in an anterior view.

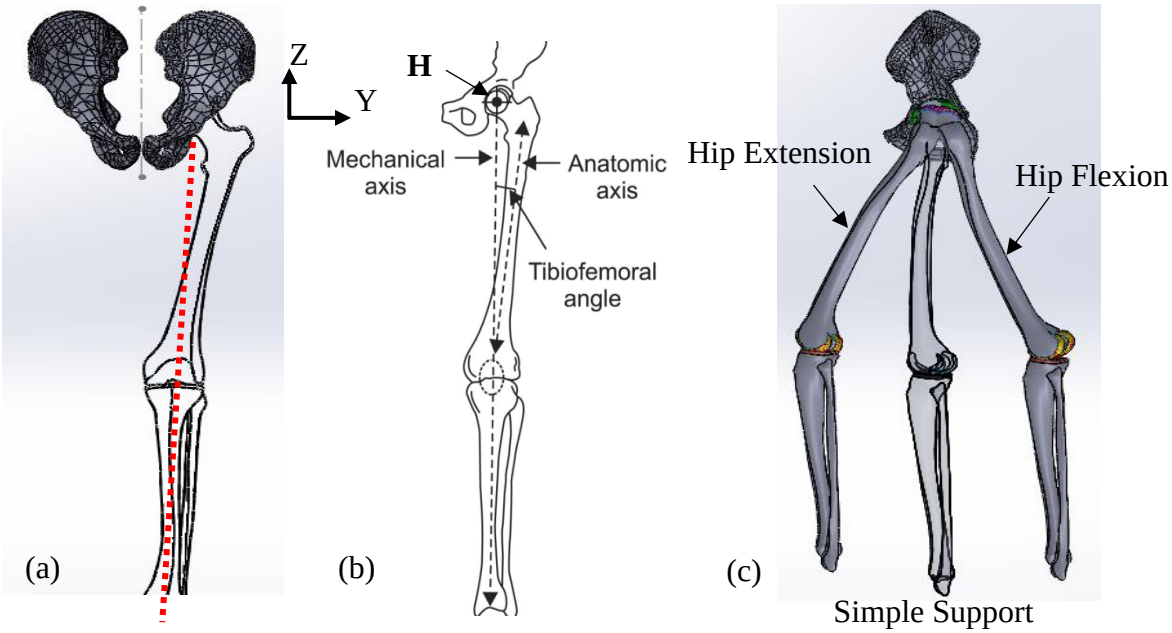

Figure 4-2: (a) The anterior view of the lower limbs. The red dotted line showing the mechanical axis, (b) the black dashed line showing the anatomical axis of the femur (Adapted from Lee & Byun, 2012), and (c) The sagittal view of a lower limbs body.

4.4.1 HCF-2D-All Mus. at 18-30% (Musculoskeletal Model)

To determine the hip contact of the targeted leg during the simple support stance, the static equilibrium was applied. Figure 4-3 shows the bony and muscles compartments for 2D study at single support stance of the gait cycle. In this stance, the hip spanning muscles group including the gluteus medius (GMED), gluteus minimus (GMIN) (containing the posterior, middle and anterior muscles compartments), and piriformis (PIR) are activated. While from the non-spanning hip muscles group, just the rectus femoris (RF) and the gastrocnemius (GAS) muscle are activated during the gait (Bnnefoy-Mazure & Armand, 2015; Igliĉ et al., 2002; Kuitunen et al., 2002; Kyröläinen et al., 2005; Mero & Komi, 1987; Pinniger et al., 2000).

Furthermore, the VL and RF as member of the quadriceps group are also activated in this stance of the gait (Pinniger et al., 2000).

The attached points (origin- insertion) of the GMED, GMIN, PIR, RF, VL, RF and GAS were reviewed and determined in chapter 3. However, the schematic attached points and their angles are shown in figure 4-3 (b). Figure 4-3 (C) shows the parallel-lines method to find the angles between the muscle act line of the RF and biomechanical axis of the femur using the SolidWorks software (v15). The computed angles were reported as $\theta_1 = 21.7^0, \theta_2 = 14^0, \theta_3 = 4.2^0, and\ \theta_4 = 4.2^0$ for the GMED & GMIN, PIR, RF and GAS respectively. Figure 4-3 ((a) and (d)) show the lower

limb geometrical parameters such as the half of the interim distance (a), the femur length (L) and other geometrical parameters (i.e. L_1 and L_2). All dimensions are determined using the real image and the obtained CAD model of the participant. The important coordinates of the lower limb are denoted in figure 4-3 (a) as F, H, B, K, and D, which are defined in table 4-2.

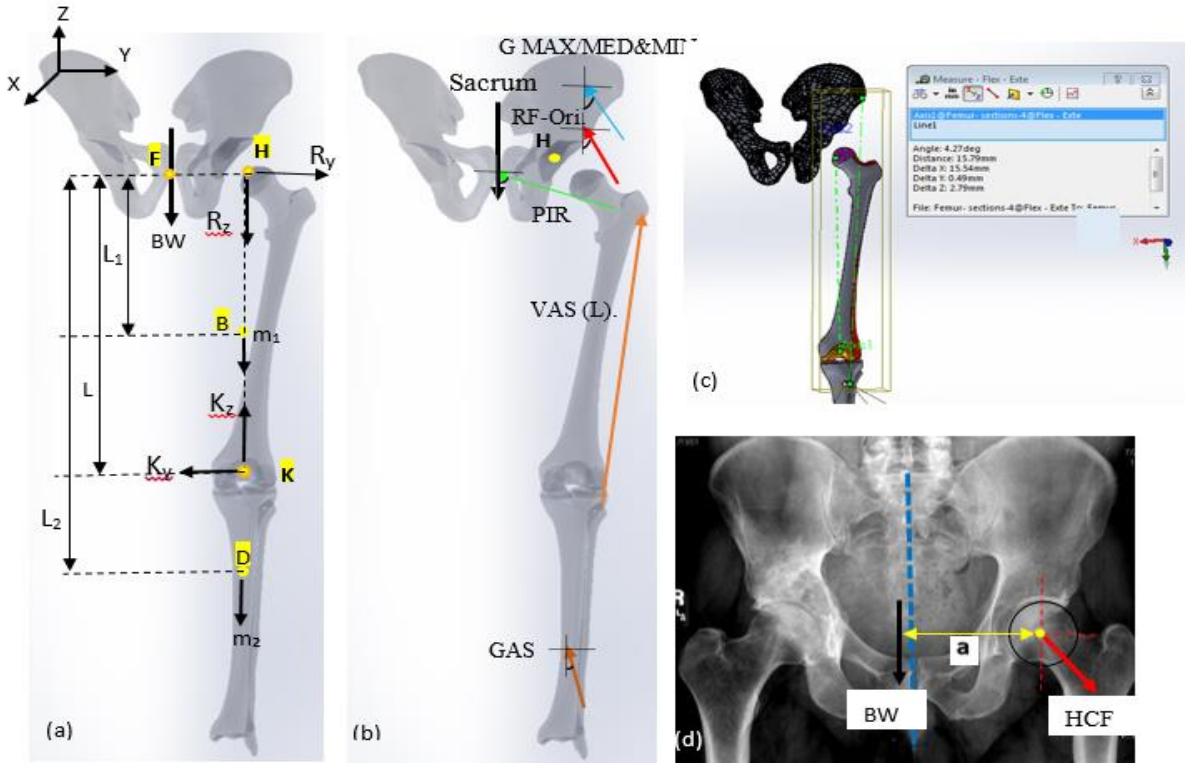

Figure 4-3: (a)The static equilibrium of the lower limbs within the simple support stance of the bony compartments, (b) attachment points and angles between the muscle act lines and a vertical axis of activated muscles, (c) the method of finding the angles, and (d) the method of finding moment arms of the bodyweight.

Table 4-2: The coordinates of the lower limb using for 2D and 3D analytical studies.

Denoted points	Definition (Dimensions are meter)	Coordinate Points (m)	
		2D Study $(Y_{(j)}, Z_{(k)})$	3D Study $(X_{(i)}, Y_{(j)}, Z_{(k)})$
H	Hip joint - The point that HCF was applied. It has considered as the reference point.	(0,0)	(0,0,0)
F	The point which body weight was applied.	(- 0.078, 0)	(0 ,- 0.078, 0)
B	Centre of the mass for the femur (m_1)	(0 ,- 0.215)	(-0.033, 0.035, -0.220)
K	Knee joint - The point that KCF was applied.	(0 ,- 0.430)	(-0.045, 0, -0.440)
D	Centre of the mass for the tibia (m_2)	(0 ,- 0.610)	(-0.061, 0.006, -0.610)
L	Length of the femur	0.430 m	
L2	Length of the femur + Half of length of the tibia	0.610 m	

Considering a static equilibrium system for the lower limb presents the hyperstatic condition of the musculoskeletal model. Hence, any attempt to solve the active-interactive forces for the hyperstatic system required assuming a compatible condition.

Therefore, researchers and researchers obtained different assumptions and methods (i.e. reduction method or optimisation method) to define the system statically and then predict the HCF analytically (Lu et al., 1997, 1998; Komistek et al., 1998; Ipavec et al., 1999; Daniel et al., 2001; Igliĉ et al., 2002; Stansfield, et al., 2003; Wang et al., 2017).

The fact that some muscles do not contribute during certain steps of the walking stances, means that they were relinquished from the static analysis in this study.

In addition, in order to simplify the static conditions, the effect of the group of muscle contraction was considered instead of the individual muscle (table 4-2 & Eq.4-1 and 4-2). Table 4-2 shows the muscular contact forces in y and z-axis and total muscle contraction (i.e. $\sum_{n=1}^{n=5} F_{Yn}^{M}$ & $\sum_{n=1}^{n=5} F_{Zn}^{M}$).

Table 4-3: Denoted muscle groups and their contact forces during the single support stance (18%) of the gait cycle. According to the geometry the x-components was neglected (Correa et al. 2010).

Muscles	N	***Force*** Y(j) - Medial lateral (×BW)	***Force*** Z (k) - (Superior- Inferior) (×BW)
G MED + MIN	1	-0.88	1.25
PIR	2	-0.13	0.11
RF	3	-0.01	0.16
VAS (L)	4	0.1	0.32
GAS	5	-0.01	0.01
Total		$F_{ny}^{MUS} = \sum_{n=1}^{n=5} F_{Yn} = -1.13$	$F_{nz}^{MUS} = \sum_{n=1}^{n=5} F_{Zn} = 1.85$

The muscle moment arm (i.e. perpendicular distance between origin of muscles and reference point of lower limb system H) was determined from the geometry. In addition, the following equations were considered to identify the total value of the moment around the point H for y and z-components of the muscles force.

$$M_{Yn}{}^{MUS} = \sum_{n=1}^{n=5} y_i \, F_{Yn}^{M} = -y_1 F_{1y} + y_2 F_{2y} - y_3 F_{3y} - y_4 F_{4y} - y_5 F_{5y} \qquad (4\text{-}1)$$

$$M_{Zn}{}^{MUS} = \sum_{n=1}^{n=5} z_i \, F_{Zn}^{M} = -z_1 F_{1z} + z_2 F_{2z} - z_3 F_{3z} - z_4 F_{4z} - z_5 F_{5z} \qquad (4\text{-}2)$$

Where the y_i and z_i are the perpendicular distance between the origin of the muscles and point H in y-direction (i.e. horizontal) and z-direction (i.e. vertical) respectively. The F_{iy}^{M} and F_{iz}^{M} are the muscular force in y and z-direction. ${M_{YN}}^{M}$ and ${M_{Zn}}^{M}$ are the total moments of the muscular force during the simple support stance of the gait cycle. The clockwise (CW) bearing was considered as a positive direction of the moment. Table 4-3 shows the created moments of the activated muscles around the hip joint.

Table 4-4: Created moment of activated muscles (in 2D for the Y and Z components) during the simple support stance (18%) of the gait cycle. CW direction considered as positive moment (Correa et al. 2010). All dimensions are meter.

Muscles	Moment - Y component (L× BW)	Moment - Z component (L× BW)
1-GMED + MIN	0.017 × 0.88 = 0.015 CCW	0.091 × 1.25 = 0.11 CCW
2-PIR	0.078 × 0.13 = 0.010 CW	0.008 × 0.11 = 0.0008 CW
3-RF	0.027 × 0.01 = 0.0002 CCW	0.038 × 0.16 = 0.0060 CCW
4-VAS (L)	0.053 × 0.1 = 0.0053 CCW	0.071 × 0.32 = 0.0227 CCW
5-GAS	0.039 × 0.01 = 0.0004 CCW	0.684 × 0.01= 0.0068 CCW
Total	$M_{Yn}^{MUS} = \sum_{n=1}^{n=5} y_i \times F_{nY}^{M} = -0.0127$ (Total moment (as well as muscle moment) in Y-direction was neglected, due to simplifying the calculation).	$M_{Zn}^{MUS} = \sum_{n=1}^{n=5} z_i \times F_{nZ}^{M} = -0.1447$

The mass of the bony compartment (m_1+ m_2) and mass of the muscles compartments of the leg were estimated as 0.16 ×BW (Clauser, et al., 1969). Finally, by employing the equilibrium static equations (i.e.$\sum F_y = 0$, $\sum F_z = 0$, and $\sum \mathrm{M}_H = 0$) at the point H and plugins force and moments values from table 4-3 and 4-3, the HCF force can be predicted.

$$\sum F_Z = -BW - R_z + K_z + F_{nz}^{M} - (m_1 + m_2) = 0 \qquad (4\text{-}3)$$

$$\sum F_y = R_y - K_y - F_{ny}^{M} = 0 \qquad (4\text{-}4)$$

$$\sum M_H = -(a \times BW) + (L \times K_y) + {M_{nZ}}^{MUS} = 0 \qquad (4\text{-}5)$$

Where, $R_y, R_z, K_y, and\ K_z$ represents the reaction forces of the hip and knee joint in y and z-direction respectively. BW is the participant's body weight, (a) is the perpendicular distance between the body axis and reference point (H). F_{nz}^{M} and F_{ny}^{M} are the vertical and horizontal

components of muscles contraction . ${M_{nY}}^{M}$ & ${M_{nZ}}^{M}$ represents the moments of the muscles around the hip joint (i.e. the reference point of the H). By solving the equation4-5 with respect to K_y, Eq. 4-6 was deduced:

$$K_y = -\frac{1}{L}\left({M_{nZ}}^{M}\right) + \frac{a}{L}\,BW \qquad (4\text{-}6)$$

Substituting K_y into the Eq. 4-4, gives

$$R_y = -\frac{1}{L}\left({M_{nZ}}^{M}\right) + \frac{a}{L}\,BW + F_{ny}^{M} = -0.60 \qquad (4\text{-}7)$$

Where (a) is 0.078 (m) (Iglič et al., 2002) and L is the length of femur bone (0.430 m).

By considering the biomechanical system and the static equilibrium equations (Eq.4-3, 6, and 7), it can be realised that the lower limb system is yielded as a hyper-static situation. Even though considering the plane stress condition to reduce the number of unknown (i.e. Rx) around the hip joint, the number of unknowns exceeds from the developed independent static equations. To solve the difficulty of an indeterminate system, a compatibility condition was considered to restrict the solution system and find the reaction force of the hip joint.

4.4.1.1 Compatibility Condition

With respect to computing the value of the Rz in Eq.4-3, it was necessary to determine the Kz from the prior research and define a system from the indeterminate situation. Hence, the total reaction force of the knee joint within the gait for the simple support stance (i.e.18- 30% of the gait) was considered. Messier et al., (2011) predicted the total knee joint reaction force 3.1×BW. While, other researchers reported peak of knee contact force at the simple support stance of the gait, between the 2.4 and 3.1× BW (Morrison 1968 & 1970; Komistek et al., 2005; Smith et al., 2008). By considering the average value (2.75 BW) of the predicted knee contact forces during the gait and applying the rule of the resultant between vertical and horizontal components (i.e. Kz and Ky respectively), the $R_z\ and\ R_y$ can be estimated with the acceptable range of the value and high level of accuracy. Equation 4-8 presents the total contact force of knee joint at simple support stance

$$K = (K_y^2 + K_z^2)^{\frac{1}{2}} = 2.75\,BW \qquad (4\text{-}8)$$

$$k_z = ((2.75\,BW)^2 - K_y^2)^{\frac{1}{2}} \qquad (4\text{-}9)$$

Substituting K_y from Eq. 4-6 into the Eq. 4-9 gives

$$K_z = [(2.75\,BW)^2 + (\frac{1}{L}\left({M_{nz}}^{M}\right) - \frac{a}{L}\,BW)^2]^{\frac{1}{2}} \qquad (4\text{-}10)$$

From Eq.4-7, considering the developed equation for the Kz (Eq. 4-10), and the value of the $(m_1 + m_2) = 0.16 \times BW$ the following equations for R_z was governed.

$$R_z = [(2.75\ BW)^2 + (\frac{1}{L}\left({M_{nz}}^M \right) - \frac{a}{L}\ BW)^2]^{\frac{1}{2}} - BW + F_{nz}^M - (0.16BW\ ) = 3.48\ BW \qquad (4\text{-}11)$$

Substituting the total values of the muscle contraction and created moments from the table 4-2 & 4-3 and replacing in Rz and Ry equations (4-7 and 4-11), the 3.48×BW and -0.60×BW were computed respectively. The total contact force of the hip joint can be calculated via the equation 4-12. Finally, the magnitude of HCF for the study 2D-HCF-All Mus. at 18-30 % of the gait is predicted 3.53×BW.

$$HCF\ (R) = (R_y^2 + R_z^2)^{\frac{1}{2}} = 3.53\ BW \qquad (4\text{-}12)$$

4.4.2 HCF-2D-No Mus. @ 18-30% (Skeletal Model)

Another study was conducted to show the role of muscle contraction within the simple support stance (i.e. 18-30% of the gait) during the normal walking. For the assumption, just the bony compartments were considered to compute the hip contact force at the reference point (i.e. H) without considering any muscles contraction force.

The equilibrium static equations were developed from Eq.4-13 to Eq. 4-15 and the same compatibility condition was used to compute the resultant force.

$$\sum F_Z = -BW - R_z + K_z - (m_1 + m_2) = 0 \qquad (4\text{-}13)$$

$$\sum F_y = R_y - K_y = 0 \qquad (4\text{-}14)$$

$$\sum M^H = -(a \times BW) + \left(L \times K_y\right) = 0 \qquad (4\text{-}15)$$

Eq. 4-14 gives the following equation

$$K_y = \frac{a}{L}\ BW \qquad (4\text{-}16)$$

Substituting K_y into the Eq. 4-15, gives

$$R_y = \frac{a}{L}\ BW \qquad (4\text{-}17)$$

By considering average knee contact force (K) at simple support stance (i.e. 18%) 2.75 BW.

$$K = (k_y^2 + k_z^2)^{\frac{1}{2}} = 2.75\ BW \qquad (4\text{-}18)$$

$$k_z = [(2.75\ BW)^2 + (\frac{a}{L}\ BW)^2]^{\frac{1}{2}} \qquad (4\text{-}19)$$

Replacing the obtained values k_z and R_Y to Eq. 4-13, gives the value of R_Z

$$R_z = [(2.75\ BW)^2 + (\frac{a}{L}\ BW)^2]^{\frac{1}{2}} - BW - (0.16BW) = [7.562+0.033]^{\frac{1}{2}} - 1 - 0.16$$
$$= 1.595\ BW \qquad (4\text{-}20)$$

To findR_y, R_Z is substituted into Eq. 4-17

$$R_y = \frac{a}{L}\ BW = \frac{0.078}{0.430} = 0.181\ BW \qquad (4\text{-}21)$$

Finally, the total magnitude of the HCF for bony parts of hip joint at 18-30% of the gait is predicted by Eq.4-22.

$$R = (R_y^2 + R_z^2)^{\frac{1}{2}} = [(1.595)^2 + (0.181)^2]^{\frac{1}{2}} = 1.603\ BW \qquad (4\text{-}22)$$

Table 4-4 compares the obtained results through equilibrium static analysis during simple support stance of normal walking. The HCF (× BW) with the contribution of activated muscles shown more than 2 times in comparison to the HCF without the contribution of activated muscles approximately.

Table 4-5: Hip contact force (× BW) of the simple support stance (18%) while considering the muscle contribution force and without the muscle contraction during the gait.

Name of Study	2D- All Mus. @ 18% (×BW) (Entire lower limb system)	2D- No Mus. @ 18% (×BW) (Just bonny system)
Resultant of Hip Contact Force (HCF)	3.53	1.603

4.4.3 HCF-2D-All Mus. @ 50 % (Musculoskeletal Model)

In this section, the HCF was predicted within the hip extension of the gait where the targeted leg was situated at the beginning of the toe-off and end of terminal stance.

In this position, the posterior muscle groups (those muscles that are attached to the posterior side of the femur) are responsible for the extension of the femur from the hip joint. The posterior hip muscles include both hamstring muscle group and the gluteus maximus muscle group. They are activated between the 31 and 62 % of the gait cycle. While the extension peak of HCF (i.e. the second peak of HCF during the gait) occurred at 50% of the gait where the hip extended 20˚. The gluteus medius and adductor magnus support the other main muscles to extend the femur bone

effortlessly (Correa, et al., 2010; Iglič et al., 2002; Streifeneder, 2016; Ogle, 2018). The attached points of the posterior muscles were shown in figure 4-4. Similar to the simple support stance, the HCF of the extension stance was calculated based on the force and moments of the bone and muscle compartments. In this study, the x component of the hip contact force and its reaction force were neglected and two reaction forces of lower limb system were considered at 20˚ of the hip extension. The hip joint was considered as the ball-socket joint with the three reaction forces including R_X^{α} R_y^{α}, and R_Z^{α}. The x and z components are rotated 20˚ (i.e. α =20) around the y-axis extensionally, while the R_y (i.e. R_y^{20}) stays fixed and not change. Due to simplification of the lower limb model including the bony parts and muscle parts the 2D forces were assumed. The Y components of the muscle force, hip, and knee reaction forces on the medial-lateral direction in frontal plane of the hip were set to be zero.

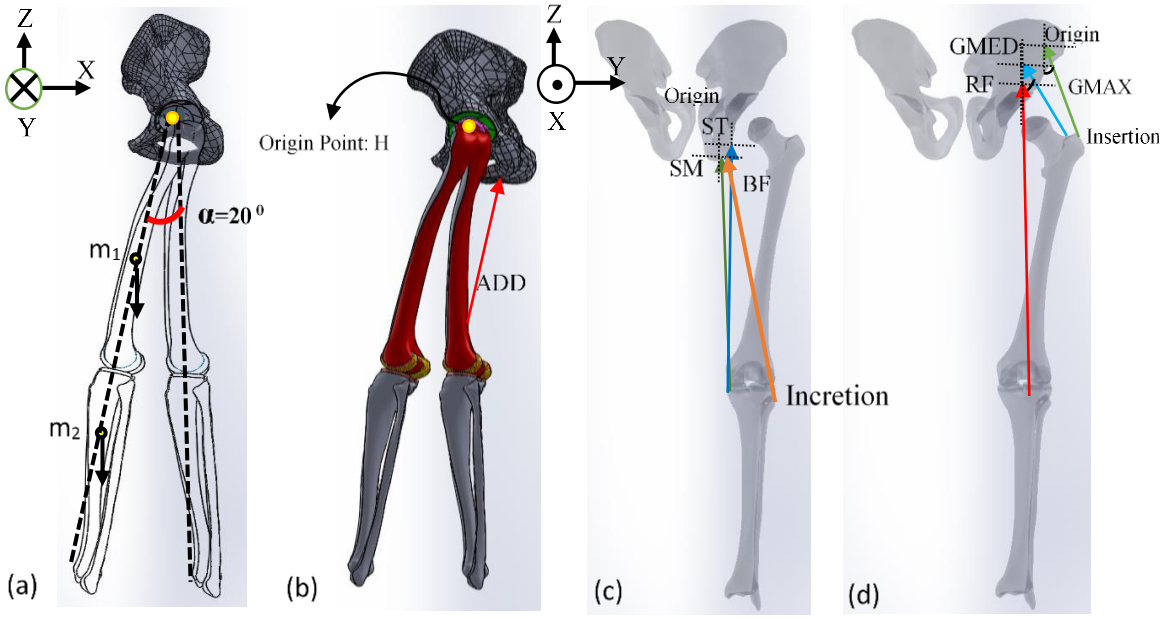

Figure 4-4: (a) Hip extension in a sagittal plane (b) the lateral view of the reference point of lower limb system (c) the hamstring muscle group including SM, BF and ST in a frontal plane, and (d) the gluteus muscle group and RF in a frontal plane.

Figure 4-5 (a) and (b) show the free body diagram of the hyperextension of the hip for the bony parts and total muscles contraction in X and Z direction (i.e.$-\Sigma F_{nx}^{M}$ and $-\Sigma F_{nZ}^{M}$).

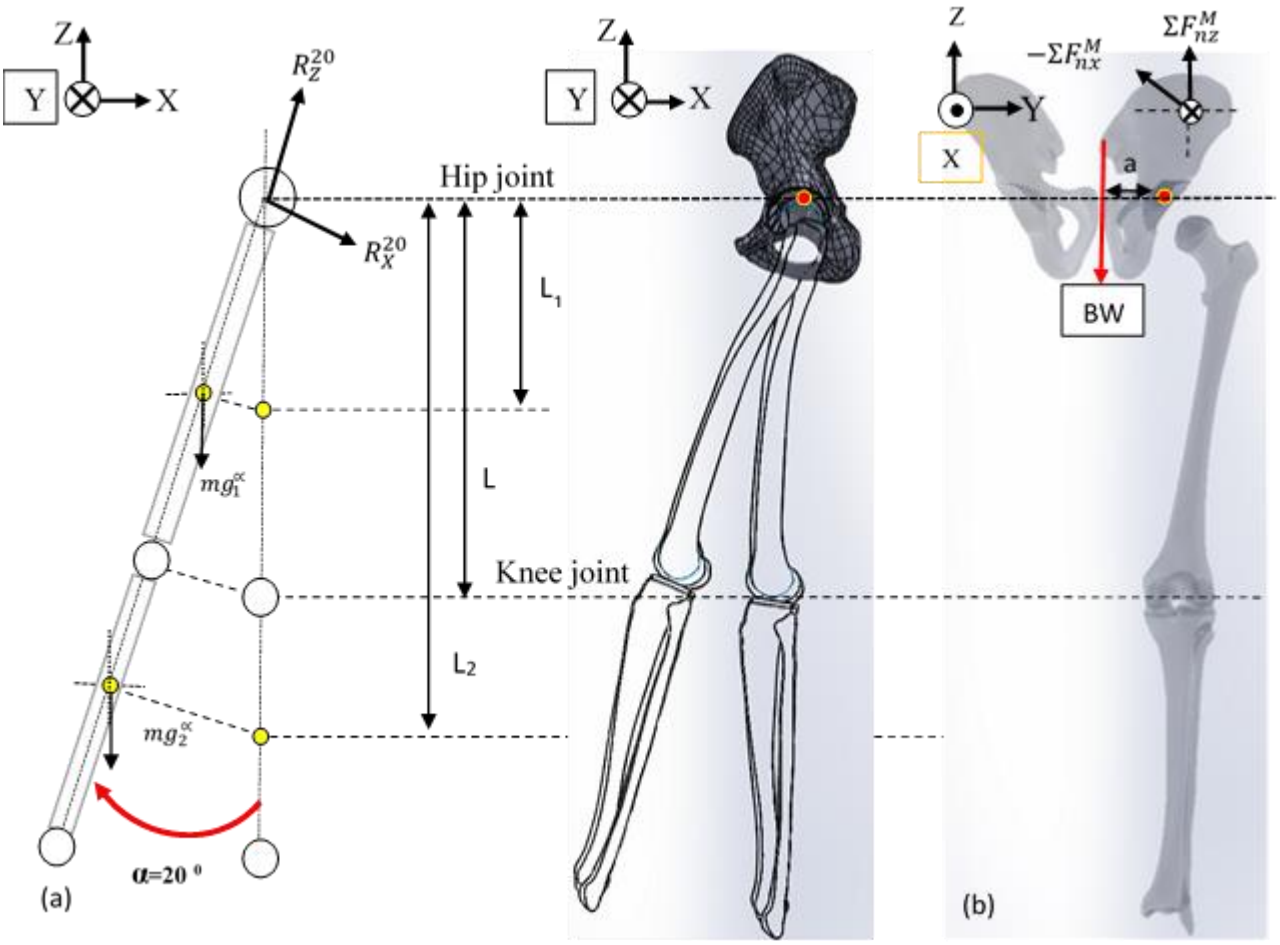

Figure 4-5: (a) Free body diagram of bony parts and (b) total muscles contraction of the hip joint during a hip extension (i.e. 50%) of the gait.

Table 4-5 and 4-6 demonstrate the muscle contraction and their created moments around (H) as the reference point. The force and created torque around the Y-axis were neglected due to simplifying the calculation steps for this section. The clockwise (CW) bearing was considered as a positive direction of the moment.

Table 4-6: The activated muscles and their contact forces (in 2D) during the hyperextension of the femur (i.e. 50%) of the gait (Correa et al. 2010).

Muscles	N	Force X(i) - Medial lateral (×BW)	Force Z (k) - Superior- Inferior (×BW)
G MED	1	0.011	1.47
G MAX	2	-0.076	0
RF	3	0.03	0.06
Add MAG	4	0	0.01
HAM-ST	5	0.0017	0.008

HAM-SM	6	0.016	0.064
HAM-BF	7	0.00032	0.0089
Total		$F_{ny}^{MUS} = \sum_{n=1}^{n=5} F_{nX} = -0.0170$	$F_{nz}^{MUS} = \sum_{n=1}^{n=5} F_{nZ} = 1.6209$

Table 4-7: Created moment of activated muscles (in 2D for the X and Z components) during the hyperextension (50%) of the gait cycle. (CW direction considered as positive moment) (Correa et al. 2010).

Muscles	N	Moment X(i) - Medial lateral (×BW)	Moment Z (k) - (Superior- Inferior) (×BW)
G MED	1	0.062	-0.001
G MAX	2	-0.003	-0.001
RF	3	0.003	-0.001
Add MAG	4	0.003	0.000
HAM-ST	5	0.000	0.000
HAM-SM	6	-0.003	0.001
HAM-BF	7	-0.00038	2.76E-05
Total		$M_{ny}^{MUS} = \sum_{n=1}^{n=7} M_{nX} = 0.0612$	$M_{nz}^{MUS} = \sum_{n=1}^{n=7} M_{nZ} = -0.0025$

Considering the various forces (which subjected on the hip and knee joints), the muscles contraction , and employing the equilibrium static equations (i.e.$\sum F_X = 0 , \sum F_Z = 0 , and \ \sum \mathrm{M}_H = 0$) at the point H, the HCF predicted at 50 % of the gait which all muscles are included.

$$\sum F_Z = -BW + R_Z \cos(20) - R_X \sin(20) + K_Z \cos(20) + K_X \sin(20) + F_{nz}^M - (m_1 + m_2) = 0 \qquad (4\text{-}23)$$

$$\sum F_X = R_Z \sin(20) + R_X \cos(20) + K_Z \sin(20) - K_X \cos(20) - F_{nX}^M = 0 \qquad (4\text{-}24)$$

$$\sum {M_Z}^H = -(a \times BW) + K_X \cos(20)\left(L_1 sin(70) cos(20)\right) - (m_1)(L_1 cos(70) cos(20)) - (m_2)(L_2 cos(70) cos(20)) + {M_{nZ}}^{Mus.} = 0 \qquad (4\text{-}25)$$

Where $F_{nz}^{M}\ and\ F_{nX}^{M}$, are the total muscle contraction in Z and X directions (extracted from table 4-5). $M_{nX}^{M}\ and\ M_{nZ}{}^{Mus.}$ represents the created moment from the activated muscles around the hip, in the Z and X-directions (extracted from table 4-6).

L_1 represents the half of the femur length and L_2 is the perpendicular distance between the centre of mass of tibia and hip.

With respect to applying same boundary condition for previous studies (i.e. 2D- All Mus. and 2D-No Mus.), the total knee reaction force ($K = (k_y^2 + k_z^2)^{\frac{1}{2}} = 2.75\ BW$) applied as compatibility condition.

By solving the Eq. 4-23, 24 and 25, the hip reaction force towards the X and Z-direction predicted 1.71×BW and -2.61×BW respectively. Hence, the total HCF computed using the Pythagoras theorem as 3.11 BW. All results are summarised in table 4-7.

Table 4-8: Total hip contact force in 2D with muscles contribution within toe-off stance of the gait (i.e. 2D- All Mus. @ 50 % of the gait).

Hip Contact Force in X axis	$R_X = 1.71$
Hip Contact Force in Y axis	$R_Z = -2.61$
Total Hip Contact Force (HCF)	$(2D - All\ Mus.) at\ 50\%\ of\ the\ gait = 3.11\ BW$

4.4.4 HCF 2D -No Mus. @ 50% (Skeletal Model)

In this section, the HCF predicted when the effect of the muscles contributions were neglected within the pre-swing of the gait cycle. The skeletal model is extended at 20˚ as shown in figure 4-5 (a). Using the same principle of the equilibrium static for the hip and knee joint without the contribution of the muscle contraction and moments, the HCF was predicted using following equations.

$$\sum F_Z = -BW - R_Z\cos(20) - R_X\sin(20) + K_Z\cos(20) + K_X\sin(20) - (m_1 + m_2) = 0 \quad (4\text{-}26)$$

$$\sum F_X = R_Z\sin(20) + R_X\cos(20) + K_Z\sin(20) - K_X\cos(20) = 0 \quad (4\text{-}27)$$

$$\sum M_Z{}^H = -(a \times BW) + K_X\cos(20)\left(L_1 sin(70)cos(20)\right) - (m_1)(L_1 cos(70)cos(20)) - (m_2)(L_2 cos(70)cos(20)) = 0 \quad (4\text{-}28)$$

The hip reaction force in X and Z-direction predicted 1.13 and -1.18×BW respectively. Hence, the total HCF computed using the Pythagoras theorem as 1.64 of BW. Results are summarised in table 4-8.

Table 4-9: Hip contact force in 2D Without muscles contribution at pre-swing (i.e. 2D-No Mus. @ 50 % of the gait).	
Hip Contact Force in X axis	$R_X = 1.13$
Hip Contact Force in Z axis	$R_Z = -1.18$
Total Hip Contact Force (HCF)	$(2D - HCF - NMU.) at\ 50\%\ of\ the\ gait = 1.64\ BW$

Table 4-9 compares the obtained results via using equilibrium static analysis during the hip extension at 20 degree. The HCF (× BW) with the contribution of activated muscles (i.e. musculoskeletal model) shown around two times in comparison to the HCF without muscles (i.e. Skeletal) approximately.

Table 4-10: Hip contact force (× BW) in 2D at pre-swing phase ***with*** the muscle force and ***without*** the muscle contraction during the gait.		
Name of Study	2D- All Mus. @ 50% (×BW) (Musculoskeletal Model)	2D-No Mus. @ 50% (×BW) (Skeletal Model)
HCF	3.11	1.64

Figure 4-6 compares the obtained results of 2D analytical studies to determine the HCF during two critical positions of the normal walking (simple support and hyperextension stances). The 2D analytical studies proved that the simple support stance (i.e. 18% of the gait) demonstrating a higher contact force on hip joint with 3.53 of BW. The analytical study included the bony parts and muscles compartments to calculate the hip contact force.

Whereas at the beginning of the toe-off and end of terminal stance (i.e. 50% of the gait and hyperextension of the hip) the HCF was reduced to the 3.11 of BW.

On the other hand, two studies were conducted to calculate the HCF at 18% and 50% of the gait using the same boundary condition and equilibrium static equations. The 2D-No Mus. was denoted to show that the muscles contractions and moments were not considered and the bony system assumed exclusively. It can be seen that the HCF demonstrated significant variation while the muscles contraction and their contributions neglected and reduced HCF up to 1.6 of BW for two recognised peaks.

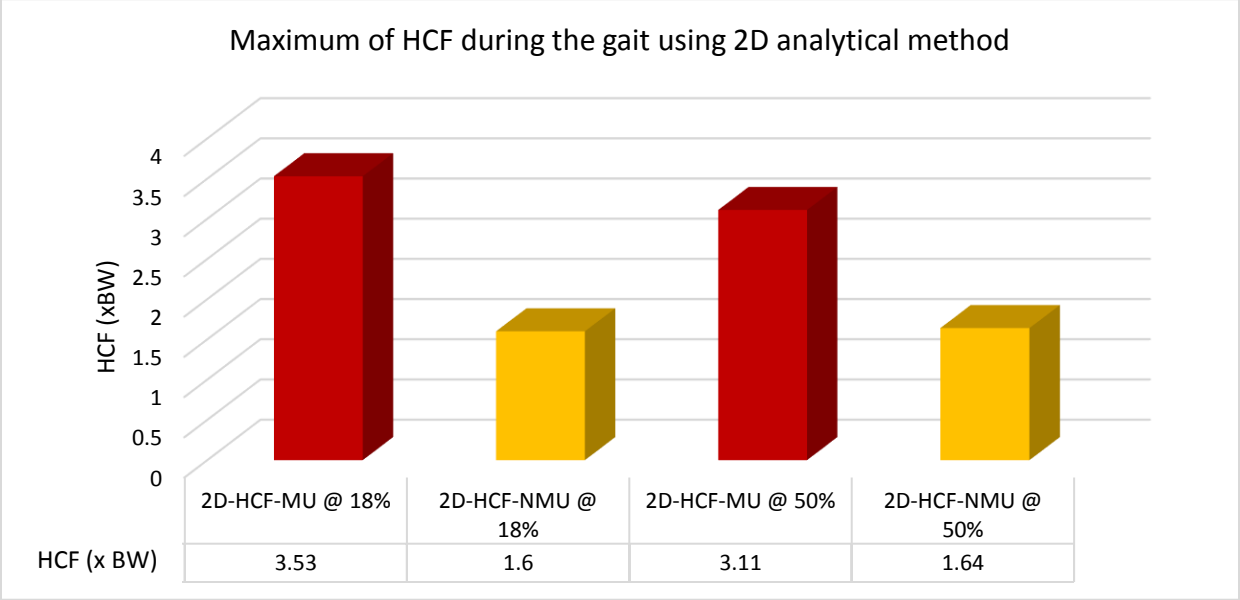

Figure 4-6: The maximum of total hip contact force during the simple support stance (i.e. 18-30%) and pre-swing stance (i.e. 50%) of the gait obtained from 2D analytical study.

4.5 HCF in 3D via Analytical Study

In this section, the 3D of the lower limb of body were considered along with eight reaction forces and fewer simplified assumptions. As previously mentioned the hip joint was replaced with universal joint and knee joint is considered as a hinge joint (Gupton and Terreberry, 2019). The purpose of this study are to enhanced the accuracy of calculation steps of predicted HCF as well as determined the effect of muscle contractions on total HCF by using 3D analytical study.

Similar to 2D analysis, two critical stances of the gait were assumed to estimate HCF including the simple support stance and beginning of the toe off where the hip was located at the hyperextension (i.e. 20˚). In addition, HCF was determined by considering two scenarios - one with muscle contact force, one without.

To determine the HCF in 3D, it is necessary to understand the cross product rule, position vector and vector of muscle contraction. Figure 4-7 shows an example of employing cross product rule to compute the force components and created torque around the reference point at the hip for the rectus femoris (RF) muscle.

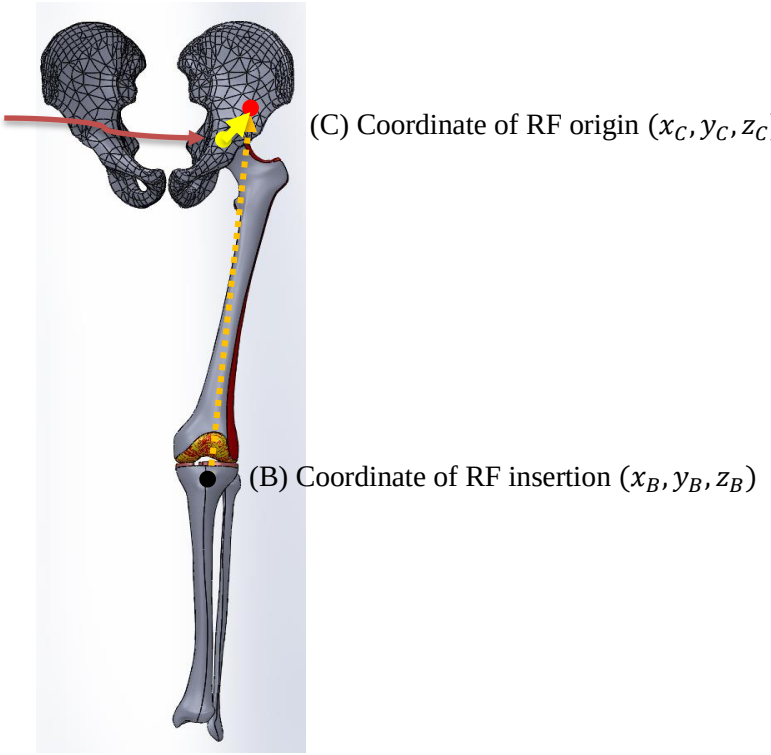

Figure 4-7:$\overrightarrow{HC}$ and $\overrightarrow{BC}$ vectors shown the position vector and contact force vector of RF muscle.

The vector $\overrightarrow{BC}$ demonstrates the line upon muscle RF acts which from its insertion to the origin. The force components (in x, y, and z direction) of RF force can be estimated via equation 4-32, if it was not reported experimentally. However, the resolutions of the muscles contraction is computed in 3D using the Eq.4-30.

$$\overrightarrow{BC} = (x_B - x_C)\hat{\imath} + (y_B - y_C)_y\hat{\jmath} + (z_B - z_C)\hat{k} \quad (4\text{-}29)$$

$$|BC| = sqrt((x_C - x_B)^2 + (y_C - y_B)^2 + (z_C - z_B)^2) \quad (4\text{-}30)$$

$$U_{BC} = \frac{\overrightarrow{BC}}{|BC|} \quad (4\text{-}31)$$

$$\vec{F} = F_{RF}.U_{BC} = F.\left(\frac{\overrightarrow{BC}}{|BC|}\right) = F_X\vec{\imath} + F_Y\vec{J} + F_Z\vec{k} \quad (4\text{-}32)$$

On the other hand, the position vector was defined as any vector whose tail started from the origin point of the system (H) to the line upon muscle RF acts which the RF (i.e.$\overrightarrow{BC}$) regardless of where the tip of a position vector is connected to a force vector.

$$\overrightarrow{HC} = (x_C - x_H)\vec{\imath} + (y_C - y_H)\vec{J} + (z_C - z_H)\vec{k} \quad (4\text{-}33)$$

Hence, the moment of the above-mentioned muscle in 3D was computed using the cross product or vector product via following equations.

$$\vec{M} = \overrightarrow{F_{RF}} \times \overrightarrow{HC} = (F_x\vec{\imath} + F_y\vec{J} + F_z k) \times (X_{HC})\vec{\imath} + (Y_{HC})\vec{J} + (Z_{HC})\vec{k} \quad (4\text{-}34)$$

$$\overrightarrow{M_{RF}} = (F_y Z_{HC} - F_z Y_{HC})\vec{\imath} + (F_z X_{HC} - F_x Z_{HC})\vec{J} + (F_x Y_{HC} - F_y X_{HC})\vec{k} \quad (4\text{-}35)$$

$$\overrightarrow{M_{RF}} = M_X\vec{\imath} + M_Y\vec{J} + M_Z\vec{k} \quad (4\text{-}36)$$

4.5.1 HCF-3D-Mus. @ 18-30% (Musculoskeletal model)

To determine the HCF of the lower limb system via 3D equilibrium static during the gait, two critical positions of the gait including the single support stance at 18% and beginning of toe off at 50% were assumed which were same as 2D studies. In this study, the equilibrium static equations ($i.e.\ \sum F_X = 0, \sum F_Y = 0, \sum F_Z = 0, \sum M_H{}^X = 0, \sum M_H{}^Y = 0\ and\ \sum M_H{}^Z = 0$) between the bony parts and activated muscles were assumed. The free body diagram of the simple support stance at mid stance (i.e. 18-30%) was shown in figure 4-8.

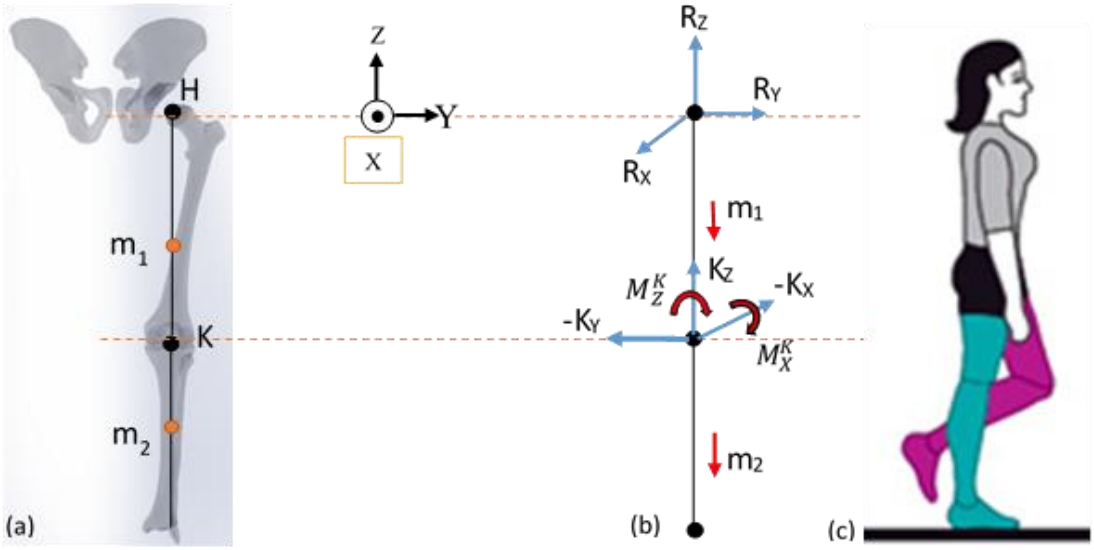

Figure 4-8: The human lower limb body (a) segmental points, (b) free body diagram and (c) the simple support stance of the gait (adapted from OptoGait, 2012) .

Following equilibrium static equation in 3D- All Mus. study have been considered to obtain the HCF at the top of femoral head.

$$\sum F_X = {R^H}_X - K_X + F_{nX}^{MUS} = 0 \qquad (4\text{-}37)$$

$$\sum F_Y = {R^H}_Y - K_Y + F_{nY}^{MUS} = 0 \qquad (4\text{-}38)$$

$$\sum F_Z = -BW + {R^H}_Z + K_Z - (m_1 + m_2) + F_{nZ}^{MUS} = 0 \qquad (4\text{-}39)$$

$$\sum {M_X}^H = (M_x^{BW} = a \times BW) - (M_x^{m1}) - (M_x^{m2}) - (k_Y \times dz) - (M_X^{Re.Knee}) + {M_{nX}}^{Mus.} = 0 \qquad (4\text{-}40)$$

$$\sum {M_Y}^H = -(M_Y^{m1}) - (M_Y^{m2}) - (k_X \times dz) + (k_Z \times dy) + {M_{nY}}^{Mus.} = 0 \qquad (4\text{-}41)$$

$$\sum {M_Z}^H = (k_Y \times dz) - (M_Z^{Re.Knee}) + {M_{nZ}}^{Mus.} = 0 \qquad (4\text{-}42)$$

Where, $F_{nX}^{MUS}, F_{nY}^{MUS}, and\ F_{nZ}^{MUS}$ represents the x, y and z components of the muscles contraction (n= 1 to 5 as shown in table 4-10) in x, y and z directions. (M_x^{m1}) and (M_x^{m2}) represent as created moments around H due to the mass of femur and tibia respectively. In addition, $k_X, k_Y, and\ k_Z$ are regarded as knee contact forces (i.e. reaction forces) which multiple their corresponding distance showing the moments round H. $M_{X,Z}^{Re.Knee}$ represents the reaction of moment in knee joint, which for the y direction granted zero due to the knee, is able to rotate around y-axis as hinge joint. ${M_{n(X,Y,Z)}}^{Mus.}$ represents as created moments from activated muscles around H point (See table 4-10). Figure 4-9 shows the normal distance between the H as reference point of this study and the centre of the knee joint. It can be realised that the normal distance in Y-direction is very small (0.0078 m) and can be neglected.

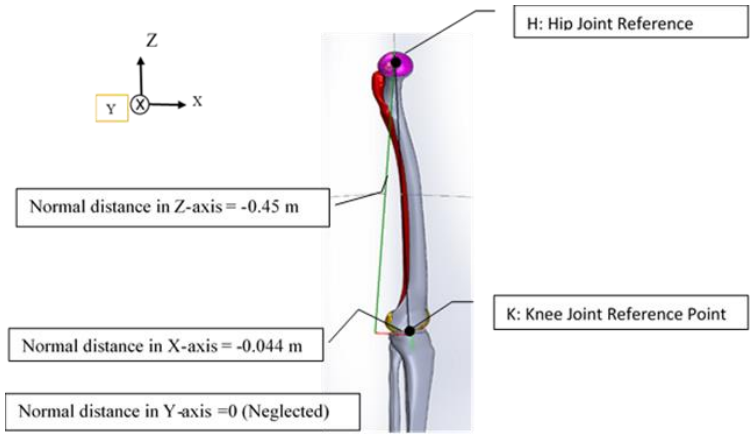

Figure 4-9: Illustration of normal distance from the knee joint (k) to the hip joint (H). The normal distance in Y-axis is neglected.

The activated muscles within the simple standing stance (18-30%) are listed in table 4-10. In addition, 3D components of the activated muscles and their created moments are summarised in table 4-10. Table 4-11 shows all activated compartments which considered to determine the reaction forces ($R_{x,y,and\ z}^H$) around H point in all 3D studies in this research, including bodyweight, mass of femur, mass of tibia bone and knee reaction forces ($K_{x,y,and\ z}$).

Table 4-11: Denoted muscle groups and their contact forces and moments during the single support stance (18%) of the gait in 3D study (Correa et al. 2010).

Muscles	N	Contact Force (× BW) $\overrightarrow{F_M} = F_X\hat{\imath} + F_Y\hat{\jmath} + F_Z\hat{k}$	Moment of muscle (× BW) $\overrightarrow{M_M} = M_X\hat{\imath} + M_Y\hat{\jmath} + M_Z\hat{k}$
G MED + MIN	1	$-0.34\,\hat{\imath} - 0.88\hat{\jmath} + 1.25\hat{k}$	$0.184\,\hat{\imath} - 0.023\hat{\jmath} + 0.034\hat{k}$
PIR	2	$-0.05\,\hat{\imath} - 0.13\hat{\jmath} + 0.11\hat{k}$	$-0.005\,\hat{\imath} - 0.001\hat{\jmath} - 0.003\hat{k}$
RF	3	$-0.03\,\hat{\imath} - 0.01\hat{\jmath} + 0.16\hat{k}$	$0.008\,\hat{\imath} + 0.005\hat{\jmath} + 0.002\hat{k}$
VAS (L)	4	$-0.19\,\hat{\imath} - 0.1\hat{\jmath} + 0.32\hat{k}$	$0.019\,\hat{\imath} + 0.014\hat{\jmath} + 0.016\hat{k}$
GAS	5	$-0.02\,\hat{\imath} - 0.01\hat{\jmath} + 0.01\hat{k}$	$-0.004\,\hat{\imath} + 0.008\hat{\jmath} + 0.001\hat{k}$
Total $\sum_{i=1}^{i=5} {}^{Muscles}_{ix,y,and\ z}$		$-0.63\,\hat{\imath} - 1.13\hat{\jmath} + 1.85\,\hat{k}$	$0.203\,\hat{\imath} + 0.004\hat{\jmath} + 0.049\,\hat{k}$

Table 4-12: All types of loading contributed during the single support stance (18-30%) of the gait in 3D study.

Other components	Contact Force (× BW) $\overrightarrow{F_M} = F_X\hat{\imath} + F_Y\hat{\jmath} + F_Z\hat{k}$	Moment around (H) (× BW) $\overrightarrow{M_M} = M_X\,\hat{\imath} + M_Y\hat{\jmath} + M_Z\hat{k}$
Bodyweight	$0\,\hat{\imath} + 0\hat{\jmath} + 1\hat{k}$	$0.0708\,\hat{\imath} + 0\hat{\jmath} + 0\hat{k}$
M_1: Mass of femur	$0\,\hat{\imath} + 0\hat{\jmath} + 0.08\hat{k}$	$-0.0028\,\hat{\imath} - 0.00264\hat{\jmath} + 0\hat{k}$
M_2: Mass of tibia	$0\,\hat{\imath} + 0\hat{\jmath} + 0.08\hat{k}$	$-0.0004\,\hat{\imath} - 0.0048\hat{\jmath} + 0\hat{k}$
Knee Reaction Force (K_i)	$-K_X\,\hat{\imath} - K_Y\hat{\jmath} + K_Z\hat{k}$	

$M_X\,\hat{\imath}$	$M_Y\hat{\jmath}$	$M_Z\hat{k}$
0	0.44 K_X	0
(-0.44) K_Y	0	0.045K_Y
0	0.045 K_Z	0

The knee reaction moments in X and Z directions were adopted from Kirkwood's, et al., (2007) study with the values of (-0.38) BW and (-0.023) BW respectively. By entering in the all above-menionoed values in the equations 4-37 to 4-42, followinq equations were devloped.

$$\sum {M_X}^H = (0.0708) - (0.0028) - (0.0004) - (0.44 \times K_Y) - (0.38) + 0.203 = 0 \quad (4\text{-}43)$$
$$\sum {M_Y}^H = -(0.00264) - (0.0048) - (0.44\, K_X) + (0.045\, K_Z) + 0.004 + (0) = 0 \quad (4\text{-}44)$$
$$\sum {M_Z}^H = (0.045\, K_Y) - (0.023) + 0.049 = 0 \quad (4\text{-}45)$$

Due to the hyperstatic situation, two various values for the K_Y obtained from equation 4-43 and 4-45 which are substituted into the following equation as a compatible condition. Similar to the 2D studies, the knee reaction force as average 2.75×BW is considered for the 3D studies.

$$K = (k_X^2 + k_Y^2 + k_Z^2)^{\frac{1}{2}} = 2.75\, BW \quad (4\text{-}46)$$

Combining equations (4-44) and (4-46) and solving using the simultaneous equation technique resulted in four different values for K_X and K_Y.

Due to the nature of equation 4-46, the replacing phrase $(K_X)$from equation 4-44 into equation 4-46, the second-degree polynomial or quadratic equation is regarded as follows.

$$1.01\, {K_Z}^2 - 0.00122\, K_Z - \begin{cases} 5.92 & if \quad K_Y = 0.57 \\ 6.19 & if \quad K_Y = -0.24 \end{cases} \quad (4\text{-}47)$$

Table 4-12 shows all possible values, which can be estimated from 4-43 and 4-45 equations to make matrix of K_Z, obtained from two various K_Y.

Table 4-13: Matrix of obtained results from second-degree polynomial, where the total knee reaction force is considered as 2.75×BW averagely.

× BW	K_Y	K_Z	
From Eq. 4-43	-0.24	$K_{Z1} = 2.644656$	$K_{Z2} = 2.692998$
From Eq. 4-45	0.57	$K_{Z3} =$ -2.63904	$K_{Z4} = -2.68904$

Considering the nature of any polynomial, there are two types of answer that can be determined through using the quadratic equation including external and internal root. The external root is not in the range of the rational hypothesis of the quadratic equation, whereas the internal root is converged with considered assumption and showed an acceptable value (Barnett, 1992).

To determine the external and internal roots of the obtained equation 4-47, the main assumption of the equation were reviewed as follows:

'By increasing the body weight of a human, it is expected to increase the reaction force in z-axis (i.e. toward inferior direction) in a knee joint.'

To assess whether the attained reaction forces (table 4-12) matched with the above-mentioned statement a separate study was conducted. It is aimed to demonstrate the convergence characteristics of four various K_Z (Z-reaction force 1 to 4) in a knee joint by increasing the value of the body weight. Figure 4-10 shows that by increasing the human body weight results in an

increase of the terms K_{Z1} and K_{Z2} and can be accepted as internal roots, whereas the K_{Z3} and K_{Z4} are decreased, which does not satisfy the considered assumption for the quadratic equation.

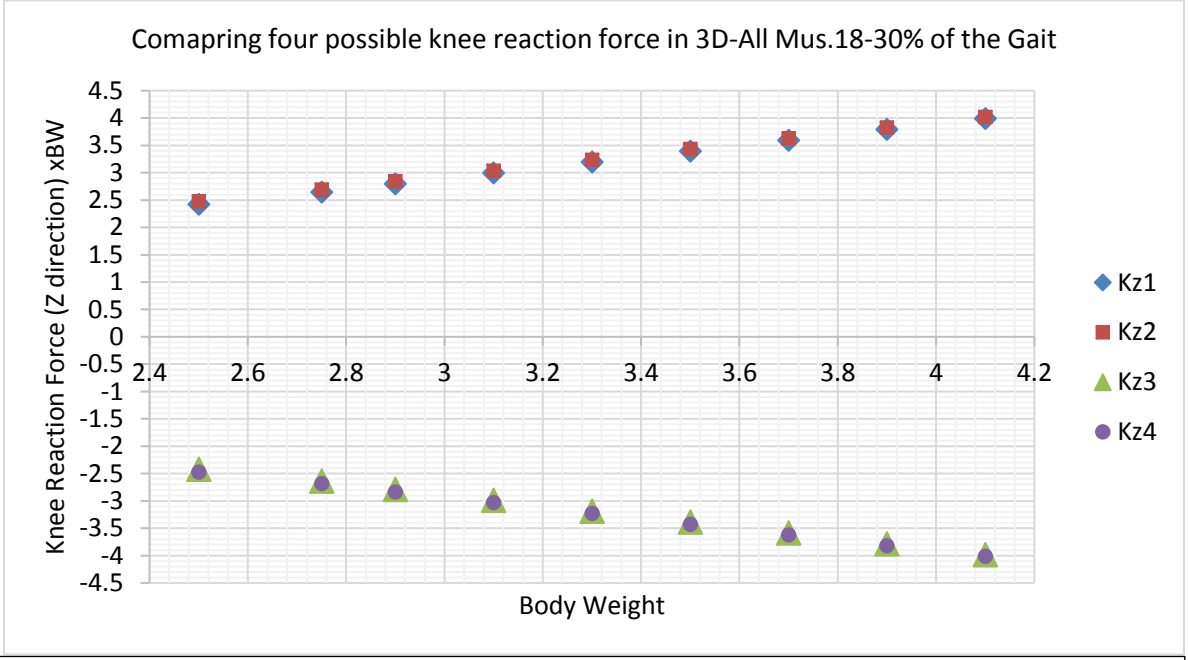

Figure 4-10: The convergence characteristic of the four obtained values from Eq. 4-47, based on the considered assumption.

Hence, by substituting K_{Z1} and K_{Z2} as accepted values into Eq. 4-44, the following equation 4-48 and two possible values of K_X were derived.

$$K_X = 0.007 - 0.102K_Z \qquad (4\text{-}48)$$

All possible and valid values for the knee reaction forces in X, Y and Z directions were replaced to equations 4-37, 4-38, and 4-39 to obtain equations 4-48, 4-49, and 4-50. By solving the following equations, the values of $R^H{}_X$, $R^H{}_Y$, and $R^H{}_Z$ were derived. Finally, the resultant values (i.e. two possible values) of the hip contact force (HCF) @ 18-30% of the gait in 3D study were estimated.

$$R^H{}_X = K_X: \begin{cases} = 0.276 \\ = 0.281 \end{cases} - (-0.63) \qquad (4\text{-}49)$$

$$R^H{}_Y = K_Y: \begin{cases} = -0.24 \\ = 0.57 \end{cases} - (-1.13) \qquad (4\text{-}50)$$

$$R^H{}_Z = 1.16 - 1.85 - K_Z: \begin{cases} = 2.644 \\ = 2.692 \end{cases} \qquad (4\text{-}51)$$

Table 4-13 shows the total HCF and its components derived from 3D study at 18-30 % of the gait with considering muscle contraction contributions.

Table 4-14: Total hip contact force and its components (× BW) in 3D whilst considering muscles contribution at single support stance of the gait (i.e. 3D-All Mus. @ 18-30% of the Gait).

Hip Contact Force in X-axis (× BW)	$R^H{}_X = 0.906\ or\ 0.911$
Hip Contact Force in Y-axis (× BW)	$R^H{}_Y = 1.7\ or\ 0.89$
Hip Contact Force in Z-axis (× BW)	$R^H{}_z = -3.33\ or -3.38$
Total Hip Contact Force (× BW)	$(3D - HCF - All\ Mus.)at\ 18\%\ of\ the\ gait = 3.84\ or\ 3.61$
Average HCF (× BW)	3.72

4.5.2 HCF-3D-No Mus. @ 18-30 % (Skeletal model)

Another study was conducted to determine HCF without considering muscles contraction within the simple support stance (i.e. 18-30% of the gait) during the normal walking. For the assumption, just the bony compartments were considered to compute the hip contact force at the reference point (i.e. H). The equilibrium static equations were developed from Eq.4-52 to Eq. 4-57 and the same compatibility condition was granted to compute the resultant force. By placing the values from table 4-11 in the following equations, HCF without considering the activated muscle at 18-30% of the gait was estimated. The total value of HCF for the skeletal model and its components is summarised in table 4-14.

$$\sum F_X = R^H{}_X - K_X = 0 \qquad (4\text{-}52)$$
$$\sum F_Y = R^H{}_Y - K_Y = 0 \qquad (4\text{-}53)$$
$$\sum F_Z = -BW + R^H{}_Z + K_Z - (m_1 + m_2) = 0 \qquad (4\text{-}54)$$
$$\sum M_X{}^H = (M_x^{BW} = a \times BW) - (M_x^{m1}) - (M_x^{m2}) - (K_Y \times dz) - (M_X^{Re.Knee}) = 0 \qquad (4\text{-}55)$$
$$\sum M_Y{}^H = -(M_Y^{m1}) - (M_Y^{m2}) - (K_X \times dz) + (K_Z \times dy) + (M_Y^{Re.Knee} = 0) = 0 \qquad (4\text{-}56)$$
$$\sum M_Z{}^H = (K_Y \times dz) - (M_Z^{Re.Knee}) = 0 \qquad (4\text{-}57)$$

Table 4-15: Total hip contact force and its components (× BW) in 3D Without muscles contribution at single support stance. (i.e. 3D-No Mus. @ 18-30% of the Gait).

Hip Contact Force in X-axis	$R^H{}_X = -0.254\ or\ -0.250$
Hip Contact Force in Y-axis	$R^H{}_Y = 0.51\ or\ 0.72$
Hip Contact Force in Z-axis	$R^H{}_z = -1.496\ or -1.449$
Total Hip Contact Force (HCF)	$(3D - HCF - MU.)at 18\%\ of\ the\ gait = 1.60\ to\ 1.63$
Average HCF (× BW)	1.615

Table 4-15 compares the obtained results throughout equilibrium static analysis during the single support stance at 18% of the gait cycle. The maximum HCF (× BW) with the contribution of

activated muscles showed more than two times (i.e. 2.36 times) in comparison to the HCF without the contribution of activated muscles.

Table 4-16: Total Hip contact Force (mean value × BW) in 3D at single support stance (i.e. 18% of the gait) with muscle contribution force and without muscle contraction.

Name of Study	3D-All Mus. @ 18% (Musculoskeletal model)	3D-No Mus. @ 18% (Skeletal Model)
Resultant of Hip Contact Force (Ave. HCF) (×BW)	3.72	1.615

4.5.3 HCF-3D- No Mus. @ 50% (Skeletal Model)

The lower limb body during toe off when the femur is located at hyperextension stance of the gait is demonstrated in figure 4-11. Figure 4-11(a) shows the free body diagram of bony parts (skeletal model). The correlation between the obtained reaction forces in a simple support stance (i.e. $R_y \; and \; R_Z$) and the reaction forces during the pre-swing phase of the gait (i.e. $R_y^{\propto}$ and $R_Z^{\propto}$) is shown. The hyperextension angle within the pre-swing phase is considered 20° (i.e. $\propto = 20\,°$) from the vertical line. According to the previous calculation for single support stance in 3D study, R_X, R_Y and R_Z without muscle contribution reported as two possible vectors $-0.250\hat{\imath} + 0.51\hat{\jmath} - 1.496\,\hat{k}$ or $-0.254\hat{\imath} + 0.72\hat{\jmath} - 1.449\,\hat{k}$. With respect to the geometry of free-body diagram at hyperextension, hip joint is rotated around the Y-axis hence the value of R_y^H is not remains constant (i.e. $R_y^H = R_Y^{20}$). While $R_X^{\propto}$ and $R_Z^{\propto}$ were rotated clockwise 20°. Therefore, the matrix of rotation around the Y-axis was used to determine R_X^{20} and R_Z^{20} (Jia, 2018).

$$\begin{bmatrix} R_X^{\propto} \\ R_Y^{\propto} \\ R_Z^{\propto} \end{bmatrix} = R_Y(\propto): \begin{bmatrix} cos(\propto) & 0 & sin(\propto) \\ 0 & 1 & 0 \\ -sin(\propto) & 0 & cos(\propto) \end{bmatrix} \times \begin{bmatrix} {R_X}^H \\ {R_Y}^H \\ {R_Z}^H \end{bmatrix} \qquad (4\text{-}58)$$

$$\begin{bmatrix} R_X^{20} \\ R_Y^{20} \\ R_Z^{20} \end{bmatrix} = \begin{bmatrix} cos(20) & 0 & sin(20) \\ 0 & 1 & 0 \\ -sin(20) & 0 & cos(20) \end{bmatrix} \times \begin{bmatrix} -0.25 \\ 0.51 \\ -1.496 \end{bmatrix} \; or \; \begin{bmatrix} -0.254 \\ 0.72 \\ -1.449 \end{bmatrix} \qquad (4\text{-}59)$$

By answering the above equation for two possible inputs, the following answers were deduced.

$$\begin{bmatrix} R_X^{20} \\ R_Y^{20} \\ R_Z^{20} \end{bmatrix} = \begin{bmatrix} -0.746 \\ 0.51 \\ -1.320 \end{bmatrix} \text{ or } \begin{bmatrix} -0.734 \\ 0.72 \\ -1.274 \end{bmatrix} \qquad (4\text{-}60)$$

Hence, the total hip contact force at H, for the bony parts without considering any muscles contribution at 50% of the gait summarised in table 4-16.

Table 4-17: Total hip contact force (× BW) in 3D without muscles contribution within pre-swing phase (i.e. 3D-HCF-No Mus. @ 50% of the gait cycle).

Hip Contact Force in X-axis	${R^{H.20}}_X = -0.746 \;\; or \;\; -0.734$

Hip Contact Force in Y-axis	$R^{H}{}_{Y} = 0.51\ or\ 0.72$
Hip Contact Force in Z-axis	$R^{H.20}{}_{z} = -1.320\ or\ -1.274$
Total Hip Contact Force (HCF)	$(3D - HCF - MU.)at\ 50\%\ of\ the\ gait = 1.44\ or\ 1.60\ BW$
Average HCF (× BW)	1.52

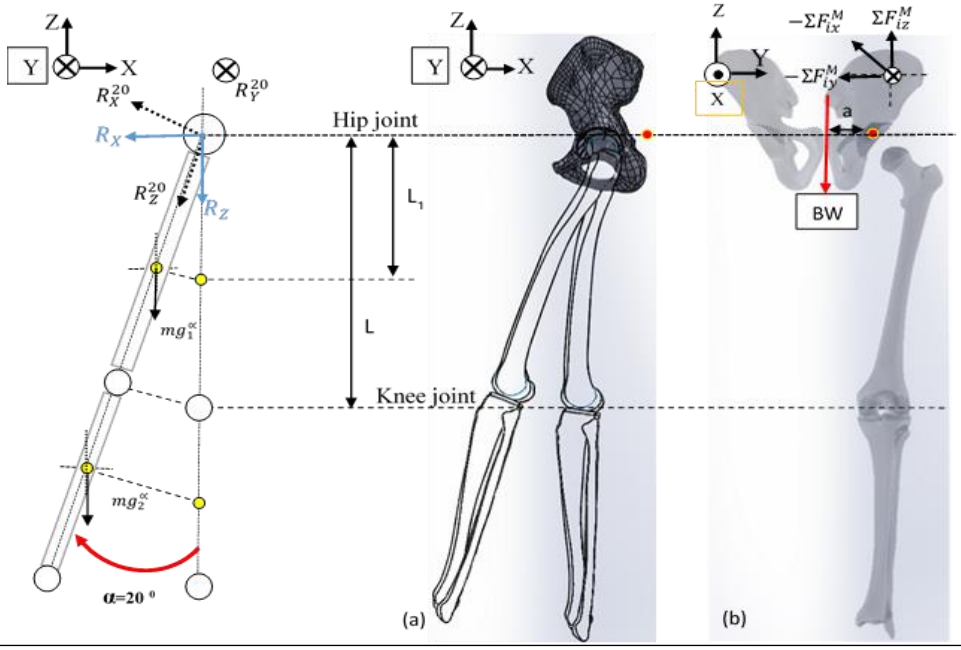

Figure 4-11: (a) Free body diagram of bony parts and (b) muscles contraction of the hip joint during a hip extension (i.e. 50%) of the gait.

4.5.4 HCF-3D-All Mus. @ 50% (Musculoskeletal Model)

In this section, the HCF was predicted while the targeted leg was situated at the beginning of the toe-off and end of terminal stance.

Within the pre-swing phase, the posterior muscle groups (which attach to the posterior side of the femur) are responsible for the extension of the femur from the hip joint. The main muscles are listed in table 4-5. The total contact force for all activated muscles in 3D study are summarised in table 4-17.

Table 4-18: Total muscle force for the activated muscles in 3D at 50% of the gait.	
$\sum_{i=1}^{i=7} F_{ix,y,and\ z}^{Muscles}$	Muscle contraction (× BW) $-0.13\,\hat{\imath} - 0.110\,\hat{\jmath} + 1.620\,\hat{k}$

Due to the simplification in the calculation steps for this section, the reaction force of the skeletal model at 50% summarised in table 4-16, are added to the correspondent values in table 4-17. For instance, to determine $R_X^{H.20-Mus.}$ for the musculoskeletal model during pre-swing phase of the gait, there are two associated forces are associated in the x-axis,

1. The hip reaction force for the skeletal model ($R_X^{20-N\ Mus.} = -0.72\ BW$) @ 50% of the gait, which summarised in table 4-16.
2. The total muscles contraction of seven muscle groups ($\Sigma F_{iX}^{M} = -0.13\ \hat{\imath}$ BW) summarised in table 4-17.

However, for the Z-axis the bodyweight and mass of femur and tibia were considered according to a free body diagram.

$$R_X^{H.20-Mus.} = R_X^{H.20-No\ Mus} + \sum_{i=1}^{i=7} F_{ix}^{Muscles} = \begin{cases} = -0.746 \\ = -0.734 \end{cases} - 0.13 = \begin{cases} -0.876 \\ -0.864 \end{cases} \qquad (4\text{-}61)$$

$$R_Y^{H.20-Mus.} = R_Y^{H.20-No\ Mus} + \sum_{i=1}^{i=7} F_{iY}^{Muscles} = \begin{cases} = 0.51 \\ = 0.72 \end{cases} - 0.11 = \begin{cases} 0.4 \\ 0.61 \end{cases} \qquad (4\text{-}62)$$

$$R_Z^{H.20-Mus.} = +\text{Bw} + (m_1 + m_2) - K_z - \sum_{i=1}^{i=7} F_{iZ}^{Muscles} = +1 + 0.16 - \begin{cases} = 2.644 \\ = 2.692 \end{cases} - 1.620$$
$$= \begin{cases} -3.104 \\ -3.152 \end{cases} \qquad (4\text{-}63)$$

Table 4-19: Hip contact force (× BW) considering the muscle contraction during the pre-swing phase of a gait (3D-All Mus. 50% of the gait).		
(× BW)	Force Components	Resultant $(R_X^2 + R_Y^2 + R_Z^2)^{1/2}$
Hip Contact Force	$(-0.876\ \hat{\imath} + 0.4\hat{j} - 3.104\ \hat{k})$	3.249
	$(-0.864\ \hat{\imath} + 0.614\hat{j} - 3.152\ \hat{k})$	3.325
Average HCF	3.287	

Table 4-19 compares the average hip contact force for 3D studies at 50% of the gait cycle. It can be seen that the muscles' contraction increased the value of total HCF two times higher than the skeletal model without any muscle contraction.

Table 4-20: The total Hip contact force (× BW) in 3D within pre-swing phase ***with*** the muscle contribution force and ***without*** the muscle contraction.		
Name of Study	3D-HCF-Mus. @ 50% (×BW) (Musculoskeletal Model)	3D-HCF-NMus. @ 50% (×BW) (Skeletal Model)

Resultant (HCF)	3.29	1.52

4.6 Analysis and Dissuasion

The total HCF and its angle (i.e. orientation) can be applied for several purposes including the stress and displacement analysis of the hip and knee joint. However, the obtained results (from the previous section) can be used for improving implants' design, eliminating the effect of local stresses, optimising the joint arthroplasty operation, and understanding the function of the hip joints. Several researchers identified two peaks of HCF during the normal walking of human at 18% and 50 % of the gait, hence this study was focused to only analyse these two peaks. (Chen et al., 2014; Dumas et al., 2012; Guess et al., 2014; Heller et al., 2001; Hast and Piazza, 2013; Lundberg et al, 2013; Lund et al., 2015; Modenese et al. 2011; Manal and Buchanan, 2013; Serrancoli et al., 2016).

The main reason to conduct the analytical methods (i.e.2D and 3D) for this study was, to determine the muscles' contraction increased the total HCF or decreased within the gait cycle.

In this section, the obtained outcomes are compared with other researchers to determine the level of validity of the obtained results. It is important to determine the authenticity of the acquired results due to using those as input data in the next chapter to calculate the stress characteristics of the restricted areas in local hip joint.

Figure 4-12 compares the obtained results of HCF for the entire analytical study including 2D and 3D. The 3D studies demonstrated higher values throughout using analytical methods; however, the variation between 2D and 3D studies did not show any significant difference. Hence, it can be concluded that the 2D analytical approaches are able to create the valid and reliable results to determine the HCF, in comparison to the 3D static methods. The maximum variance between 2D and 3D studies is computed as 1.205% using equation 4-64 (Hyndman & Koehler, 2006).

$$\sigma^2 = \frac{\sum(X_i - \mu)^2}{N} \qquad (4\text{-}64)$$

Where, σ^2 is donated as variance, X_i is the value of each element, μ is the mean value, and N is number of samples.

On the other hand, the main aim of conducting analytical studies (either 2D or 3D) was to support the assumption of this study. It has been acknowledged that the activated muscles within the gait (at 18-30% and 50%), significantly increased the hip contact force (HCF), in comparison to the skeletal model of the lower limb. The maximum variation of HCF between musculoskeletal (i.e.

3D-All Mus.) and skeletal model (i.e. 3D- NO Mus.) is estimated to be 230% by using 3D analytical approach within a single support stance of the gait.

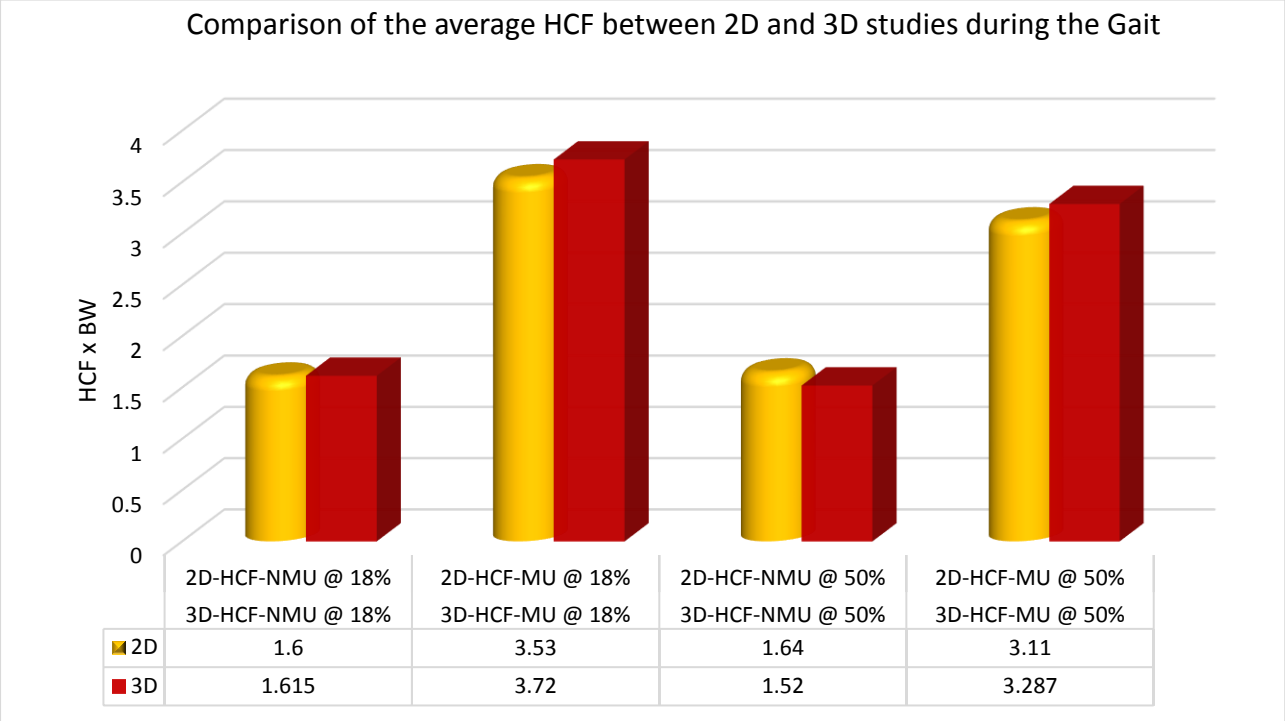

Figure 4-12: Comparison of the maximum HCF during the simple support (18-30 %) and pre-swing (50 %) stance of the gait using 2D and 3D analytical approach. Terms MU and NMU denoted as all muscle contribution and No muscle contribution.

1.1.1 HCF Result Verification

Although various analytical technique and mathematical methods can be used to estimate the HCF within the gait, it is not avoidable to consider the compatibility condition during the formation of equation.

It is therefore necessary to inspect the validity of the obtained results by comparing them with the preceding evidence from other researchers. Several researchers reported the hip contact force over the past 30 years applying the instrumented hip implants, mathematical modelling, and numerical methods. Their obtained HCF value ranged from 2.4 to 4.5 times BW (Bergmann et al., 1993, 2001; Brand et al., 1994; Chen et al., 2014; Damm et al., 2013; Davy et al., 1988; Debrunner, 1975; Kotzar et al., 1991; Pauwels, 1978; Paul, 1966; Schwachmeyer et al., 2013; Zhang et al., 2015).

ISO-14242-1 (2002) standardise the requirements of preclinical testing of the THR implants for normal walking. The loading and motion analysis defined the ISO for the hip wear simulation

according to a historical inverse dynamic modelling of healthy individuals. The hip contact force at the single support stance was reported at 3.4 × BW by ISO standard.

The recorded result by ISO standard for the HCF is consistent with the obtained results for 3D study in the current investigation 3.72×BW. However, there is less than 9 % deviation between the two case studies. The variation can be justified by considering the difference between the age for this research 56 years old (see section 4-4) and an average of ISO dataset around 65 years old. The above-mentioned reason is also stated by Chester and Wrigley, (2008) and DeVita and Hortobagyi, (2000). They highlighted that the age of the case study affected the hip moment and power during the normal walking as well as might affect the HCF.

NG et al., (2018) conducted controlled laboratory studies to determine the role of the muscles contraction on HCF during the walking for eighteen patients. They applied the motion capture system and static optimisation method to obtain HCF for the healthy case studies named as 'healthy control participants (CON)'. They estimated the maximum HCF 3.35 (± 0.1) × BW at single support stance.

Brand et al., (1994) conducted the experimental and mathematical approaches for a case study. They measured the peak resultant force in the range of 2.5-3.5× BW during the gait for a freely selected speed. Their results for 2D analysis with the muscles contribution highly matched with the presented results at 18%. However, for 3D analysis, their estimated HCF values were slightly higher (0.35× BW) than the obtained value in this study. The main reason to justify the reported variation is attributed to their assumption for the knee joint moments.

They assumed the knee ligaments and knee geometry could be satisfied with the rotational moment around the knee and hip. Hence, the created moments for those joints belong entirely to the muscles around the hip and the knee moment so can be neglected. While in the current study considered the knee reaction moment, including rotational moments in X and Z-axis, to enhance accuracy.

Later, Heller et al., (2001) applied the custom-made software to determine the hip superior-inferior contact force for own his human model. They considered the muscle path between the insertion and origin as point action and modelled 95 muscular lines. They reported the superior-inferior contact force (i.e. parallel to the vertical axis of human body) for the single support stance between 2.8 to 3.8 ($\pm$ 0.1) x BW, whereas this study estimated the hip contact force in the superior-inferior direction using 3D analysis at 18-30% of the gait at a value of 3.3 ($\pm$ 0.05) × BW (see table 4-13). It can be seen that the obtained results were situated in the above-mentioned range, which

supports the findings of this study. Chen et al., (2014) utilised the Anybody Software, the human model provided by Horsman et al., (2007) and the inverse dynamics-based optimisation to find the HCF. They reported HCF as 2600 N, which was 3.3 of BW. The maximum HCF estimated by Chen et al., (2014), is slightly less (i.e. 11%) than the obtained results in this study. The reported difference can be attributed to using an alternative computer-based model, optimisation method, and the number of leg muscles considered.

On the other hand, Dumas et al., (2012) conducted a study using the MATLAB software using Delp's (1990) model, and optimisation via inverse dynamics to determine the hip joint contact force. By considering 43 muscles act lines as a point-to-point attachment between the main muscle attachments they reported HCF around 4.5 x BW. Their acquired results were 20% higher than those find in this study, which was due to their use of the inverse dynamic approach with the objective of the sum of squared muscle stresses to determine the muscles contraction as well as number of muscles.

The inverse dynamic method mostly applied because of the hyperstatic condition of the human body. This method reduced the number of unknowns as well as predicted the muscles contraction from the anatomical model. According to Raikova & Prilutskyb, (2001), the potential reason for any variation in the obtained results with the optimisation-based model could be linked with the setup parameters of their model (such as muscle moment arms and number of muscles). The mentioned parameters might affect the predicted results for the muscle force. They emphasised that in the inverse dynamic approach makes the predicted muscles contraction more sensitive to the moment arm of the muscle and reference point in the model. Hence, any changes in the moment arms or reference point might significantly affect the magnitude of the muscle forces (Raikova & Prilutskyb, 2001). In addition, the selected anatomical model for the current study differed from the lower limb body adapted from Delp (1990) in Dumas et al.'s (2012) study.

Bergmann et al., (2001) conducted studies to determine the HCF using two types of instrumented hip implants including cemented and non-cemented joints with the aid of telematics data transmission. They reported the hip contact forces for three case studies in a range of 2.39 to 2.55× BW. Subsequently, Eschweiler, et al., (2012) challenged Bergmann et al.'s, (2001) results by comparing different approaches and techniques to compute the hip resultant force or HCF. They compared the results of various mathematical models with the *in-vivo* dynamic techniques after total hip replacement (THR). Eschweiler, et al., (2012) stated that using dynamic techniques to

predict HCF after THR created different values than the static measurement of HCF. They listed several reasons to justify the differences between the two methods, including the level of accuracy, the realistic number of muscle considered, and the assumed compatibility conditions.

In addition, the instrumented hip implants applied by Bergmann et al., (2001) summarised in the database of the OrthoLoad are only available for a small number of patients and case studies (three case studies). On the other hand, the Bergmann et al., (2001) used instrument implants for the patients and examined their HCF from one to ten-months after their operations within their rehabilitation period. It can be considered that the patient's health condition with a hip joint disease and after THR might not be fully recovered within a month. Hence, the instrumented hip implant might not reflect the actual value of the total hip reaction force. On the other hand, the diverse stiffness between the bone and applied materials in an implant (i.e. titanium or stainless steel) could capture the hip reaction force and therefore demonstrate a lower value for the HCF.

Figure 4-13 compares the values of HCF x BW obtained from various techniques conducted by different researchers. There is a wide range of results from minimum 2.52 x BW for the average of three studies (Igliĉ, 2002) to a maximum value of 4.5 x BW (Dumas et al., 2012). However, close analysis of the obtained results demonstrated that the experimental or clinical studies shows lower values for HCF in comparison to the analytical or mathematical predictions.

There is an exceptional value reported for HCF as a maximum of 6.54 x BW for the mean values of three studies reported from Blumentritt (1990). The main possible reason to justify the large difference is attributed to his consideration for the weight-bearing surface as a reference point. He assumed that the surface of the femoral head has a perpendicular angle to the longitudinal axis. He therefore expected that the direction of the HCF axis was parallel to the Z-axis and respectively perpendicular to the surface. Eschweiler, et al., (2012) analysed the Digitally Reconstructed Radiograph (DRR) images of pelvic-hip joint and accepted that the orientation of the HCF is not parallel to the longitude axis (alongside superior-inferior) hence Blumentritt's procedure to validate his model is questionable.

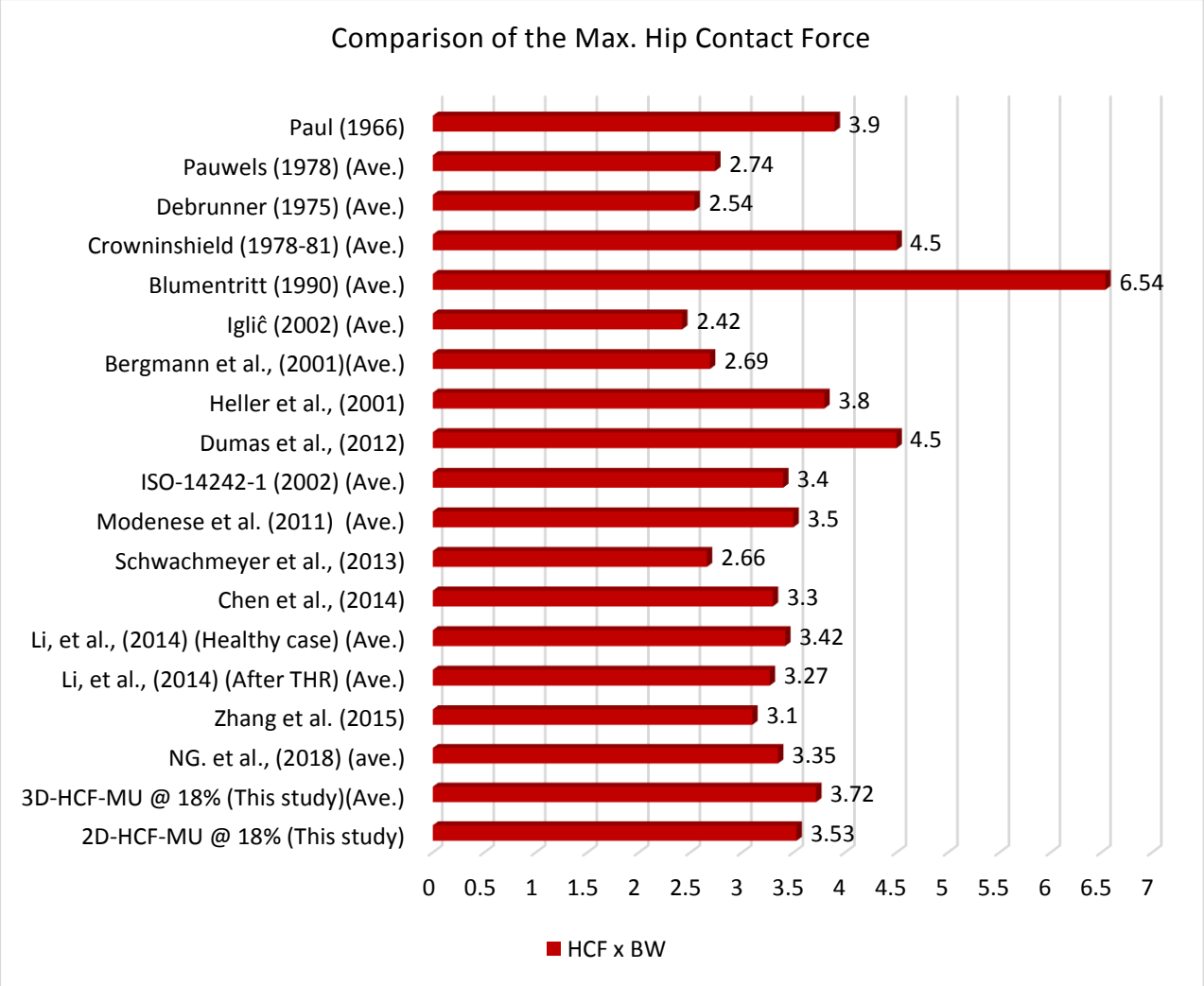

Figure 4-13: Comparison of the average HCF determined in this study and obtained results from other scholars during the simple support stance (18-30%) of the gait cycle. Term 'Ave.' denoted as a mean value of across all case studies.

4.6.1 Analysis of the HCF angles

In this section, the angles of the HCF components and resultant for the 3D studies at 18-30% and 50% are analysed analytically. The α, β and γ are defined based on the angle between the components of the X, Y, and Z-axis with their corresponding resultant. To determine the direction angles of HCF at 18-30% and 50% in 3D studies the following equations were applied (Giancoli, 2016) and results are summarised in table 4-20.

$$A_x = |A|\cos(\alpha) \quad (4\text{-}65)$$
$$A_y = |A|\cos(\beta) \quad (4\text{-}66)$$
$$A_z = |A|\cos(\gamma) \quad (4\text{-}67)$$

Figure 4-14 shows the orientation of the HCF and its reaction based on the obtained components of the HCF in the x, y, and z. directions. The values of the components are not drawn to scale and the green arrow is used to demonstrate the direction of the HCF. However, the overall orientation of the HCF angle completely matched within the simple support and hyperextension stances.

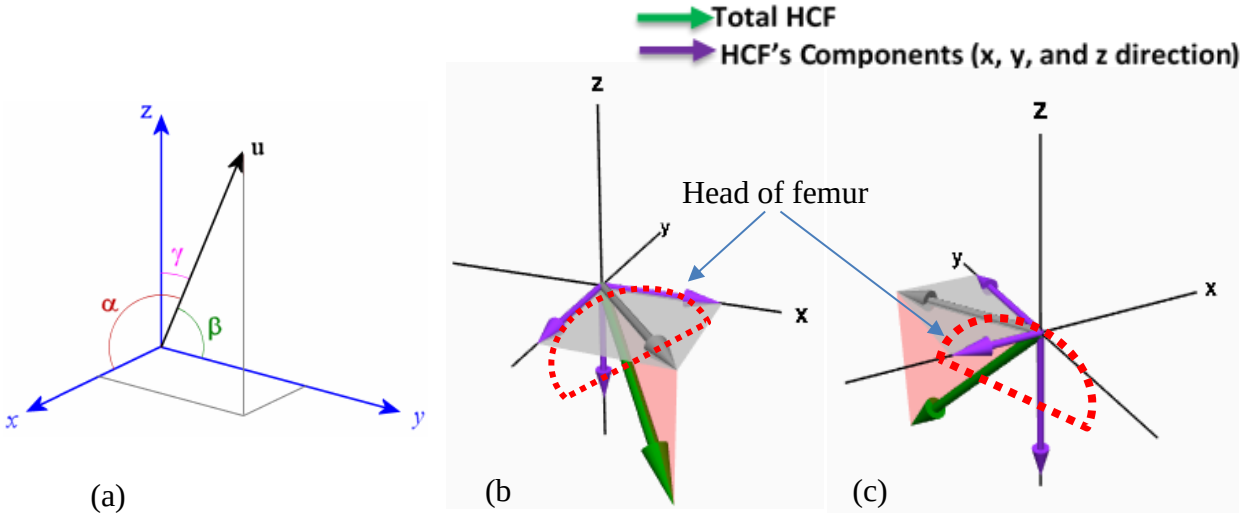

Figure 4-14: (a) Illustration of 3D angles of a vector including $\alpha, \beta, and\ \gamma$ (b) the HCF at 18 %, and (c) the HCF at 50 % of the gait at the top of femoral head. The red dotted line shows the head of femur.

It was expected that in the single support stance (18%), the direction of the HCF transferred the resultant force to the superior-inferior (i.e. negative Z-axis) of the femur bone. In this case, the femur bone is the most stiffened element in the lower limb and engaged to yield a large proportion of the applied force and therefore balancing the human body. The selected lower limb model from the volunteered patient has a femoral head-neck (red dashed line) axis with an angle of 41.5˚ from the superior-inferior axis of the body.

The estimated HCF@18% shows that an average angle of 25.24 for a 3D study ($\pi - \gamma = 25.24$ Ave. degrees) between the range of 20 to 30˚ is demonstrated schematically in figure 4-15 by the yellow arrow. Hence, the variation between the HCF angle and femoral head-neck axis was calculated as (41.5 - 25.24 = 16.26 °) degrees which supports the above-mentioned prospect. Because the highest portion of the HCF is subjected at the head of the femur and can be transferred to the diaphysis of femur via the femoral neck.

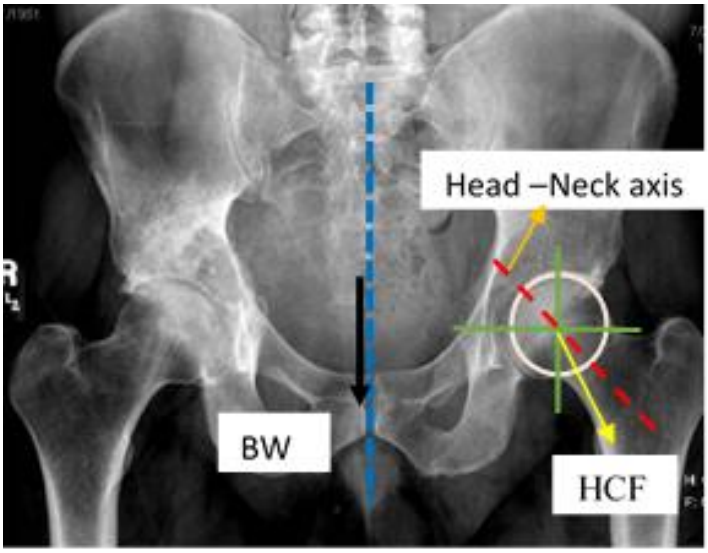

Figure 4-15: Schematic image of variation between the HCF direction and axis of head-neck femur at 18 % (Pcir, 2007).

Furthermore, figure 4-14 (c) shows the orientation of HCF resultants and its components at 50% of the gait, where the head of the femur extend 20˚ around the y-axis. Hence, it is expected the total HCF oriented accordingly towards the extension angle. The obtained results of the 3D analytical (3D-All Mus. @ 50 %) matched well with above expectation and natural position of the femoral head. The calculated direction (i.e. angle) from the predicted components (i. e. $-0.85\,\hat{\imath} + 0.614\hat{\jmath} - 3.1\,\hat{k}$) in 3D-All Mus. @ 50 % was orientated towards the extension of the femoral head direction. Hence, it can be concluded that the orientation of HCF resultant (i.e. the green arrow in figure 4-14 (C)) is located towards the above-mention circumstance and correlated with the preliminary assumption.

The total difference between the angle of the femoral head-neck and HCF axis at 50% of the gait increased slightly in comparison to the 18-30% of the gait cycle. The variation is increased from 16.26 to the 23.6 ° due to the contribution of the posterior muscles. Within the pre-swing phase, the hip joint is located at hyperextension therefore the posterior muscles support the human body position and balance the effect of hip contact force accordingly. In addition, the resultant of HCF at hyperextension decreased by 11% in comparison to the single support and therefore less pressure and force is transferred to the femoral head. This demonstrated a wider angle of the body reaction force to equilibrium the lower limb position @ 50%. Table 4-20 shows the computed HCF angles across the 2D and 3D studies.

Table 4-21: The analysis of angles in 3D studies where the muscle contributed to the HCF (Average between the maximum and minimum in degrees).		
3D-HCF-Mus. @ 18 %	$\alpha = 75.86$	The HCF angle towards the superior-inferior direction $(\pi - \gamma) = 25.24^0$
	$\beta = 79.7$	
	$\gamma = 154.76$	
3D-HCF-Mus. @ 50 %	$\alpha = 105.45$	$(\pi - \gamma) = 17.9^0$
	$\beta = 81.135$	
	$\gamma = 162.1$	
2D-HCF-Mus. @ 18 %	$\gamma = 170.5$	9.5^0
2D-HCF-Mus. @ 50 %	$\gamma = 147.0$	32.9^0

4.7 Results verification (HCF Angle)

Although there is insufficient data to compute the angle of the HCF at hip hyperextension analytically or numerically from the prior studies and investigations, the obtained angle (25.24˚ average) in this study for 3D occurred at 18% (i.e. single support stance). The obtained angle for HCF in this study is consistent with Bergmann et al., (2016)'s results where the range of HCF angle at the single support stance of the gait was reported from 16 ° to 29 °. In addition, they reported a mean value of 24 ° for the stand-up situation similar to the single support stance in walking activity. However, the range of HCF angle for their three patients in the walking activity is reported with a range of 9 - 21 °.

For the free walking rate (i.e. normal walking rate without a specific rate given by scholar), the HCF angle is reported as 15.71 ° from the heel strike to toe-off stance. According to prior discussion, they obtained data from volunteered patients after THR operation, which could restrict patient's motion during the activity and reduced the HCF and its related angle. Pauwels' (1978) computed the mean value of HCF angle at single-legged stance around 18.64 ° showing 26.14% variance with the computed angle in the current study (25.24 °). Zavatsky, A., et al., (2014), reported the angle of HCF for the normal walking for children 6-12 years old. They estimated HCF angle an average 17 ° within the same stance of the gait cycle. Conversely, Blumentritt (1990) reported the lowest value for the HCF angle at 5.95 ° due to his wrong assumption of the HCF as discussed previously. Igliĉ (2002) calculated an approximate the mean value of hip contact force angle with respect to the Z-axis approximately 9.15^o that was matched with the 2D study of the current study 9.5^0.

Chapter 5

Stress Analysis using Analytical Approach

5.1 Introduction

There are various types of structural analyse to determine the reaction forces, stress and deformation of a structure engineer statically. To achieve reliable results, it is required to define the loading conditions, boundary conditions, and the mechanical and physical properties of materials.

This chapter aims to provide a comprehensive review of the fracture of femur and identify the most susceptible segments, which cause failure or fracture. In addition, the unique method known as parallel planes will be applied to divide or discretise three susceptible regions of the femur into the infinitesimal planes. The main aim of this chapter is to determine the effect of muscle contraction on local stress in the susceptible regions of a femur via analytical approach. To accomplish this aim, it is required to consider the HCF with the muscles and without muscle contribution. Hence, the predicted results from the previous chapter are employed for two main case studies named HCF-All Mus. and HCF-No Mus. within a single support and pre-swing phase of the gait cycle.

5.2 Reviewed Related Work

Wang, et al., (2004) employed a 2D modelling procedure to predict the femoral hip stress in the sagittal plane while assuming the distribution loading for the entire cross-section of the femoral head. The femoral peak stress reported 7.1 MPa for the particular geometry of a participant. They considering participant's mass of 700 N, femoral articular thickness 1 mm, and radius of the femoral head 21 mm. Wang et al., (2017) conducted both analytical and computational studies to determine the stress distribution on the femoral surface. For the analytical method, they considered the right femoral head as a rigid sphere and determined its spherical coordination system. In addition, an acetabulum was modelled as a rigid hemispherical shell. For the numerical study, the elastic modulus of the femur and cartilage compartments are considered as 17.3 MPa and 0.1 GPa

respectively, and the Poisson's ratio was considered at 0.29 and 0.4 respectively. They determined the maximal principal stress at various angles of the femoral head within the gait and reported a maximum stress of 6.23 MPa where the centre of the femoral head is placed vertically at an angle of 50 ° with the outer edge of the acetabulum.

Some researchers utilised the analytical and mathematical modelling to examine stress and strain of the lower limb body segmentations and hip joint contact force instead of using the computational approaches. The real geometry and bony segmentation were employed partially or completely for their mathematical or analytical models however, some geometries were occasionally simplified (Michaeli et al., 1997; Ipavec et al., (1999); Daniel et al., 2001; Stansfield, et al., 2003; Wang, et al., 2004, Wang, et al., 2017).

Michaeli et al., (1997) employed idealized geometries as various layers of the spherical shapes for the acetabulum, articular cartilage of femoral head, and the head of the femur. They reported the contact hip joint stress between 0.29 to 1.2 MPa. However, they found these were roughly seven times less than the quantities calculated experimentally.

The Discrete Element Analysis (DEA) is another type of analytical methods to examine the mechanics of the hip joint. This method separates the joint contact region into discrete elements by combining the shearing and compressive components of stress which dependent upon the biomechanical condition of the joint force.

Genda et al., (2001) developed a DEA hip joint model as a discrete spherical model for the femoral head and acetabulum. They examined both the influence of anatomical characteristics and the patient's gender on foot contact pressure. They developed the 3D contact geometry from a 2-D radiograph image. The maximum contact pressure was reported at 2MPa. Yoshida et al., (2006) conducted another study with the same methodology and built a 3-D hip joint model from radiography images. They estimated a maximum contact pressure of 3.26 MPa during ordinary walking.

Daniel et al., (2001) determined the maximal stress for a particular geometry (the vertical internship distance: 17 cm, pelvis width: 4.5 cm, pelvis height: 13 cm, and femur radius: 2.5 cm). They applied 750 N on their model and estimated the maximum contact pressure (i.e. P_{max}) as 3.0 MPa.

5.3 Susceptible Regions of Femur

To determine the effect of the muscles forces on the stress-strain configuration of the femur, it is essential to simplify the lower limb geometry. Hence, the stress analysis can be restricted to the most important and vulnerable regions of the femur. In this section, the most susceptible segment of the femur will be introduced to examine the stress-strain analysis analytically.

Although the femur is the strongest bone in the human body, failure can occur through fracture. This is particularly prevalent in older adults and adults who experience a significant loss of calcium in the chemical composition of the femur bone. The American Academy of Orthopaedic Surgeons, (2010) reported that four-fifths of hospitalised elderly patients have a hip fracture and are suffered from the various types of femur failure modes. Fracture of the femur in an elderly adult often occurs following minor trauma. In younger ages, femur fracture can occur after high energy-trauma associated with high-risk activities or accidental injuries. The term hip fracture refers to the fracture of the proximal femur location, which is placed 5 cm below the lesser trochanter of the femoral bone up to the surface of the femoral head.

Figure 5-1shows the hip fracture regions, which occur in the extracapsular segment (including the area is 5 cm lower than lesser trochanter, and the trochanteric area itself), and intracapsular region (NICE, 2017). Approximately half of the femoral fractures are categorised as intracapsular, which occur between the neck of femur and the edge of the femoral head. Extracapsular fractures are restricted into two regions including trochanteric and sub-trochanteric. The femur fracture may occur in simple or complex shapes depending on the degree of the subjected force on the planes and can be classified as avulsion fracture or oblique hip fracture (Davidovitch et al., 2010). Furthermore, femoral shaft fracture or diaphysis fracture are caused by high-energy injury such as an accident, pathological fracture, or high-risk activities such as sports injuries. These include a transverse fractures (horizontally fissures across the diaphysis of the shaft), oblique fractures, spiral (due to the torsion force), comminuted (where three or more points of fracture happened) or oblique plane fractures. In conclusion, four regions of the femur were identified as vulnerable regions and susceptible segments of the hip joint including the femoral head, femoral neck, trochanter area and extracapsular segment. The next section, explains how to articulate the equations for the identified regions and determination of the formula for cross-sectional areas.

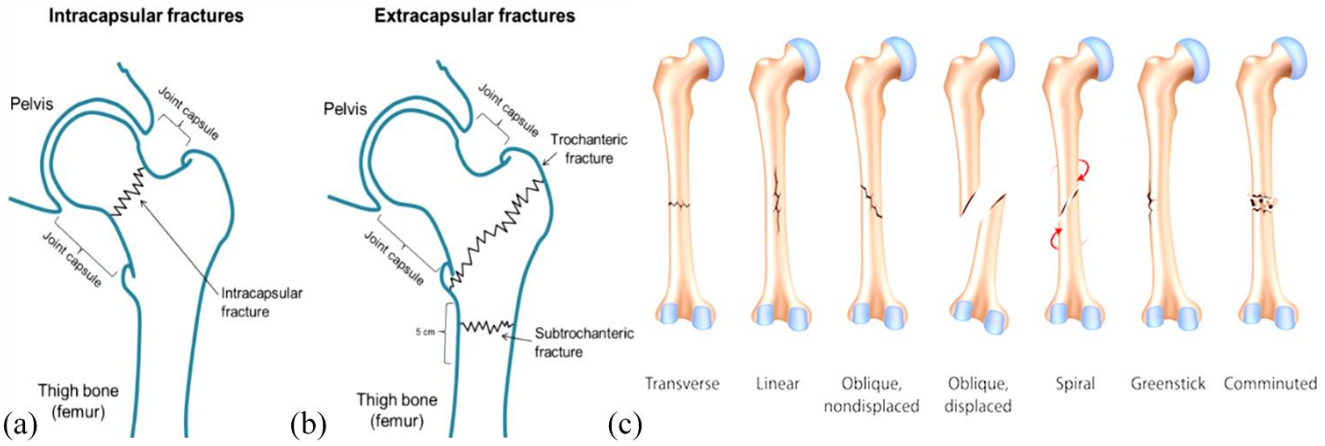

Figure 5-1:The hip fracture regions including (a) intra-capsular fractures, (b) extracapsular fracture and (c) the various types of the femoral diaphysis fracture (Van der Plas, 2014).

5.4 Governing Equations for Femoral Segments

It is necessary to determine the cross-section areas of the surfaces in the susceptible regions of the femur bone analytically in order to accomplish the stress analysis. Hence, three equations were developed to calculate the cross-section areas of the vulnerable regions as shown in Figure 5-2. The first function is governed by the intra-capsular region (A-Section) which determines the radius of a circular area at any preferred distance from the head of the femur and along with the direction of the femur-neck axis. The second function is developed to compute the area of any planes on the neck (B-Section) parallel to the femur-neck axis. The third function governs the central area of the diaphysis region and computes the area at any preferred distance from the head of the femur (C-Section) parallel to the anatomical axis of the femur.

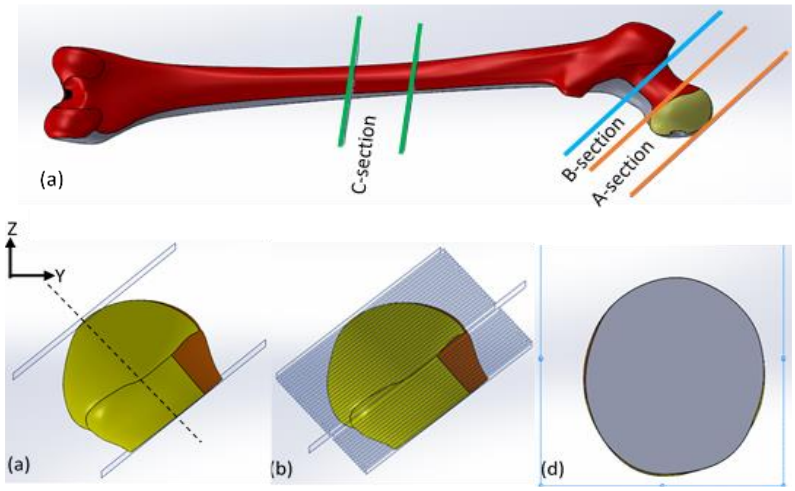

Figure 5-2 : (a) Schematic posterior view of the left femur and its susceptible regions. The sections are not shown to scale and just demonstrate the approximate positions. (b) The anterior view of femoral head-neck and its oblique axis (black dashed line) (c) Infinite planes employed to create the parallel surface, and (d) Mid-plane cross-section.

The process of choosing the curve of best fit for section A of the femur including the femoral head is summarised in appendix D. Figure 5-3 shows the line of best-fit graph for the femoral head profile, related to the OA axis. Equation 5-1 was developed accordingly using Microsoft excel (V.2016). The equation estimated the radius of the cross sections planes (blue planes in figure 5-3 (c)) with respect to the distance from origin of the head-neck axis (OA).

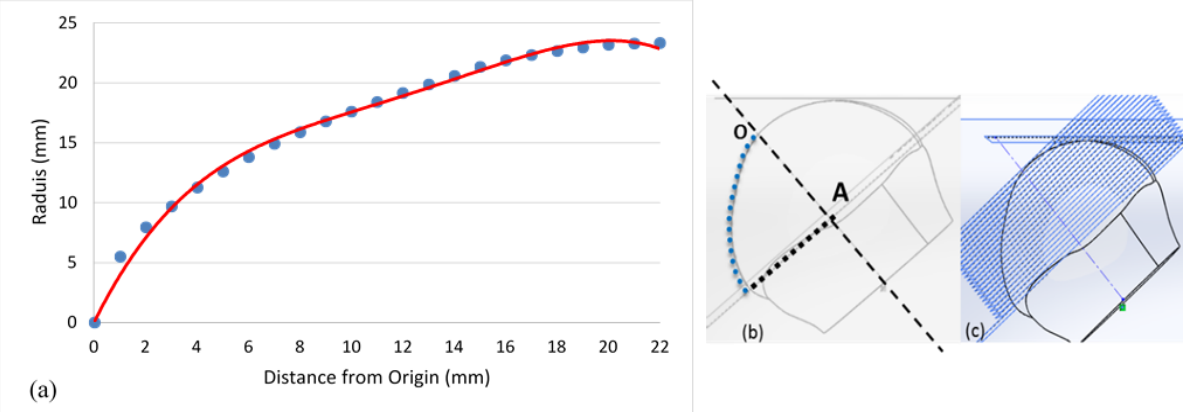

Figure 5-3: (a) The best polynomial graph (red solid line) fitted to the femoral head profile (blue dots), (b) the femoral head with the diagonal femur-neck axis (black dashed line-OA), and (c) application of the parallel planes to govern the best-fitted equation for the femoral head.

Hence, the best-fitted curve to the femoral section A is reported as follows:

$$R(z) = -0.0007\,(z^4) + 0.0312\,(z^3) - 0.5253\,(z^2) + 4.5459\,(z) \qquad (5\text{-}1)$$

Similarly, two other best-fitted equations (Eq.5-2 and Eq. 5-3) are developed to determine the area for any preferred distance along with the femoral neck axis and the mid-plane axis segment of the diaphysis:

$$A(z) = -0.0916(z^3) + 13.703(z^2) - 686.08\,z + 12250 \qquad (5\text{-}2)$$

$$A(z) = 0.0171(z^2) - 5.9053\,z + 1032.2 \qquad (5\text{-}3)$$

Where A is the cross-section area and z shows any distance from the origin point (O) in (mm).

The RMSE for femoral neck equation and mid-plane of diaphysis equation is reported as 10.27 and 0.011 respectively.

The CAD model considered detached the femoral neck according to its anatomy where it is placed between plane B and plane C (Subburaj at al., 2010). For this study, the reference point is considered at the top of the femoral head (O) and all planes assumed to be normal to the head-neck axis (OA), as shown in the Figure 5-4. The reference point for the femoral diaphysis study, places the top of femur head in the same position as in the prior study. However, the orientation of the assumed planes as well as the inferior anatomical axis of the femur were changed, as shown in figure 5-5 (b).

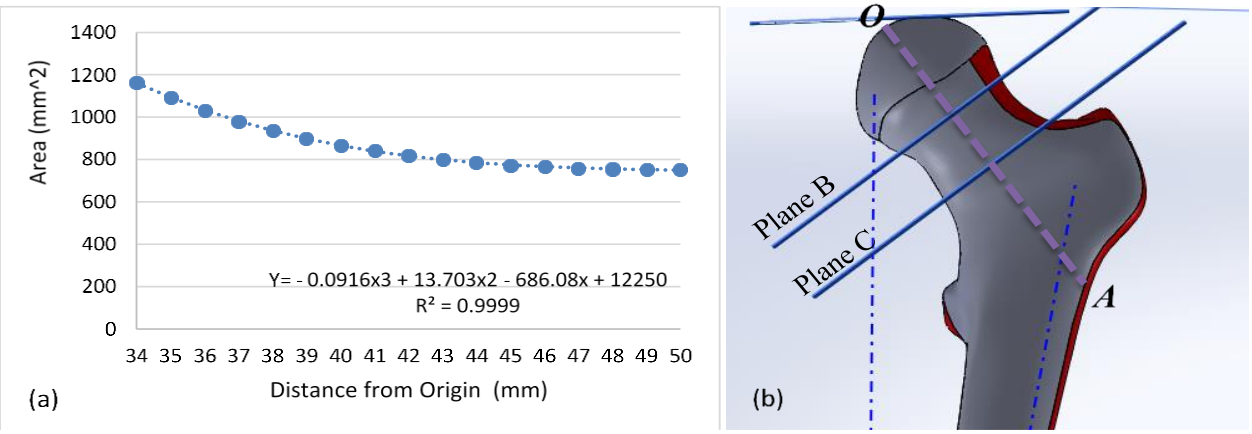

Figure 5-4: (a) The best-fit graph and its function to determine the cross section area for arbitrary distance between the BC planes, (b) the femoral neck section (BC- section) and the femoral head-neck axis (OA).

Figure 5-5 (a) shows the best-fitted graph to determine the cross-section areas of the diaphysis region. The governed equation showed R-squared one. The developed equation for the femoral diaphysis was exclusively restricted to the mid-plane areas of diaphysis. This area is placed between plane E (198 mm from the head of a femur as origin, O) and plane F (238 mm from O), and with the anatomical axis (orange dashed line) of the femur located inferiorly. The assumed distance has a vital position in a femur anatomy and typically, diaphysis fracture occurs in this region. The developed equation can estimate any cross-section area of this segment with high accuracy according to the calculated RSME.

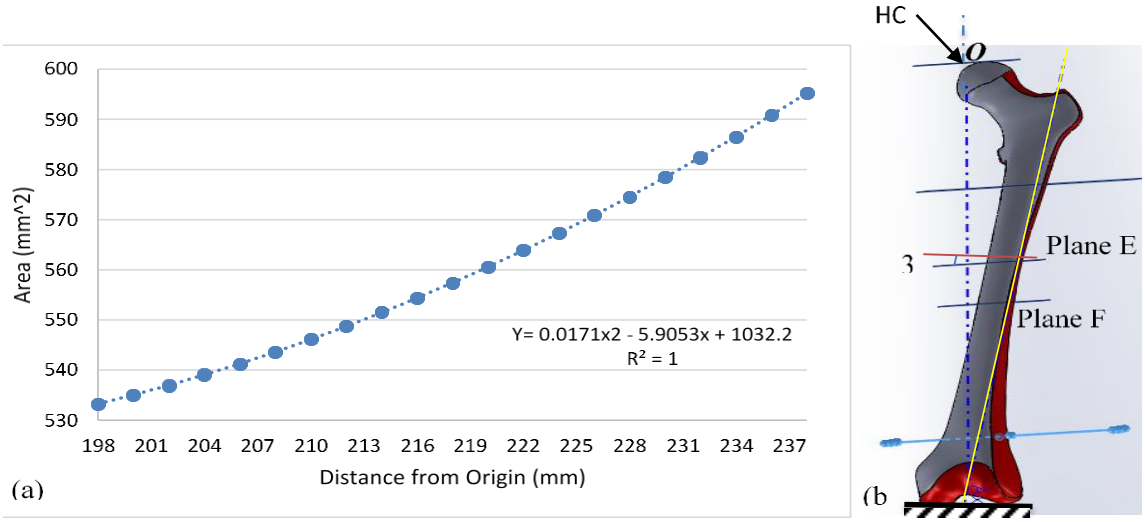

Figure 5-5: (a) The best-fit graph and its function to determine the cross-section area for EF region, (b) the mid-Plane of femoral diaphysis (EF- section) and the anatomical femur axis (Yellow dashed line).

Table 5-1 summarises the developed functions for the three various segments of the femur to determine the cross-section area of any arbitrary distance from the origin point. The RMSE demonstrated the amount of error and R-squared display differences between the observed value (from realistic anatomy) and governed equations. The error analysis of section A is reviewed in appendix D and the same procedure was followed for other functions.

Table 5-1: The developed equations for the femur sections to determine the area for an arbitrary distance from the origin.

Femur section	Governed Equation	R^2	RMSE	Function
Femoral Head (A-section)	$R(z) = -0.0007\ (z^4) + 0.0312\ (z^3) - 0.5253\ (z^2) + 4.5459\ (z)$	0.994	0.22	Radius-Distance $0 < Z \leq 20$ mm
Femoral Neck (B-section)	$A_1(z) = -0.0916(z^3) + 13.703(z^2) - 686.08\ z + 12250$	0.999	10.52	Area – Distance $34 \leq Z \leq 50$ mm
Femur Diaphysis (C-section)	$A_2(z) = 0.0171(z^2) - 2.5543(z) + 617.72$	1	0.011	Area – Distance $198 \leq Z \leq 237$mm

5.5 Stress Analysis via Analytical method

In order to simplify the calculation steps, the stress condition assumed for stress analysis shown in figure 5-6 (c). The infinitesimal element was assumed as a square with equal sides, in which normal stresses act perpendicularly to the surface and create σ_z. The shear stresses were assumed to be parallel to the y- and z-directions and tangent to the surfaces, which generated $\tau_{yz} = \tau_{zy}$ respectively, as shown in figure 5-6.

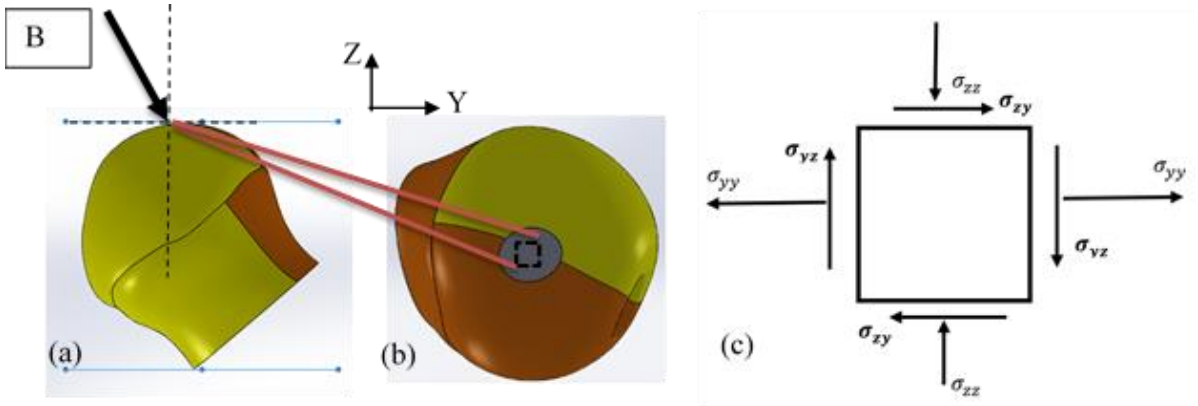

Figure 5-6: Schematic illustration of (a) the anterior view of the femoral head and the hip joint contact force (b) the infinitesimal element, normal to the Z-axis in the transverse plane and superior direction (i.e. Z-principal plane), and (c) the stress components on the element.

Figure 5-7 demonstrates the angle of the computed HCF in the 3D study named 3D-HCF- All Mus. at single support of the gait and angle of inclined planes parallel to the femoral head-neck axis. It can be seen that the femoral head-neck axis has an angle of 41.5˚ to the horizontal axis (X-axis) which was computed using the parallel planes method from the CAD model. For the Femoral head and neck, the HCF at a single support stance has an average angle of 25.24˚ while at the swing phase has an average angle of 17.9˚. For the femoral diaphysis, the HCF angles for the single support stance and pre-swing phase reported an average angle of 25.4˚ and 17.9˚ respectively. Hence, the HCF created with two components of force including a normal (i.e. perpendicular) and parallel (i.e. shear) force. On the other hand, the inclined surfaces for the femoral head and neck were formulated and summarised as $R(z)$,$A_1(z)$, and $A_2(z)$ in table 5-1. Therefore, the normal (i.e. perpendicular) and shear components of the total HCF created two stresses correspondingly when subjected to the infinitesimal cube. According to the definition of the stress the following formula were employed for each region.

$$f(Z) = \begin{cases} \sigma_N^h = \dfrac{HCF(@\ 18-30\%\ or\ 50\%) \times Cos(\propto)}{\pi\ R(z)^2}, & 0 < Z \leq 20 \\ \sigma_T^h = \dfrac{HCF(@\ 18-30\%\ or\ 50\%) \times Sin(\propto)}{\pi\ R(z)^2}, & 0 < Z \leq 20 \end{cases} \quad (5\text{-}4)$$

Where, $R(z)$ is the formulated radius related to the normal distance from the reference point at the top of the femur. σ_N^h is the normal stress, and σ_T^h is the shear stress or shear stress for the femoral head. $\propto$ shows the angle difference between the HCF and head-neck axis angles (i.e. 30.95˚).
Similarly, for the head-neck femur the following formula were developed to determine the normal and shear stresses.

$$\sigma_N^{h-n} = \frac{HCF(@\ 18-30\%\ or\ 50\%) \times cos(\propto)}{A_1(z)} = \frac{HCF \times cos(23.26\ or\ 30.6)}{A_1(z) = -0.0916(\mathrm{z}^3) + 13.703(\mathrm{z}^2) - 686.08\,\mathrm{z} + 12250} \quad (5\text{-}5)$$

$$\sigma_T^{h-n} = \tau^{h-n} = \frac{HCF(@\ 18-30\%\ or\ 50\%) \times sin(\propto)}{A_1(z)} = \frac{HCF \times sin(23.26\ or\ 30.6)}{A_1(z) = -0.0916(\mathrm{z}^3) + 13.703(\mathrm{z}^2) - 686.08\,\mathrm{z} + 12250} \quad (5\text{-}6)$$

Where, Z is the distance from the top of the femur along the superior-inferior axis. Index (h-n) is denoted for the femoral head-neck axis. In addition, for the diaphysis of the femur equations 5-7 and 5-8 were governed for the restricted section between 198 - 237 mm distances from the top of the femoral diaphysis.

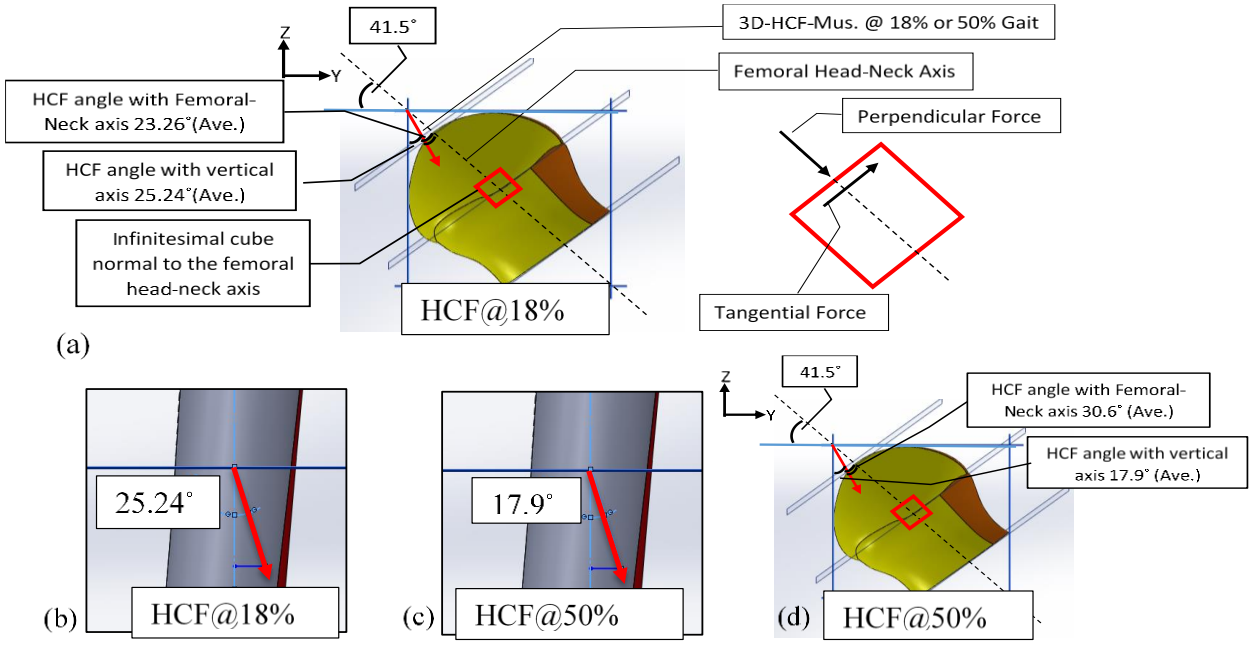

Figure 5-7: (a) The anterior view of the femoral head at single support stance. Three main inclined planes normal to the femoral axis, femoral-neck axis, and perpendicular and tangential forces are indicated, (b) HCF applied on the diaphysis femoral at 18% of the gait, (c) HCF applied on the femoral diaphysis at 50% of the gait, and (d) HCF applied on the femoral head and femoral –neck axis at 50% of the gait.

Equation 5-7 predicted the normal stress in the diaphysis region and Eq. 5-8 and 5-9 estimated the shear stress according to figure 5-7 (c) and based on the angle between the HCF and diaphysis planes as 17.54˚. While, the bending moment stress can be estimated from Eq. 5-10. It should be noted that there is the small angle (i.e. 3˚) between the normal surface and the applied planes (between planes E to F) of this segment, which was neglected to simplify the calculation steps.

$$f(Z) = \sigma_N^d = \frac{HCF(@\ 18-30\%\ or\ 50\%) \times cos(\propto)}{A_2(z)} = \frac{HCF\ (\ 18-30\%\ \ or\ 50\%)\ \times cos(25.24\ or\ 17.9)}{A_2(z) = 0.0171(z^2) -\ 2.5543(z) +\ 617.72} \qquad 198\ \ \leq Z \leq 237 \qquad (5\text{-}7)$$

$$f(Z) = \sigma_{T-X}^d = \tau^d = \frac{HCF(@\ 18-30\%\ or\ 50\%) \times sin(\propto)}{A_2(z)} \qquad (5\text{-}8)$$

$$f(Z) = \tau^d = \frac{HCF(@\ 18-30\%\ or\ 50\%) \times sin(25.24\ or\ 17.9)}{A_2(z)} \qquad (5\text{-}9)$$

$$f(Z) = \ \sigma_B^d = \frac{M_{HCf} \times y}{I(Z)} \qquad (5\text{-}10)$$

Where, (y) represents the vertical distance from the neutral axis (the biological axis of femur, which is displayed as a yellow dashed line in figure (5-5)). I (Z) represents the moment of inertia around

the neutral axis and depends on the Z distance. Z shows the distance from top of the femoral head to any plane in this region. M_{HCf} shows the bending moment that is created due to applied HCF. σ^{d}_{T-X}represents the shear stress (i.e. shear stress) on the anterior direction and σ^{d}_{T-X} represents the shear stress (i.e. shear stress) on the lateral side of the body.

All governed equations in this section (5-4 to 5-10), were applied to determine both the normal stress and shear stress values for the related segments in a femur. Table 5-2 shows all 24 possible studies for the analytical chapter; however, some outcomes related to the shear stress were neglected. The main aim of this study to examine the effect of muscle contribution within the single support and 50% of the gait analytically.

Table 5-2: Selected analytical studies to determine the stress for three susceptible regions of the femur.

Name of study	Femur Regions	Type of stress	Stance of the gait	
3D-HCF- Mus. Considering effect of muscles contact forces	Head	σ_N = Normal stress σ_T = Shear (shear) stress	$18-30\%$ Standing on one leg (single support stance)	50% Hyperextension (prior of toe-off and pre-swing of the targeted leg)
	Head – Neck			
3D-HCF-N Mus. Effect of muscles contraction ignored				
	Diaphysis			
Max. possible studies	2 (Muscle effect) ×3 (Regions)×2 (Stress) ×2 (Gait stance) = 24			

5.6 Results and Discussion

This section covered the stress characteristics of the susceptible regions in the femur via using the static analysis method as well as the related discussion. For each selected regions the normal stress at a single support and pre-swing phase of the gait were compared to determine the effect of muscle contractions on local stress contribution. It has to be noted that the effect of muscle contraction is presented as a comparative or dimensionless study to comprehend the variation between two different trials.

5.7 Stress Analysis of Femoral Regions

As previously stated, the femur is divided into the three sections, which were identified as the most susceptible regions for fracture failure. Subsequently, each discrete section was further divided into several thin planes to satisfy the stress conditions and decrease the level of complexity.

Figure 5-8 compares the normal stress of all susceptible and vulnerable regions in the femur bone during single support stance of the gait cycle. It can be realised that the femoral head (red columns) regions are under a high risk of normal stress with a maximum stress of 17.8 MPa. The stress magnitude was significantly reduced from the top of the femoral head towards the neck due to the increased surface area of the head region. The mid-plane of the femoral diaphysis (i.e. $198 \leq Z \leq 237$ mm), where the diaphysis has a minimum cross-section area also experienced a maximum stress of 5.05 MPa. It can be seen that the stress magnitude of the diaphysis section from the top to the bottom region demonstrated less variation and fluctuating state because the cross-section area in this section was not altered. However, the normal stress of the femoral neck increased from the upper surface (close to a femoral head) towards the Greater Trochanter of the femur, with a maximum normal stress in this region estimated at 3.63 MPa analytically.

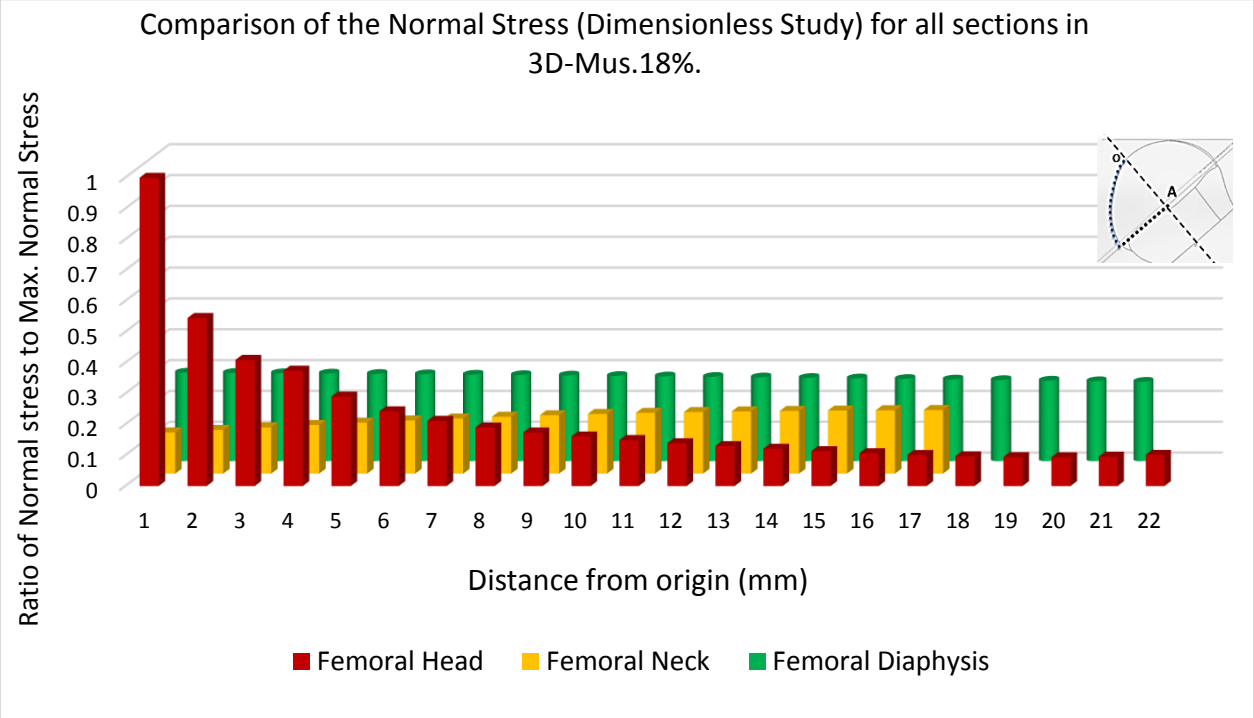

Figure 5-8: Comparison of obtained normal stress for three regions in the femur where muscles contraction considered at 18% of the gait.

For the femur at hyperextension position, (i.e. 50% of the gait), a similar trend of stress was observed however the magnitude value of stresses is reduced due to employing analogues planes while the value of HCF was slightly reduced. In essence, the dimensionless study (i.e. normalised all stress values concerning the maximum stress at each stance of the gait) provided a great fortune for the comparative studies without considering the variation between the absolute values. Hence,

another study was conducted to predict average normal and shear stress across each region analytically. In this case, the stress characteristic of three selected regions can be compared by reducing the effect of various cross-sectional areas in each segment. Hence, the average stress in this region was defined as follows:

$$\sigma_N{}^{Ave} or\ \sigma_T{}^{Ave} = \frac{\sum_{i=1}^{n} \sigma_N\ or\ \sigma_T}{n} \qquad (5\text{-}11)$$

Where N is the number of the predicted stresses in a region, σ_N is the normal stress, and σ_T is the shear stress. $\sigma_N{}^{Ave}$ shows average stress, and (i) represents the number of planes in the region.

Figure 5-9 compares the average values of normal and shear stress for three regions at a single support stance. Although, the femur head experienced the absolute maximum normal stress around of 17.60 MPa, the diaphysis presented with the maximum average of normal stress of 4.82 MPa across the three selected sections. For the diaphysis region, the quadriceps angle or tibiofemoral angle (Q angle) of the lower limb model was considered to calculate stress for the femoral shaft.

The Q angle developed from the computed tomography images of the male participant (Pcir, 2007) which has been measured around 5.6˚. In addition, the average of shear stress for perpendicular planes to the diaphysis are calculated 2.27 MPa. However, the bending moment stress was neglected in this region and for simplifying calculations steps. Furthermore, the average value of normal and shear stress for the neck region decreased 19.10% in comparison to the femoral head similarly. According to Sivananthan, et al., (2012), the fracture of femoral diaphysis occurs most frequently in young men after high-energy trauma or due to the high-risk activities and elderly women after a low-energy fall. The main reason to justify of increasing the local stress of the femoral shaft may be attributed to numbers of the muscle group, which are attached to the region and surrounded it. The femoral shaft is surrounded by various groups of muscles which are protected the shaft including two vasti muscles (i.e. vastus medialis and vastus lateralis), vastus intermedius, short head biceps femoris, adductors, glutes maximus and pectineus (Muscles of thigh, 2012). Thus, the surrounded muscles cause to increase the local stress (i.e. normal and shear stress) because the attachment site of muscles may induce more local stress into the diaphysis. Hence, according to the obtained results and considering the combination of shear and normal stress, it can be acknowledged that femoral diaphysis experienced higher local stress in comparison to other segments.

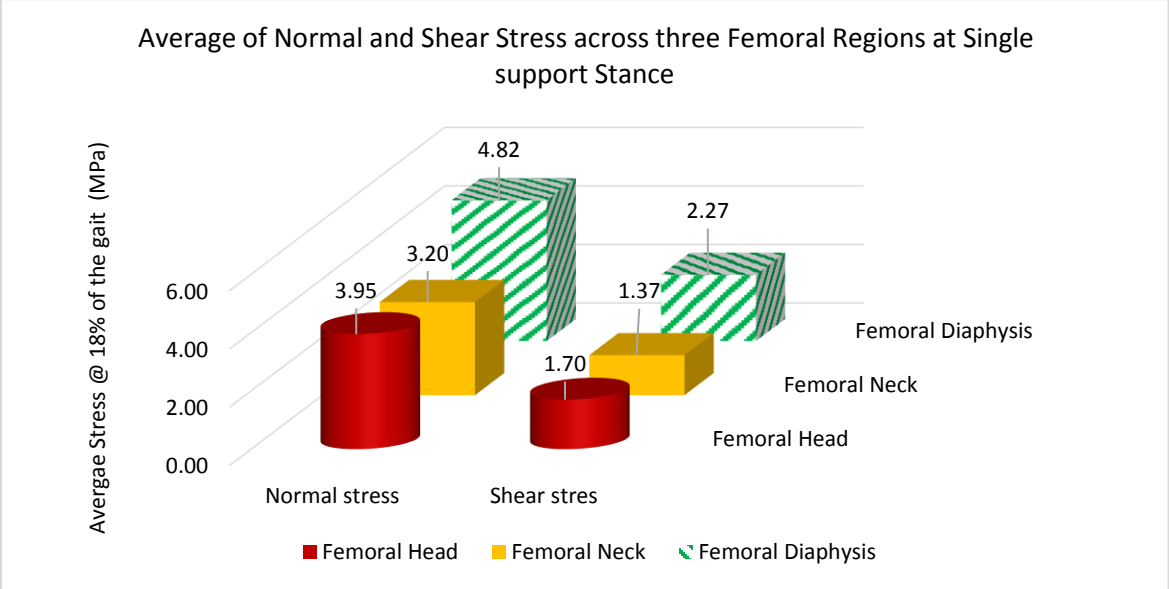

Figure 5-9: Comparison of the average of normal and tangential stress for three selected regions in the femur where muscles contraction considered at 18% of the gait.

5.8 Effect of Muscle Contraction on Stress

5.8.1 Femoral Head Stress (3D-All Mus vs. No Mus.) at 18% of the Gait

In this section, the analytical comparison was conducted to determine the effect of muscle contraction between musculoskeletal and skeletal model at the single support stance of the gait cycle. As previously mentioned, in the 3D-All Mus. model the muscle contraction was considered, whereas in the No Mus. model the effect of muscle contraction was neglected. Figure 5-10 compares the predicted normal stress for 3D studies where muscle contraction is considered within the single support of the gait cycle. It can be realised that the muscle contraction increased the predicted normal stress across the selected region of the femoral head. The femoral head of the musculoskeletal model with muscle contraction was experienced a maximum normal stress of 17.60 MPa during the normal walking. While the maximum normal stress in the same region of the skeletal model (without any muscle contribution) estimated 7.64 MPa at 18% of the gait cycle. Moreover, this study showed that the maximum stress has occurred at the top of the femoral head where the stress concentration occurred. It can be seen that the muscle contraction (i.e. 6 major muscle groups) significantly increased the local normal stress (i.e. 131%) at their attachment sites on the femoral head region compared to the skeletal model without muscle at the single support stance.

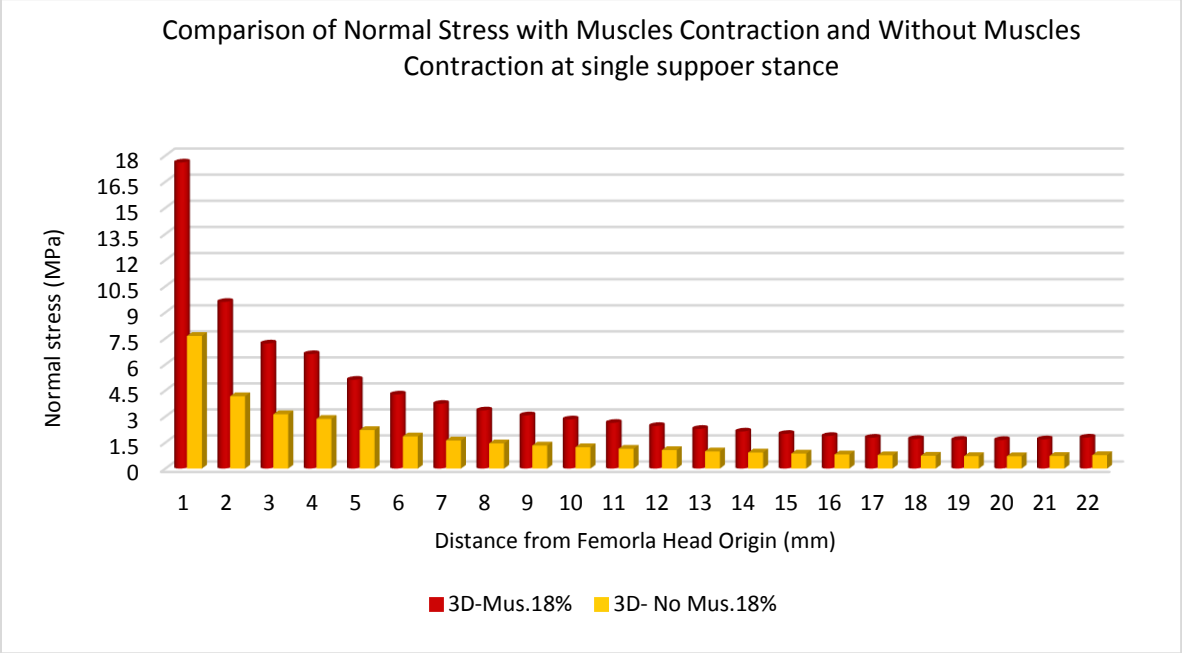

Figure 5-10: Comparison of predicted normal stress with muscles contribution and without muscles contraction at single support stance via analytical method.

Figure 5-11 compares the shear stress created by HCF in the femoral head at single support stance when the muscles contraction are considered as variable parameters. The best-fitted line as regression curve, its equation, and R-squared value are reported for the two main case studies 3D-All Mus and No Mus. For both studies, the maximum shear stress occurred at the top of the femoral head. By using developed equations, the value of shear stress can be estimated at any favourite point at a distance from the origin. The R-squared value (0.99) indicated an acceptable level of accuracy of the governed equation to predict the shear stress. Nevertheless, the error function analysis and root mean square evaluation was required to determine the reliability of created data. Evaluating the governed equations ($\sigma = 7.5164*\varepsilon^{-0.789}$) could be suggested as further research. Furthermore, it can be realised that muscle contraction created more shear stress on the femur from the top of the femoral head towards the Great Trochanter (GT). The maximum shear stress on femoral head for the musculoskeletal model predicted at 7.56 MPa while the skeletal model without any muscles experienced 3.28 MPa. Hence, it can be seen that the muscle contraction increased the predicted shear stress at a value 2.30 times greater than the skeletal model (where the effect of muscles was neglected) and therefore it can be concluded that the muscle attachment site is increased the local shear stress on the femoral head region.

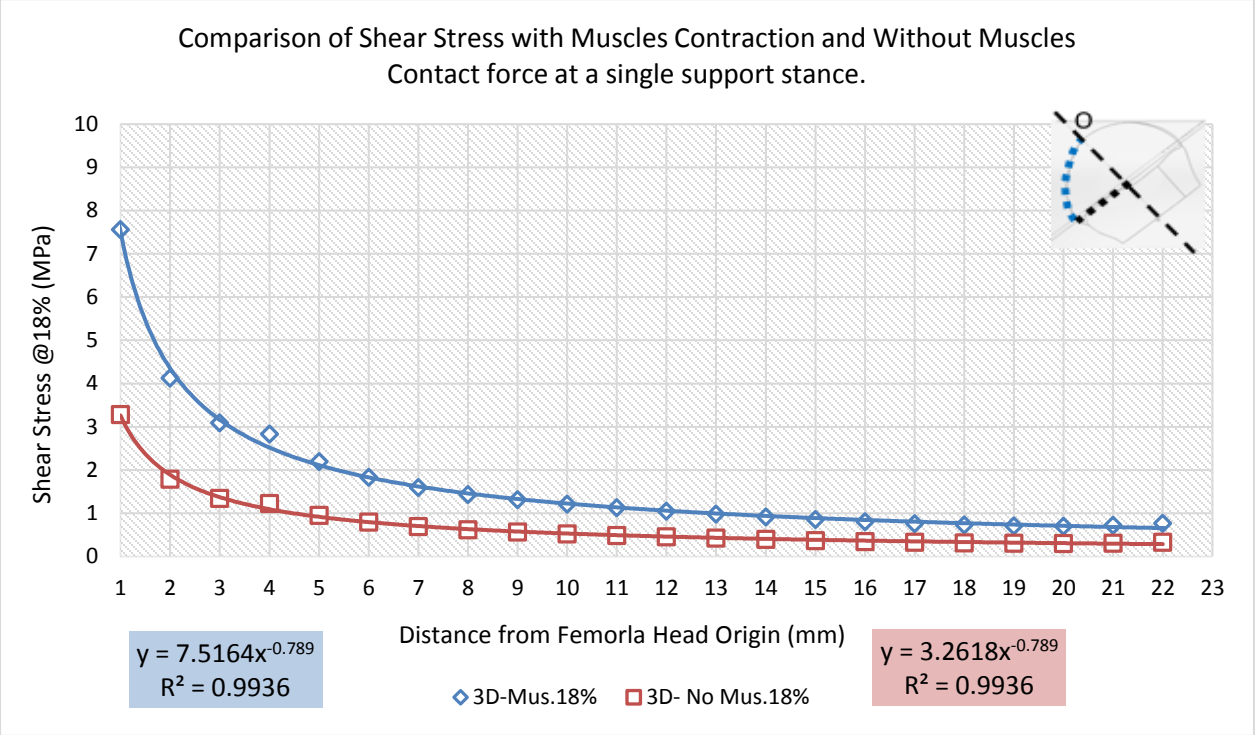

Figure 5-11: Comparison of predicted shear stress with muscles contribution and without muscles contraction at single support stance via analytical method.

Figure 5-12 compares the normal and shear stresses created on the femoral head due to muscle contraction at a single support stance and pre-swing phase. Although the maximum value of normal and share stress at a single support stance (i.e. 18-30% of the gait) are not equal and estimated at 17.60 and 14.63MPa respectively, the ratio of both stresses for the musculoskeletal to skeletal model is computed as the same value (i.e. 2.30). Hence, it can be observed that the muscle contraction on the musculoskeletal model increased the normal and shear stress by an average value of 230% compared to the skeletal model which muscle contraction was neglected. The main reason can be attributed to the role of spanning muscles around the femoral head region (i.e. hip joint) because at the absence of the muscles, the amount of normal and shear stress, which locally induced to their attachment sites, were reduced significantly.

On the other hand, the effect of muscle contraction on the normal and shear stress on the femoral head at pre-swing phase slightly reduced in comparison to the single support stance. In this case, the muscle contraction increased the normal and shear stress by 215% and 219% at pre-swing phase respectively. The main reason to justify the significant variation between two models during the pre-swing phase attributed to the position of the targeted leg and the activated muscles. During the hip hyperextension at 50% of the gait, the body position locates the trunk's centre of mass behind

the hip joint and creates a passive hip extension torque (Harvey, 2008). Thereafter, to balance the body position, it was expected that the muscle contraction (such as gluteal muscle) contribute more in an anterior hip joint force (i.e. HCF) to stabilise the position of the femur and hip joint (Lewis at al., 2007). Hence, this study underlines the Lewis' findings that the activated muscle induces the contact force (i.e. contraction) on their local attachments and therefore creates higher normal and shear stress (minimum 215%) on the femoral head in comparison to the skeletal model without muscles. Furthermore, it can be observed that the muscle contraction creates lower normal and shear stresses within the toe-off stance (i.e. 50% of the gait) compared to the single support stance due to the amount of HCF at 18% of the gait is higher than pre-swing phase.

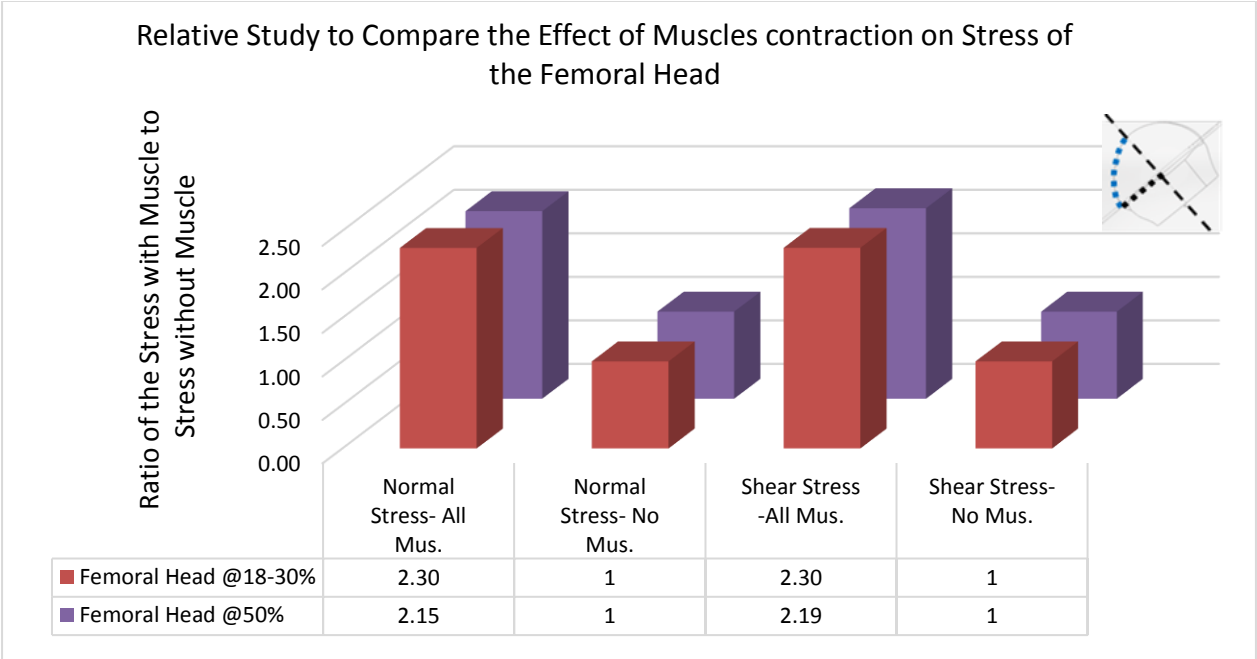

Figure 5-12: Relative study of normal and shear stresses on femoral head region when the obtained stress of model with muscles divided to model without muscles at single support stance and pre-swing phase. The stress of study without muscles is considered as a reference.

5.8.2 Femoral Neck Stress (3D- All Mus vs. No Mus.)

In this section, the average of normal and shear stress on the femoral neck was compared to determine the effect of muscle contribution on stress values at the single support and toe-off stance (i.e. 18% and 50% of the gait). The obtained results were summarised in figure 5-13. The analytical approach predicted the average of normal stress on the femoral neck for the musculoskeletal model at 3.20 MPa during a single support stance. While the normal stress on the femoral neck region was computed by an average value of 1.39 MPa, for the skeletal model (i.e. the model without muscles). Furthermore, the average of shear stress due to muscle contraction at the musculoskeletal

model was computed at 1.37 MPa, whereas this value has been reduced to be 0.6 MPa for the skeletal model at single support stance. Hence, it was identified that the muscle contraction increased the average of normal and shear stress on the femoral neck by 230% and 228% respectively. On the other hand, at the toe-off stance, the average of normal stress was predicted at 2.66 MPa for the musculoskeletal model, while this value was reduced to an average value of 1.23 MPa for the skeletal model. Moreover, the average of shear stress of the femoral neck for the musculoskeletal model (i.e. the effect of muscles is considered) was computed at 1.55 MPa, whereas this value was predicted 0.71 MPa during the pre-swing phase. Thus, the effect of muscle contraction caused to increase in the average of normal and shear stress at the pre-swing phase by 216% and 218% respectively. Overall, the muscles' contraction are created higher normal stress in comparison to the shear stress for both single support and pre-swing stances. The main reason to explain this fact can be attributed to the position of the femur at single support and 50% of the gait cycle. Within a single support stance, entire body weight subjected to the targeted leg from superior direction toward an inferior direction (i.e. perpendicular direction), caused to increase the average of normal stress, and less proportion of the HCF created the shear stress on the femoral neck region.

It can be concluded that the muscles' contraction creates the local stress at their attachment sites and causes to increase the average of normal and shear stress within the single support and pre-swing phases (i.e. toe-off) for the musculoskeletal model compared to the skeletal model.

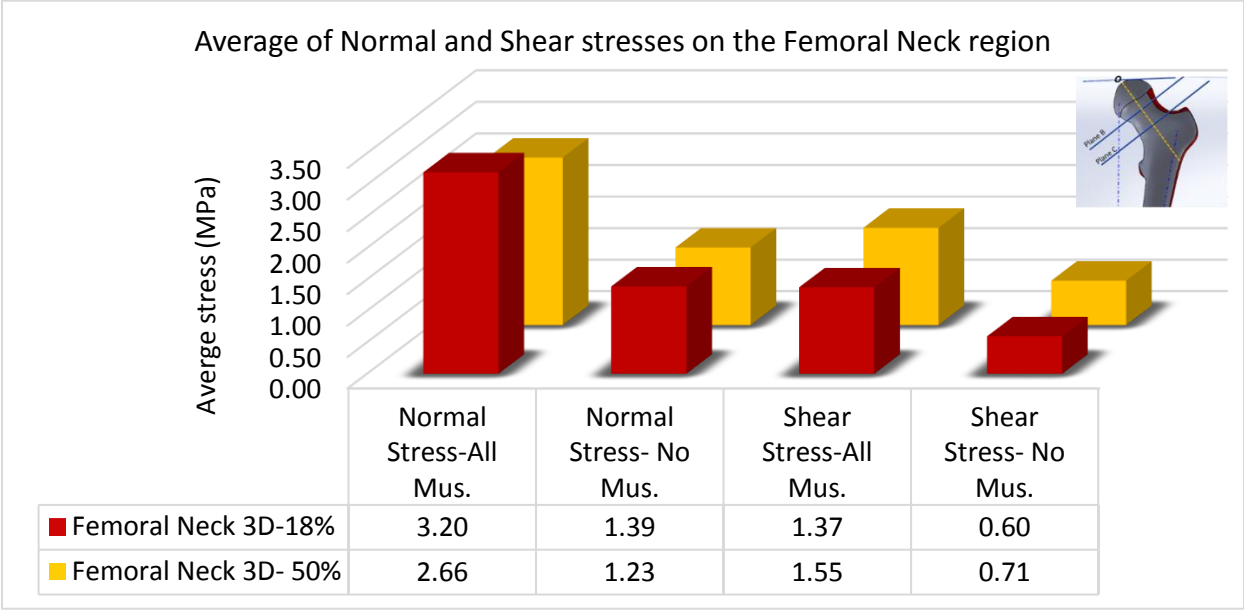

	Normal Stress-All Mus.	Normal Stress- No Mus.	Shear Stress-All Mus.	Shear Stress- No Mus.
Femoral Neck 3D-18%	3.20	1.39	1.37	0.60
Femoral Neck 3D- 50%	2.66	1.23	1.55	0.71

Figure 5-13: Comparison of the average of normal and shear stress on the femoral neck with and without muscle contraction at 18-30% and 50% of the gait via the analytical method.

5.8.3 Femoral Diaphysis Stress (3D-All Mus vs. No Mus.)

In this section, the effect of muscles' contraction of the shear and normal stress on the femoral diaphysis region at the single support stance and pre-swing phase. As previously mentioned, the selected planes in a diaphysis region have 3˚ of deviation from the mechanical axis of the femur, which was neglected in this study to simplify the calculation steps. In addition, the shear stress created on the anterior-posterior axis (i.e. direction) of the femoral diaphysis and the bending moment stress were not examined in this study, which could be suggested as future work.

The predicted maximum normal stress (i.e. 5.03 MPa) on the selected planes occurred at the single support stance of the gait where one leg was subjected to the entire bodyweight. It was expected that an increase in the stress level would occur in comparison to the predicted maximum normal stress (i.e. 4.69 MPa) at 50% of the gait cycle. Furthermore, it was expected the mid-plane of the diaphysis demonstrated a maximum normal stress due to the lowest diameter in the diaphysis region (the main reason to select this region for this study). While the amount of normal and shear stress of the femoral diaphysis is, lower than the femoral head for both 18% and 50% of the gait cycle. The main reason to justify this difference was attributed to the variation between the cross-section areas of the femoral head and diaphysis. According to section 5- 4, the selected planes at top of the femoral head have a less cross-sectional area and therefore the stress concentration has occurred on those planes at the top of the femoral head. Whilst the cross-sectional areas of selected planes of the diaphysis (i.e. femoral shaft) are changed uniformly (from top to down of the diaphysis region) and therefore there is no stress concentration has been occurred.

For the femoral shaft, the variation between the shear stress at 18% and 50% of the gait cycle is reported by 2%, whilst the difference between the normal stress at 18% and 50% of the gait cycle is 6%. It can be realised that there is no significant difference between the two types of stress at single support stance and pre-swing phase of the gait cycle. Figure 5-14 compares the normal and shear stress for the femoral diaphysis within the two crucial stances of the gait cycle. Considering the amount of stress for the skeletal model as a reference (i.e. using the ratio between the stresses) aids this analysis to demonstrate the relative study between all calculated stresses. The muscle contraction increased the normal and shear stress on the musculoskeletal model by 229% and 236% respectively in comparison to the skeletal model (i.e. 3D-No Mus.) at single support stance. On the other hand, the effect of the muscles' contraction increased the amount of normal and shear stress on the musculoskeletal model at the pre-swing phase by 216% and 218% respectively. It can be realised that the major muscle groups which are attached to the up and down of the femoral

diaphysis increased the normal and shear stress significantly in comparison to the skeletal model without muscle contraction at 18% and 50% of the gait cycle.

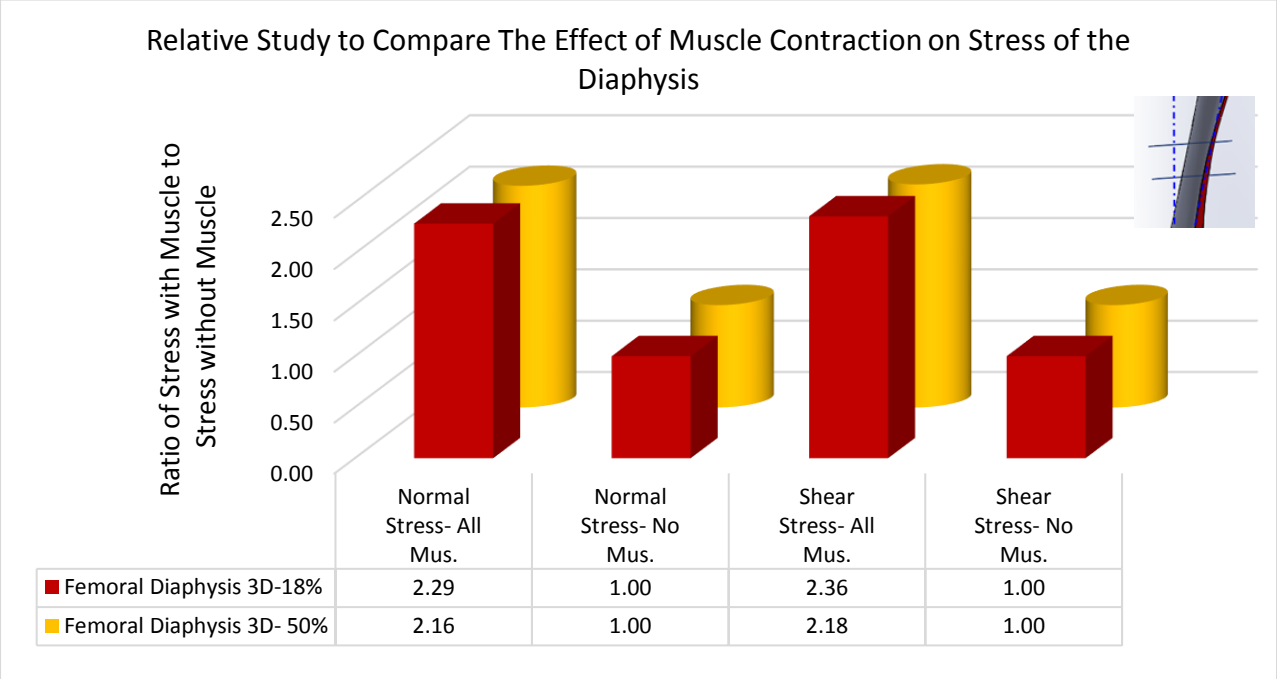

Figure 5-14: Comparison of predicted normal and shear stress on of the femoral diaphysis with muscles to stresses without muscle contraction at 18-30% and 50% of the gait via the analytical method. The stress of study without muscles is considered as a reference.

5.9 Concluding Remarks

This chapter designed to determine the most susceptible regions of the femur to compare the stress behaviour of the selected sections via using an analytical approach. The main aim of this chapter was, to analysis the role of muscles' contraction on stress behaviour of the femur and hip joint during the normal walking via an analytical approach. Hence, two crucial stances of the gait (18% and 50% of the gait) were considered to determine the magnitude of normal and shear stresses for three selected regions including femoral head, neck, and diaphysis.

The parallel planes method was applied to discretize each region to several thin wall layers due to obtaining stress magnitudes for all possible regions. In addition, the method aids to determine the average stress across each region rather than one surface area. Furthermore, it was demonstrated that diaphysis of the femur experienced a higher average of stress across the region compared to the femoral head and neck. While the maximum magnitude of stress has occurred on the femoral head where the small surface area has been discretized. Although, the articulated stress-position

formula for each region demonstrated acceptable R-squared to estimate the normal and shear stresses for each region, nevertheless further analysis including error function analysis required to ensure whether the obtained equations could predict the stress for each section accurately.

The obtained results proposed that muscles' contraction increased the stress of the femoral regions at musculoskeletal model up to a minimum of 215% greater than stress on the skeletal model. While, muscle contraction increased the stress on the musculoskeletal model up to a maximum of 236% compared to the skeletal model in which muscles are neglected depends on the femoral sections, type of stress, and stances of the gait cycle. Hence, it can be acknowledged that the muscle contraction is increased the normal and shear stresses during the normal walking at the single support stance and pre-swing phase significantly.

Chapter 6

Definition of Finite Elements Parameters

6.1 Introduction

For the past 50 years, the Finite Element Method (FEM) has exhibited increased as a numerical structural analysis to solve complex structure and practical issues. From the initial attempt to conduct FEM by Demirdˇzi´c et al., (1993), wide ranges of issues and structural problems have been addressed. There are many studies conducted in the biomechanics field to analyse bone and joint with various forces and tensions using FEA (Goel et al., 1978; Dalstra et al., 1995; Bachtar et al., 2006; Silvestri et al., 2008 and 2009; Harris et al., 2011). They assumed various boundary conditions and meshes in their studies, but the muscular boundary conditions were not assumed or partially neglected from the lower limb. A few studies applied a full lower limb model and point loading condition as the most direct method to include muscle boundary conditions (BSc) (Brekelmans et al., 1972; Goel et. al., 1978). Brekelmans et al. (1972) included an abductor muscle group as a point load, from one of the prior FE models of the femur. He provd that the incorporation of muscle BCs could affect the stress distribution. Brown and DiGioia (1948) and Goel et al. (1678) used comparable procedures to analyse the contact stress numerically in the pelvis where musculotendon point loads are involved. They confirmed that the effect of muscle BCs should not be ignored from the FE model. In this thesis, the muscles contact force, body weight, and ligaments contact force acquired from previous studies considered to generate boundary conditions of 3D musculoskeletal model. Table 6-1 defines four main studies that were used to show the effect of muscles on the stress-strain configurations and deformation of lower extremities. The 3D-All Mus., Hip Mus., Knee Mus. and 3D-No Mus. defined to examine the role of muscles contribution within the gait.

Table 6-1: Defined studies for the nonlinear analysis using Ansys (18.1) software package.		
No	Type of study	Specification
1	3D-All Mus. (Musculoskeletal Model)	Whole Lower limb body Weight
		Muscle force including 19 hip spanning and non-spanning muscles groups (Hip and Knee Muscle Groups)
		Patella-Tibia force
		Ligaments force (ACL,MCL LCL)
2	3D-Hip Mus.	Including Hip Muscles contraction (Hip Muscles)
3	3D-Knee Mus.	Including Knee Muscles contraction (Knee Muscles)
4	3D-No Mus.(Skeletal Model)	Excluding Muscles Contact Force

6.2 Model segmentation

The 3D CAD models can be created from computed tomography images to help researchers studying various aspects of the human body as well as aid them to develop bio-models via reverse engineering. The bio models can be used to simplify the medical rehabilitation, therapeutic, and diagnostic procedures using Reverse Engineering (RE), Rapid Prototyping (RP), and medical imaging (Carlesimo, Lombardi & Caltagirone, 2011). Furthermore, the reverse engineering technique via CT images can be used for designing the orthopaedic devices, structural modelling of tissue, and computer-aided surgery (Menaka et al., 2011).

The MRI and CT techniques are the most famous 2D non-invasive methods in medical diagnostics and surgical planning in which human anatomical data can be obtained from Digital Imaging and Communication in Medicine (DICOM) format. For visualization or modelling development of 2D to 3D models is possible by applying scanning approaches and contemporary computer graphics (Sun et al., 2005; Hongsheng et al., 2009). There are two main methods that can be considered for the reconstruction of 3D Bio-CAD models from medical images: the counter based or volume based method. The counter-based method is a helpful method to convert CT image models into CAD based solid models. In this case, the Stereolithographic (STL) model is demonstrated as a first medium between the CT and CAD software. The STL is restricted by other boundaries conditions, which are classified as ‘boundary representation’ conditions. The bounding surface can be described by polynomial functions that include B-Spline curves and Non-Uniform Rational B-Spline (NURBS) functions. In this thesis, the image processing methods from non-invasive medical images including CT / MRI scans were used to process 3D CAD model. There is a general

recommendation to use image-processing techniques for extracting point cloud data from the stalk of CT scan images.

The acquired points from the cloud data are contained unequally spaced, many noises and complicated shapes and details, which cannot be seen in standard CAD (Archip et al., 2006). Hence, the pre-processing techniques including smoothening, sorting and B spline curve fitting are employed to distinguish between the internal and external boundaries and smoothening of point cloud data. Subsequently, the B-spline curves are fitted to reduce the volume of the file and finalise the surface finishing of the CAD model.

The Hounsfield unit (HU) scale is a linear function to transform the measured original linear attenuation coefficient into one number of radio density at standard pressure and temperature (STP) in HU scale. According to the HU scale, the radio density of distilled water at STP considered zero (0) while the radio density of air at STP is 1000 HU. In addition, various HU has been saved in the materialise software which can be used to segment the bone and muscle from CT or MRI.

6.3 Conversion of CT scan images to CAD model

The MRI and CT were acquired from the healthy male (54 years old) subject (ID: 24759123) with the anthropometric measurements of 81.74 Kg (± 0.8) and 182 cm (±0.5). His MRI was recorded in January 2001 and uploaded to the www.Pcir.org for public used in November 2007 (Pcir, 2007). The Siemens machine and its compatible software (Syngeo MR 2002B V.) were employed to record the entire lower limb images, which spanned from the subject's mid femur to the second lumbar vertebra. The pixel spacing and resolution of images were 0.292 x 0.292 and 512 × 512 respectively. The CT and MRI sets were acquired from a different subject who participated in the gait analysis.

For the visualisation and segmentation of soft tissue and bone segments, the commercial software Materialise - Mimic Medical (V.19) was applied. The cortical bone (default as compact bone for adult CT) was extracted by selecting the image pixels in the range of (662) - (1585) HU and the soft tissue was segmented by choosing the pixels from (-700) – (225).

For this study, the automatic thresholding technique was used to create the lower limb segmentation from DICOM images. In addition, the manual separation and mask operation were applied to observe the exterior bone surface of the femur, pelvic, and tibia. Several researchers have extensively employed the automatic thresholding technique including global and local thresholding

for segmentation of lower extremities (Lagravère et al., 2006; Zaidi & Erwin, 2007; Zhang et al., 2010; Yoo, 2011; Grove et al., 2011). The automatic thresholding technique was identified as the simplest and most accurate method to extract the lower limb models from the point cloud data. However, the different types of noise can affect the obtained CAD models. Hence, the smoothing method as a part of pre-processing was applied to filter the noises and finalise the CAD models. The CT images and 3D CAD models obtained from the advanced image-processing module is presented in figure 6-2.

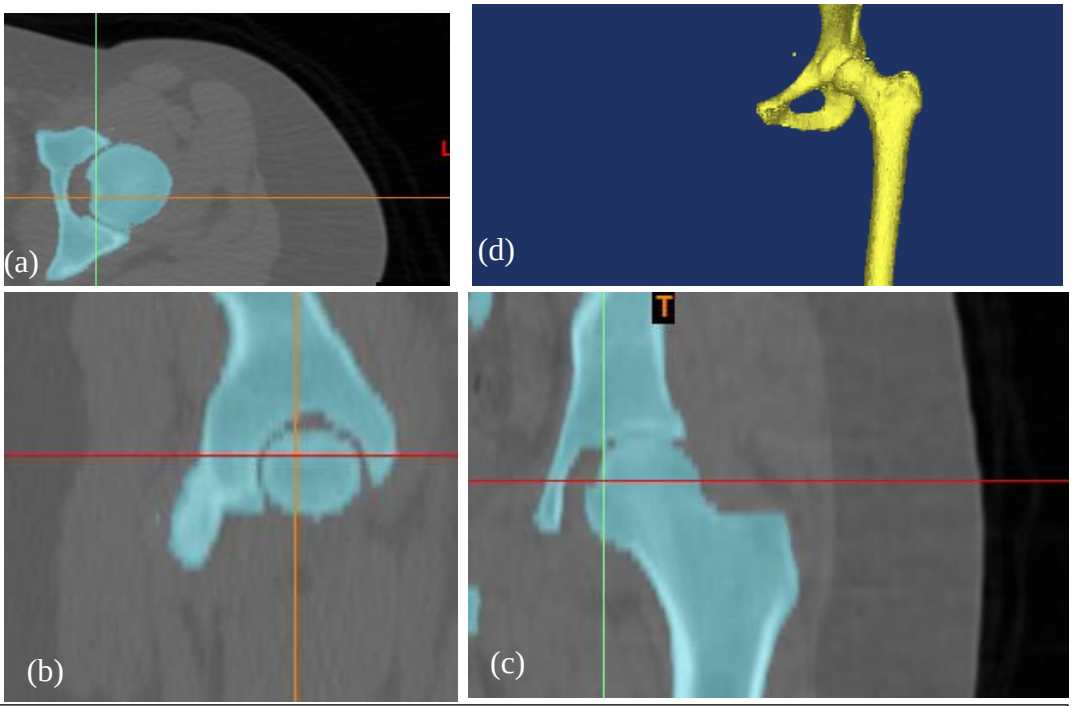

Figure 6-2: CT Images (a, b and c) and the 3D model of the left lower limb. (a) Transverse, (b) sagittal, and (c) frontal plane. The CT images are adapted from Pcir, (2007).

6.4 Contact Regions and Boundary Conditions

The CAD model generated in the previous section was forwarded in design modular software to complete the assembly and define the contact regions between the lower limbs.

Contact regions in Ansys software (R 18.1) includes two various sections the master (i.e. main body) and target surface (or body). The material with a higher stiffness or finer mesh should be selected for the master body or contact body to avoid any mesh deformation within the analysis.

There are different types of contact defined in ANSYS (R18.1) software that are assigned to the various compartments of hip and knee joint. The fully bonded contact constrained each node of the targeted body to the corresponding point in the main body to transfer the same displacement. Whilst

the frictional contact was defined to represent the sliding motion.in this type of contact the surface-to-surface regions are coupled to ensure there is no intersects or large penetration occurred, however may restricted penetrations occurred between nodes. Table 6-1 defines the contact regions between the applied CAD models in this study. To stabilise the CAD geometry of the full lower extremities, the surfaces between pelvic cartilage and the pelvic bone assumed to be bonded. In addition, in order to converge the FE study, a bonded contact joint has been assumed between the surfaces of the femur and femoral head cartilage, articular cartilage and femur, tibia and tibia cartilage, and tibia and meniscus.

Unworthy et al., (1975) reported the coefficient of friction in the human hip joint between the femoral head and pelvic cartilage between 0.01-0.04. Later on, Scholes et al. (2004) conducted study to measure the coefficient of friction between surface of cartilage and meniscus in a knee with synovial fluid. They reported the coefficient of friction 0.02 for their case study. However, in this study the coefficient of friction was considered as 0.05 to stabilise whole structure.

Figure 6-3 shows the entire CAD model including the hip and knee joint compartments. To achieve the stability of the FEA model the various coefficients of the friction have been examined to determine the optimised coefficient of friction for the developed models regardless of the above-mentioned values that other researchers are reported. Hence, the applied coefficient is two times higher than Scholes et al. (2004)' study to stable the FEA model. Furthermore, the elastic support from 10 to 100 (N/mm^3) was applied to protect the cartilage and meniscus surfaces from the early failure and help the geometry to transfer the applied loading to the other parts. The fixed support also was employed to stabilise the tibia and pelvic from the lower and upper parts respectively.

Table 6-1**:** The contact regions of the human CAD models employed for the numerical method.

Contact Regions	Type of Joint	Type of Contact	Specification
Tibia to Tibia Cartilage	Knee Joint	Bonded	No sliding and Penetration
Tibia to Meniscus	Knee Joint	Bonded	No sliding and Penetration
Meniscus to Articular cartilage	Knee Joint	Frictional	μ=0.05, sliding motion
Articular cartilage to Femur	Knee Joint	Bonded	No sliding and Penetration
Femur to Femoral head cartilage	Hip Joint	Bonded	No sliding and Penetration
Femoral cartilage to Pelvic AC	Hip Joint	Frictional	μ=0.05, sliding motion
Pelvic AC to Pelvic bone	Hip Joint	Bonded	No sliding and Penetration

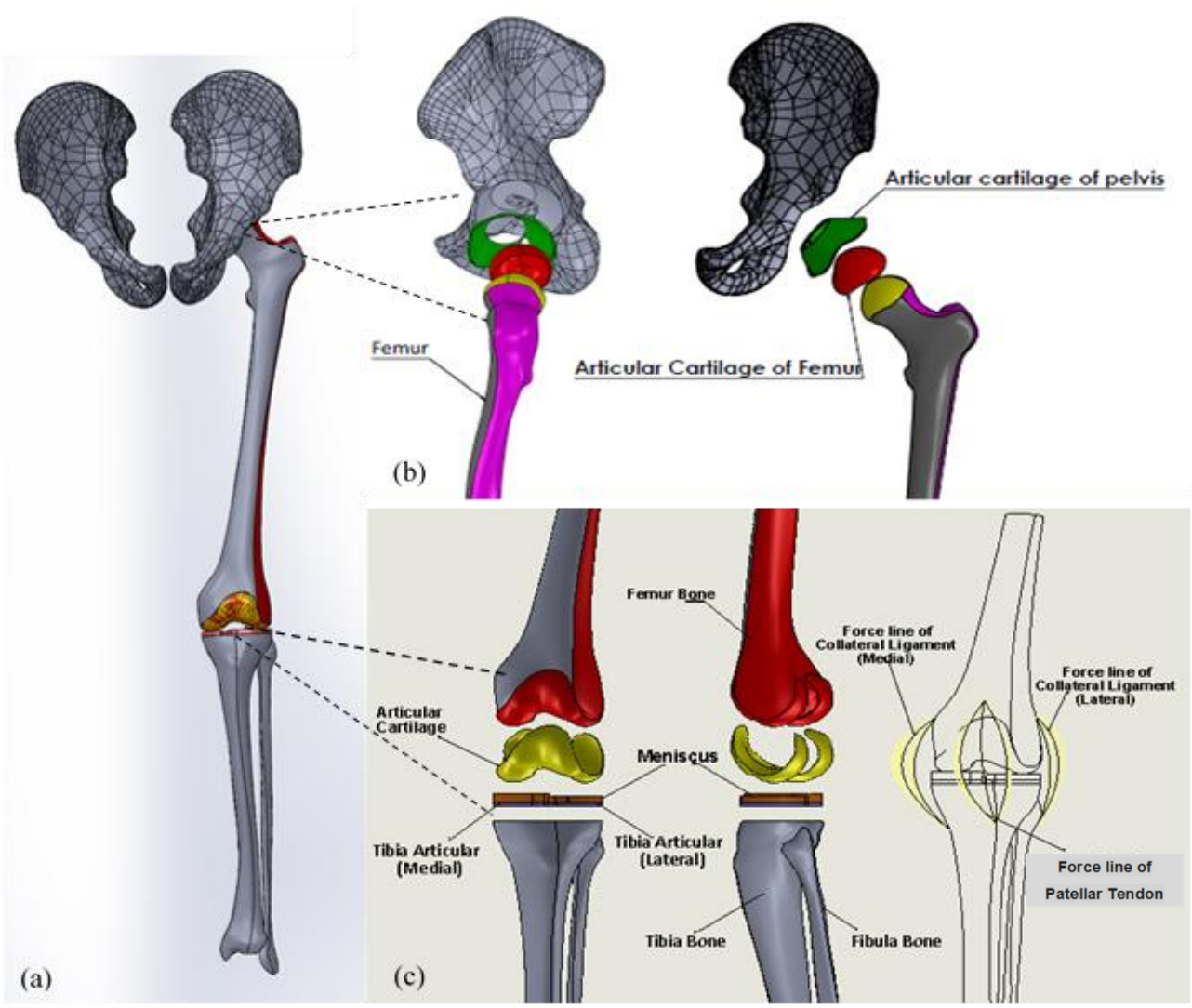

Figure 6-2:Illustration of (a) the entire lower limbs CAD model applied in FE analysis including (b) hip joint, and (c) knee joint.

6.5 Review of Muscular-fibre Simulation

There are various methods, including physiological and phenomenological models to study the effect of muscle contraction by incorporating muscle models into simulations of the human body or body segments.

Huxley (1975) studied muscle force using microstructural cross-bridges, which are governed by multiple differential equations. He presented a set of complex mathematical models that were excessively complicated to simulate, particularly for modelling multiple muscles in a system. Hence, a phenomenological model was developed to consider the behaviour of muscles in comparison to their physiology and therefore give the opportunity to model multiple muscles in a system. Many researchers applied the phenomenological model to create a relatively inexpensive

design to simulate musculotendon force using the springer and damper (Anderson et al., 2010; Anderson et al., 2009; Phillips, 2009; Piszczatowski, 2008; Olivetti et al., 2006; Phillips et al., 2006; Anoka, 2002; Winters, 1990; He and Levine, 1988; Hill, 1938). The spring-based muscle model offers many advantages, including simplifying the modelling muscles using the mechanical properties of the spring, such as a spring constant, to estimate complex muscle loading with relative ease and considering the attachment sites of the spring-based muscle as separate regions. Nevertheless, the Hill-type muscle model created unrealistic local stress at its attachment sites because the spring was attached to a restricted number of mesh nodes (Cardiff et al., 2013; Baldwin et al., 2012; Phillips, 2009; Flavin et al., 2008 and 2009; Piszczatowski, 2008; Silvestri et al., 2008 and 2009; Phillips et al., 2006). Furthermore, considering the muscle boundary conditions at point loads created further issues for dynamic simulations because during daily activity and muscle movements, muscle length and muscular force are altered and, therefore, the muscle attachment sites should react accordingly. By simulating the musculotendon area as a small number of nodes, the reaction of the attachment site does not represent the realistic conditions of local mechanics because the entire musculotendon force acts over a small area, creating erroneous stress.

Clinger et al. (2007) applied 3D finite element modelling to analyse the hemiarthroplasty of the human hip joint. They connected the origin and insertion of each muscle as the boundary conditions of point loading, which created local stress around the muscle attachment sites of the model. Therefore, to achieve realistic stress behaviour over the muscle attachment sites and eliminate unrealistic local stress concentration from small areas, several methods have been developed. Dalstra et al. (1995) and Majumder et al. (2004) eliminated muscle local stress by distributing the muscular force to the actual physiological areas of the insertion and origins and, therefore, local stress distribution represented the bone loading conditions. Recently, Li et al. (2019) developed a finite element musculoskeletal model with the ability to predict contractions of 3D muscles. They applied the physiological method to model eight non-spanning hip muscles considering realistic 3D geometry, spatial muscle fibre alignment and muscle-muscle and muscle-bone interactions. The muscles and tendons were assigned as incompressible transversely isotropic Mooney-Rivlin material incorporating muscle fibres that aligned along the geometry of muscles. They reported maximum tensile stresses concentrated in the tendon regions connecting the bones due to point loading conditions in the muscle attachment sites.

The phenomenological model also represented other methods to define how the musculotendon fibres are attached to the corresponding bones and therefore estimated the loading distribution of

muscles. These methods were uniform, point and mapped load to attach the meshing nodes over the areas of the muscle attachment sites during the FE analysis. As discussed, the point load strategy repeats the famous method in the studies, which accept the connection between musculotendon units to the bone at an exclusive node (Olivetti, 2006; Cilingir, et al., 2007; Piszczatowski. 2008; Anderson, et al., 2009; Anderson, et al., 2010). The uniform method has been regionalised to where the musculotendon loading is exerted to a physiologically naturalistic connection points as origin and incretion, with a specific end goal. This method created better results in comparison to the point loading method because it eliminated the local stress peak and stress concentration. The mapped method was the third technique applied to address the point load issue (Cardiff, et al., 2013). This method was progressed to where the musculotendon loading is exerted to the natural attachment points (i.e. insertion and origin) as selected elements and nodes. The angle and direction of the muscular fibres were also considered to improve muscle-loading distribution. In this study, the modified mapped method was applied to ensure the elastic and natural boundary conditions of the musculotendon fibres were satisfied, as shown in figure 6-3.

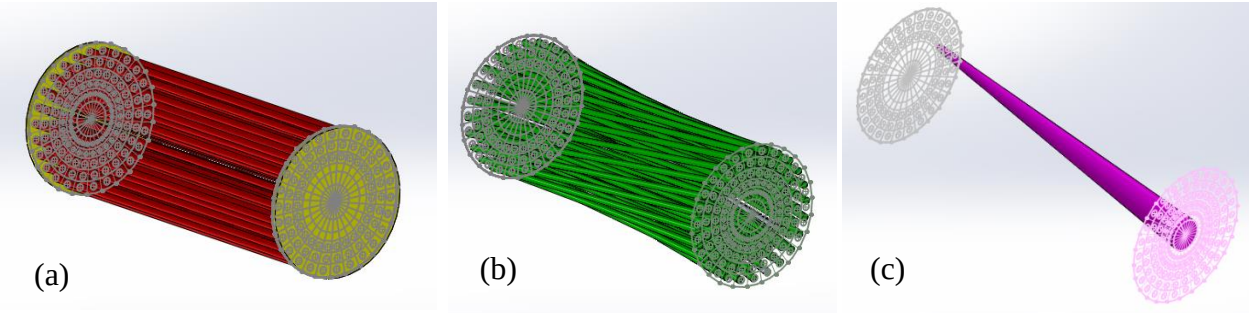

Figure 6-3:Simulation of the effect of musculotendon fibres contact force (a) Modified mapped distribution model, (b) uniform distribution load, and (c) Point load.

6.6 Meshing Strategies

Selecting an appropriate strategy for meshing parts and assembly plays a very important role to create an applicable FEA model and therefore generate reliable and accurate results. Although there are a wide range of strategies to employ mesh for FEA, based on the connectivity of the meshes across the parts and components, this work used the following classifications (Thompson, 1990; Anderson, 1995):

Structured Strategy: This is defined based on the repeated pattern of a specific mesh for an original shape or regular form in space. In this case, the vertex connection of symmetric topology followed a specific pattern (Anderson, 1995).

Unstructured Strategy: This type of strategy is applied to complex shapes and morphology, in which all parts or components are completely asymmetrical. Hence, there is not any specific pattern to follow by vertex connection of mesh. The unstructured meshes are ordinarily less challenging to create and the procedure can be generated by the automated mesh. However, the structured mesh strategy is time-consuming and requires a high degree of manual processing in order to create accurate estimations due to the symmetrical nature of the shape and morphology.

A wide range of cell shapes can be used to create structured meshes, as long as the cell mesh are rehashed and repeated in a specific pathway, such as hexahedra as shown in figure 6-5 (a). Likewise, the unstructured meshes can be created by using different distinctive cell shapes, but because of their simplicity, the tetrahedral structure is usually employed in figure 6-5 (b). Hexahedra dominant (Hex-Dominant) and voxel based meshes are two subcategories of unstructured meshes. Figure 6-5 (c), shows an example of a general polyhedron, which can be used to generate the unstructured mesh. Alongside unstructured and structured meshes, hybrid or mixed meshes can be created using a strategy that combines two types of mesh. The main advantage of a hybrid mesh is the existence of its innate precision due to the use of structured meshes for the main areas of geometry, whilst the rest of the spaces are filled using unstructured cells. In this study, the hybrid mesh strategy was applied with respect to the complexity of the lower limb geometries. For the whole structure, 572440 nodes and 380112 elements were created. However, the skewness criteria to control the quality of the mesh and its statistical parameters are shown in Appendix E. Additionally, the application of mesh in human lower extremities have been reviewed in appendices (See Appendix E).

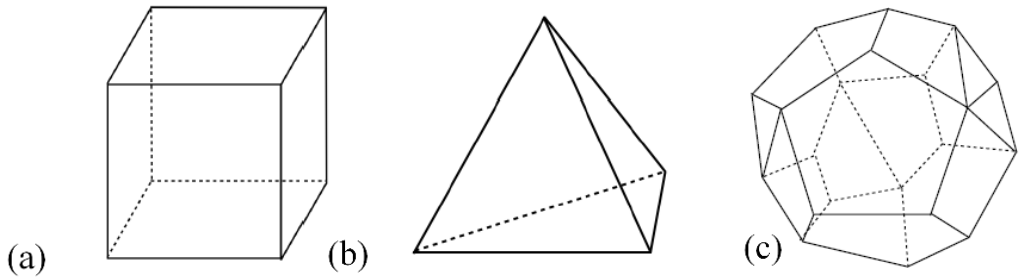

Figure 6-4: Various types of mesh including (a) Hexahedron, (b) Tetrahedron, and (c) General Polyhedron (Adapted from Cardiff, et al., 2013)

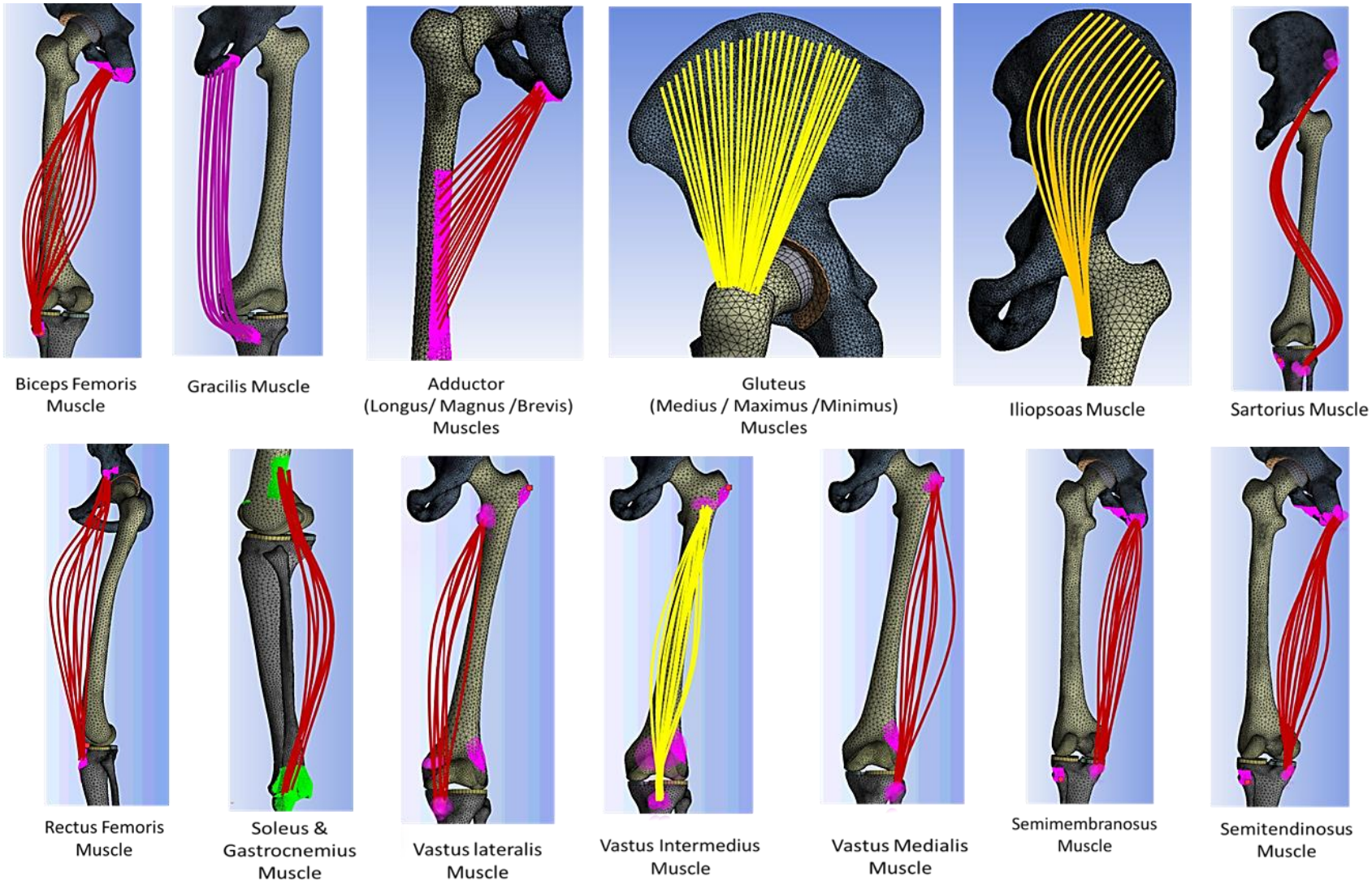

Figure 6-5: Schematic of the selected muscles, their insertion and origins, and adapted mesh for the entire lower limbs body applied for FEA study.

6.7 Material Selection

Wide ranges of complicated methodologies have been created to simulate the lower limb bone structure in humans, and define the appropriate mechanical and physical properties according to their natural behaviour. The Sandwich model is defined by considering the cortical, cancellous, marrow cavity, and inhomogeneous structure. The homogenous bone structure refers to the allocation of a cortical as stiffened materials for all layers of bony parts. Venäläinen, et al., (2016) conducted a study to determine the effect of inhomogeneity on the mechanics of tibiofemoral contact during the normal walking. They reported that the maximum contact pressure for the inhomogeneous tibia was 4.16 MPa, while the inhomogeneous elastic bones demonstrated 4.06 MPa laterally. In addition, the analogous mean contact pressure for the inhomogeneous and homogenous tibia bone was reported as 2.83MPa from the medial direction. The mechanical properties of the selected materials for the biomechanical compartments can be classified into three main categories including isotropic, orthotropic, and anisotropic. The isotropic characteristic refers to the ideal concept of a material in which the mechanical properties and characteristics of materials are independent of any directions or orientations. Conversely, an anisotropic property refers to a material, which exhibits various behaviours and characteristics for each possible direction. Hence, different elastic-plastic constants should be defined for each possible orientation. An orthotropic property is part of anisotropic, which demonstrates various characteristic and behaviour in three common perpendicular planes and directions.

By nature, most of lower limbs compartments in the human body are composed from more anisotropic materials than isotropic. Isaza, et al., (2013) conducted a finite element analysis study using Comsol software to compare the mechanical behaviour of isotropic and anisotropic materials applied for an inhomogeneous femur bone. The obtained results proved that the isotropic materials predicted the fracture loading 16% higher than the realistic value. Whilst the anisotropic material of the femoral predicted the fracture loading close to the observed value by 4.1% differences.

Several researchers applied the orthotropic materials for the tibia, femur and meniscus (Keller, 1994; Bitsakos et al., 2005; Peng et al., 2006; Gray et al., 2008; Yang et al., 1999; Gu, & Li, 2011). However, some researchers applied the isotropic material for the soft tissues such as cartilages (i.e. femoral head and pelvic cartilage) (Li, et al., 2002; Moglo et al., 2003; Peña et al., 2008; Papaioannou et al., 2010). In this study, the homogeneous (single-phase) orthotropic material was selected for the main parts of the FE model including femur, tibia, and meniscus.

The isotropic homogeneous material was selected for the cartilage and pelvic region to simplify the whole concept, stabilise geometry, and reducing the time of analysis.

Some researchers specified that the type of material does not show a significant difference during the short time loading condition in nonlinear study (Armstrong, Lai and Mow, 1984; Eberhardt et al., 1990; Donahue et al., 2002). Hence, the selected material for the cartilage can be presented as the mechanical response during the short conducting time of FEA, which was allocated 1.06 seconds in this study. Table 6-3 summarised the previous studies, structural characteristics and their most important mechanical properties.

For this study, more than twenty-six various forces in different ordinations based on the nature of the lower limb were assigned for the FE model. Figure 6-6 shows the level of complexity in loading conditions of the FE analysis model in this study. However, the end of tibia and top of pelvis were fixed to stabilise structure statically. In addition, the effect of ground reaction force was neglected for the analysis.

Table 6-3: Density and mechanical properties of the orthotropic properties applied for the FE models.

Material Properties	Femur - orthotropic (Korsa & Mares, 2012)	Tibia - orthotropic (Kerem & Çalık, 2016)	Meniscus-orthotropic (Yang et al., 2010)
Density (kg/ mm^{-3})	2200	2200	1100
Young's Modulus X direction (E- MPa)	1200	6900	120
Young's Modulus Y direction MPa	13400	8500	20
Young's Modulus Z direction MPa	20000	18400	20
Poisson's Ratio XY - υ	0.38	0.49	0.3
Poisson's Ratio YZ	0.22	0.12	0.3
Poisson's Ratio XZ	0.24	0.14	0.2
Shear Modulus XY (G-MPa)	4350	2400	57.7
Shear Modulus YZ MPa	5610	3600	57.7
Shear Modulus XZ MPa	6230	4900	8.33
Density and mechanical properties of the isotropic properties applied for the FE models			
Material Properties	All Cartilages - isotropic (Mootanah et al., 2014)	Pelvic - isotropic (Ritchie et al., 2005)	Equation of the isotropic elasticity constants
Density (kg/ mm^{-3})	1100	2210	

Young's Modulus (E-MPa)	25	1340	$G = \frac{E}{2(1+\upsilon)}$ $K = \frac{E}{3(1-2\upsilon)}$
Poisson's Ratio - υ	0.45	0.31	
Shear Modulus XY (G-MPa)	86	51145	
Bulk Modulus (K- MPa)	83	11754	
0.2% Compressive Yield Strength MPa	8.2	---	
Ultimate Tensile Strength MPa	---	150	

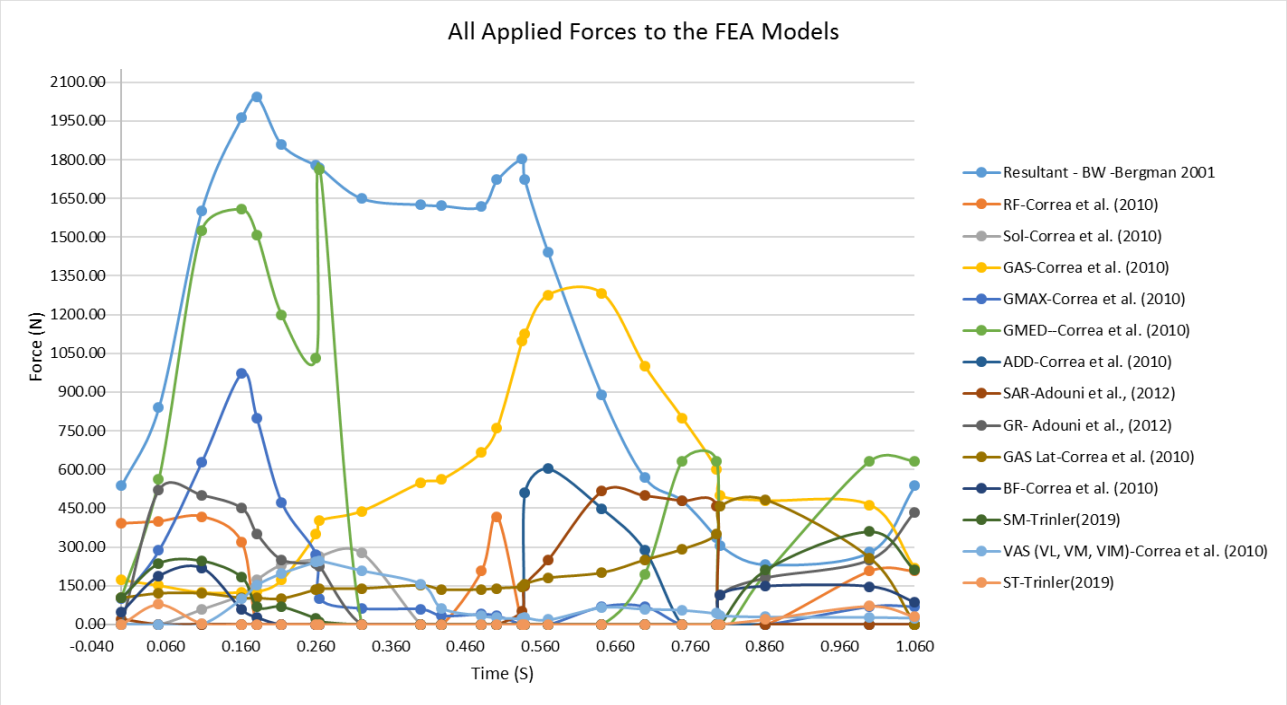

Figure 6-6: Graphical representation of all applied forces for the 3D-Mus. study in FE analysis.

The muscle coordinates system and contact force were summarised previously in chapter 3 (See section 3.9.2 and appendix B). The lists of all applied loadings as well as the maximum contact force for each muscle are summarised in appendix F.

6.8 Numerical Solver Approach

To solve the complex equations numerically the principal of the linear approximation followed by differential equations can be applied. The Newton-Raphson approach or simply Newton method is a powerful approach, which was applied for the solver data of the software package. According to SHARCNet, (2018) the FE analysis and discretization procedure produce the set of simultaneous equations as follows

$$[K]\{u\} = \{F^a\} \qquad (6\text{-}1)$$

Where, [K] is the matrix of stiffness coefficient, {u} is an unknown vector of DOF values, and $\{F^a\}$ presented as loading vectors.

Depending on the nature of the study, the [K] can be function of the DOF values or other types of derivative thus creating a nonlinear equation. To solve the nonlinear equations, Newton-Raphson technique proposed the iterative process, which can be demonstrated as follows (SHARCNet, 2018). .

$$[K_i^T]\{u_i\} = \{F^a\} - \{F^{nr}{}_i\} \qquad (6\text{-}2)$$

$$\{u_{i+1}\} = \{u_i\} + \{\Delta u_i\} \qquad (6\text{-}3)$$

Where, $[K_i^T]$is a Jacobean matrix or tangent matrix, $\{F^{nr}{}_i\}$represented as a vector of restoring loads for the element internal loads, and (i) represents the current equilibrium iteration. The terms $\{F^{nr}{}_i\}$ and $[K_i^T]$ are evaluated based on the given valued from$\{u_i\}$. For the current study, which defined structural analysis, the term $[K_i^T]$ represents the tangent stiffness matrix,$\{u_i\}$ indicates the displacement vector and $F^{nr}{}_i$ is the restoring force vector calculated from the stress elements. Figure 6-7 shows the Newton-Raphson iteration methods step by step to solve the complex case studies (SHARCNet, 2018).

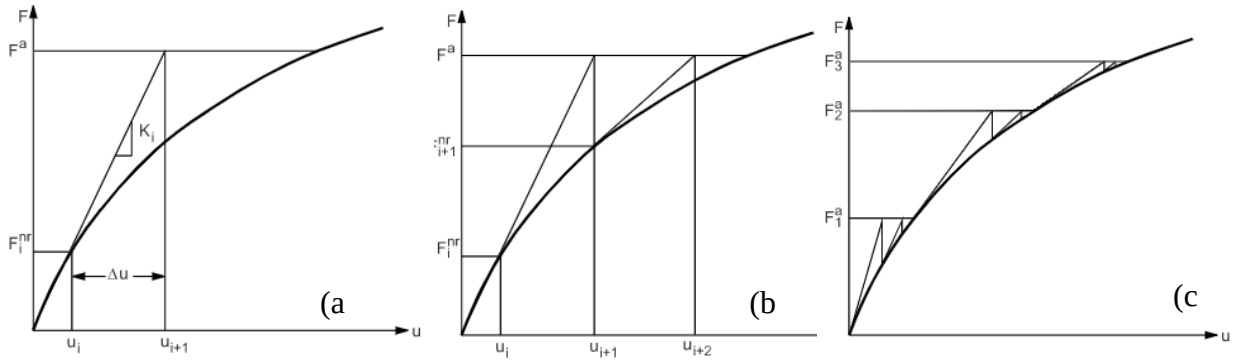

Figure 6-7: Newton-Raphson Procedure for (a) the first iteration, (b) the second iteration, and (c) the incremental path-dependent nonlinearities (Adapted from SHARCNet, 2018).

The force convergence steps and assigned time for the gait in contradiction of the cumulative iteration numbers shown in appendix E. The applied software package conducted 44 iterations to solve the assigned FE model via Newton-Raphson solver. Due to the number of the iterations and associated complexity, it was noted that the conducted study was non-linear with respect to the numerical analysis and assigned time of loading (SHARCNet, 2018). However, the CAD model was designed statically without any movements; hence, the complete CAD model and

FE analysis can be considered as the static-dynamic or quasi-dynamic study. Figure 6-8 shows the mesh convergence study of the femur where all muscles are attached to the FE model. The main reason to conduct the mesh convergence is to ensure the obtained results are not affected by changing the size of the mesh and therefore the smallest size of the mesh was attained. It can be seen that the maximum principal stress has been increased by reducing the size of the mesh (i.e. increasing the number of elements) until it shows the minimum variation at 18.5 MPa. In this case, the smallest size of the element for the femoral stress analysis is selected 3.5 mm, which produced 87799 mesh elements, since by reducing the size of the element, the value of maximum principal stress was not changed.

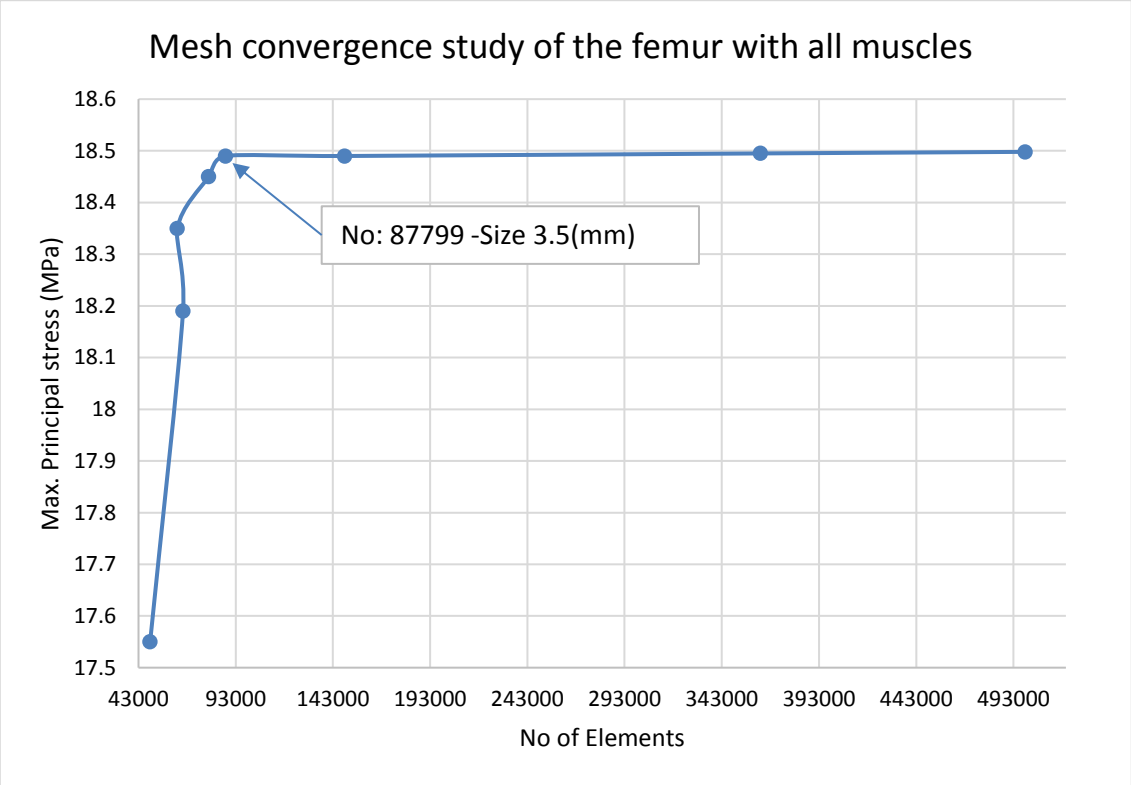

Figure 6-8: Graphical representation of the maximum principal stress MPa vs. number of elements for the femur as a main part of the lower limbs.

Chapter 7

Results and Discussion
Numerical and Analytical Methods

7.1 Introduction

In this chapter, the results obtained from the numerical approach will be reported followed up by a discussion based of the bio-functional analysis. The loading characteristics of the human musculoskeletal model were also considered to justify the acquired results. This chapter contains two main sections. The first section includes non-comparative analysis to determine whether the obtained results can present validated evidence against the natural behaviour of the human body during the gait cycle. In addition, the outcomes of this study were compared with the preceding evidence from other researchers to comprehend a certain level of result verification. This section includes femoral stress analysis within the gait and strain analysis of hip-knee compartments including femur, femoral head cartilage and femur condyle articular cartilage.

The second part of this chapter contains a comparative analysis across four defined models (see table 6-1). The aim was to determine whether the conducted FE analysis can create adequate evidence to support the main assumption of this study. In this chapter, the effect of muscle contraction on femoral principal stress, shear stress, compressive (i.e. normal) stress, and femoral principal strain will be reported and analysed

7.2 Verification of FE Analysis

7.2.1 Stress Analysis of Femur (3D-All Mus. FEA)

The 3D- All Mus. study was used to evaluate the effect of hip spanning and non-spanning muscles (i.e. Hip and Knee muscles) contribution on stress, strain and deformation of the femur during the normal walking. Figure7-1 compares three main stress indexes including von-Mises, maximum principal, and maximum shear stress (YZ) of the femur within the gait cycle. It can be realised that the maximum principal stress 18.39 MPa, von-Mises stress 19.50 MPa and shear stress 9.06 MPa (on lateral-superior or -YZ plane) occurred at the single support stance. While, the second maximum stress was observed at 50% of the gait where the toe-off stance

occurred. The acquired stresses configuration were highly coordinated with the applied bodyweight and overall loading condition reported by several researchers. They described the first maximum BW occurred at single support stance and the second peak happened at 50% of the gait (Bergmann et al., 2001, 2016; Chen et al., 2014; Damm et al., 2013; Debrunner, 1975; Kotzar et al., 1991; Pauwels, 1978; Paul, 1966; Schwachmeyer et al., 2013; Zhang et al., 2015, Ng, et al., 2018).

Hence, it can be comprehended a certain level of harmony exists between the applied loading condition and obtained stress configuration during the gait cycle. This level of coordination between force-stress proved that this FE study had a level of certainty and accuracy to create the anticipated outcomes.

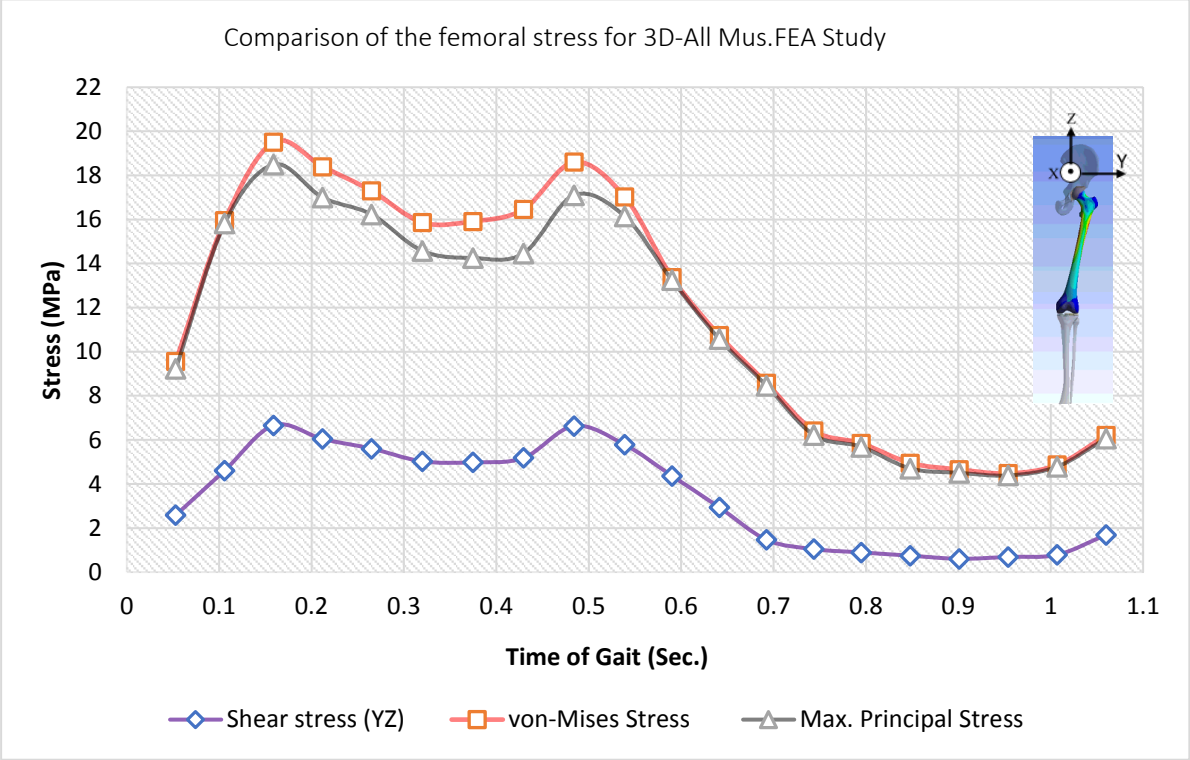

Figure 7-1: Stress analysis of the femur during the gait for the 3D-All Mus. FEA study.

7.2.2 Stress Results Verification

In this section, the predicted femoral stress via FE analysis is compared with the estimated stress obtained from the analytical approach (see section 5-8) and other researchers' analysis.

Comparing the acquired values from literature, the predicted stress including von-Mises and maximum principal stress are vary from 10 to 61 MPa (Anderson, et al., 2010; Harris, et al., 2012; Jade et al., 2014; Jonkers, et al., 2008; Rapperport, et al., 1985; Montanini & Filardi, 2010; Russell, et al., 2006; Taylor, et al., 1955; Phillips, et al., 2007).

Montanini & Filardi (2010) The predicted equivalent stress for this study 19.05 MPa is highly consistent with Antonio, et al.'s results with a maximum of 5.5% deviation due to applying various CAD model. Although the obtained von-Mises stress (i.e. 10 MPa) for the Rapperport, et al., (1985) study showing the significant variation with the results of current study (i.e. 19.50 MPa), but this variation can be explained by considering the differences between loading condition as explained in the literature. Jade et al., (2014) reported the maximum von-Mises stress via FE software and CT scan 18 and 21 MPa respectively which shown 10% variation with the predicted results of this study at the same stance. The main reasons to justify the variation between the two studies can be attributed to the difference of applying boundary and loading conditions. Jonkers et al., (2008) simplified the lower extremities and merely considered half of the femur geometry, which created the huge variation in obtaining results. According to comprehended literature, Chethan, et al., (2018) and Cook et al., (2017) are estimated the von-Mises stress 57.1 MPa and 63.01 MPa respectively without considering any femoral head cartilage or other lower extremities for their CAD model. They applied the static loading as a point load on top of the femoral head and fixed the femur condyle at the end. This type of FE simulation is questionable because they neglected the effect of other lower limbs such as pelvic, muscles and cartilages. In this case, the applied force directly on the femur bone increases the risk of stress concentration and may not have created valid results. Figure 7-2 compares the obtained femoral stress in this study including analytical and numerical methods with other researchers.

Although it is very difficult to conduct an inter-study comparison to verify the estimated results of FE analysis, it can be acknowledged that the predicted results of maximum femoral stress highly coordinated with other similar studies and confirmed the reliability and validity of acquired results in this study.

7.2.3 Strain Analysis of Hip-Knee Components (3D-All Mus.)

In this section, the maximum principal strain for the femoral head cartilage, femur, and Articular Cartilage (AC) analysed for 3D –All Mus. model within the normal walking. The main aim of this study is to examine the obtained result of the numerical method with the bio-functionality of the cartilage and femur bone. Figure7-3 shows the maximum principal strain on a logarithmic scale due to presenting small strain of the femur in comparison the cartilage.

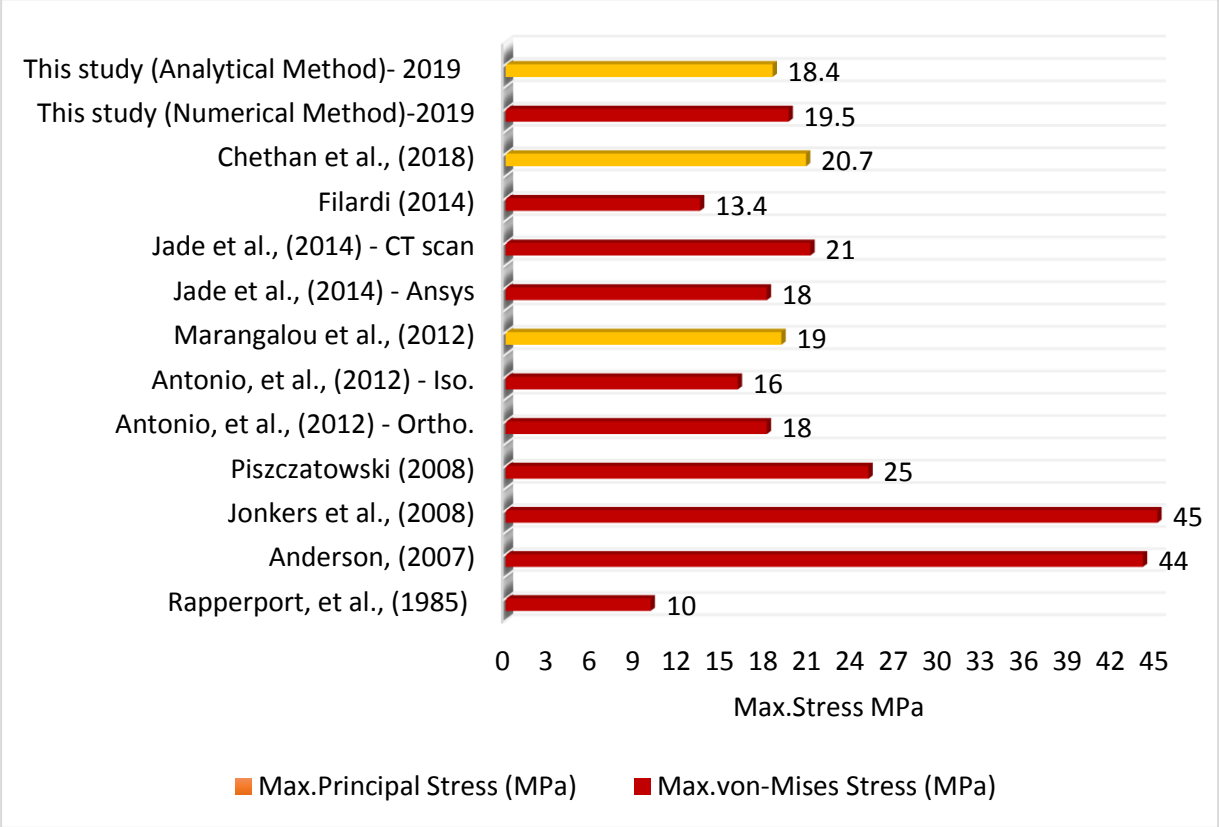

Figure 7-2: Stress analysis of femur, comparison between current study and other scholars.

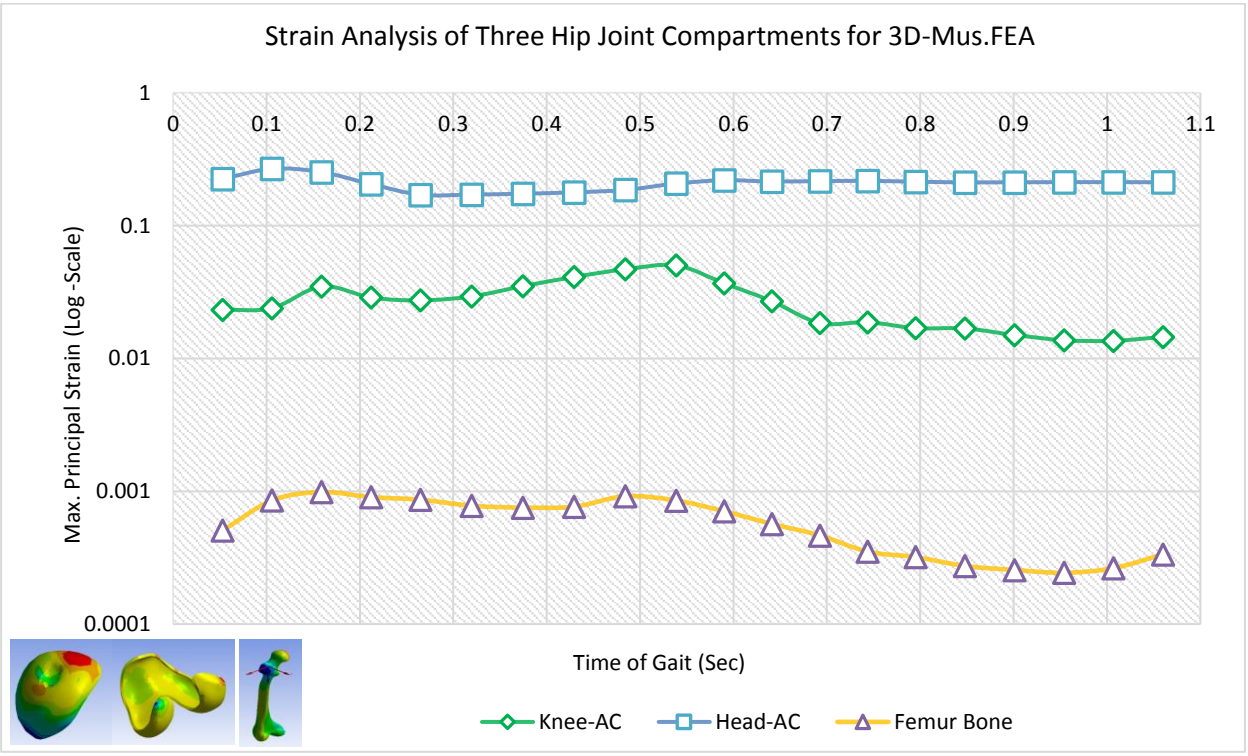

Figure 7-3: Strain analysis of femur, knee AC and femoral head AC for 3D-Mus. FEA study during the gait.

It can be seen that the femoral head cartilage experienced significant strain approximately 5 times higher than knee articular cartilage, while both cartilages had similar material. The main reason can be attributed to their various surface areas and attachment sites.

The surface area of the femoral head cartilage is 3791.5 mm^2, which is 150% less than surface area of the knee AC model, which attached to the femur condyle (6009.3 mm^2). Hence, the subjected loading were distrusted on the surface area of AC, exhibited less strain. On the other hand, femoral head cartilage had less surface area and therefore experienced higher stress and correspondent strain within the same loading and boundary conditions. The above-mentioned assumption coordinated with the principle of the stress equation, Hooke's law. According to Hooke's law, under the same loading condition, by increasing surface area, it can be expected the stress is reduced and therefore its corresponding strain decreased. Furthermore, the femoral head cartilage attached at the top of femur where was subjected to direct HCF during the simulation. The AC attached to the end of femur (i.e. femur condyle) experienced less loading condition, because the femur as a stiffer medium endured the applied forces significantly.

Furthermore, Figure 7-3 shows that the femur bone experienced minimum strain (980 micro strain) in comparison to the femoral head cartilage and AC. The strain of head cartilage and knee cartilage was estimated around 272, which was 50 times more than femur strain respectively. The possible interpretation for the observed variation can be attributed to the assigned materials for the lower limb. The stiffness of cortical bone is significantly higher than the stiffness of cartilages and therefore it can endure greater loading and stress without showing the massive strain. In conclusion, it can be stated that attained results demonstrated a certain level of certainty and validity, while further discussion and result comparison was considered for the next section.

Another study was conducted to compare the maximum principal strain of femur across all four FE models in micro-strain (με) and results were summarised in figure 7-4.

It can be seen that the maximum strain (986.36 με) occurred for the 3D-All Mus. model at 16% of the gait before the single support stance started. On the other hand, the principal strain of the femur for 3D- No Mus. case study was estimated as 737.02 (με) at 50% of the gait. Although the maximum strain for the hip and knee muscle studies were predicted in the same range, by reducing the numbers of muscles from the musculoskeletal model, the amount of strain reduced by an average value of 18%.

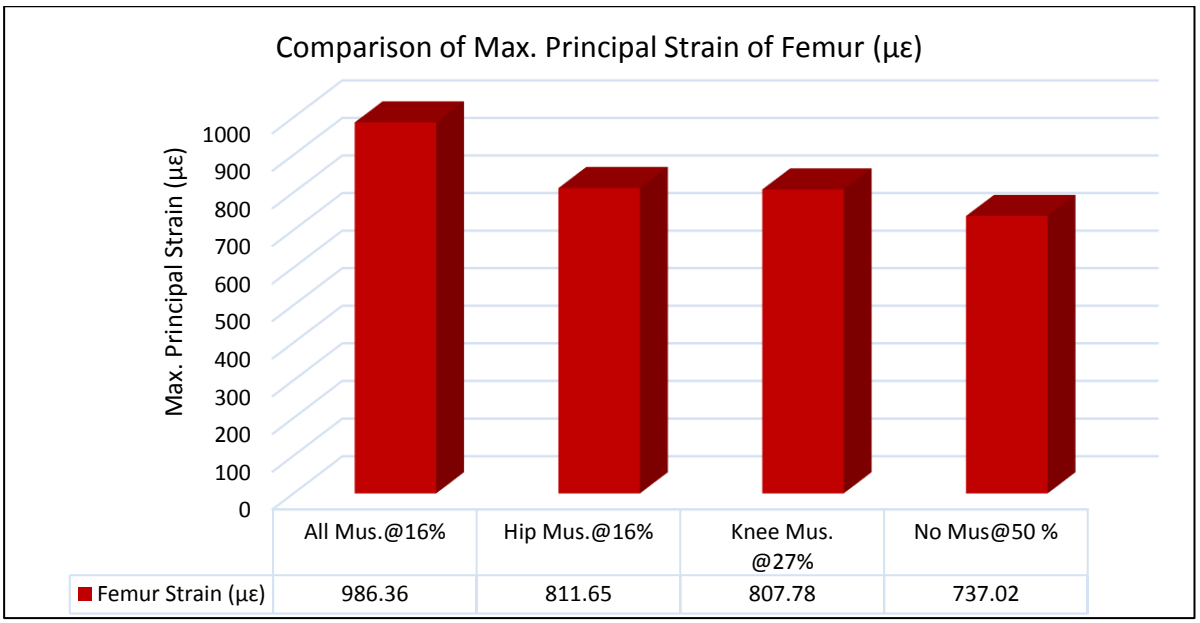

Figure 7-4: Effect of muscle contraction on Max. Principal strain of femur for all numerical studies within the normal walking activity.

7.2.4 Strain Results Verification

Nimit et al., (2016) conducted a study to measure strain for different thicknesses of the articular cartilage via FE analysis. They simulated the femur as well as all other compartments of the knee joint before applying the force during the gait cycle. The local maximum strain was reported between 3% and 8% and depended on the thickness of the cartilage within the gait cycle. Their results were also consistent with the results of Sutter, et al., (2015) who reported the maximum strain of the AC around 6% and 3% in the medial and lateral side of femoral condyle. The obtained maximum compressive strain of AC for the 3D-All Mus. model in this study reported (5%) medially which highly matched with the results of Nimit et al., (2016) and Sutter, et al., (2015). As discussed, the cortical bone demonstrated higher stiffness and density, which causing the femur to endure higher loading without deformation or strain and therefore less principal strain apparent within the gait.

According to the literature, the main function of the hyaline cartilage as the main component of the fibrocartilage is to reduce the friction between the bones, thus enabling bones to slide or glide smoothly over one another (Phan et al., 2009; Klika, et al., 2016). Theoretically, assigned materials for the cartilage have a less density and stiffness in comparison to the femur bone as a homogeneous orthotropic cortical. The porous-viscoelasticity properties of the cartilage demonstrated massive deformation within the loading between the two bones without failure. The obtained results of the comparative analysis in figure 7-3 confirmed that the femoral head AC and condyle AC experienced higher strain as compared to the femur. The achieved outcome

completely coordinated with its bio-function, cellular physiology and preceding evidence from other researchers (Eckstein, et al., 2001; Cotofana, et al., 2011; Coleman, et al., 2013; Widmyer, et al., 2013).

Pal, et al., 2010 conducted a study to examine the strain on an intact femur and implemented femur under various static loading from 600 to 1350 N by experimental and FE analysis. They assigned an isotropic material for the femur and reported the maximum strain 549 με without considering the muscles contact force. In this study, for 3D-No Mus. model the maximum principal strain was reported 737 με (see figure 7-4) which showed a 34% increase in comparison to Pal, et al.'s results.

The possible explanation for the observed difference can be attributed to the application of the maximum loading condition between studies. In this study, the maximum average applied force considered was 3.72 × BW for a volunteer with 80.1 (Kg) within the dynamic loading condition of gait cycle. Whereas, Pal, et al., considered the static loading maximum 1350 N, which certainly created less strain compared to this study.

In addition, Martelli, et al. (2015) predicted the femur strain by modelling a participant's pelvis, femur and tibia with a weight loading 66 ± 2.5 kg. They conducted linear static analysis by segmenting a femur in nine different sections from the femoral neck to diaphysis in a distal-proximal direction. The maximum femoral strain was reported from 570 to 1053 με in the head-neck section; however, the average femoral diaphysis reported 3668 με. In this study, the obtained femoral strain in the head-neck section area was estimated between 396 and 650 με and for the femoral diaphysis, maximum strain 985 με computed across the region. The significant difference can be justified by considering the quasi-dynamic loading, an anisotropic material, and various loading condition, which were applied in the current FE study.

Cristofolini, et al., (1995) conducted an experimental study to examine the femoral strain. They fixed sixteen biaxial strain gauges in different sites of the femur on various aspects including posterior, anterior, lateral and medial planes. They applied static loading with the angle of 12˚ from the Z-axis towards the inferior direction. Cristofolini, et al.'s results exhibited that the strain in the lateral side of the femoral diaphysis to be 1100 με while in the posterior side of the femur the amount of strain increased by up to -1750 με. The maximum principal strain for the current analysis (3D-All Mus. model) predicted (985 με) which occurred in a lateral side of the femoral diaphysis and showing approximately 10% variation from the Cristofolini, et al.'s results. According to Small, et al., (2017) it is very difficult to verify the true value of femoral strain via inter-study comparisons due to the used of various loading and boundary condition as well as different measurement techniques. Nevertheless, they reported strain for the intact

femur between 500 and 700 με while the acquired strain range for this study reported 500 to 985 με within the normal walking.

From above analyses, it is comprehended that the results obtained from FE analysis for 3D-All Mus., produced adequate evidence to justify the function of femoral head cartilage and femur condyle articular cartilage. Despite the wide range of femoral strain values reported from the use of a diverse range of boundary conditions, the femoral strain of the current study reported several times by other researchers (Finlay, et al., 1988; Cristofolini, et al., 1995; Small, et al., 2017). Hence, it can be stated that the created FE model, its loading boundary conditions, and CAD model could create valid and reliable outcomes compared to bio-functional of femur and cartilages. In addition, the achieved outcome can produce a certain level of consistency with the preceding evidence from other studies.

7.3 Stress Analysis of Muscle Attachment sites (3D-All Mus.)

The current analysis was conducted to identify the stress of muscle attachment sites (i.e. insertion and origin), which generated muscle contraction during the normal walking activity. To accomplish this evaluation, the origin and insertion of each muscle were defined in the FE model based on the local coordinates of origin and insertion of the muscles, as summarised in section 3.7 and Appendix B. For instance, the stress configuration of Bicep Femoris (BF), Gracilis (GR), and Vastus Medialis Oblique (VMO) as non-hip spanning muscles were analysed and reviewed, while the peak stress of attachment sites for all other muscles were summarised and compared separately.

7.3.1 Biceps Femoris (BF) Muscle

The attachment sites of the muscle (i.e. origin and insertion) experience stress due to muscle contraction. Hence, it is necessary to investigate the effect of the muscles contraction on stress behaviour of their attachment locations. The selected nodes belong to the origin (O) and insertion (In) of the biceps femoris, and are connected via imaginary muscle fibres. Figure 7-5 (a) shows stress of the origin and insertion nodes subjected to the BF contact force (as an activated muscle) due to muscle contraction and extension. Figure 7-5 (b) shows the elemental areas between the origin and insertion of BF were selected based on the actual anatomy of the hamstring muscle group is activated. The maximum shear stress, and normal stress (stress towards muscle act-line) were reviewed. The same trend is observed for both stresses with two maximum values at the beginning and end of the gait when the flexion of femur occurres. Conversely, the stress configurations are steadily decreased from 10% of the gait towards the mid-stance of the gait (at 50%) where they show minimum values.

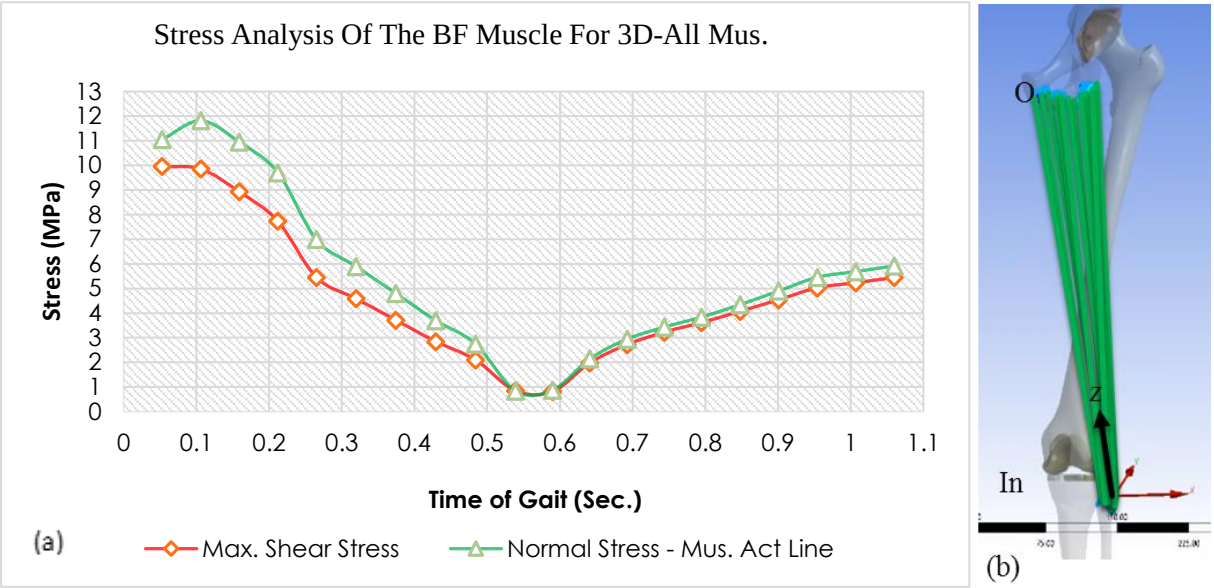

Figure 7-5: Applied shear and normal stress to the origin and insertion of BF muscle due to its muscle contraction during the gait.

To understand the stress behaviour of the BF's attachment sites and justify the stress fluctuation during the walking, it is necessary to explain the function of the BF muscles group (i.e. BFSH and BFLH). The BF is part of the hamstring muscle, which connects the fibular head and Ischial Tuberosity region. It is responsible for the hip flexion, supports knee flexion, and lateral tibia rotation. Hence, the BF muscles are not fully activated during the single support stance, toe-off (i.e. femur extension), and swing phase which presented in figure 7-6.

Figure 7-6: BF Muscle activation during the gait (Adapted from Howard, 2017).

By comparing figure 7-5 and 7-6, it is observed that the BF muscle created maximum stress due to the muscle activation period during heel strike at the beginning and end of the gait (see figure 7-6). While from 10% up to 85% of the gait, minimum stress created because the muscle is not fully activated. Therefore, the results obtained highly coordinate with the anatomical facts and function of the BF reported by other researchers (Shelburne et al., 2005; Shelburne et al., 2006; Adouni et al., 2012; Thorpe, 2015; Lin et al., 2015; Howard, 2017).

7.3.2 Gracilis (GR) Muscle

Figure 7-7 shows the applied maximum principal and normal stress (alongside the muscle activation-line) due to the activated gracilis (GR) muscle within the gait cycle.

From the stress configuration, it was observed that the muscle applies stress to its attachment sites at the beginning of the gait between 0 to 10% when the hip flexed at heel strike. The stress configuration of the GR muscle is then reduced from 10% up to 80% of the gait cycle. Within the flexion stance at the end of the gait the applied stress on GR's attachment sites increased again. To identify any synchronisation between the muscle activation period and obtained stress configuration, the main function and activation period of GR were reviewed.

The red squares in figure 7-7 indicate the muscle activation model during the gait reported by Howard, (2017), however several researchers have also reported the same results (Shelburne et al., 2005; Shelburne et al., 2006; Adouni et al., 2012; Lin et al., 2015;). In addition, Barclay and Curreli, (2015) reported the main functions of GR muscle, including adduction motion of the femur, flexion motion of the knee, and rotation of the tibia on the femur medially. The GR muscles also provides great support to other muscle groups in this region. Considering the above evidence, it can be comprehended why the applied stress by GR muscle on their attachments sites was recorded at the beginning and end of the gait cycle.

Furthermore, the maximum principal stress subjected to the attachment sites by GR muscle estimated 2.9 MPa on its origin (i.e. ischiopubic ramus) when the hip flexion is completed.

The significant variation between applied stress by GR (2.9 MPa) and BF muscle groups (11.05 MPa) can be justified by their function and characteristics. The BF muscle is a group of two strong muscles including BFSH and BFLH, which their activated time is slightly higher than GR muscle. In addition, BF has a main role during the heel strike to support the hip flexion position. Hence, any muscle contraction generated huge stress on its attachment points. On the other hand, GR is an individual muscle with short activation time. This muscle is supportive and assists to complete the function of other muscles during the hip flexion and therefore, it may not to generate significant stress on its origin. In conclusion, by comparing the obtained stress configuration and muscle function, it can be concluded that the applied stress by GR highly harmonised with its behaviour and activation model.

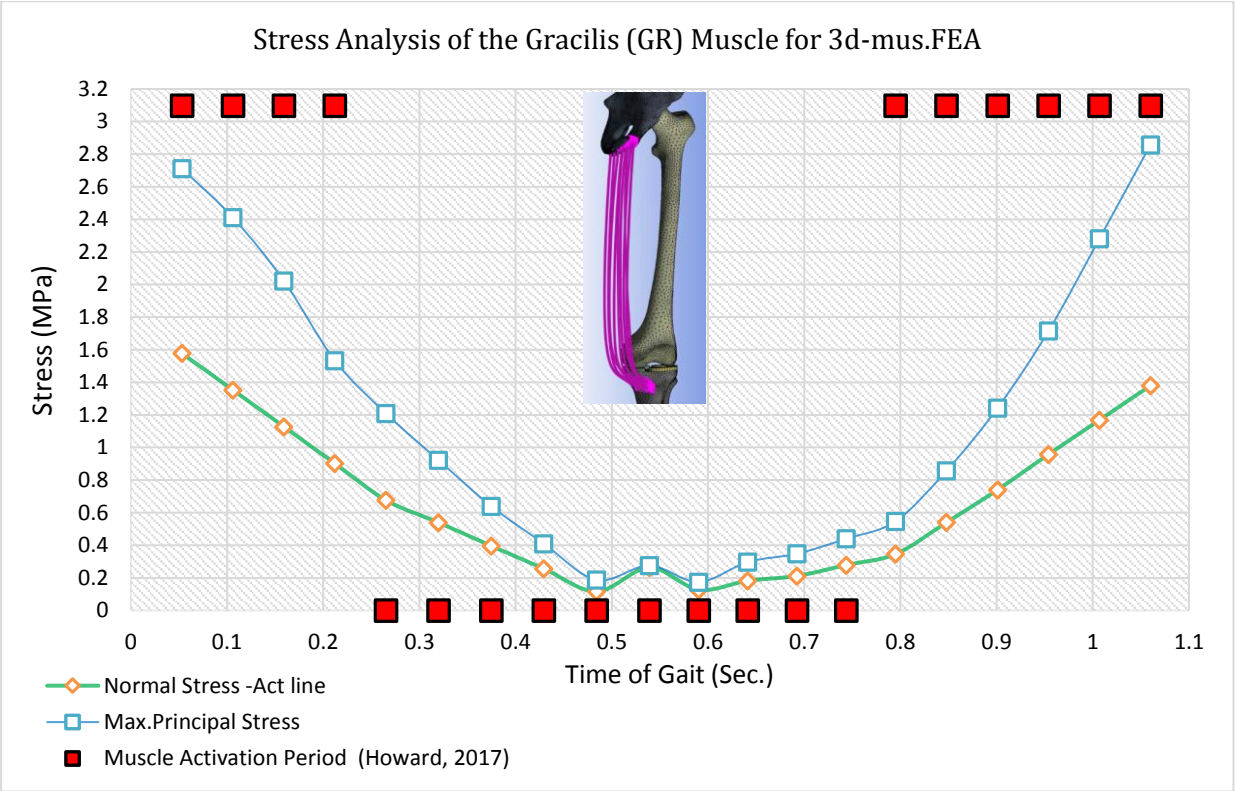

Figure 7-7: Normal stress and maximum principal stress MPa subjected to the GR muscle attachments sites due to its contraction during the gait cycle.

7.3.3 Vastus Medialis Oblique (VMO)

With respect to the obtained stress configuration during walking, the VMO applied the second peak stress to its attachments sites. It generated 11.37 MPa in its origin at 25% of the gait cycle. In this section, the stress analysis of the VMO's attachments sites was conducted to justify the obtained stress configuration. The VMO forms part of the quadriceps muscle (Q-muscle), which is attached medially to the femur and is responsible for the knee flexion, control position of the patella, and reduce the effect of lateral force component of other Q-muscles (Elias, et al., 2009).

Several researchers have presented two-phase models for the activation period of VMO during the gait. The first stage occurs between heel strike up to single support stance and the second stage occurs after the swing phase towards end of the gait (Anderson & Pandy, 1990, 2001; Kim et al., 2009; Correa, et al., 2010; Alexander and Schwameder, 2016; Howard, 2017). Trinler, et al., (2019) estimated a contact force of VMO by AnyBody and Open Sim software and reported two peaks during the walking at 18% and 50% of the gait cycle. However, they did not predict any muscle contraction at the end of the gait cycle.

Conversely, Adouni, et al., (2012), predcited the maximum contact force of VMO at 25% of the gait by using the static optimisation model and small contact force at the end of the gait cycle. Figure 7-8 compares the normal stress and applied force of VMO presented by Howard (2017) (red squares).

It can be seen that the stress configuration is increased by intensifying the muscle contraction at 25% of the gait then the stress reduced where the muscle was not activated. While, at the end of the gait, the muscle attachments sites experienced tangible normal stress via a small incremental increase of muscle contraction. The obtained stress configuration highly coordinated with the VMO activation force at the beginning and end of the gait which has also been presented by several researchers (Anderson & Pandy, 1990, 2001; Kim et al., 2009; Correa, et al., 2010; Alexander and Schwameder, 2016; Howard, 2017). However, it is partially synchronised (at single support stance) with other researchers who predict the activation period for VMO in 18% and 50% of the gait (Trinler, et al., 2019; Adouni, et al., 2012; Liu et al., 2008).

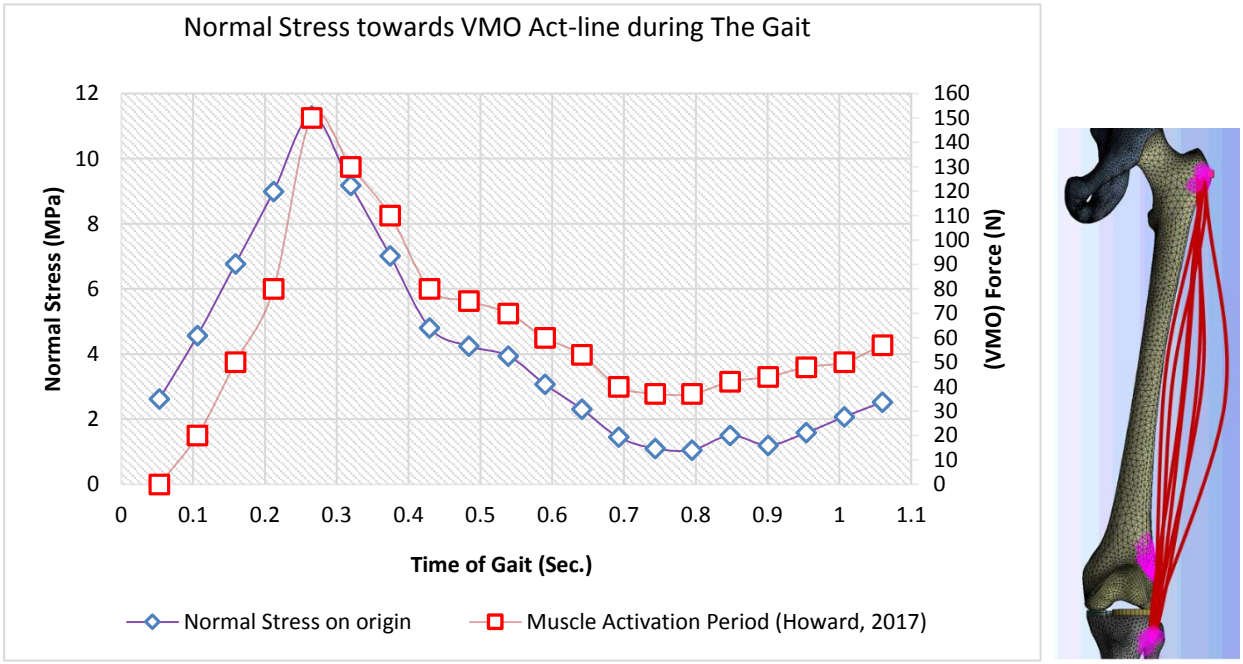

Figure 7-8: Configuration of normal stress MPa subjected to the VMO muscle attachments sites due to its contraction during the gait cycle.

7.3.4 Normal stress of all Activated Muscles (3D-All Mus. FEA)

In this section, the peak of normal stress for all muscles was compared using FE analysis. Normal stress defined alongside the imaginary activation-line from muscle insertion towards its origin. Meanwhile, nineteen muscles are classified into eight individual and five muscle groups. The location of peak stress and the stance time of the gait when the maximum stress

occurred is reported for each muscle. Figure 7-9 summaries maximum normal stress for all activated muscles in the 3D-All Mus. model within the walking activity. For instance, the peak of compressive stress for the adduction muscles group occurred in its insertion at 15% of the gait cycle. The adduction muscle create 8 MPa compressive stress on its insertion and the obtained stress configuration has coordinated with the muscle activated period at the heel strike stance of the gait cycle (Anderson & Pandy, 2001; Kim et al., 2009; Correa, et al., 2010; Arnold & Delp, 2011). Furthermore, the sartorius muscle created the normal stress 3 MPa on a small area of its origin (i.e. at anterior-superior of the iliac spine) within the simple support stance of the gait cycle. The sartorius muscle is the longest muscle in the human body, which is located on the anterior side of the other muscles in the femur area and has minimal contact with the femur alongside its fibres (Barclay & Curreli, 2015). By considering the sartorius position which lies right below the skin (Netter, et al., 2019), it can be assumed that the muscle contraction is distributed along its fibres and pressurised other muscles rather than its attachment sites, and therefore less stress subjected to its origin.

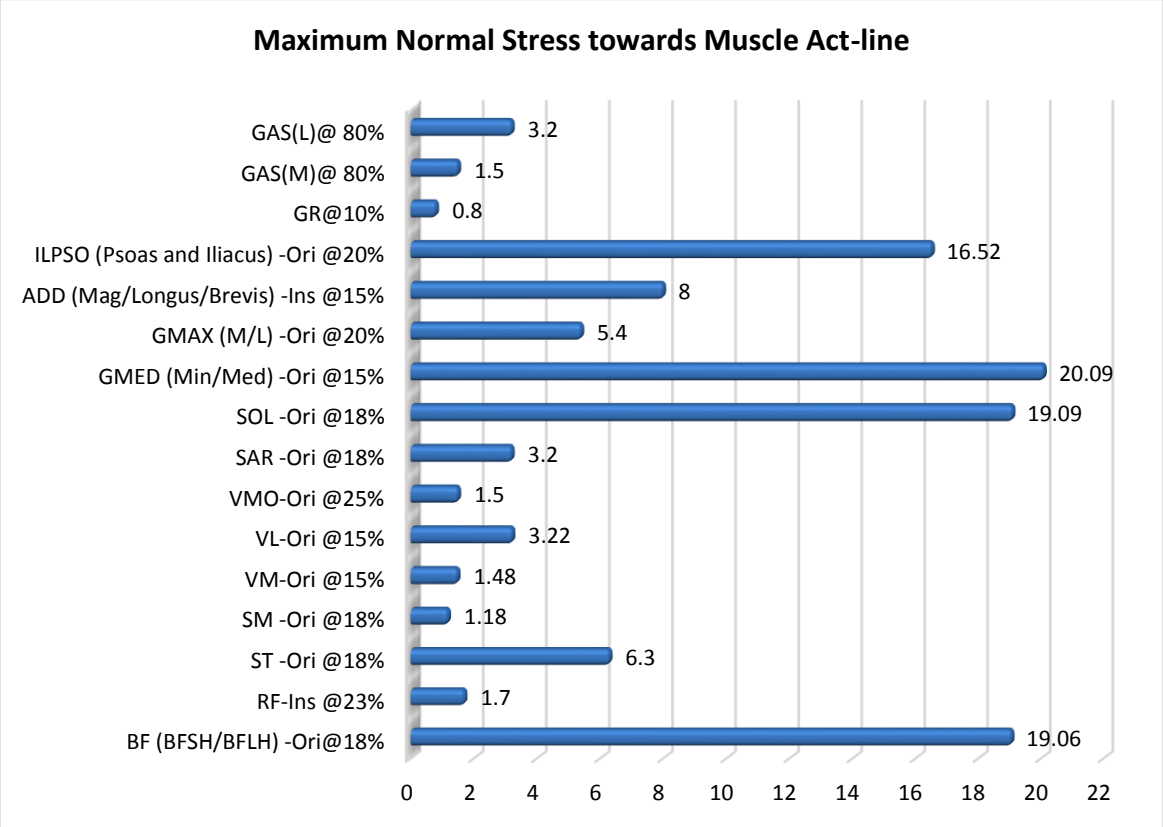

Figure 7-9: Maximum normal stress for all activated muscles for 3D-Mus. FEA study, within the walking activity. The terms (Ori.) and (Ins.) represent muscle origin and insertion.

7.4 Effect of the Muscle Contraction

The main aim of this study was to determine the effect of the muscle contraction (contraction-extension) on magnitude and configuration of femoral stress within the normal walking activity. To achieve this objective, four various studies were defined and are summarised in table 6-1. To make it clear, for 3D-H Mus. model all hip muscles considered including ILPSO, ADLB, ADM, GMEDA, GMEDP, GMAXM, GMAXL, SAR, and GR.

For the 3D-Knee Mus. model, the hamstring and quadriceps muscles (see appendix F) were defined. To support the obtained outcome for the femoral principal stress, other stress characteristics of the femur include comparing maximum shear stress and compressive stress across all studies. In addition, to evaluate whether the obtained results provided adequate evidence to verify the main assumption of this study, other components of hip and knee joint were analysed during the gait, including deformation of the femur cartilage and normal stress of meniscus.

7.4.1 Effect of Muscle contraction on Femoral Principal Stress

Figure 7-10 compares the maximum principal stress of the femur for all various studies conducted via FEA method within the human normal walking. The obtained stress configuration of all FE models followed the characteristic of bodyweight during the gait, which is supported by most researchers (Bergmann et al., 2001; Chen et al., 2014; Damm et al., 2013; Debrunner, 1975; Kotzar et al., 1991; Pauwels, 1978; Paul, 1966; Schwachmeyer et al., 2013; Zhang et al., 2015, Bergmann et al., 2016; Ng et al., 2018).

As discussed previously, the maximum HCF due to bodyweight occurs at 18-30% and 50% of the gait, which can be interpreted as the single support and toe-off stance. The maximum obtained principal stresses for all studies significantly synchronised with the approved pattern of the bodyweight during the gait cycle. However, the intact lower limb body (model without any muscle contraction) demonstrated slightly different results in its 18% of the gait cycle. The maximum peak of femoral stress for the 3D-No Mus. model occurred at 50% rather than 18% of the stance, which was reported 11.80 and 9.67 MPa respectively.

Furthermore, it can be realised that the muscles contraction increased the principal stress from for 3D-No Mus. 9.67 MPa to 18.49 MPa for 3D-All Mus. model at single support stance of the gait.

On the other hand, within the toe-off stance of the gait, the maximum principal stress of the femur in skeletal model (i.e.3D-No Mus. model) was predicted at 11.80 MPa. Whereas, for 3D-All Mus. model which all muscles attached to the skeletal model, the principal stress was

estimated at 17.10 MPa. Hence, it can be concluded that the muscle contraction increased the femoral stress by 90% and, 30% within the single support and toe-off stance respectively.

Moreover, by detaching the number of muscles from 3D. All Mus. (i.e. musculoskeletal) model and making 3D-Hip Mus. model, the principal stress configuration reduced within the normal walking activity. In the hip muscle FE model, the hamstrings and quadriceps muscle groups (i.e. 8 muscles) detached from the skeletal and therefore the femur experienced 24% less stress in comparison to the musculoskeletal model. In addition, this maximum variation between All Mus. and Hip Mus. models observed at the end of the single support stance and before toe-off phase occurred.

The knee muscle model (i.e. 3D-Knee Mus.) was used to determine the effect of hamstring and quadriceps muscles on femoral principal stress, and was absent from the hip and groin muscles.

In this case, more than twelve muscles were detached from the musculoskeletal model to identify whether the obtained results from the previous studies were not achieved randomly.

It can be seen that by only considering the knee muscles group, the principal stress decreased by 175% approximately from the musculoskeletal model within the end of the swing phase of the targeted leg. (i.e. 80%) of the gait.

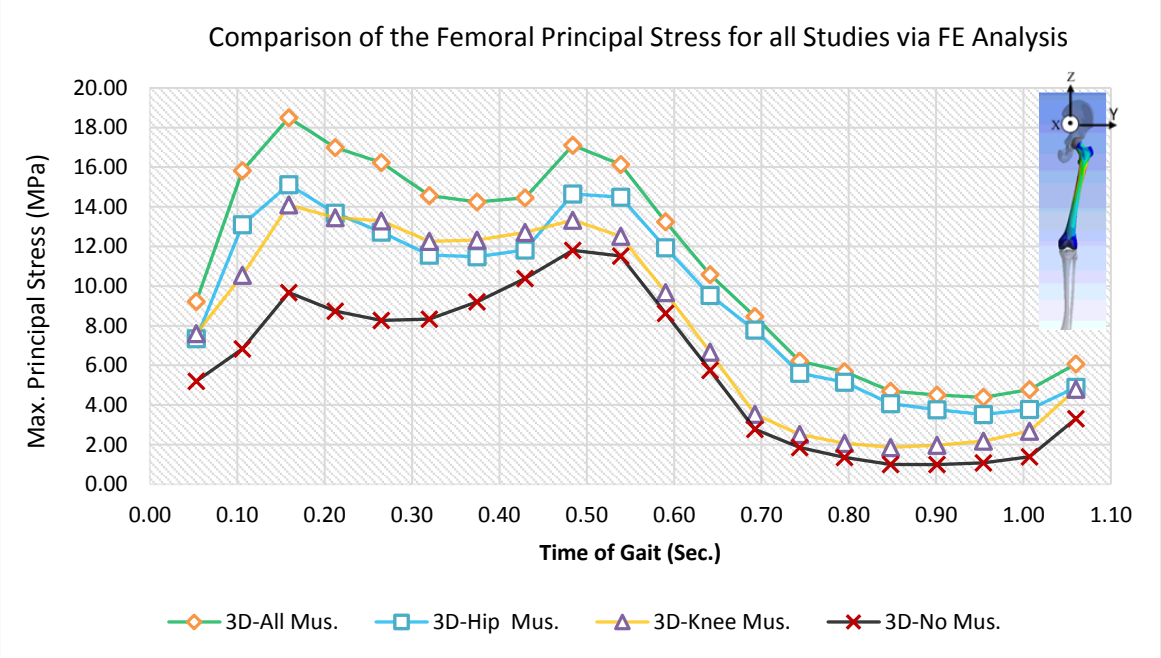

Figure 7-10: Effect of muscle contraction on magnitude of Max. Principal stress of femur for all numerical studies within the normal walking activity.

Another study was conducted to determine the amount of increasing stress at single support and toe-off stance of the gait as well as the maximum variation during the gait cycle. The relative study was conducted to show how detaching muscles from the virtual musculoskeletal model, reduced the amount of local stress during the gait cycle. In this study, the 3D- No Mus. model was used as a reference point (i.e. one) to which other studies were compare by using the fraction ($\frac{\text{Stress with muscle}}{\text{Stress without muscle}}$). The obtained values summarised in figure 7-11. It can be seen that the muscles contraction increased the maximum principal stress on the femur for all three studies including all muscles (All Mus.), hip muscles (H Mus.), and knee muscles (K Mus). The attached muscles to the skeletal model in 3D-All Mus. increased the maximum principal stress by 193% and 143% compared to 3D-No Mus. within the single support and pre-swing phase of the gait, respectively. In addition, the maximum principal stress at the heel strike stance increased from a minimum of 143% up to a maximum of 470% at the end of the gait within the swing phase of targeted leg.

The local stress on the femur due to the muscle's contraction for another two models (with the hip and knee muscles) was reduced relatively and presented the lower values because the number of attached muscles into the FE models was reduced as well

For instance, the attached hip muscles to the skeletal model in the 3D-H Mus. increased the maximum principal stress by 157% and 125% compared to the 3D-No Mus. within the single support and pre-swing phase of the gait, respectively. Furthermore, for the 3D-K. Mus. model the muscle contraction is increased the maximum principal stress by 150% and 111% compared to the 3D-No Mus. within the single support and pre-swing phase of the gait, respectively.

There is an abnormal reduction for the 3D-K. Mus. model at the end of the pre-swing phase (at 80% of gait), which is showing a significant reduction compared to the 3D-All Mus. and H Mus. models from 470% and 407% to 201% respectively. The main reason is, at the end of the swing phase (i.e. 80% of the gait), the limited number of muscles are activated around the knee, and therefore the stress locally induced to their attachment sites was reduced significantly.

Hence, the conducted FE analysis is demonstrated that the acquired outcomes are not achieved randomly and by reducing the number of attached muscles, the local stress on the femur was reduced as well. On the other hand, it can be concluded that the muscle attachment sites were increased the local maximum principal stress on the femur in comparison to the study without muscles during the normal walking activity.

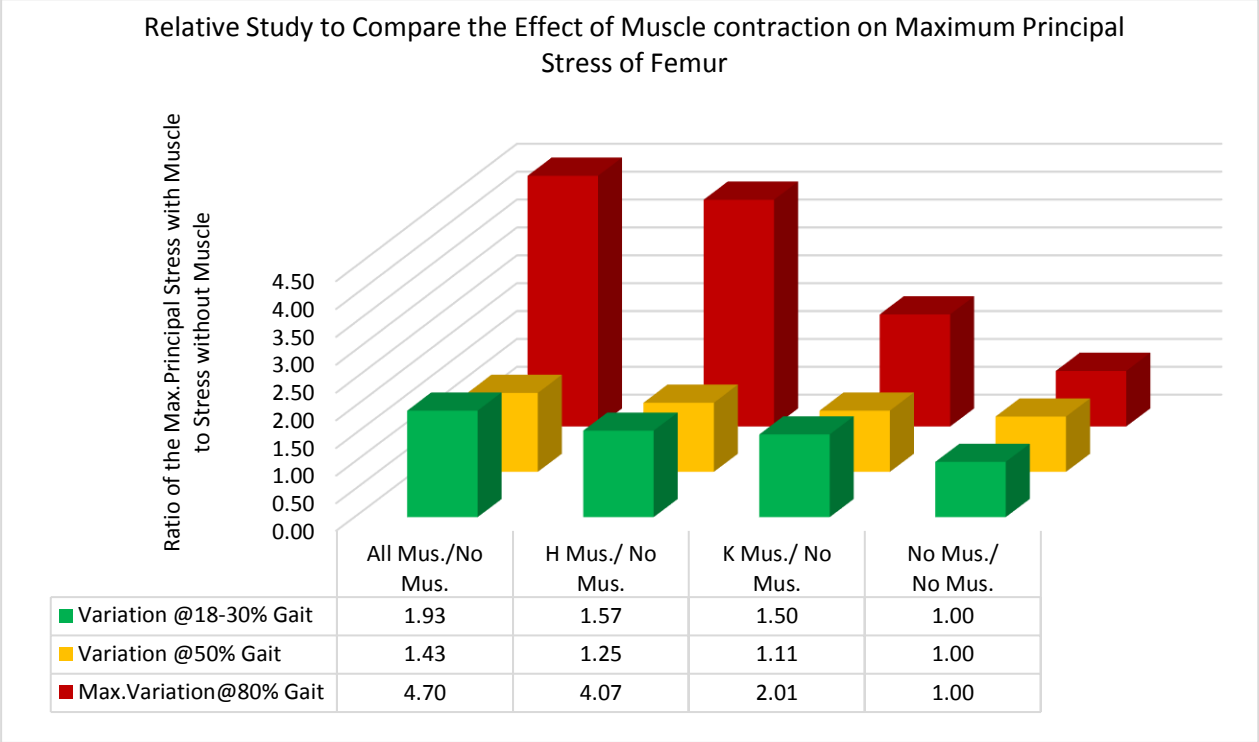

Figure 7-11: Comparison the effect of muscle contraction on the femoral Max. Principal stress within the normal walking activity. Dimensionless study conducted to comprehend the effect of muscles on stress.

7.4.2 Femoral Compressive and Shear stress

Figure 7-12 compares the maximum shear stress and normal stress (i.e. stress towards the inferior direction (-Z) or compressive stress) on the femur at single support stance. It can be realised that the same tendency observed in the previous section occurs when examining the principal stress. In 3D- All Mus. model, the shear and normal stress showing maximum values 6.91 and 16.30 MPa at single support stance of the gait respectively. While simplifying the FE models and neglecting the effect of muscles contraction (i.e. 3D-No Mus.) decreased the shear and normal stress 6.61 and 11.26 MPa respectively. Furthermore, it can be seen that the lack of hip muscle created greater shear stress in the femur in comparison to the knee muscle at the single support stance.

In figure 7-13, the relative study was conducted to demonstrate the effect muscle contraction on the shear stress and normal stress on the femur during the gait cycle. Two crucial stances of the gait were selected to compare the obtained results; these included the single support stance (i.e. 18% - 30%) and the pre-swing phase (50%) of the gait. Three defined studies with muscle contractions exhibited higher shear and normal stresses at all stances of the gait cycle, while the muscle contraction showed greater influence on the normal stress compared to the shear stress. In addition, the femur during single support stance experienced higher stress in

comparison to the toe-off. The maximum variation occurred at 80% of the gait when the targeted leg was positioned at the terminal swing phase. The main reason can be attributed to the loading conditions and femoral stress behaviour of 3D-No Mus study. In 3D-No Mus. model, no muscle contraction was considered in the skeletal model and therefore the HCF is subjected to the femoral head. The loading configuration of HCF demonstrated that the minimum force occurred when the targeted leg was located at the initial swing phase at 80% of the gait (Bergmann et al., 1993, 2001; Chen et al., 2014; Damm et al., 2013; Schwachmeyer et al., 2013; Zhang et al., 2015, Bergmann et al., 2016; Ng, et al., 2018). Hence, there was inadequate body-weight loading to create stress at the end of the gait and therefore the absolute value of the femoral stress significantly decreased at 80% of the gait onward. Therefore, the relative study between All-Mus. and No Mus. models presented a significant variation between two studies at 80% of the gait cycle.

Consequently, it can be acknowledged that the shear and normal stress configuration highly coordinated with the acquired outcomes of the principal stress and agreed with the main assumption of this study. It is observed that the muscles contraction increased the local stress on the femur from minimum 100% to maximum 418% depending on the type of stress and stance of the gait cycle.

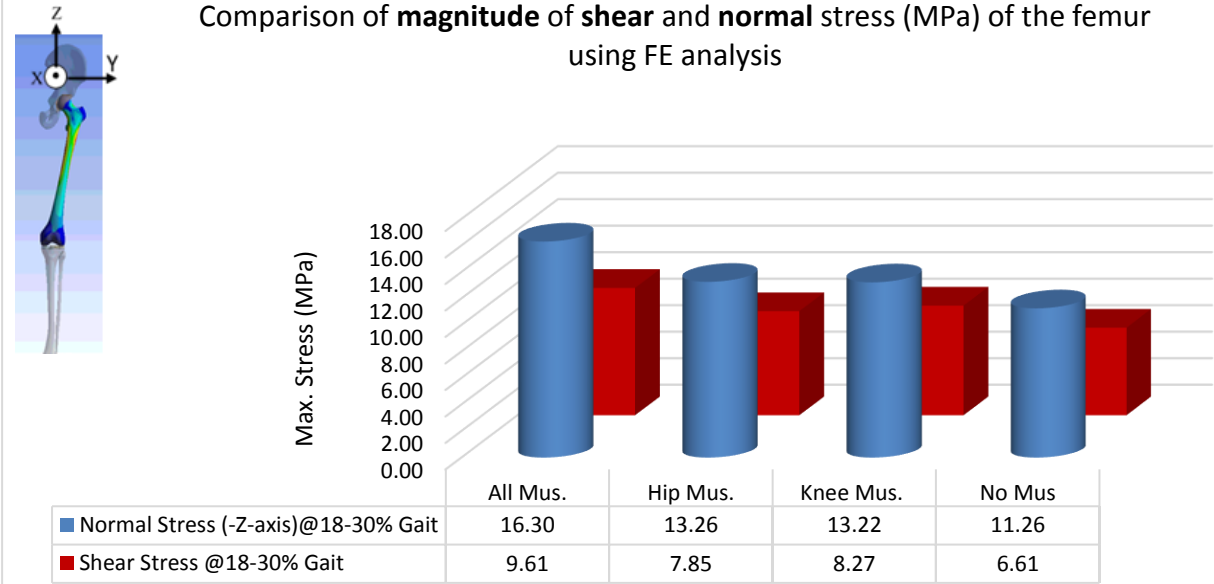

Figure 7-12: Effect of muscle contraction on Max. Normal stress and shear stress of the femur for all numerical studies within the normal walking activity.

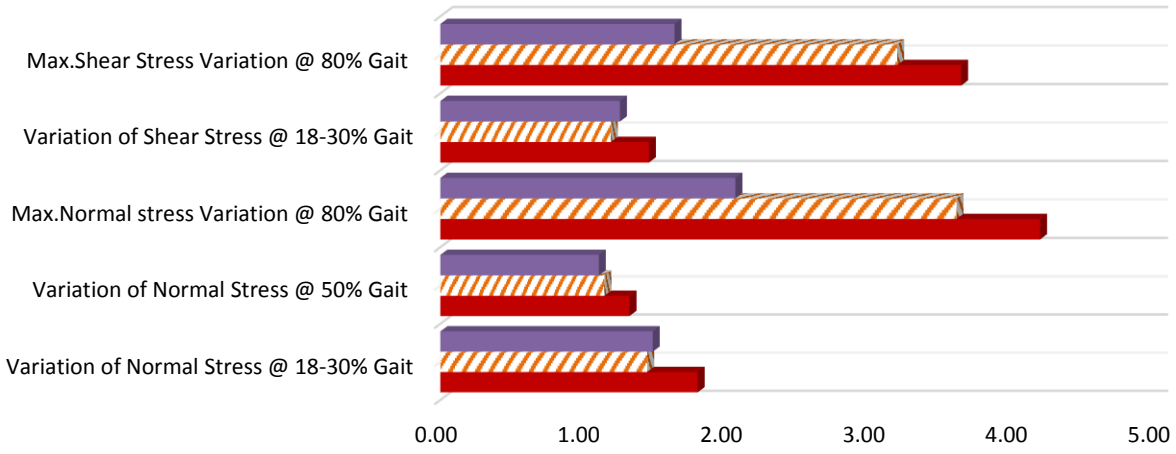

	Variation of Normal Stress @ 18-30% Gait	Variation of Normal Stress @ 50% Gait	Max.Normal stress Variation @ 80% Gait	Variation of Shear Stress @ 18-30% Gait	Max.Shear Stress Variation @ 80% Gait
Knee Mus./No Mus.	1.48	1.10	2.06	1.25	1.63
Hip Mus./No Mus.	1.44	1.14	3.60	1.19	3.19
All Mus./No Mus.	1.79	1.32	4.18	1.45	3.63

Figure 7-13: Comparison of the variation between the normal and shear stress on the femur (dimensionless study) within the gait cycle. The stress of 3D-No Mus. considered as a reference point and all other stress compared with this study.

7.5 Effect of Muscle contraction on Femoral Stress Distribution

Study and analysis of stress distribution and its configuration are important to identify the stress concentrations in the model and aim to mitigate or reduce the risk of injuries.

Figure 7-14 shows the principal stress distribution on the femur for all defined studies using numerical analysis at single support stance. For 3D-Mus. and 3D-H Mus. models, in which all the muscles and hip muscles are attached to the skeletal respectively, the amount of stress is distributed evenly on the shaft of femur. However, for the knee muscle study, which just considered the attachment of the hamstring and quadriceps muscles to the FE model, the stress concentration was observed on the diaphysis of the femur.

Furthermore, the maximum principal stress of 3D-No Mus. at 18-30% of the gait, was computed at 11.84 MPa, which was approximately 36% less than the 3D-All Mus., whilst two sites of stress concentrations were identified on the femoral diaphysis and neck for 3D-No Mus. model (see black and red circles in figure 7-13 (d)).

It was expected that by decreasing the stress magnitude in the 3D-No-Mus. model the stress distribution and configuration of the femur would enhance, whereas the obtained results (see figure 7-13 (d)) demonstrated two sites of stress concentration against the above-mentioned assumption. This rather contradictory observation could be attributed to the following assumption.

It was assumed that muscles contraction increased the magnitude of local stress on their attachment sites to the femur (see section 7-3). The existing muscles around the hip and knee joint may help to distribute the stress all over the musculoskeletal model uniformly and therefore eliminate the stress concentration positions. In this case, both contrary facts can be interpreted to support each other.

The above-mentioned hypothesis supported by several clinical researches (Scott & Winter,1990; Kim, et al., 1997; Donahue, 2001; Cattrysse, et al., 2002; Moncayo, et al., 2009 Liu, et al., 2011; Avin, et al., 2015).

Functionally, the absence of any muscle in lower extremities could affect the musculoskeletal manoeuvre and therefore the skeletal bone could not accomplish its function effectively. Hence, the lack of muscles may increase the stress concentration on the bone (Kim, et al., 1997; Cattrysse, et al., 2002; Moncayo, et al., 2009 Liu, et al., 2011).

For instance, Avin, et al., (2015) reviewed the biomechanics aspect of muscle-bone interaction to determine how the applied muscles force on the bone can be adapted by bone homeostasis. They stated that the relationship between the muscle attachment sites and bone generated motion through active contraction. In addition, they suggested that muscle function encourages the skeleton to adapt to loading conditions and mechanical stimuli as well as protecting the bone during the loading and reducing the chance of bone failure. The preceding studies and evidence supported Avin, et al.'s finding and the above-mentioned assumption for the stress configuration. Donahue, (2001) also stated that the risk of bone overloading injuries, such as fracture stress, is reduced by muscle protection and distributing the loading. Scott and winter (1990) conducted a study to predict the magnitude of the loading condition at injury sites during running. They stated that muscles are able to attenuate the applied shock and redistribute the transmitted load to the bone within the applied impact loading on the musculoskeletal model.

Confirming the obtained results in this study, Scott and Winter's results acknowledged that any dysfunctionality of muscles including weakening or fatigued may compromise the transmitted loading and increase the bone bending moment. In addition, Scott and Winter (1990)

commented that any muscle injuries (i.e. lack of muscle or dysfunctionality) can lead to interference in the loading distribution of the skeletal sites and restrict the skeletal mobility.

Cardiff, et al., (2013) conducted the numerical analysis to determine the stress magnitude on femur and femoral head cartilage by varying the cartilage thickness during the gait analysis. Three distinct stances of the gait including the heel strike, midstance, and toe-off were analysed separately. They observed the same phenomenon, which reduced the thickness of the cartilage (i.e. increasing the contact friction), therefore altering the stress distribution and creating local stress concentration sites. Furthermore, they stated that simulating the muscle contraction as point load rather than as a mapped technique changed the stress distribution and which may have created the local stress sites.

Although it might be concluded that the aforementioned hypothesis is proved, further discussion and analysis for AC and meniscus (see section 7.6 and 7.7) were conducted to collect more evidence whether the decreasing stress due to the lack of muscles contraction generates the stress concentration on the bone.

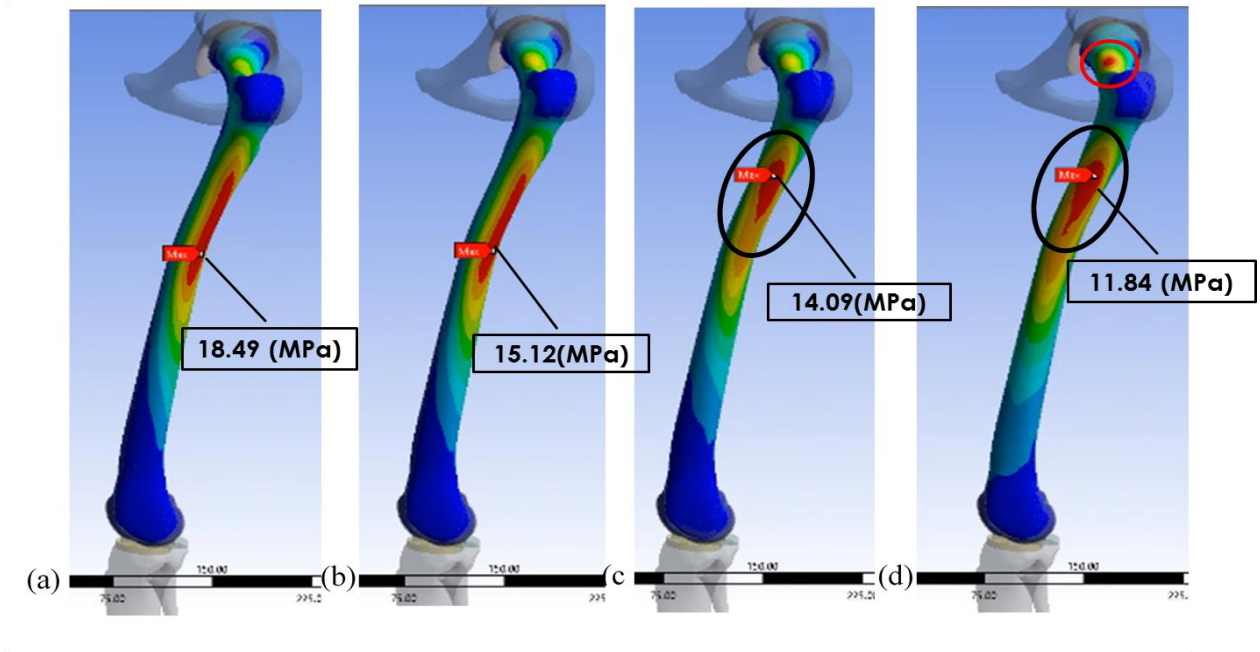

Figure 7-14: Effect of the muscle contraction on max. principal stress distribution for (a) 3D-All Mus.FEA, (b) 3D-Hip Mus.FEA, (c) 3D-Knee Mus.FEA, and (d) 3D-No Mus.FEA within the normal walking activity.

7.6 Effect of Muscle Contraction on Femoral Strain

The aim of this analysis was to examine the effect of the muscle contraction on femur strain during the gait via the numerical approach. Following this, the relative study was conducted to determine the maximum variation of femoral strain between all studies due to the muscle contraction during the gait cycle. In this dimensionless analysis, the strain of the 3D-No Mus. model was considered as the reference point (i.e.one) and all other studies were compared with this model. Figure 7-15 shows that by increasing the number of muscle attachment sites in the musculoskeletal model significantly increases the amount of maximum principal strain. In addition, it can be realised that the maximum difference between four studies predicted at the swing phase stance when the minimum portion of bodyweight acted on the swing leg.

By reviewing the absolute values of principal strain, it was identified that for three models, which the muscle contraction stimulated in the FE model, the femoral strain did not change significantly during the gait cycle. Whereas for the 3D-No Mus., model, the magnitude of strain decreased from 359.73με at 70 % of the gait to 68.5 με at 84% of the gait cycle. This is occurred because of the lack of any muscle contraction and reduction of the bodyweight at the end of gait cycle. Hence, the maximum variation between all studies occurred after 80% of the gait, when the bodyweight is at its minimum and no muscle contraction existed to stimulate the femur in 3D-No muscle Model. It was noted that the results obtained for strain behaviour were highly coordinated with the preceding acquired evidence from femur stress analysis (see figure 7-9).

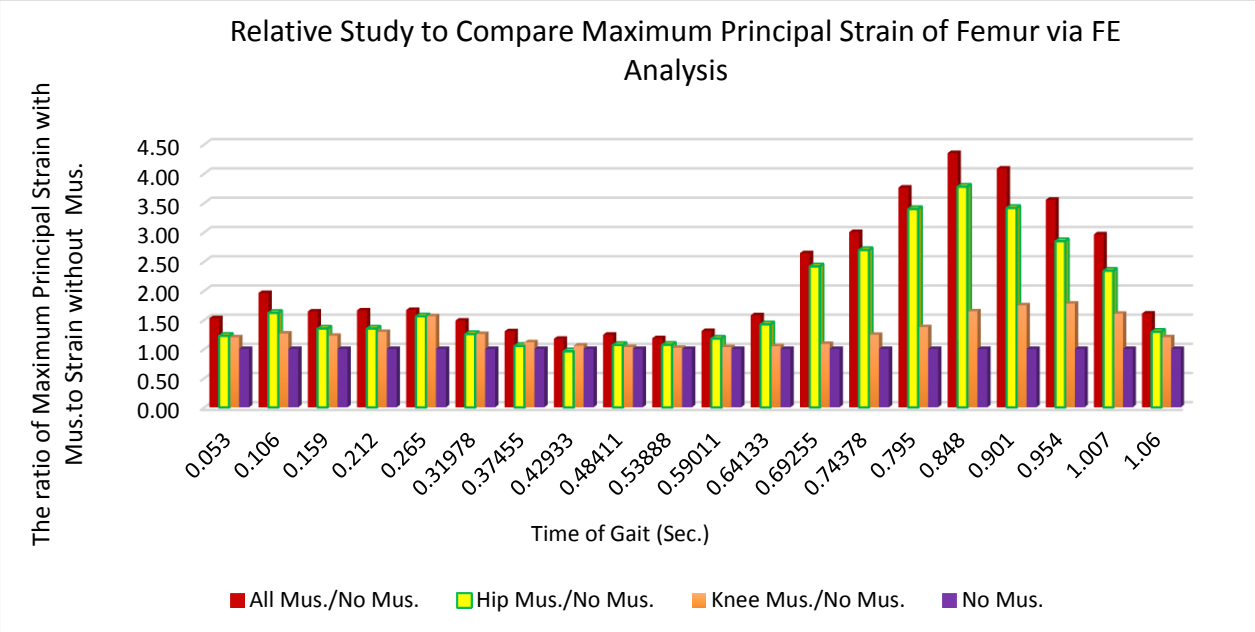

Figure 7-15: Effect of muscle contraction on femoral maximum principal strain via FE analysis within the normal walking activity. The strain of NO Mus. model considered as one.

7.7 Femoral Cartilage Deformation Analysis

In this section, the main assumption of the thesis was evaluated to examine whether muscle contraction had the same influence (as observed for the femoral stress and strain) on other compartments of the lower extremities within the gait.

Hence, the effect of muscle contraction on total deformation of articular cartilage was examined for all four studies via the numerical approach. The attained results of total deformation mm of femoral condyle cartilage known as 'Articular Cartilage (AC)' within the normal walking are presented in figure 7-16.

It can be seen that the full musculoskeletal model considering the muscles contraction (i.e.3D-All Mus.) showed maximum deformation 1 mm on the lateral side of the AC at single support stance. Whilst the maximum total deformation for skeletal model (i.e. 3D-No Mus.) predicted 0.01 mm during the pre-swing phase of the gait cycle. Furthermore, no considerable difference was observed for the AC deformation between 3D-All-Mus. and Knee Mus. models. In fact, the elimination of hip muscle contraction (i.e. nine muscle groups in this study) in 3D- knee Mus. model did not change the AC deformation significantly.

Conversely, by detaching the knee muscle groups (i.e. the hamstring and quadriceps muscles group) from 3D-All Mus. model, the total deformation decreased from 1 to 0.6 mm in the 3D-Hip Mus. The main reasons to justify the effect of muscles on AC deformation is associated with the location of AC and the position of hip and knee muscle attachments sites. The aforementioned AC deformations confirm that the knee muscles' group play a vital role in this region.

The knee muscles' group include the hamstring and quadriceps, which are located around the femoral AC and support the function of the knee joint and its locomotion. For 3D-Hip Mus., the effect of muscles around the knee joint are eliminated and only hip spanning muscles around the groin are simulated in this model. For this model, the hip muscles shifted up the lower extremities to the superior direction of the body and less AC deformation 0.6 mm occurred compared to the All Mus. (i.e. 1 mm) and Knee Mus. (i.e. 1.02 mm).

On the other hand, in the 3D-Knee Mus. model the knee muscles are attached to femur, patella, and tibia around the knee joint increased the total deformation of AC compared to the 3D-Hip Mus.(i.e. from 0.6 mm to 1 mm). Hence, it can be concluded that the total deformation of AC in 3D-knee Mus. model increased due to increasing the effect of muscles contraction and their attachment sites around the knee joint.

Liu et al., (2010) investigated the deformation of tibiofemoral cartilage within the gait using *in-vivo* method. They examined eight healthy participants without any history of knee injuries and reported maximum deformations (3.6 ± 0.3) and (1.6 ± 0.4) mm for the medial and lateral side of AC respectively. Conversely, Eckstein et al., (2005) examined ten healthy volunteers to determine deformation and strain on femoral condyle cartilage during the gait and other daily activity. They estimated AC deformation occurred between 0.5 and 1 mm for the medial and lateral side of AC respectively which strongly supports the outcome of this study in terms of magnitude and location of the maximum deformation.

Furthermore, Rakhsha et al., (2019) used the numerical method in a study to determine the surface deformation on AC. They simulated the knee joint compartment including the femur, the tibia, and the patella during the gait cycle. They predicted the maximum total deformation 1.1 mm on the medial side of the AC within the first peak of tibiofemoral loading. Their predicted results highly correlate with the results of this study without any significant differentiation in the magnitude of deformation and stance of the gait cycle.

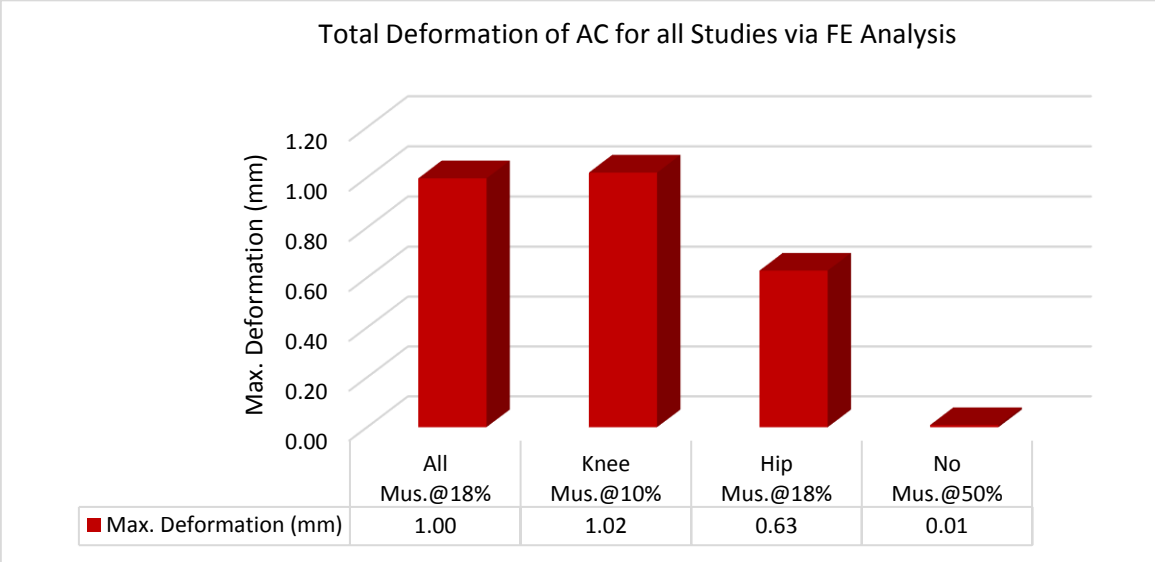

Figure 7-16: Effect of muscle contraction on the maximum total deformation of AC for all studies during the normal walking.

7.7.1 Effect of Muscle on AC Deformation Configuration

Another study was conducted to investigate the effect of muscles contraction on the configuration of AC deformation within the normal walking. Figure 7-17 (a), (b), (c) and (d) demonstrate the total deformation of AC for all FE models, including the study with all muscles, hip muscles, knee muscle, and no muscles.

It was identified that the muscles are able to distribute the maximum contact pressure throughout the surface area of the cartilage in the 3D-All Mus. and Knee Mus. models. Therefore, no distinct concentration sites were observed on the surface of AC in figure 7-17 (a) and (c). While, in the 3D-Hip Mus. model, by detaching the quadriceps and hamstring muscles from the FE model showed the maximum deformation concentrated on the medial and lateral sides of anterior direction.

In addition, by considering the skeletal model without any effect of muscles significantly reduced the maximum deformation (by approximately 100%). However, the configuration of deformation presented considerable concentration sites in anterior-lateral and posterior-medial of AC. Hence, the absence of knee muscles created the non-uniform deformation, which causing to increase the risk of wear -and- tear in articular cartilage in 3D-Hip Mus. and No Mus. models during the normal walking.

The concentration of deformation on restricted area of AC may affect the superficial and transitional zone of the chondrocyte section in femoral cartilage for a long period of walking. Øiestad, et al., (2015) examined 5707 participants including men and women via an experiment meta-analysis approach. They concluded that the weakness of knee extensor muscles (such as RF, VL, VMO, and VI) increased the risk of knee osteoarthritis. Their results matched the evidence acquired in this study, where the knee muscles were neglected in Hip Mus. and No Mus. models.

The preceding evidence from other researchers confirmed that the complex and non-uniform deformation in the AC field might affect the chondrocyte section of AC, its surface, and ultimately influence the joint loading response (Schinagl, et al., 1996; Chen, et al., 2001; Choi, et al., 2007; Bae, et al., 2006; Sanchez-Adams, et al., 2014).

Furthermore, Bennell et al., (2013) and Mikesky et al., (2000) conducted separate studies to examine the relationship between muscle strength, muscle dysfunction and knee articular osteoarthritis. Their results demonstrated that any muscle weakness and muscle dysfunction around the joint caused an atypical gait mechanic. They concluded that muscle weakness created a non-uniform loading condition and consequently increased the risk of wears-and-tear of the cartilage (Liu et al., 2014; Mills et al., 2013; Mundermann et al., 2005).

Finally, the results for deformation configuration supported the evidence obtained from the effect of muscles contraction in stress distribution of femur (see figure 7-14).

It was observed that by considering the muscle contact force, the deformation concentration on AC and the risk of AC osteoarthritis were lowered. Nevertheless, another study was conducted

to examine the effect of muscles on stress configuration of meniscus due to obtaining more evidence about the aforementioned assumption.

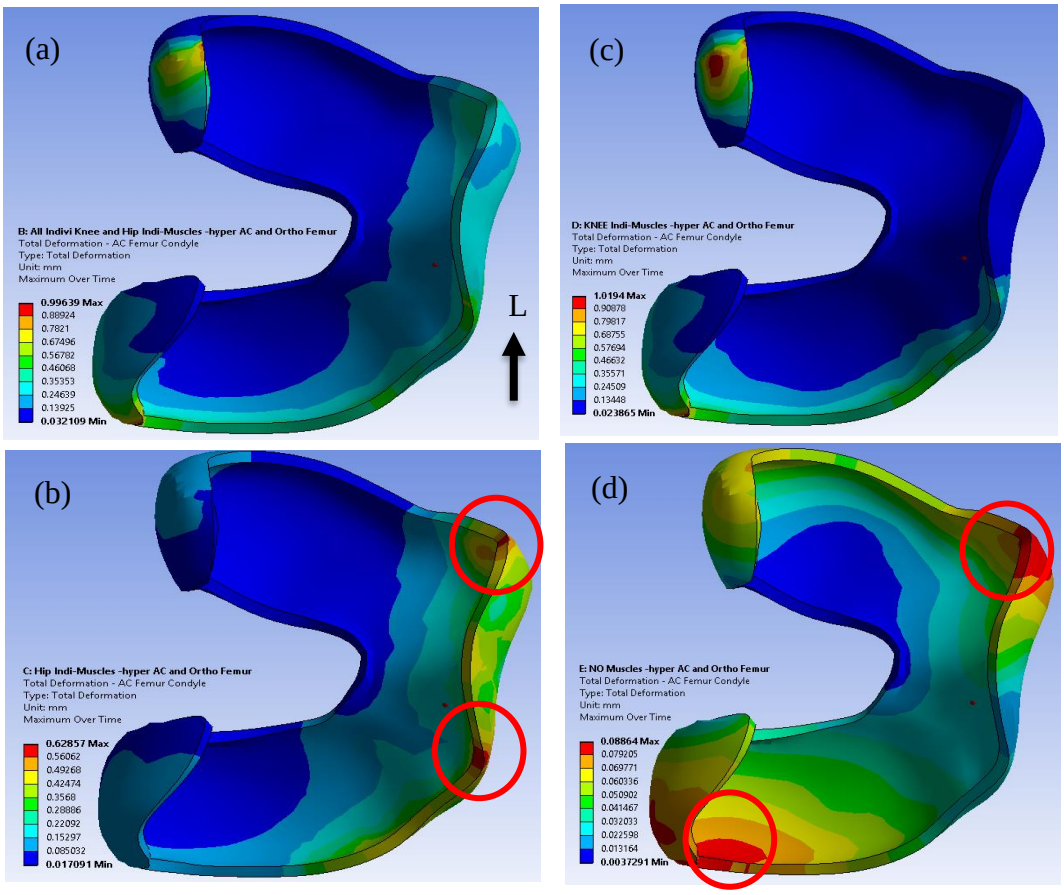

Figure 7-17: Effect of muscles contraction on the total deformation configuration of femur condyle articular cartilage for (a) 3D-All Mus.FEA, (b) 3D-Hip Mus.FEA, (c) 3D-Knee Mus.FEA, and (d) 3D-No Mus.FEA. Circle red lines show the concentration sites and black arrow shows the lateral side of body.

7.8 Stress Analysis of Meniscus

In this section, the stress magnitude and distrubution of the meniscus was used to determine the effect of muscles contraction and their contraction via numerical approach. The selected maximum shear, compressive, and principal stress were compared with the four FE models in this analysis and results are summarised in figure 7-18.

It can be realised that the maximum shear stress across three studies including All Mus., Hip Mus., and Knee Mus. decreased steadily without any significant of variation. However, the shear stress of the intact skeletal model (i.e. No Mus. study) reduced considerably.

A similar tendency is observed for all other types of stress, in which the FE model without considering muscle contraction (i.e. No Mus. Model) experienced less localised stress due to eliminating the muscle attachment sites from the lower extremities. The results obtained in this

work also ascertained the main assumption of the thesis whereby muscle contraction increases the local stress magnitude within the normal walking activity. It was predominantly expected that the 3D-All Mus. model demonstrated the highest stress compared to the 3D-Knee Mus. model due to attaching more muscles in All Mus study. However, the maximum compressive and principal stresses on the meniscus that were observed in the 3D-knee Mus. model are reported at 3.52 and 4.01 MPa respectively (see figure7-18).

The main reason for justifying the stress behaviour of the meniscus associated with the location of the meniscus and attachment sites of the knee muscle groups was due to the presence of hamstring and quadriceps muscles. These muscles created higher local stress level to the knee joint components (like AC and meniscus) in comparison to the hip muscles, which are spanning around the hip joint. Hence, the effect of knee muscles contraction on stress magnitude of the meniscus is higher than the influence of hip muscles contact force.

An identical phenomenon was observed in section 7.7.1, where the AC demonstrated greater deformation due to the knee muscles contraction in comparison to the hip or all muscles models. In addition, it can be assumed that for 3D-All. Mus study, in which all muscles contraction contributed to the musculoskeletal model, the effect of the knee muscle was slightly counteracted by the hip muscles and which resulted in the lower extremities to balance in their natural position. This meant that the meniscus and other knee joint compartments were subjected to reduced stress levels. The small variation (i.e. 26% to 18%) between the maximum stresses of 3D-All. Mus. and Knee Mus. models supported by the above-mentioned assumption.

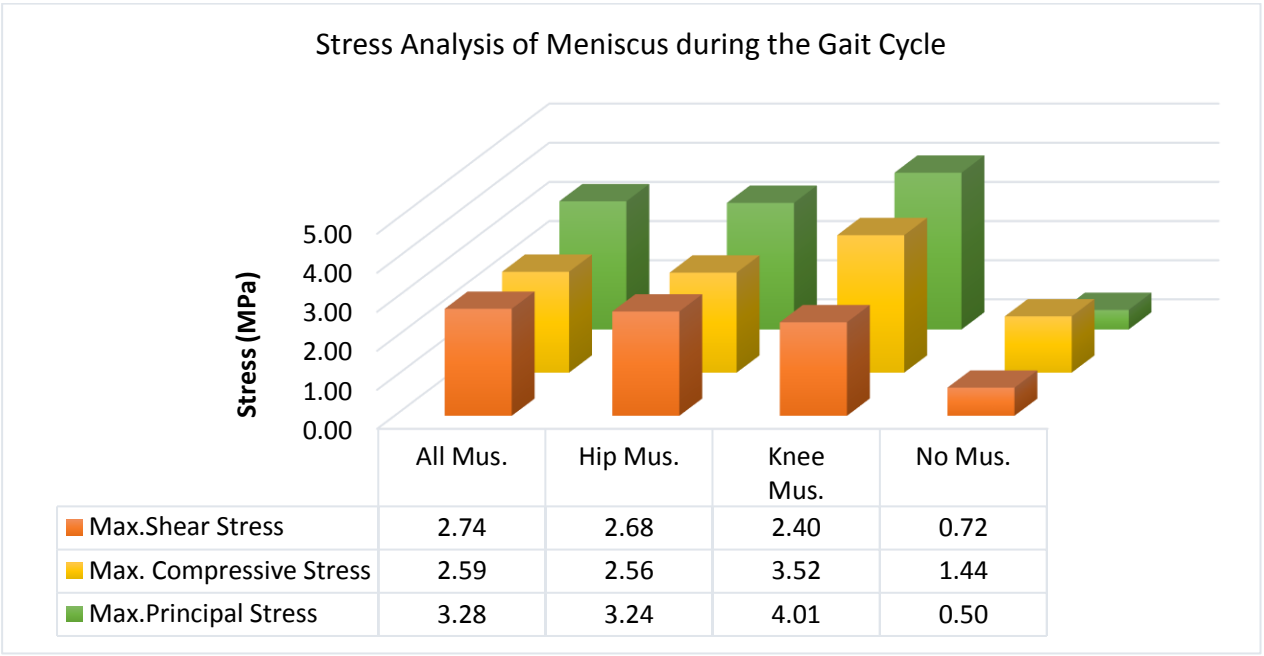

	All Mus.	Hip Mus.	Knee Mus.	No Mus.
Max.Shear Stress	2.74	2.68	2.40	0.72
Max. Compressive Stress	2.59	2.56	3.52	1.44
Max.Principal Stress	3.28	3.24	4.01	0.50

Figure 7-18: Effect of muscles contraction on stress magnitude of meniscus for all studies via numerical method.

Bendjaballah, et al., (1995) conducted a numerical study to analyse the compressive stress and contact pressure on the AC and meniscus for the healthy knee joint. They applied a static load with a magnitude of 1300 N over the femur head and estimated the compressive stress of 4 MPa for the meniscus. Donahue, et al., (2002) achieved the similar results via conducting the experimental tests on healthy knee joint. They reported a maximum stress of 3.46 MPa on the medial side of meniscus. Consistent with the obtained results of this study in 3D- knee Mus. model, Peña, et al., (2005) reported the maximum compression stress -3.82 MPa in the lateral side of meniscus using finite element analysis and experimental studies.

Furthermore, Dong, et al., (2014) conducted a FE study to analyse the biomechanical mechanism of meniscus and cartilage using finite element analysis. They assigned a transversely elastic isotropic material for the meniscus under single-leg stance loading statically. They predicted maximum compressive stress to be 3 MPa. Their obtained results highly coordinated with the maximum compressive stress of the current study (2.59 MPa) with 15% variation, which can be attributed to the various loading conditions and alternative materials that were assigned in each study. Figure 7-19 (a), (b), (c), and (d) show the distribution of compressive stress on the meniscus for 3D-All Mus., Hip Mus., Knee Mus., and 3D –No Mus. models respectively.

It can be realised that by decreasing the stress magnitude from the 3D-All Mus. to Hip Mus. and Knee Mus., the stress distribution was not changed significantly and therefore no stress concentration site can be seen. However, with respect to obtaining the highest stress in the Knee Mus. model, the entire surface of meniscus subjected to the compressive stress (See 7-18 (C)).

On the other hand, in 3D-No Mus. model, despite significant stress reduction in comparison to the 3D-All Mus., two-stress concentration sites (red circles) were observed on the medial and lateral meniscus. This phenomenon has been observed for the femoral stress distribution and AC deformation configurations in section 7-5 and 7-7 respectively. The main reasons and associated justification of assumptions were comprehensively reviewed. It can be acknowledged that the effect of muscle contraction significantly reduced the risk of stress concentration sites by redistributing the stress on all surface of the meniscus.

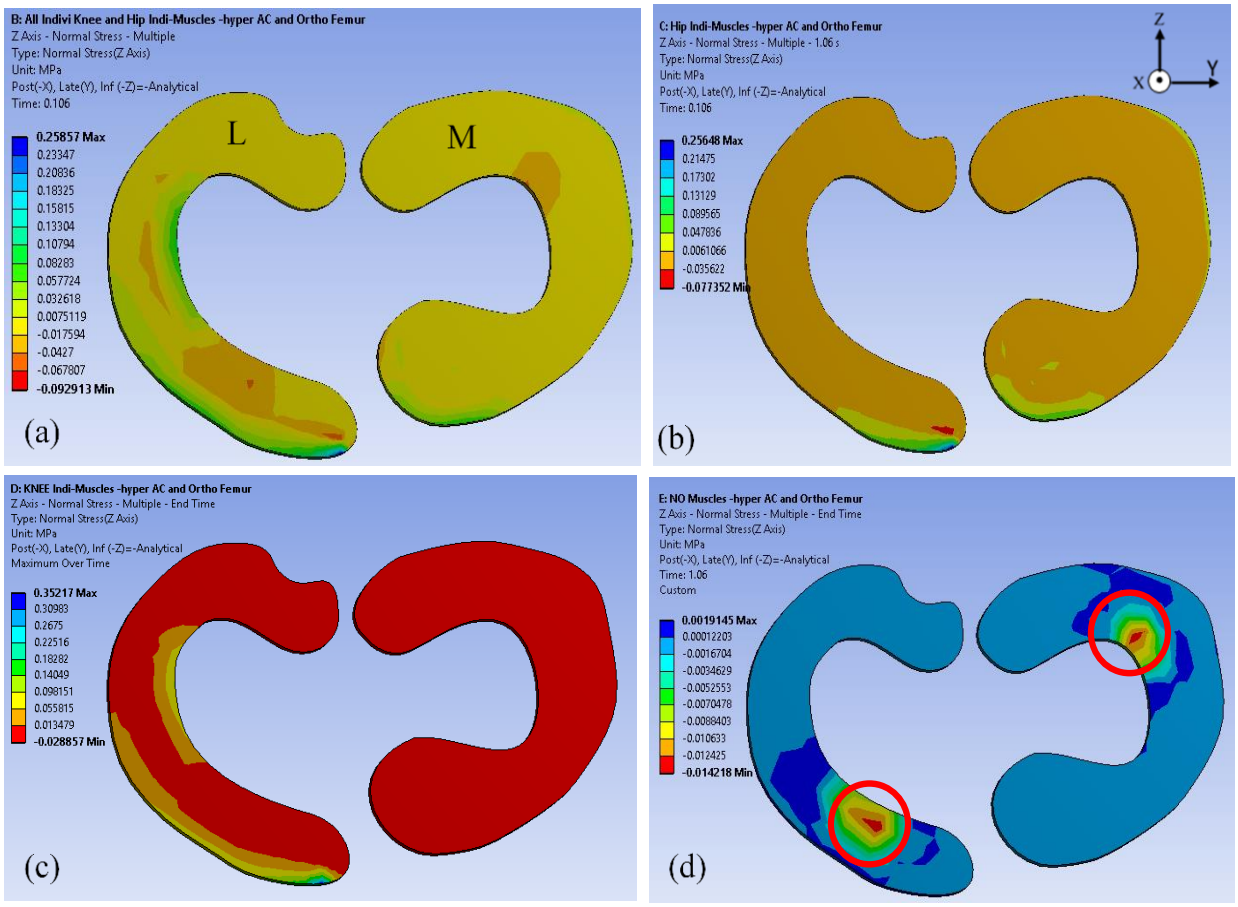

Figure 7-19: The superior view of the distribution of normal stress (towards inferior direction of the body) on the meniscus for (a) 3D-Mus.FEA, (b) 3D-H Mus.FEA, (c) 3D-K Mus.FEA, and (d) 3D-No Mus.FEA. The red circle showing stress concentration.

7.9 Concluding Remarks

Figure 7-20 compares the obtained results of the femoral stress analysis through use of analytical and numerical approaches for the simple support and pre-swing phase of the gait. In this study, the maximum normal and shear stresses of the skeletal model without considering muscle contraction (i.e. 3D-No Mus.) were considered as a reference point. The obtained stress from the musculoskeletal model (i.e. 3D-All Mus.) was reported as a percentage of a ratio by using of the simple fraction $\left(\frac{\textbf{Stree With Muscle}}{\textbf{Stree Without Muscle}}\right)$. It can be seen that the numerical and analytical methods predicted a very similar normal stress ratio (i.e. 1.93 and 1.92) to present the effect of the muscle contraction on the whole femur at the single support stance. While, at the pre-swing phase of the gait cycle, the normal stress was predicted by the analytical method is 30% greater than the normal stress, which was estimated by FE analysis for the whole femur. Furthermore, for the femoral shear stress, the analytical method predicted greater values in comparison to the numerical method at the single support stance and pre-swing phase of the gait cycle. The effect of muscle contraction on the shear stress of the musculoskeletal model was estimated on the

average ratio of 1.96, while the FE approach predicted the shear stress of the femur on the average ratio of 1.45. It can be realised that the FE analysis estimated the average of shear stress 35% less than the value obtained from the analytical method at a single support stance. In addition, a maximum variation of 68% between the numerical and analytical methods was observed on the femoral shear stress at the pre-swing phase of the gait cycle. It was realised that the analytical analysis predicted the average of the femoral shear force ratio 1.78 for the musculoskeletal model, whereas the numerical method estimated the value of 1.05.

Overall, the estimated stress using the analytical method was greater than the FE analysis due to the solver equation used in FEA software. The solver uses certain assumptions, including the convergence of the force-displacement iterations, in order to reduce associated computational costs. In addition, the analytical approach only predicted the stress on three susceptible regions of the femur and the average of three regions used to develop the comparison analysis between the two selected methods, therefore the predicted stress might not show the realistic estimation of the stress on femur in the analytical approach. However, it was observed that using both methods the muscle contraction increased the stress on the femur for both shear and normal stresses, which acknowledged the main assumption of this study.

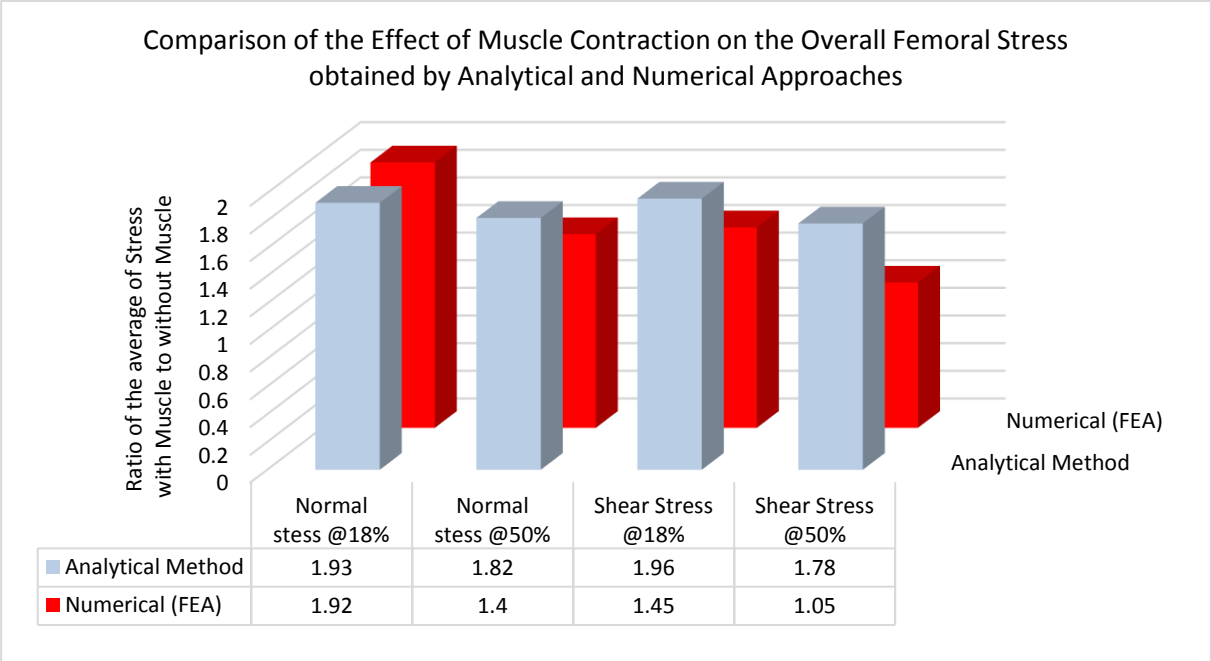

Figure 7-20: Relative study to compare the effect of muscle contraction on the normal and shear stresses of the femur using the analytical and numerical approaches. The stress of skeletal model (a model without any muscle) has been considered as a reference point.

Chapter 8

Summary and conclusion

8.1 Summary

In this thesis, two possible research methodologies including numerical and analytical approaches were selected to achieve the main purpose of the research. The literature review of this study presented comprehensive knowledge of the anatomy of human lower extremities, their functions, and structures. The coordinate system of the activated muscles was analysed and reviewed to define muscle origins and insertion during the gait cycle. Although muscle contraction and bodyweight configuration during normal walking were not acquired experimentally, authentic data sources were selected to acquire the reliable input for the analytical and FE analyses.

This study presented an analytical method by applying the equilibrium static equation in 2D and 3D environments, to determine the hip contact force (HCF) during normal walking activity. The outstanding achievements noted in Chapter 4 include determining the role of muscle contraction on the magnitude of HCF within the single support stance of the gait cycle. Another significant achievement was accomplished by using equilibrium static equations in 2D and 3D to predict HCF in the hyperextension position of the femur at 50% of the gait, which has not been observed previously.

Despite applying a restricted number of muscle groups for predicting the HCF using the analytical method, the obtained results highly matched with the range of reported HCF in other studies (See section 4.6.1, figure 4-13).

Furthermore, another research study was conducted to generate the infinitesimal planes for three susceptible regions of the femur. This aimed to express the relationship between the femoral cross-section areas at any distance, from the top of the femoral head as a reference point. Three governing equations for the susceptible sections of the femur facilitated the prediction of local stress analysis using a simple analytical paradigm. The error analysis, including root means squared error (RMSE) and R-squared, demonstrated that the governed equations generated a reliable set of data and information (See Appendix D).

A unique CAD model included seven major hip and knee joint components and 19 muscle groups were employed. This CAD model was obtained from the lower extremities of a healthy volunteer, using both CT scan and MRI. Furthermore, contact region and loading condition were defined based on the quasi-dynamic and non-linearity assumptions.

The orthotropic mechanical properties were assigned to the material properties of the tibia, menisci and femur. While, the material properties of the soft tissues in the cartilage were considered as homogenised isotropic properties.

The Newton-Raphson method was employed via ANSYS software (R18.1) to accomplish the nonlinear finite elements analysis of defined models. Four FE models (i.e. 3D-All Mus, Hip Mus., Knee Mus, and 3D-No Mus.) were defined in order to avoid obtaining random results via FE analysis. A comparative inter-study was conducted to verify the predicted femoral stress, strain, and deformation for the musculoskeletal model (i.e. 3D-All Mus.). The obtained results via FE analysis significantly improved the outcomes of existing research.

8.2 Conclusion

The main purpose of the thesis was to determine the effect of the muscle contraction (i.e. muscle contraction) on stress behaviour of the lower extremities. This work highlighted the following conclusions:

8.2.1 HCF Analysis

- The predicted hip contact force (HCF) at single support stance was higher than pre-swing phase in both 2D and 3D studies via analytical approach. The obtained HCF was highly coordinated with the preceding HCF from the other researchers.
- The effect of muscle contraction in the musculoskeletal (i.e. 3D-All Mus) model significantly increased the amount of HCF (230%), compared to using the skeletal model (i.e. 3D No Mus.) via analytical model.
- The predicted HCF via equilibrium static equations showed no considerable variation between 2D and 3D studies.

8.2.2 Stress Analysis by Numerical Approach

- During the single support stance, muscle contraction in a human musculoskeletal (i.e. 3D-All Mus) model increased the normal and shear stress on the femoral head on average by 230%, compared to the skeletal model (i.e. 3D-No Mus.)

- Within the pre-swing phase of the gait, muscle contraction in the 3D-All Mus. increased the **shear stress** on the **femoral head** region on average of 215%, compared to the shear stress in the skeletal model (i.e. 3D-No Mus).
- The effect of muscle contraction on the normal stress magnitude of the neck confirmed the acquired stress analysis for the femoral head. A considerable increase was observed (on average 192% at a single support stance and 216% at the pre-swing phase) between 3D-All Mus. and No Mus. models, using the analytical approach.
- The muscle contraction in the 3D-All Mus. increased the **shear stress** on the **femoral neck** region at a single support stance and pre-swing phase of the gait cycle on average of 228% and 218% respectively, compared to the shear stress in the skeletal model (i.e. 3D-No Mus).
- During the single support stance, muscle contraction in a human musculoskeletal (i.e. 3D-All Mus) model increased the normal and shear stress on the **femoral diaphysis** on average by 229% and 236% respectively, compared to the skeletal model (i.e. 3D-No Mus).
- Within the pre-swing phase of the gait cycle, muscle contraction in a human musculoskeletal (i.e. 3D-All Mus) model increased the normal and shear stress on the **femoral diaphysis** on average by 236% and 218% respectively, compared to the skeletal model (i.e. 3D-No Mus).

8.2.3 Analysis by Numerical Approach

- The results obtained from the strain analysis confirmed that the femur endured more loading without showing deformation or strain within the gait cycle. However, due to the porous-viscoelastic properties of cartilage, it experienced significant strain during the gait.
- The applied stress to the muscle attachment sites (including muscle origin and insertion) predicted by FE analysis during the human gait cycle. The presented results that were considered are a novel contribution to this study (see section 7-3). It was concluded that the gluteus medius and biceps femoris muscle groups applied the maximum stress on their attachment sites; however, the gracilis and vastus medialis applied minimum stress to their connection sites.

- The effect of muscle contraction on the maximum principal stress on the femur demonstrated that muscle contraction considerably increased the magnitude of principal stress (190% and 143%) at single support and pre-swing phase of the gait, respectively.
- It was observed that the muscle contraction created a significant increase (470%) in femoral principal stress within the swing phase at the end of gait.
- The effect of muscles contraction on total deformation of femoral condyle articular cartilage (i.e. AC) was analysed. It was observed that the muscle contraction significantly maximised AC deformation (from 0.01 to 1 mm) by increasing the number of muscles in the musculoskeletal model.
- The principal, shear, and compressive stress of the meniscus demonstrated that the knee muscle groups significantly increased stress magnitude, compared to the model that did not consider muscles (i.e. maximum 800% increase observed for the principal stress).
- The femoral stress distribution demonstrated that by excluding the muscle contraction from the FE model, the risk of stress concentration on the neck and diaphysis of the femur is increased.
- The stress distribution of meniscus showed that by excluding muscle contraction from the FE model, the risk of stress concentration increased, which confirmed the observed phenomenon of the femoral principal stress.
- The deformation configuration of the AC showed that by excluding the effect of muscles in the skeletal model, the risk of strain concentration increased significantly.
- The predicted values using numerical and analytical methods presented highly similar results including the normal stress ratio on the femur (i.e. 1.93 and 1.92 respectively) to present the effect of the muscle contraction at the single support stance.
- Within the pre-swing phase of the gait cycle, the **femoral normal stress** was predicted by the analytical method is 30% greater than the normal stress, which was estimated by FE analysis.
- Within the pre-swing phase of the gait cycle, maximum deviance of 68% was observed for the femoral shear stress estimated by numerical and analytical approaches.

8.3 The main contributions to the knowledge

The advantage of estimating the effect of muscle contractions on femoral stress is not only crucial for scientific purposes but can be applied to other clinical complications such as total

hip replacements and physiotherapy treatment. The results obtained from this study create a new paradigm for understanding the effect of muscles in femoral stress responses in a musculoskeletal model undertaking normal walking activity. The main contributions to existing research are as follows:

- Contrary to the common assumption, an outstanding contribution of this study indicates that muscle contraction increases the femoral principal stress response by 190% and 143% within the normal walking activity (thereby covering the first research objective).
- The applied research methodologies acknowledged the consideration of muscle contraction in redistributing stress configurations on the femoral surface to eliminate stress concentration sites. Further evidence and analysis accredited the observed phenomenon for the meniscus and femur condyle articular cartilage (thereby covering the first research objective).
- The data obtained from muscular stress on the muscle attachment sites (see section 7.3) demonstrated that muscle contraction significantly increased local stress on the attachment sites as well as the overall stress magnitude in the lower extremities (thereby covering the second research objective).
- The present study provided adequate evidence for developing an assumption for the stress response of soft tissue in a knee joint, such as menisci and articular cartilage.
  The maximum principal and shear stress of the meniscus significantly increased (by a maximum of 800% and 330%, respectively) when considering the effect of muscle contraction in the skeletal model (thereby covering the third research objective).
- Another important contribution of this thesis was the determination of the effect of muscle contraction in HCF via an equilibrium static equation (2D and 3D) in a single support stance and the pre-swing phase of the gait cycle. It was observed that a lack of muscles generated the stress concentration sites on the femur and increased the magnitude of principal stress by 192%. Implant design and the implementation of hip and knee arthroplasty can be improved considering the areas associated with the femoral stress concentration and the realistic value of local femoral stresses.

8.4 Limitations and future work

A crucial limitation of this study was the number of simulated muscles in the lower limb for both analytical and numerical approaches. For analytical analysis, 13 muscle groups were considered for both single support and mid-stance of the gait cycle. For the FE analysis, the

impact of 19 muscle groups were simulated, which were primarily activated during the stance phase of gait, when the loading condition reached a maximum.

Adding more muscles can improve the level of accuracy in the stress analysis; however, this can create a very complicated loading condition, and increase the cost of the FE and analytical analyses.

Hip contact force was predicted by static equilibrium equations at single support and toe-off stances to determine the effect of muscle contraction; however, the values of HCF for femur flexion and hyper-flexion were neglected. The main reason for this was attributed to the magnitude of HCF at femoral flexion. This value did not change the maximum shear and normal stress, and did not affect the outcome of the thesis.

The assigned materials that were assigned for cartilage were homogenous and isotropic to decreasing the complexity level of the FE model. While the pro-viscoelasticity and biphasic materials mostly applied for the cartilages. Hence, further investigation is required to address this concern, and can be recommended as possible future work. Due to the aim of this thesis, no attempts were made to determine the stress characteristics of the tibia and pelvic bone with respect to examining the effect of muscle contraction, which can also be recommended as future work. The devolved analytical model and method for predicting the HCF included some assumptions for simplifying the hyperstatic condition.

The knee reaction force, obtained from an authentic source of data reported range of 2.4 to 3.1×BW, depended on the loading and boundary conditions, and the measurement technique used. To avoid achieving any preferred results, the average of 2.75 ×BW was considered. The calculation steps of the analytical approach were examined several times to reduce the chance of any error occurrence. The source of errors for obtained bodyweight and muscles contraction were not specified by the selected reference and researchers. However, the maximum error for reported numbers in FE analysis and the analytical method can be estimated as roughly 0.001 (m), as it relates to the digits presented in millimetres throughout this study.

Reference

Ackerman, M. (1991). The visible human project. Biocommunication, 18, p.14.

Adouni, M., Shirazi-Adl, A. & Shirazi , R., 2012. Computational biodynamics of human knee joint in gait: From muscle forces to cartilage stresses. Journal of Biomechanics, Volume 45, pp. 2149–2156.

Ackerman, I.N., Bohensky, M.A., Zomer, E. et al., 2019. The projected burden of primary total knee and hip replacement for osteoarthritis in Australia to the year 2030. BMC Musculoskelet Disord 20, 90 (2019). https://doi.org/10.1186/s12891-019-2411-9

Alexander. N., Schwameder, H., 2016. Lower limb joint forces during walking on the level and slopes at different inclinations Gait Post., 45, pp. 137-142

An, K. N., Tankakashi, K., Harrigan, T. P. and Chao, E. Y.,1984. "Determination of the Muscle Orientation and Moment Arms." Journal of Biomechanical Engineering 106(3), pp, 280-282.

An, Y. H. and Draughn, R. A. 2000. Mechanical Testing of Bone and the Bone-Implant Interface, CRC Press LLC.

Andersen, M. S., Damsgaard, M. and Rasmussen, J., 2009. "Kinematic Analysis of over-Determinate Biomechanical Systems." Computer Methods in Biomechanics and Biomedical Engineering 12(4), pp, 371-384.

Anderson, A. E., Ellis, B. J., Maas, S. A., and Weiss. J. A., 2010. Effects of idealized joint geometry on finite element predictions of cartilage contact stresses in the hip. Journal of Biomechanics, 43:1351-7.

Anderson, F. & Pandy, M., 2001. Dynamic optimisation of human walking. Journal of Biomechanical Engineering, Volume 123, pp. 381–390.

Anderson, J. E., 1978. Grant's Atlas of Anatomy, 7th ed. Williams & Wilkins, Baltimore, MD.

Anderson. J.D. 1995.Computational fluid dynamics: an introduction. Springer.

AOANJRR, 2016. Australian Orthopaedic Association National Joint Replacement Registry. [Online] Available at: https://aoanjrr.sahmri.com/documents/10180/275066/Hip%2C%20Knee%20%26%20Shoulder%20Arthroplasty. [Accessed 15 August 2018].

Archip, N., Clatz, O., Fedorov, A., Kot, A., Whalen, S., Kacher, D., et al. (2007). Non-rigid alignment of preoperative MRI, fMRI, dt-MRI, with intra-operative MRI for enhanced visualization and navigation in image-guided neurosurgery. Neuroimage 35, 609–624. doi: 10.1016/j.neuroimage.2006.11.060

Arnold, M. and Delph, Scott L. 2011. Fibre operating lengths of human lower limb muscles during walking. 366. Phil. Trans. R. Soc. B., pp. 1530–1539, https://doi.org/10.1098/rstb.2010.0345.Available at: http://www.njrreports.org.uk/Portals/0/PDFdownloads/NJR%2014th%20Annual%20Report%202017.pdf. [Accessed 15 August 2018].

Available at: https://registercentrum.blob.core.windows.net/shpr/r/Annual-report-2013-HJnnK8Tie.pdf [Accessed 15 August 2018].

Avin, K. G., Bloomfield, S. A., Gross, T. S., & Warden, S. J. (2015). Biomechanical aspects of the muscle-bone interaction. Current osteoporosis reports, 13(1), 1–8. doi:10.1007/s11914-014-0244-x

Bachtar, F., Chen, X., and Hisada, T., 2006. Finite element contact analysis of the hip Joint. Medical & biological engineering & computing, 44, pp, 643-651.

Bae, WC., Lewis, CW., Levenston, ME., 2006. Indentation testing of human articular cartilage: effects of probe tip geometry and indentation depth on intra-tissue strain. J Biomech. pp; 39(6):1039–47.

Barclay, T. & Curreli, S., 2015. Gracilis Muscle. [Online].Available at: https://www.innerbody.com/image_musfov/musc67-new.html. [Accessed 31 July 2019].

Barnett, S., 1992. Hermite's Method of Separation of Solutions of Systems of Algebraic Equations and its Applications. Linear Algebra and its Applications, Elsevier Science Publishing Co., Volume 177, pp. 49-88.

Barsoum, W. K., Patterson, R. W., Higuera, C., Klika, A. K., Krebs, V. E., and Molloy, R., 2007. A computer model of the position of the combined component in the prevention of impingement in total hip replacement. The Journal of Bone & Joint Surgery, 89. pp, 839-845.

Basicmedicalkey, 2016. Lower Limb. [Online] Available at: https://basicmedicalkey.com/lower-limb-2/[Accessed 15 August 2018].

Bendjaballah MZ, Shirazi A, Zukor DJ. 1995. iomechanics of the human knee joint in compression: reconstruction, mesh generation and finite element analysis. Knee.;2, pp.69e79.

Bergmann G, Bender A, Dymke J, Duda G, Damm P (2016) Standardized Loads Acting in Hip Implants. PLoS ONE 11(5): e0155612. https://doi.org/10.1371/journal.pone.0155612

Bergmann, G. (2015). "Orthoload." from www.orthoload.com.

Bergmann, G., Deuretzbacher, G., Heller, M., Graichen, F., Rohlmann, A., Strauss, J., Duda, G.N., 2001. Hip contact forces and gait patterns from routine activities. Journal of Biomechanics 34, pp, 859–871.

Bergmann, G., Graichen, F. and Rohlmann, A., 1993. "Hip Joint Loading During Walking and Running, Measured in Two Patients." Journal of Biomechanics 26(8).pp. 969-980.

Bitsakos C, Kerner J, Fisher I, Amis A., 2005.The effect of muscle loading on the simulation of bone remodeling in the proximal femur. Journal of Biomechanics. 38(1):133–9.

Blumentritt S. 1990. The relationship between the gait of humans and the hip joint structure in the frontal plane. Gegenbaurs Morphol Jahrb. 136(6): 677–693.

Baldwin, M. A., Clary, C. W., Fitzpatrick, C. K., Deacy, J. S., Maletsky, L. P., and Rullkoetter, P. J., 2012. Dynamic Finite element knee simulation for evaluation of knee replacement mechanics. Journal of Biomechanics, 45(3), pp 474-83, 2012.

Bnnefoy-Mazure, A. & Armand, S., 2015. Normal Gait cycle. Nova Science Publishers, pp. 198-213.

Boguszewsk,i DV., Joshi, NB., Yang, PR., Markolf, KL., Petrigliano FA., McAllister DR.,2016. Location of the natural knee axis for internal-external tibial rotation. Knee. 2016 Dec; 23(6):1083-1088.

Brand, R. A., 1978. A biomechanical investigation of the human hip. J. Biomechanics, 11, pp, 76-85.

Brand, R. A., Pedersen, D. R., Davy, D. T., Kotzar, G. M., Heiple, K. G. and Goldberg, V. M. 1994. "Comparison of Hip Force Calculations and Measurements in the Same Patient." The Journal of Arthroplasty 9(1): 45-51.

Brekelmans, W. A. M., Poort, H. W., and, Sloo, T. J. J. H., 1972. A New Method to Analyse the Mechanical Behaviour of Skeletal Parts. Acta Orthopaedica, 43(5), pp, 301-317.

Brown, T. D., and DiGioia. A. M., 1984. A contact-coupled Finite element analysis of the natural adult hip. Journal of Biomechanics, 17:437-48.

Buchanan, T. S., Lloyd, D. G., Manal, K. T., and Besier, T. F., 2004. Neuro musculoskeletal modelling: Estimation of muscle forces and joint moments and movements from measurements of neural command. Journal of Applied Biomechanics, 20. pp, 367-395.

Caligaris, M. & Ateshian, G., 2008. Effects of sustained interstitial fluid pressurization under migrating contact area and boundary lubrication by synovial, on cartilage friction. Osteoarthritis and Cartilage, 10(16), pp. 1220-1227.

Callister, W. D., 2000. Materials Science and Engineering. An Introduction. John Wiley and Sons.

Cardiff, P., 2012. Development of the Finite Volume Method for Hip Joint Stress Analysis, Dublin: University College Dublin.

Cardiff, P., Karač, A., Fitzpatrick, D., & Ivankovic, A. 2013. Development of a hip joint model for finite volume simulations. Journal of biomechanical engineering, 136 1, 011006 .

Carter, D. and Hayes, W., 1977. "The Compressive behaviour of bone as a two-phase porous structure." Journal of Bone and Joint Surgery (Am.) 59(7), pp. 954-962.

Cattrysse E, Barbaix E, Janssens V, Alewaeters K, Van Roy P, Clarijs JP. 2002. Observation of a supernumerary hamstring muscle: a state of the art on its incidence and clinical relevance. Morphologie. 86: 17–21

Chen, Z., Zhang, X., Ardestani, M., Wang, L., Liu, Y., Lian, Q., He, J., Li, D. and Jin, Z., 2014. Prediction of *in-vivo* joint mechanics of an artificial knee implant using rigid multi-body dynamics with elastic contacts. Proceedings of the Institution of Mechanical Engineers, Part

H: Journal of Engineering in Medicine, [online] 228(6), pp.564-575. Available at: http://dx.doi.org/10.1177/0954411914537476.
Chester, V.L., Wrigley, A.T., 2008. The identification of age-related differences in kinetic gait parameters using principal component analysis. Clin. Biomech. 23, 212–220.
Chethan K.N., Zuber ., Bhat N SH., Shenoy S. B., 2018. Comparative Study of Femur Bone Having Different Boundary Conditions and Bone Structure Using Finite Element Method. The Open Biomedical Engineering Journal.12, pp. 115-134DOI: 10.2174/1874120701812010115,
Chèze, L., Moissenet, F. and Dumas, R. (2012). State of the art and current limits of musculo-skeletal models for clinical applications. Movement & Sport Sciences - Science & Motricité, [online] (90), pp.7-17. Available at: http://dx.doi.org/10.1051/sm/2012026.
Choi, JB., Youn, I., Cao, L., 2007. Zonal changes in the three-dimensional morphology of the chondron under compression: the relationship among cellular, pericellular, and extracellular deformation in articular cartilage. J Biomech. pp; 40(12):2596–603.
Choi, JB., Youn, I., Cao, L., 2007. Zonal changes in the three-dimensional morphology of the chondron under compression: the relationship among cellular, pericellular, and extracellular deformation in articular cartilage. J Biomech. pp; 40(12):2596–603.
Cilingir, A. C., Ucar V., and Kazan R., 2007. Three-dimensional anatomic Finite element modelling of hemi-arthroplasty of human hip joint. Trends Biomater. Artificial Organs, 21, PP 63-72.
Clauser, C.E., McConville, J.T. and Young, J.W., 1969. Weight, Volume and Centre of Mass of Segments of the Human Body. Aerospace Medical Division, WPAF Base, OH- USA.
Clemente, C. D., 1981. Anatomy. A Regional Atlas of the Human Body, 2nd. Urban & Schwarzenberg, Baltimore, MD.
Coleman, J.L. M.R. Widmyer, H.A. Leddy, G.M. Utturkar, C.E. Spritzer, C.T. Moorman 3rd, F. Guilak, L.E. DeFrat. 2013. Diurnal variations in articular cartilage thickness and strain in the human knee J. Biomech., 46), pp. 541-547
Cook, G.E., Samiezadeh, S., Morison, Z., M.S.R. Aziz, H. Bougherara, R. Zdero, and E.H. Schemitsch, 2017. Biomechanical optimisation of the angle and position for surgical implantation of a straight short stem hip implant, Med. Eng. Phys., vol. 39, pp. 23-30. [http://dx.doi.org/10.1016/j.medengphy.2016.10.002].
Coquim j., et al., 2018. Research Article Biomechanical Analysis Using FEA and Experiments of Metal Plate and Bone Strut Repair of a Femur Midshaft Segmental Defect. BioMed Research International. Volume 2018, Article ID 4650308, 11 pages. https://doi.org/10.1155/2018/4650308.
Correa, T. A., Crossley, K. M., Kim, H. J. & Pandy, M. G., 2010. Contributions of individual muscles to hip joint contact force in normal walking. Journal of Biomechanics, Volume 43, p. 1618–1622.
Cotofana, S. , Eckstein, F., Wirth, W., R.B. Souza, X. Li, B. Wyman, M.P. Hellio-Le Graverand, T. Link, S. Majumdar 2011. *In-vivo* measures of cartilage deformation: patterns in healthy and osteoarthritic female knees using 3T MR imaging Eur. Radiol., 21 pp. 1127-1135
Cowin, S. C. (2001). Bone Mechanics Handbook.
Cristofolini, L., Viceconti,M., Toni, A., Giunti,A., 1995. Influence of thigh muscles on the axial strains in a proximal femur during early stance in gait, Journal of Biomechanics, Volume 28, Issue 5. pp. 617-624,
Crow, B. D., Haltom, D. J., Carson, W. L., Greene, W. B. and Cook, J. L. 2007. Evaluation of a Novel Biomaterial for Intrasubstance Muscle Laceration Repair. Journal of Orthopaedic Research 25(3), pp, 396-403.
Crowninshield, R.D., Johnston, R.C., Andrews, J.G., Brand, R.A., 1978. A biomechanical investigation of the human hip. Journal of Biomechanics 11, pp, 75–85.
Cummings, S.R., Melton, L.J., 2002. Epidemiology and outcomes of osteoporotic fractures. Lancet 359, 1761–1767.
Currey JD., 1988. The effect of porosity and mineral content on the Young's modulus of elasticity of compact bone. J Biomech. 1988; 21(2):131–9.
Dalstra, M., Huiskes, R., and van Erning. L., 1995. Development and validation of a three- dimensional finite element model of the pelvic bone. Journal of biomechanical engineering, 117:272-278.

Damsgaard, M., Rasmussen, J., Christensen, S., Surma, E. and de Zee, M. (2006). Analysis of musculoskeletal systems in the AnyBody Modeling System. Simulation Modelling Practice and Theory, [online] 14(8), pp.1100-1111. Available at: http://dx.doi.org/10.1016/j.simpat.2006.09.001.

Dash, P. P., Kishor, K., & Panda, Subrata, (2013). Biomechanical stress analysis of human femur bone.

Davy, D.T., Kotzar, G.M., Brown, R.H., Heiple, K.G., Goldberg, V.M., Berilla, J., Burstein, A.H., 1988. Telemetric force measurements across the hip after total arthroplasty. Journal of Bone and Joint Surgery (Am) 70, pp.45–50.

Debrunner, HU. 1975. Biomechanics of the hip joint. I. A new model for the calculation of the forces in the hip joint. Z Orthop Ihre Grenzgeb; 113(3): 377–388.

De-la-Herran, A. M., Garcia-Zapirain, B. & Mendez-Zorrilla, A., 2014. Gait Analysis Methods: An Overview of Wearable and Non-Wearable Systems, Highlighting Clinical Applications. Sensors, Volume 14, pp. 3362-3394.

Delp, S., Anderson, F., Arnold, A., Loan, P., Habib, A., John, C., Guendelman, E. and Thelen, D. (2007). OpenSim: Open-Source Software to Create and Analyze Dynamic Simulations of Movement. IEEE Transactions on Biomedical Engineering, [online] 54(11), pp.1940-1950. Available at: http://dx.doi.org/10.1109/TBME.2007.901024.

Delp, S.L., Anderson, F.C., Arnold, A.S., Loan, P., Habib, A., John, C.T., Guendelman, E.Thelen, D.G., 2007. OpenSim: open-source software to create and analyse dynamic simulations of movement. IEEE Transactions on Biomedical Engineering 54, pp, 1940–1950.

DeMers, M., Pal, S. and Delp, S. (2014). Changes in tibiofemoral forces due to variations in muscle activity during walking. Journal of Orthopaedic Research, [online] 32(6), pp.769-776. Available at: http:// dx.doi.org/10.1002/jor.22601.

Demird I.zic, E. Dzafarovi c, and A. I. Ivankovi c., 2005. . Finite-volume approach to thermos-viscoelasticity. Numerical Heat Transfer, Part B: Fundamentals, 47(3):pp. 213-237.

Devita, P., Hortobagyi, T., 2000. Age causes a redistribution of joint torques and powers during gait cycle. J. Appl. Physiol. 88, 1804–1811.

Ding, Z., Nolte, D., Kit Tsang, C., Cleather, D., Kedgley, A. and Bull, A. (2016). *In-vivo* Knee Contact Force Prediction Using Patient-Specific Musculoskeletal Geometry in a Segment-Based Computational Model. Journal of Biomechanical Engineering, 138(2), p.021018.

Donahue TL, Hull ML, Rashid MM, Jacobs RC. 2002. A finite element model of the human knee joint for the study of tibiofemoral contact. ASME J Biomech Eng.124pp.273-280.

Donahue, SW., 2001.The role of muscular force and fatigue in stress fractures. In: Burr, DB. Milgrom, C., editors. Musculoskeletal fatigue and stress fractures. CRC Press; Bota Raton:pp. 131-49.

Dong, Y., Hu, G., Dong, Y., Hu, Y., & Xu. Q., 2014. The effect of meniscal tears and resultant partial meniscectomy on the knee contact stresses: a finite element analysis, Computer Methods in Biomechanics and Biomedical Engineering, 17:13, 1452-1463, DOI: 10.1080/10255842.2012.753063.

Dong XN, Acuna RL, Luo Q, Wang X. 2012. Orientation dependence of progressive post-yield behaviour of human cortical bone in compression. J Biomech. 2012; 45:2829–34

Dowson. D., Unsworth, A., Cooke, A. F. and Gvozdanovic, D. 1981. Lubrication of joints. An Introduction of the Biomechanics of Joints and Joint Replacement (Edited by Dowson, D. and Wright, V.). pp. 120-145. Mechanical Engng. London.

Dumas, R., Moissenet, F., Gasparutto, X. and Cheze, L. (2012). Influence of joint models on lower-limb musculo-tendon forces and three-dimensional joint reaction forces during gait cycle. Proceedings of the Institution of Mechanical Engineers, Part H: Journal of Engineering in Medicine, [online] 226(2), pp.146-160. Available at: http://dx.doi.org/10.1177/ 0954411911431396.

Ebacher, V., Tang, C., McKay, H., Oxland, T. R., Guy, P. and Wang, R. 2007. "Strain Redistribution and Cracking Behaviour of Human Bone During Bending." Bone 40(5), pp.1265-1275.

Eberhardt, A. W., Keer, L. M., Lewis, J. L. and Vithoontien, V. (1990) An analytical model ofjoint contact. J. biomech. Engng ASME 112, 407-413.

Eckstein F, Lemberger B, Gratzke C, et al., 2005. *In-vivo* cartilage deformation after different types of activity and its dependence on physical training status Annals of the Rheumatic Diseases;64:291-295.

Eckstein, F., Winzheimer, M.,Hohe, J., K.H. Englmeier, Reiser, M. 2001. Interindividual variability and correlation among morphological parameters of knee joint cartilage plates: analysis with three-dimensional MR imaging Osteoarthr.Cartil.,pp. 101-111

Enoka, R.M., 2002. Neuromechanics of human movement. Human Kinetics, 3rd edition, 2002.

Elias, J. J., Kilambi, S., Goerke, D. R., & Cosgarea, A. J. 2009. Improving vastus medialis obliquus function reduces pressure applied to lateral patellofemoral cartilage. Journal of orthopaedic research: official publication of the Orthopaedic Research Society, 27(5), 578–583. doi:10.1002/jor.20791.

Elkins, M. J., 2013. Biomechanics of failure modalities in total hip arthroplasty. [Online] Available at: https://ir.uiowa.edu/cgi/viewcontent.cgi?referer=https://www.google.co.uk/&httpsredir=1&article=4615&context=etd [Accessed 15 August 2018].

Erdemir, A., McLean, S., Herzog, W. and van den Bogert, A. (2007). Model-based estimation of muscle forces exerted during movements. Clinical Biomechanics, [online] 22(2), pp.131-154. Available at: http://dx.doi.org/10.1016/j.clinbiomech.2006.09.005.

Erochko, J., 2015. Introduction to Structural Analysis. [Online] Available at: http://www.learnaboutstructures.com/[Accessed 13 August 2019].

Eschweiler, J. et al., 2012. Application and evaluation of biomechanical models and scores for the planning of total hip arthroplasty. Journal of Engineering in Medicine, pp. 1-11.

Eschweiler, J. et al., 2012. Application and evaluation of biomechanical models and scores for the planning of total hip arthroplasty. Journal of Engineering in Medicine, pp. 1-11.

Feikes, J., O'Connor, J. and Zavatsky, A. (2003). A constraint-based approach to modelling the mobility of the human knee joint. Journal of Biomechanics, 36(1), pp.125-129.

Fellows, CR., Matta, C., Zakany, R., Khan, IM. Mobasheri A., 2016. Adipose, Bone Marrow and Synovial Joint-Derived Mesenchymal Stem Cells for Cartilage Repair. Front Genet. 2016; 7:213.

Filardi, V., 2014. FE analysis of stress and displacements occurring in the bony chain of leg, Journal of Orthopaedics,Volume 11, Issue 4,pp. 157-165

Finlay, J. B., Rorabeck, C. H., Boume, R. B. and Tew, W. M.1989. In vitro analysis of proximal femoral strains using PCA femoral implants and a hip-abductor muscle simulator. J. Arthroplasty 4, 335-349.

Flavin, R., Halpin, T., O'Sullivan, R., FitzPatrick, D., Ivankovic, A., and Stephens. M. M., 2008 A Finite-element analysis study of the metatarsophalangeal joint of the hallux rigidus. The Journal of Bone & Joint Surgery, 90 (10):1334-1340, 2008.

Fletcher, J., 2017. What is abnormal gait? [Online] Available at: https://www.medicalnewstoday.com/articles/320481.php [Accessed 13 August 2019].

Fregly, B., Besier, T., Lloyd, D., Delp, S., Banks, S., Pandy, M. and D'Lima, D. (2011). Grand challenge competition to predict *in-vivo* knee loads. Journal of Orthopaedic Research, 30(4), pp.503-513.

Fyhrie DP, Milgrom C, Hoshaw SJ, Simkin A, Dar S, Drumb D, et al. 1998. Effect of fatiguing exercise on longitudinal bone strain as related to stress fracture in humans. Ann Biomed Eng. 26:660–5.

Garrett, W. E. and Duncan, P. W. (1988). Muscle Injury and Rehabilitation, Williams & Wilkins.

Genda, E., Iwasaki, N. , G. Li, B. A. MacWilliams, P. J. Barrance, and E. Y. Chao. 2001. Normal hip joint contact pressure distribution in single-leg standing of gender and anatomic parameters. Journal of Biomechanics, 34(7)-pp-895- 905.

Gerus, P., Sartori, M., Besier, T., Fregly, B., Delp, S., Banks, S., Pandy, M., D'Lima, D. and Lloyd, D. (2013). Subject-specific knee joint geometry improves predictions of medial tibiofemoral contact forces. Journal of Biomechanics, 46(16), pp.2778-2786.

Giancoli, Douglas C., 2016. Physics: Principles with Applications (7th Edition) - Standalone book. Pearson.

Gibson, L. J., 2005. "Biomechanics of Cellular Solids." Journal of Biomechanics 38(3): 377-399.

Giesen, E.B.W, et al., 2001. Mechanical properties of cancellous bone in the human mandibular condyle are anisotropic, Journal of Biomechanics 34, PP 799–803.
Gislason, M. K., Ingvarsson, P., Gargiulo, P., Yngvason, S., Guðmundsdóttir, V., Knútsdóttir, S., & Helgason, Þ. 2015. Finite Element Modelling of the Femur Bone of a Subject Suffering from Motor Neuron Lesion Subjected to Electrical Stimulation. European journal of translational myology, 24(3), 2187. https://doi.org/10.4081/ejtm.2014.2187.
Goel, V. K., Valliappan, S., and Svensson, N. L. 1978. Stresses in the normal pelvis. Computers in biology and medicine, 8: pp, 91-104.
Gray HA, Taddei F, Zavatsky AB, Cristofolini L, Gill HS. 2008. Experimental validation of a finite element model of a human cadaveric tibia. Journal of Biomechanical Engineering; 130(3):031016.
Gray, H., 1918. Anatomy of the Human Body. [Online] Available at: www.bartleby.com/107/.[Accessed 15 August 2018].
Grosland, N. M., Shivanna, K. H., Magnotta, V. A., Kallemeyn, N. A., DeVries, N. A., Tadepalli, S.C., and Lisle., C., 2009. IA-FEMesh: an open-source, interactive, multiblock approach to anatomic Finite element model development. Computer methods and programs in biomedicine, 94(1):pp.96-107.
Grove et al. O., Rajab, K.,Piegl, L. A., Lai-Yuen, S., (2011) From CT to NURBS: Contour Fitting with B-spline Curves. Computer-Aided Design & Applications, Volume 8(1), pp. 3-21.
Gu, K. B. and Li, L. P. 2011. "A human knee joint model considering fluid pressure and fiber orientation in cartilages and menisci," Medical Engineering and Physics, vol. 33, no. 4, pp. 497–503, 2011. View at Publisher · View at Google Scholar · View at Scopus.
Guess, T., Stylianou, A. and Kia, M. (2014). Concurrent Prediction of Muscle and Tibiofemoral Contact Forces during Treadmill Gait cycle. Journal of Biomechanical Engineering, [online] 136(2), p.021032. Available at: http://dx.doi.org/10.1115/1.4026359.
Gupton M, Terreberry RR. Anatomy, Hinge Joints. [Updated 2019 Apr 4]. In: StatPearls [Internet]. Treasure Island (FL): StatPearls Publishing; 2019 Jan-. Available from: https://www.ncbi.nlm.nih.gov/books/NBK518967
Hamill, J., & Knutzen, K. M. (2009). Biomechanical Basis of Human Movement (Third Ed.). Baltimore, MD, USA: Lippincott Wiliams & Wilkins.
Harris, M. D., Anderson, A. E., Henak, C. R., Ellis, B. J., Peters, C. L., and Weiss, J. A., 2011. Finite element prediction of cartilage contact stresses in normal human hips. Journal of orthopaedic research: ocial publication of the Orthopaedic Research Society, pages 1133-1139,
Harris, S. & Anderson, S., 2009. Care of the Young Athlete. 2nd, IL: 2009:410. Elk Grove Village: American Academy of Paediatrics and American Academy of Orthopaedic Surgeons.
Harvey, L. (2008). Management of Spinal Cord Injuries. Chapter 6: Standing and walking with lower limb paralysis, Editor(s) Churchill Livingstone, pp 107-133, ISBN 9780443068584.
Hansen, U., Zioupos, P., Simpson, R., Currey, JD., Hynd, D., 2008.The effect of strain rate on the mechanical properties of human cortical bone. J Biomech Eng. 2008 Feb;130(1):011011. doi: 10.1115/1.2838032.
Hashin, Z., 1980. Failure criteria for unidirectional fibre composites, ASME Journal of Applied Mechanics, Vol. 47 (2), pp 329-334.
Hast, M.W., Piazza, S.J., 2013. Dual-joint modeling for estimation of total knee replacement contact forces during locomotion. J. Biomech. Eng. 135, 021013. http://dx.doi.org/10.1115/1.4023320.
He, J. and Levine, W., 1988. The modelling of the neuro-musculo-skeletal control system of a cat hind limb. IEEE International Symposium on Intelligent Control, 1988.
Heintz, S. & Gutierrez-Farewik, E. M., 2007. Static optimisation of muscle forces during gait in comparison to EMG-to-force processing approach. Gait & Posture, Volume 26, p. 279–288.
Helgason, B., Perilli, E., Schileo, E., Taddei, F., Brynjólfsson, S. and Viceconti, M. 2008."Mathematical Relationships between Bone Density and Mechanical Properties: A Literature Review." Clinical Biomechanics 23(2). pp. 135-146.
Heller, M., Bergmann, G., Deuretzbacher, G., Claes, L., Haas, N. and Duda, G. 2001. Influence of femoral anteversion on proximal femoral loading: measurement and simulation in four patients. Clinical Biomechanics, 16(8), pp.644-649.

Heller, M.O., Bergmann, G., Kassi, J.P., Claes, L., Haas, N.P., Duda, G.N., 2005. Determination of muscle loading at the hip joint for use in pre-clinical testing. Journal of Biomechanics 38, pp, 1155–1163.

Hill, A. V., 1938.The heat of shortening and the dynamic constants of muscle. In proceedings of the Royal Society of London, University College, London, 1938.

Hodgskinson, R. and Currey, J. D., 1992. "Young's Modulus, Density and Material Properties in Cancellous Bone over a Large Density Range." Journal of Materials Science: Materials in Medicine 3(5).pp. 377-381.

Homminga, J., et al., 2002. Cancellous Bone Mechanical Properties From Normal and Patients With Hip Fractures Differ on the Structure Level, Not on the Bone Hard Tissue Level. Bone Vol. 30, No. 5, 2002:759 –764.

Hooke, R., 1678. De Potential Restitutiva, or of spring. Explaining the Power of Springing Bodies, London.

Howard, R. 2017. The application of data analysis methods for surface electromyography in shot putting and sprinting. 10.13140/RG.2.2.15907.04640.

Hug, F., 2011. Can muscle coordination be precisely studied by surface electromyography? Journal of Electromyography and Kinesiology, 21 (1), pp. 1-12.

Huijing. P. A. 1995. Parameter interdependence and the success of skeletal modelling. Human Movement Science, 57(95).

Huiskes, R., Boeklagen, R., 1988. The application of numerical shape optimisation to artificial-joint design R.L. Spilker, B.R. Simon (Eds.), Computational Methods in Bioengineering, BED-Vol. 9, The Mechanical Society of Mechanical Engineers, New York, pp. 185-197

Humananatomyly, 2011. Long bone femur labelled. [Online] Available at: https://humananatomyly.com/long-bone-femur-label/long-bone-femur-label-long-one-diagram-labeled-worksheet-human-anatomy-chart. [Accessed 15 August 2018].

Huxley, A. F.1974. Muscular contraction. The Journal of physiology, 243(1), pp.1-43, 1974.

Hyndman, R. J., & Koehler, A. B. 2006. Another look at measures of forecast accuracy. International Journal of Forecasting, 22, 679–688.

Igliĉ, A., Kralj-Igliĉ, V. & Daniel, M., 2002. Computer Determination of Contact Stress Distribution and Size of Weight Bearing Area in the Human Hip Joint. Computer Methods in Biomechanics and Biomedical Engineering, 5(2), p. 185–192.

Isaza, E., Salazar, E.,& Florez, L. 2013. Determination of Mechanic Resistance of Osseous Element Through Finite Element Modeling. COMSOL Conference in Boston.

ISO-14242-1 2002, 2002. Implants for surgery — wear of total hip-joint prostheses — part 1: loading and displacement parameters for wear-testing machines and corresponding environmental conditions for test.

Jade, S. Tamvada, K.H. Strait,D.S, Grosse,I.G. 2014. Finite element analysis of a femur to deconstruct the paradox of bone curvature, Journal of Theoretical Biology, Volume 341, 2014, PP. 53-63,

Jarquio, R. V., 2007. Structural Analysis: The Analytical Method. 1st ed. Boca Raton: CRC Press.

Jennett, S., 2008. Churchill Livingstone's Dictionary of Sport and Exercise Science and Medicine. 1st ed. Glasgow, UK: Elsevier Health Sciences.

Jia, Y.-B., 2018. Rotation in the Space. In: J. B. Kuipers, ed. Quaternions and Rotation Sequences. Princeton: Princeton University Press, pp. 1-14.

Jonkers, I., Sauwen, N., Lenaerts, G., Mulier, M., Van Der Perre, G., and Jaecques, S., 2008. Relation between subject-specific hip joint loading, stress distributions in the proximal femur and bone mineral density changes after total hip replacement. Journal of Biomechanics, 41:3, pp. 405-413.

Jung, Y., Phan, C. and Koo, S. (2016). Intra-Articular Knee Contact Force Estimation during Walking Using Force-Reaction Elements and Subject-Specific Joint Model2. Journal of Biomechanical Engineering, [online] 138(2), p.021016. Available at: http://dx.doi.org/10.1115/1.4032414.

Kääriäinen, M., Kääriäinen, J., Järvinen, T., Sievänen, H., Kalimo, H. and Järvinen, M. (1998). "Correlation between Biomechanical and Structural Changes during the Regeneration of Skeletal Muscle after Laceration Injury." Journal of Orthopeadic Research 16(2), pp, 197-206.

Kayabasi O., Erzincanl F., 2006. Finite element modelling and analysis of a new cemented hip prosthesis. Advances in Engineering Software. 37. pp 477–483478.
Keller T.S., 1994. Predicting the compressive mechanical behaviour of bone. Journal of Biomechanics 1994; 27(9):1159–68.
Ken-hub, ©. 2013. Illustrator: Liene Znotina. [Online] Available at: https://www.kenhub.com. [Accessed 5 August 2018].
Kerem Ün & Ahmet Çalık. 2016. Relevance of inhomogeneous–anisotropic models of human cortical bone: a tibia study using the finite element method, Biotechnology & Biotechnological Equipment, 30:3, 538-547, DOI: 10.1080/13102818.2016.1154803
Knarr, B.A., Higginson, J.S., 2015. Practical approach to subject-specific estimation of knee joint contact force. J. Biomech. 48 , 2897–2902. http://dx.doi.org/10.1016/j.jbiomech.2015.04.020.
Keyak, J. H. and Rossi, S. A., 2000. "Prediction of Femoral Fracture Load Using Finite Element Models: An Examination of Stress- and Strain-Based Failure Theories."Journal of Biomechanics 33(2).pp. 209-214.
Kingston, B. (1996). Understanding Muscles: A Practical Guide to Muscle Function, Stanley Thornes (Publishers) Ltd.
Kia, M., Stylianou, A. and Guess, T. (2014). Evaluation of a musculoskeletal model with prosthetic knee through six experimental gait trials. Medical Engineering & Physics, [online] 36(3), pp.335-344. Available at: http://dx.doi.org/10.1038/nbt.3121.ChIP-nexus.
Kim YC, Yoo WK, Chung IH, Seo JS, Tanaka S., 1997.Tendinous insertion of semimembranosus muscle into the lateral meniscus. Surg Radiol Anat. 19: 365–369.
Kim, H.J., Fernandez, J.W., Akbarshahi, M., Walter, J.P., Fregly, B.J., Pandy, M.G. 2009. Evaluation of predicted knee joint muscle forces during gait using an instrumented knee implant. Journal of Orthopaedic Research 27, pp, 1326–1331.
Kirkwood, R. N., Gomes, H. d. A., Culham, E. & Costigan, P., 2007. Biomechanical analysis of hip and knee joints during gait in elderly subjects. Acta Ortopédica Brasileira, 15(5), pp. 267-271.
Kirtley, C., 2002. Sensitivity of the modified Helen Hates model to marker placement errors. [Online] Available at: http://www.clinicalgaitanalysis.com/faq/hayes.[Accessed 12 August 2018].
Klein Horsman, M., Koopman, H., van der Helm, F., Prosé, L. and Veeger, H. (2007). Morphological muscle and joint parameters for musculoskeletal modelling of the lower extremity. Clinical Biomechanics, 22(2), pp.239-247.
Klika, V. et al., 2016. An overview of multiphase cartilage mechanical modelling and its role in understanding function and pathology. Journal of the Mechanical Behavior of Biomedical Materials. Volume 62, pp.139-157
Knee and Hip muscles, 2017. Muscles-in-the-knee. [Online] Available at: https://www.cunninghamforcouncil.com/muscles-in-the-knee/amazing-muscles-in-the-knee-29-on-anatomy-of-the-human-brain-with-muscles-in-the-knee.[Accessed 11 August 2018].
Komistek RD, Kane TR, Mahfouz M, Ochoa JA, Dennis DA., 2005. Knee mechanics: a review of past and present techniques to determine *in-vivo* loads. J Biomech 38(2)-p: 215–228.
Komistek, R.D., Stiehl, J.B., Dennis, D.A., 1998. Mathematical model of the lower extremity joint reaction forces using Kane's method of dynamics. Journal of Biomechanics 31, 185–189
Kopperdahl, D. L. and Keaveny, T. M., 1998. "Yield Strain Behavior of Trabecular Bone." Journal of Biomechanics 31;7. Pp. 601-608.
Korenczuk CE, Votava LE, Dhume RY, et al. Isotropic failure criteria are not appropriate for anisotropic fibrous biological tissues. ASME. J Biomech Eng. 2017;139(7):071008-071008-10. doi:10.1115/1.4036316.
Korsa, R., Mares, T. (2012). Numerical Identification of Orthotropic Coefficients of the Lamella of a Bone's Osteon, Bulletin of Applied Mechanics, 8(31), pp. 45-53.
Kotzar, G.M., Davy, D.T., Goldberg, V.M., Heiple, K.G., Berilla, J., Brown, R.H., Burstein, A.H., 1991. Telemeterized *in-vivo* hip joint force data: a report on two patients after total hip surgery. J. Orthop. Res. 9, 621–633.
Kuitunen, S., Komi, P. V., & Kyröläinen, H. (2002). Knee and ankle joint stiffness in sprint running. Medicine & Science in Sports & Exercise, 34, 166-173.

Kurtz, S., Ong, K., Lau. E., Mowat F., and Halpern, M., 2007. Projections of primary and revision hip and knee arthroplasty in the united states from 2005 to 2030. Journal of Bone & Joint Surgery, 89(4), pp, 780-785,

Kyröläinen, H., Avela, J., & Komi, P. V. (2005). Changes in muscle activity with increasing running speed. Journal of Sports Sciences, 23, 1101-1109. doi: 10.1080/02640410400021575 Lanyon, L. E., Hampson, W. G. J., Goodship, A. E. and Shah, J. S., 1975. "Bone Deformation Recorded *in-vivo* from Strain Gauges Attached to the Human Tibial Shaft." Acta Orthopaedica 46(2).pp. 256-268.

Lagravère et al. , M. O., Fang, Y., Carey, J., Toogood, R. W., (2006) Density conversion factor determined using a conebeam computed tomography unit NewTom QR-DVT 9000. Dentomaxillofacial Radiology, Volume 35(6), pp. 407-409.

Lee, D. C. & Byun, S. J., 2012. High tibial osteotomy. Knee Surg Relat Res- PubMed, 24(2), pp. 61-69.

Lee, S., Porter, M., Wasko, S., Lau, G., Chen, P., at al., 2012. Potential Bone Replacement Materials Prepared by Two Methods. MRS Proceedings, 1418, Mrsf11-1418-mm06-02. doi:10.1557/opl.2012.671

Lerner, Z.F., DeMers, M.S., Delp, S.L., Browning, R.C., 2015. How tibiofemoral alignment and contact locations affect predictions of medial and lateral tibiofemoral contact forces. J. Biomech. 48., 644–650.

Lewis, C. L. & Sahrmann , S. A., 2015. Effect of posture on hip angles and moments during gait cycle. Manual Therapy, Volume 20, pp. 176-182.

Lewis, C. L., Sahrmann, S. A., & Moran, D. W., 2007. Anterior hip joint force increases with hip extension, decreased gluteal force, or decreased iliopsoas force. Journal of biomechanics, 40(16), 3725–3731. https://doi.org/10.1016/j.jbiomech.2007.06.024

Li, G., Sakamoto, M. and Chao, E. 1997. A comparison of different methods in predicting static pressure distribution in articulating joints. Journal of Biomechanics, 30(6), pp.635-638.

Li, G., Suggs, J., and Gill, T. 2002. "The effect of anterior cruciate ligament injury on knee joint function under a simulated muscle load: a three-dimensional computational simulation," Annals of Biomedical Engineering, vol. 30, no. 5, pp. 713–720.

Li, X., 2017. Structural Design of a 6-DoF Hip Exoskeleton using Linear Series Elastic Actuators. Semantic scholar.

Li, J. et al., 2014. Hip contact forces in asymptomatic total hip replacement patients differ from normal healthy individuals: Implications for preclinical testing. Clinical Biomechanics, Volume 29, p. 747–751.

Li, J. et al., 2019. Development of a finite element musculoskeletal model with the ability to predict contractions of three-dimensional muscles. Journal of Biomechanics, pp. 1-5, https://doi.org/10.1016/j.jbiomech.2019.07.042.

Lin, Y.C., Walter, J.P., Banks, S.A., Pandy, M.G., Fregly, B.J., 2010. Simultaneous prediction of muscle and contact forces in the knee during gait cycle. Journal of Biomechanics 43, pp, 945–952.

Lin, Yi-Chung & Walter, Jonathan & Banks, Scott & G Pandy, Marcus & Fregly, Benjamin. 2009. Simultaneous Prediction of Muscle and Contact Forces in the Knee During Gait cycle. Journal of biomechanics. 43. 945-52. 10.1016/j.jbiomech.2009.10.048.

Liu, F. at al., 2010ek. *In-vivo* tibiofemoral cartilage deformation during the stance phase of gait cycle. Journal of Biomechanics 43 – pp 658–665

Liu, H., Fletcher, J., Garrison, M. K. & Holmes, C., 2011. Bilateral Absence of Quadratus Femoris and Semimembranosus. International Journal of Anatomical Variations (IJAV), Volume 4, pp. 40-42.

Liu, X., Govindarajan, S. & Subham , S., 2010. Bone remodeling simulation using abaqus subroutine usdfld. Florida, USA, ASME.

Ljung, C., 2014. Muscle Activation and Movement Coordination, Stockholm: Department of Mechanics School of Engineering Science, Royal Institute of Technology.

Lotz, J.C., Cheal, E.J. & Hayes, W.C. 1995. Stress distributions within the proximal femur during gait and falls: Implications for osteoporotic fracture. Osteoporosis Int 5: 252. https://doi.org/10.1007/BF01774015.

Lu, T.W., O'Connor, J.J., Taylot, S.J.G., Walker, P.S., 1998. Validation of a lower limb model with *in-vivo* femoral forces telemetered from two subjects. Journal of Biomechanics 31, 63–69.

Lu, T.W., Taylor, S.J.G., O'Connor, J.J., Walker, P.S., 1997. Influence of muscle activity on the forces in the femur: am *in-vivo* study. Journal of Biomechanics 30, 1101–1106.

Lund, M.E., Andersen, M.S., de Zee, M., Rasmussen, J., 2015. Scaling of musculoskeletal models from static and dynamic trials. Int. Biomech. 2, 1–11.http://dx.doi.org/10.1080/23335432.2014.993706.

Lundberg, H.J., Knowlton, C., Wimmer, M.A., 2013. Fine tuning total knee replacement contact force prediction algorithms using blinded model validation. J. Biomech. Eng. 135, 1–9. http://dx.doi.org/10.1115/1.4023388.

Machado, M., Moreira, P., Flores, P. and Lankarani, H. (2012). Compliant contact force models in multibody dynamics: Evolution of the Hertz contact theory. Mechanism and Machine Theory, 53, pp.99-121.

Majumder, S., Roy Chowdhury, A., and Pal, S., 2004. Variations of stress in pelvic bone during normal walking, considering all active muscles. Trends Biomater. Artif. Organs. 17(2): pp, 48-53.

Maharaj S., Maheswaran R., Vasanthanathan, A., 2013. Numerical Analysis of Fractured Femur Bone with Prosthetic Bone Plates P.S.R. International Conference on Design and Manufacturing, IConDM, 2013 Procedia Engineering 64. pp1242 – 1251.

Malagelada, F. et al., 2014. Knee Anatomy and Biomechanics of the Knee. DeLee & Drez's Orthopaedic Sports Medicine,Elsevier Health Sciences , Issue 4th.

Malik, A. and Dorr, L. D. 2007. "The Science of Minimally Invasive Total Hip Arthroplasty." Clinical Orthopaedics and Related Research 463, pp, 74-84.

Manal, K., Buchanan, T.S., 2013. An electromyogram-driven musculoskeletal model of the knee to predict *in-vivo* joint contact forces during normal and novel gait patterns. J. Biomech. Eng. 135, 21014. http://dx.doi.org/10.1115/1.4023457.

Mancuso, C. A., Salvati , E. A. & Joh, N. A., 1997. Patients' expectations and satisfaction it total hip arthroplasty. The Journal of Arthroplasty, 12(4), pp. 387-396.

Mansour, J. M. and Pereira, J. M., 1987. Quantitative functional anatomy of the lower limb with application to human gait cycle. J. Biomechanics 20, p, 51-58.

Marangalou, J. H., K. Ito, and Rietbergen, B. B. van., 2012. A new approach to determine the accuracy of morphology-elasticity relationships in continuum FE analyses of human proximal femur", J. Biomech., vol. 45, no. 16, pp. 2884-2892, [http://dx.doi.org/10.1016/j.jbiomech.2012.08.022]

Marin, J., 1975. Theories of strength for combined stresses and nonisotropic materials, J. Aeron. Sci., 24 (4) 265 69. 8.

Martin, R.B., Burr, D.B., Sharkey, N.A., 1998. Skeletal Tissue Mechanics. Springer Verlag, New York, pp. 32–48, 143–172

Marra, M., Vanheule, V., Fluit, R., Koopman, B., Rasmussen, J., Verdonschot, N. and Andersen, M. (2015). A Subject-Specific Musculoskeletal Modeling Framework to Predict *In-vivo* Mechanics of Total Knee Arthroplasty. Journal of Biomechanical Engineering, [online] 137(2), p.020904. Available at: http://dx.doi.org/10.1115/1.4029258.

Martelli, S., Kersh, M.E.,. Pandy, M.G., 2015. Sensitivity of femoral strain calculations to anatomical scaling errors in musculoskeletal models of movement. Journal of Biomechanics, Volume 48, Issue 13, pp. 3606-3615,

Martin, R., Burr, D. & Sharkey, N., 1998. Skeletal tissue mechanics. New York: Springer, Max. Stress Criterion, 2019. Composites failure theories. [Online] Available at: http://www.ist.edu.pk/downloads/amss/lecturers/composites-failure-theories.pdf. [Accessed 29 July 2019].

Menaka, R., Chellamuthu, C., Karthik, R., (2011) Efficient 3D Point Cloud Generation from Medical Images in Frequency Domain using Discrete Curvelet Transform. European Journal of Scientific Research ISSN 1450- 216X , Volume 60 No.2, pp. 305-315.

Meneghini, R. M., Pagnano, M. W., Trousdale, R. T. and Hozack, W. J. 2006. "Muscle Damage during Mis Total Hip Arthroplasty: Smith-Peterson versus Posterior Approach." Clinical Orthopaedics and Related Research 453, pp, 293-298.

Mero, A., & Komi, P. V. (1987). Electromyographic activity in sprinting at speeds ranging from sub-maximal to supra-maximal. Medicine & Science in Sports & Exercise, 19, 266 - 274.

Messier, S. P. et al., 2011. Does high weight loss in older adults with knee osteoarthritis affect bone-on-bone joint loads and muscle forces during walking? Osteoarthritis Cartilage, 19(3), p. 272–280.

Mirzaali MJ, Schwiedrzik JJ, Thaiwichai S, Best JP, Michler J, et al. 2016. Mechanical properties of cortical bone and their relationships with age, gender, composition and microindentation properties in the elderly. Bone. 2016;93:196–211.

Milgrom C, Radeva-Petrova DR, Finestone A, Nyska M, Mendelson S, Benjuya N, et al. 2007. The effect of muscle fatigue on *in-vivo* tibial strains. J Biomech.pp 40:845–50.]

Miller SL, Webb GR., 2008. The proximal origin of the hamstrings and surrounding anatomy encountered during repair. Surgical technique. J Bone Joint Surg Am; 90 (Suppl 2 Pt 1): 108–116.

Mishra N., Raji & Kumar, Veerendra. 2011. Biomechanical analysis of human femur bone. International Journal of Engineering Science and Technology (IJEST), ISSN : 0975-5462 Vol. 3 No. 4.,- PP3090 -3094.

Modenese, L., Gopalakrishnan, A. and Phillips, A. (2013). Application of a falsification strategy to a musculoskeletal model of the lower limb and accuracy of the predicted hip contact force vector. Journal of Biomechanics, [online] 46(6), pp.1193-1200. Available at: http://dx.doi.org/10.1016/j.jbiomech.2012.11.045.

Modenese, L., Phillips, A. and Bull, A. (2011). An open source lower limb model: Hip joint validation. Journal of Biomechanics, 44(12), pp.2185-2193.

Mo, F. et al., 2017. A Lower Limb-Pelvis Finite Element Model with 3D Active Muscles. Annals of Biomedical Engineering, Vol. 46, No. 1, January 2018 (2017) pp. 86–96 DOI: 10.1007/s10439-017-1942-1.

Moglo, K. E., and Shirazi-Adl, A., "Biomechanics of passive knee joint in drawer: load transmission in intact and ACL-deficient joints," Knee, vol. 10, no. 3, pp. 265–276, 2003. View at Publisher · View at Google Scholar · View at Scopus

Moissenet , F., Modenese , L. & Dumas, R., 2017. Alterations of musculoskeletal models for a more accurate estimation of lower limb joint contact forces during normal gait: A systematic review. Journal of Biomechanics 63, Volume 63, p. 8–20.

Molini, L., Precerutti, M., A. Gervasio, F. Draghi, S. Bianchi, 2011.Hip: Anatomy and US technique, Journal of Ultrasound, Volume 14, Issue 2,pp. 99-108.

Moncayo, V.M., Carpenter, W.A., Pierre-Jerome, C., Smitson, R.D., & Terk, M.R. 2009. Congenital absence of the semimembranosus muscle: case report. Surgical and Radiologic Anatomy, 32, 519-523.

Montanini R, Filardi V. 2010. In vitro biomechanical evaluation of integrate femoral nailing at early and late postoperative stages. Med Eng Phys.; 32pp 889-897.

Moore KL, Dalley AF. 2006. Clinically Oriented Anatomy. 5th Ed., Philadelphia, Lippincott Williams & Wilkin. 592–594, 610–617.

Moore, K. & Agur, A., 2005. Essential clinical anatomy.5th ed. Philadelphia: Lippincott Williams & Wilkins.

Mootanah, R. et al., 2014. Development and validation of a computational model of the knee joint for the evaluation of surgical treatments for osteoarthritis. Computer Methods in Biomechanics and Biomedical Engineering, Vol. 17, No. 13, 1502–1517, http://dx.doi.org/10.1080/10255842.2014.899588.

Morgan, E. F. and Keaveny, T. M., 2001. "Dependence of Yield Strain of Human Trabecular Bone on Anatomic Site." Journal of Biomechanics 34(5). Pp .569-577.

Morgan, E. F., Unnikrisnan, G. U., & Hussein, A. I., 2018. Bone Mechanical Properties in Healthy and Diseased States. Annual review of biomedical engineering, 20, 119–143. https://doi.org/10.1146/annurev-bioeng-062117-121139.

Morlock, M., Schneider, E., Bluhm, A., Vollmer, M., Bergmann, G., Muller, V. and Honl, M. 2001. "Duration and Frequency of Every Day Activities in Total Hip Patients." Journal of Biomechanics 34(7), pp, 873-881.

Morrison JB. Bioengineering analysis of force actions transmitted by the knee joint. Biomed Eng.1968; 3(4):164–170.

Morrison JB. The mechanics of the knee joint in relation to normal walking. J Biomech. 1970; 3(1):51–61.

Netter, F. H., Hansen, J. & Lambert, D., 2019. Netter's clinical anatomy, s.l.: Icon.

Ng, K. C. G. et al. (2018) 'Altered Walking and Muscle Patterns Reduce Hip Contact Forces in Individuals With Symptomatic Cam Femoroacetabular Impingement', The American Journal of Sports Medicine, 46(11), pp. 2615–2623. doi: 10.1177/0363546518787518.

Mughal, Uzair N., Khawaja, H. A. and Moatamedi M., 2015. Finite element analysis of human femur bone. Int. Jnl. of Multiphysics Volume 9 · Number 2.

Muscles of thigh, 2012. Femur. [Online] Available at: https://www.anatomynext.com/femur/.[Accessed 18 April 2020].

Nimit K. L., et al., 2016. Effect of normal gait on *in-vivo* tibiofemoral cartilage strains,Journal of Biomechanics, Volume 49, Issue 13,2016, pp. 2870-2876,

NJR, 2017. 14th Annual Report of National Joint Registry for England, Wales, Northern Ireland and the Isle of Man. [Online]

Norris, C. B. 1962. Strength of orthotropic materials subjected to combined stresses, FP.I. Report No. 1816, May, 1962.

Obbink-Huizer, C., 2020. Optimization of hip implant done with SIMULIA Abaqus & SIMULIA Tosca. [Online] Available at: https://info.simuleon.com/blog/optimization-of-hip-implant-done-with-simulia-abaqus-simulia-tosca. [Accessed 12 June 2020].

Ogle, M., 2018. hip-extension basics. [Online] Available at: ttps://www.verywellfit.com/hip-extension-basics-2704334 [Accessed 19 Novamber 2018].

Øiestad, B.E. et al., 2015. Knee extensor muscle weakness is a risk factor for development of knee osteoarthritis. A systematic review and meta-analysis Osteoarthritis and Cartilage, Volume 23, Issue 2, 171 – 177.

Olivetti, N.,2006. Development of a hills model of the human knee-thigh-hip region for frontal car crash simulations. Master's thesis, Politecnico di Milano, 2006.

OptoGait, 2012. Gait Analysis. [Online] Available at: http://www.optogait.com/Applications/Gait-Analysis. [Accessed 16 May 2020].

Oonishi, H., Isha, H., and Hasegawa. T., 1983. Mechanical analysis of the human pelvis and its application to the artificial hip joint- by means of the three dimensional finite element method. Journal of Biomechanics, 16. Pp. 427-444.

Orwoll, E. S. et al., 2009.Finite element analysis of the proximal femur and hip fracture risk in older men. Journal of Bone and Mineral Research, 24(3).

Ota, T., Yamamoto, I., and Morita. R., 1999. Fracture simulation of the femoral bone using the Finite-element method: how a fracture initiates and proceeds. Journal of bone and mineral metabolisms, 17(2):108-112.

Pandy, M. and Andriacchi, T. (2010). Muscle and Joint Function in Human Locomotion. Annual Review of Biomedical Engineering, [online] 12(1), pp.401-433. Available at: http://dx.doi.org/10.1146/annurevbioeng- 070909-105259.

Papaioannou, G., Demetropoulos, C. K. & King, Y. H., 2010. "Predicting the effects of knee focal articular surface injury with a patient-specific finite element model," Knee, vol. 17, no. 1, pp. 61–68, 2010. View at Publisher · View at Google Scholar ·

Parvizi, J., Picinic, E., and Sharkey P. F., 2009. Revision total hip arthroplasty for instability: surgical techniques and principles. Instructional course lectures, 58, pp, 183-191.

Painkra, R., Sanyal, S., Bit, A. 2018. An Anisotropic Analysis of Human Femur Bone with Walking Posture: Experimental and Numerical Analysis. Bio Nano Science (2018) 8:1054–1064 https://doi.org/10.1007/s12668-018-0560-1

Paul, J. P., 1966. Forces Transmitted By Joints in the Human Body. Institution of Mechanical Engineers, Volume 181, pp. 8-14.

Pauwels, F., 1978. Biomechanics of the Normal and Diseased Hip. Berlin Heidelberg: Springer.
Pcir, 2007. Researchers /24759123_20010101. [Online] Available at: http://www.pcir.org/researchers/24759123_20010101.html.[Accessed 11 August 2018].
Pedotti, A., 1977. A study of motor coordination and neuromuscular activities in human locomotion. Biol. Cybernetics, 26, pp. 53-62.
Peña, E. Calvo, B., Martínez, M. A and Doblaré, M, 2006. A three-dimensional finite element analysis of the combined behaviour of ligaments and menisci in the healthy human knee joint, Journal of Biomechanics, vol. 39, no. 9, pp. 1686-1701,.. s.l.:s.n.
Peña, E., Calvo, B., Martínez, M. A and Doblaré, M. 2008. "Computer simulation of damage on distal femoral articular cartilage after meniscectomies," Computers in Biology and Medicine, vol. 38, no. 1, pp. 69–81, View at Publisher ·
Perotto, A., 1992. Anatomical guide for the electromyography—the limbs and trunk Springfield: Charles C., s.l.:
Phan, M.N. et al., 2009. Functional characterization of TRPV4 as an osmotically sensitive ion channel in porcine articular chondrocytes Arthritis Rheumatol., 60 (2009), pp. 3028-3037.
Phillips A. T. M., Pankaj, P., Howie, C. R., Usmani, A. S., and Simpson, A. H. R. W., 2007. "Finite Element Modelling of the Pelvis: Inclusion of Muscular and Ligamentous Boundary Conditions," Med. Eng. Phys., 29(7), pp. 739–748.
Phillips, A. T. M., 2009. The femur as a musculo-skeletal construct: a free boundary condition modelling approach. Medical engineering & physics, 31(6), pp 673-80, 2009.
Pierrynowski, M. R. and Morrison, J. B. 1985. A physiological model for the evaluation of muscular forces in human locomotion, theoretical aspects. Math1 Biosci, 75, p. 69-101.
Pinniger, G. J., Steele, J. R., & Groeller, H. (2000). Does fatigue induced by repeated dynamic efforts affect hamstring muscle function? Official Journal of the American College of Sports Medicine, 32, 647-653. doi: 10.1097/00005768-200003000-00015.
Piszczatowski. S., 2008. Analysis of stress and strain in hip joint of the children with adductors spasticity due to cerebral palsy. Acta of Bioengineering and Biomechanics, 10:7-12.
Pitzen T, Geisler F, Matthis D, Muller-Storz H, Barbier D, Steudel WI., 2002. A finite element model for predicting the biomechanical behavior ofthe human lumbar spine. Control Engineering Practice,10(1):83–90.
Pustoc'h, A., and Cheze, L., 2009. Normal and osteoarthritic hip joint mechanical behaviour: a comparison study. Medical & biological engineering & computing, 47(4).pp.375-383.
Raikova , R. T. & Prilutskyb, B. I., 2001. Sensitivity of predicted muscle forces to parametersof the optimisation-based human leg model revealed by analyticaland numerical analyses. Journal of Biomechanics, Volume 34, p. 1243–1255.
Rakhsha M. et al., 2019. Simulation of surface strain in tibiofemoral cartilage during walking for the prediction of collagen fibre orientation, Computer Methods in Biomechanics and Biomedical Engineering: Imaging & Visualization, 7:4, 396-405, DOI: 10.1080/21681163.2018.1442751
Rapperport DJ, Carter DR, Schurman DJ. 1985. Contact finite element stress analysis of the hip joint. J Orthop Res. 3:pp. 435e446.
Rho, JY, Hobatho, MC, Ashman, RB., 1995. Relations of mechanical properties CT numbers in human bone. Med Eng Phys. 1995;17(5):347–55.
Rice, J. C., Cowin, S. C. and Bowman, J. A., 1988. "On the Dependence of the Elasticity and Strength of Cancellous Bone on Apparent Density." Journal of Biomechanics 21(2), pp. 155-168.
Richard. W., (2004). Standard Handbook of Biomedical Engineering & Design. Toronto, McGraw-Hill 1St Ed.
Richards, C., Zeni,Jr , J. & Higginson, J., 2010. Two methods to determine muscle forces and joint contact force:comparison to experimenatal muscle activity, Delaware: Department of Mechanical Engineering.
Ritchie, R. O., Kinney, J. H., Kruzic, J. J. And Nalla, R. K., 2005. A fracture mechanics and mechanistic approach to the failure of cortical bone. Fatigue & Fracture of Engineering Materials & Structures, 28: 345-371. doi:10.1111/j.1460-2695.2005.00878.

Rockville, M., April 2018. Data Resources, Content last reviewed , Agency for Healthcare Research and Quality. [Online] Available at: http://www.ahrq.gov/research/data/index.html. [Accessed 15 August 2018].

Rohen, J. W. and Yokochi, C., 1983. Colour Atlas of Anatomy. A Photographic Study of the Human Body. Igaku-Shoin Medical, New York.

Rohrle, H., Scholten, R., Sigolotto, C., Sollbach, W. and Kellner, H., 1984. Joint forces in the human pelvis-leg skeleton during walking. J. Biomechanics 17, p. 409-424.

Russell, M. E., Shivanna, K. H., Grosland, N. M., and Pedersen. D. R., 2006. Cartilage Contact pressure elevations in dysplastic hips: a chronic overload model. Journal of orthopaedic Surgery and research, pp 1:6,

Rydell, N. W. 1966. "Forces Acting on the Femoral Head-Prosthesis." Acta Orthopaedica 37(Supplement 88).pp. 1-132.

Sanchez-Adams, J., Leddy, H. A., McNulty, A. L., O'Conor, C. J., & Guilak, F., 2014. The mechanobiology of articular cartilage: bearing the burden of osteoarthritis. Current rheumatology reports, 16(10), 451. doi:10.1007/s11926-014-0451-6

Schileo, E., Dall'Ara, E., Taddei, F., Malandrino, A., Schotkamp, T., Baleani, M. and Viceconti, M., 2008. "An Accurate Estimation of Bone Density Improves the Accuracy of Subject-specific Finite Element Models." Journal of Biomechanics 41(11).pp. 2483-2491.

Schinagl, RM., Ting, MK., Price, JH. 1996. Video microscopy to quantitate the inhomogeneous equilibrium strain within articular cartilage during confined compression. Ann Biomed Eng. pp.24(4):500–12.

Schwachmeyer V, Damm P, Bender A, Dymke J, Graichen F, et al. (2013) *In-vivo* Hip Joint Loading during Post-Operative Physiotherapeutic Exercises. PLoS ONE 8(10): e77807. doi:10.1371/journal.pone.0077807.

Scott SH, Winter DA., 1990. Internal forces at chronic running injury sites. Med Sci Sports Exerc.pp. 22:357–69.

Serrancolí, G., Kinney, A., Fregly, B. and Font-Llagunes, J. (2016). Neuromusculoskeletal Model Calibration Significantly Affects Predicted Knee Contact Forces for Walking. Journal of Biomechanical Engineering, [online] 138(8), p.081001. Available at: http://dx.doi.org/ 10.1115/1.4033673.

Schaffler, MB, Burr, DB., 1988. Stiffness of compact bone: effects of porosity and density. J Biomech.21(1):13–6.

Sharcnet, 2018. Mesh skewness. [Online] Available at: https://www.sharcnet.ca/Software/Ansys/17.0/en-s/help/wb_msh/msh_skewness.html [Accessed 2019 July 26].

SHARR, 2013. Swedish Hip Arthroplasty Register Annual Rreport 2013. [Online]

Senalp A. Z., Kayabasi O., Kurtaran H., 2007. Static, dynamic and fatigue behaviour of newly designed stem shapes for hip prosthesis using finite element analysis. Materials and Design 28, pp 1577–1583.

Schulze-Bauer, C. A. J., Regitnig P., and Holzapfel, G. A., 2002. Mechanics of the human femoral adventitia including the high-pressure response. American Journal of Physiology-Heart and Circulatory Physiology, 282:6, pp 2427-2440.

Shelburne, K. B., Torry, M. R. and Pandy, M. G. 2006, Contributions of muscles, ligaments, and the ground-reaction force to tibiofemoral joint loading during normal gait cycle. J. Orthop. Res., 24: 1983-1990. doi:10.1002/jor.20255

Shelburne, K.B., Pandy, M.G., Anderson, F.C., Torry, M.R., 2004. Pattern of anterior cruciate ligament force in normal walking. Journal of Biomechanics 37, pp, 797–805.

Shelburne, Kevin & Torry, Michael & G Pandy, Marcus. 2005. Muscle, Ligament, and Joint-Contact Forces at the Knee during Walking. Medicine and science in sports and exercise. 37. 1948-56. 10.1249/01.mss.0000180404.86078.ff.

Silvestri C. and Ray, M. H., 2009. Development of a finite element model of the knee- thigh-hip of a 50th percentile male including ligaments and muscles. International Journal of Crashworthiness, 14, pp, 215 229.

Silvestri C., Mongiardini, M., and Ray, M. H., 2009. Improvements and validation of an existing LS-DYNA model of the knee-thigh-hip of a 50th percentile male including muscles and ligaments. In 7th European LS-DYNA Conference,.

Silvestri. C., 2008. Development and validation of a knee-thigh-hip LSDYNA model of a 50th percentile male. PhD thesis, Worcester Polytechnic Institute.

Sivananthan, S., Sherry, E., Warnke, P. & D Miller, M., 2012. Mercer's Textbook of Orthopaedics and Trauma. Tenth ed. NW: Taylor and Francis Group.

Small, S.R. et al., 2017. Characterization of Femoral Component Initial Stability and Cortical Strain in a Reduced Stem-Length Design, The Journal of Arthroplasty, Volume 32, Issue 2,PP. 601-609,

Smith SM, Cockburn RA, Hemmerich A, Li RM, Wyss UP., 2008. Tibiofemoral joint contact forces and knee kinematics during squatting. Gait & posture. 27(3):376–386.

Snell, R. S. 1973, Clinical Anatomy for Medical Students. Little, Brown, Boston, MA.

Stansfield, B. W., Nicol, A. C., Paul, J. P., Kelly, I. G., Graichen, F. and Bergmann, G., 2003. "Direct Comparison of Calculated Hip Joint Contact Forces with Those Measured Using Instrumented Implants. An Evaluation of a Three-Dimensional Mathematical Model of the Lower Limb." Journal of Biomechanics 36(7), pp. 929- 936.

Steele, K., DeMers, M., Schwartz, M. and Delp, S. (2012). Compressive tibiofemoral force during crouch gait cycle. Gait & Posture, [online] 35(4), pp.556-560. Available at: http://dx. doi.org/10.1016/j.gaitpost.2011.11.023.

Stegeman, D. F., & Hermens, H. J. 1998. Standards for surface electromyography: the European project "Surface EMG for non-invasive assessment of muscles (SENIAM)". Aachen: SENIAM.

Streifeneder, 2016. Eight phases of the human gait cycle. [Online] Available at: https://www.streifeneder.com/downloads/o.p./400w43_e_poster_gangphasen_druck.pdf [Accessed 8 August 2018].

Subburaj, Karupppasamy & Ravi, B & Agarwal, Manish. 2010. Computer-aided methods for assessing lower limb deformities in orthopaedic surgery planning. Comp. Med. Image and Graph. 34. 277-288.

Sun, W., Starly, B., Nam, J., Darling, A, (2005) Bio-CAD modeling and its applications in computer-aided tissue V.N. Chougule et al. / Procedia Engineering 97 (2014) 212 – 219 219 engineering. Computer-Aided Design , Volume 37 , p. 1097–1114.

Taddei, F., Martelli, S., Reggiani, B., Cristofolini, L., and Viceconti. M., 2006. Finite element modelling of bones from CT data: sensitivity to geometry and material uncertainties. IEEE transactions on bio-medical engineering, 53(11):2194-2200.

Taylor, M. & Prendergast, P., 2015. Four decades of finite element analysis of orthopaedic devices: where are what and we now are the opportunities? J Biotech. 18; 48(5), pp. 767-78.

Taylor, S. J. G. and Walker, P. S., 2001. "Forces and Moments Telemetered from Two Distal Femoral Replacements During Various Activities." Journal of Biomechanics 34(7).pp. 839-848.

Taylor, M., Tanner, K. E., Freeman, M. A. R., and Yettram, A. L., 1995. "Cancellous Bone Stresses Surrounding the Femoral Component of a Hip Prosthesis: An Elastic-Plastic Finite Element Analysis," Med. Eng. Phys., 17(7), pp. 544–550.

Teitz, C. & Graney, D., 2003. Musculoskeletal Atlas: A Musculoskeletal Atlas of the Human Body". [Online] Available at: https://depts.washington.edu [Accessed 06 August 2018].

The American Academy of Orthopaedic Surgeons, 2010. [Online] Available at: https://www.aaos.org. [Accessed 7 September 2018].

Thomas. Peng L, Bai J, Zeng X, Zhou Y., 2006. Comparison of isotropic and orthotropic material property assignments on femoral finite element models under two loading conditions. Medical Engineering and Physics; 28(3):227–33.

Thompson, J.F. Soni, B.K. and Weatherill, N.P., 1999. Handbook of grid generation. CRC Press.

Thorpe, M., 2015. Human-body. [Online] Available at: https://www.healthline.com/human-body-maps/rectus-femoris-muscle#1[Accessed 5 August 2018].

Tozeren, A., 2000. Human Body Dynamics: Classical Mechanics and Human Movement. New York: Springer.

Trinler, U., Schwameder, H., Bakera, R. & Alexander, N., 2019. Muscle force estimation in clinical gait analysis using AnyBody and OpenSim. Journal of Biomechanics, Volume 86, p. 55–63.

Unsworth AA, Dowson DD, Wright VV., 1975. Closure to "Discussion of 'the Frictional Behaviour of Human Synovial Joints—Part I: Natural Joints', ASME J. Lubr. Technol., 97, p. 376). ASME. J. of Lubrication Tech. 1975; 97(3):376. doi:10.1115/1.3452607.

Van der Plas, A., 2014. Fracture general principles. [Online] Available at: http://www.startradiology.com/the-basics/fracture-general-principles.[Accessed 7 September 2018].

Vaughan, C., Davis, B., and O'Connor, J.C., 1999. Dynamics of Human Gait cycle. Kiboho, Cape Town, South Africa, 2nd edition.

Verim, Ö, Taşgetiren, S., ER, M.S., et al. 2013. Anatomical comparison and evaluation of human proximal femurs modelling via different devices and FEM analysis. Int. J Med Robot Compute Assist Surg, 12.pp. 459-897.

Van Wynsberghe, D. V., Noback, C. R. and Carola, R. 1995. Human Anatomy & Physiology, WCB/McGraw-Hill.

Venäläinen, M.S. et al., 2016. Effect of bone inhomogeneity on tibiofemoral contact mechanics during physiological loading. Journal of Biomechanics Volume 49, Issue 7(3), pp.1111-1120.

Viceconti, M. et al., 2000. Large-sliding contact elements accurately predict levels of bone-implant micro motion relevant to osseointegration. Journal of Biomechanics, 33(12), pp. 1611-1618.

Voo, L., Armand, M. & Kleinberger, M., 2005. Stress Fracture Risk Analysis of the Human Femur Based on Computational Biomechanics. Johns Hopkins Apl. Technical Digest, 25(3), p. 224.

Wang, M., Wang, L., Li, P., & Fu, Y. 2017. A novel modelling and simulation method of hip joint surface contact stress. Bioengineered, 8(1), 105–112. doi:10.1080/21655979.2016.1227630.

Wang, J., Ye, M., Liu, Z., Wang, C., 2009. Precision of Cortical Bone Reconstruction Based on 3D CT Scans. Computerized Medical Imaging and Graphics, Volume 33, p. 235–241.

Wang, X., Breton-Gadegbeku, B.L., Bouzon, L., 2004. Biomechanical evaluation of the comfort of automobile clutch pedal operation. Int. J. Ind. Ergon., 34 (3), pp. 209-221.

Widmyer, M.R. et al., 2013. High body mass index is associated with increased diurnal strains in the articular cartilage of the knee Arthritis Rheumatol., 65 pp. 2615-2622

White, C., Yack, H. & Winter, D., 1989. A three-dimensional musculoskeletal model for gait analysis. Anatomical variability estimates. Journal of biomechanics, 22(8/9), p. 885-983.

Wang, X., et al., 2010, Fundamental Biomechanics in Bone Tissue Engineering, Synthesis Lectures on Tissue Engineering, Morgan & Claypool Publisher, Vol. 2, No. 1, PP 75-86, https://doi.org/10.2200/S00246ED1V01Y200912TIS004.

Winter, D. A., 2009. Biomechanics and Motor Control of Human Movement. Fourth ed. Waterloo, Ontario, Canada: Wiley.

Winters, J. M., 1990. Hill-based muscle models: a systems engineering perspective. Springer-Verlag Berlin and Heidelberg GmbH & Co. K, 1990.

Wright, T.M., Hayes, W.C., 1976. Tensile testing of bone over a wide range of strain rates: effects of strain rate, microstructure and density. Med. & biol. Engng. 14, 671 (1976). https://doi.org/10.1007/BF02477046.

Yoo, D. J., (2011) Three-dimensional surface reconstruction of human bone using a B-spline based interpolation approach. Computer-Aided Design, Volume 43, p. 934–947.

Yang NH, Canavan PK. & Nayeb-Hashemi H., 2010. The effect of the frontal plane tibiofemoral angle and varus knee moment on the contact stress and strain at the knee cartilage. Journal of Applied Biomechanics; 26: 432–43. PMID: 21245503.

Yang G, Kabel J, van Rietbergen B, Odgaard A, Huiskes R, Cowin SC. 1999. The anisotropic Hooke's law for cancellous bone and wood. Journal of Elasticity.53:125–46.

Yosibash, Z., Padan, R., Joskowicz, L., and Milgrom, 2007. A CT-based high-order Finite element analysis of the human proximal femur compared to in-vitro experiments. Journal of biomechanical engineering, 129(3):297-309.

Yoshida, H. A. Faust, J. Wilckens, M. Kitagawa, J. Fetto, and E. Y. S. Chao. 2006. Three-dimensional dynamic hip contact area and pressure distribution during activities of daily living. Journal of Biomechanics, 39:pp.1996-2004,

Yoshikawa T, Mori S, Santiesteban AJ, Sun TC, Hafstad E, Chen J, et al. 1994. The effects of muscle fatigue on bone strain. J Exp Biol. 188:217–33.

Zaidi, H., Erwin, W. D.., (2007) Quantitative Analysis in Nuclear Medicine Imaging. 10.2967/jnumed.107.042598, J.Nucl.Med., Volume 48(8).

Zavatsky, A., et al., 2014. Influence of altered gait patterns on the hip joint contact forces, Computer Methods in Biomechanics and Biomedical Engineering, 17:4, 352-359, DOI: 10.1080/10255842.2012.683575.

Zioupos, P., Cook, R. B. and Hutchinson, J. R., 2008. "Some Basic Relationships between Density Values in Cancellous and Cortical Bone." Journal of Biomechanics 41(9): pp, 1961-1968.

Zimmermann, E., Schaible, E., Gludovatz, B. et al. 2016. Intrinsic mechanical behaviour of femoral cortical bone in young, osteoporotic and bisphosphonate-treated individuals in low- and high energy fracture conditions. Sci Rep 6, 21072 (2016). https://doi.org/10.1038/srep21072.

Zhang, X., Chen, Z., Wang, L., Yang, W., Li, D. and Jin, Z. (2015). Prediction of hip joint load and translation using musculoskeletal modelling with force-dependent kinematics and experimental validation. Proceedings of the Institution of Mechanical Engineers, Part H: Journal of Engineering in Medicine, [online] 229(7), pp.477-490. Available at: http://dx.doi.org/10.1177/0954411915589115.

Zhang, J.,Yan, C. H., Chui, C. K., Ong,S. H., (2010) Fast segmentation of bone in CT images using 3D adaptive thresholding. Computers in Biology and Medicine, Volume 40, p. 231–236.

Zhao, D., Banks, S.A., Mitchell, K.H., D'Lima, D.D., Colwell, C.W., Fregly, B.J., 2007. Correlation between the knee adduction torque and medial contact force for a variety of gait patterns. Journal of Orthopaedic Research 25, pp, 789–797.

Appendices

Appendix A: Overview of selected Computational Modelling to Predict HCF

Appendix A: Overview of selected computational modelling including generic musculoskeletal model, validation method, and hip and tibiofemoral joint contact force accuracy.				
Reference	Joint	Musculoskeletal model	Validation method	Outcome
Chen et al., (2014)	TF	Software: Anybody Model: Variant of the Horsman et al., (2007) model DoFs: 6 pelvis, 3 hip, 1 TF, 1 ankle, 1 subtalar Muscular lines of action: 163 per leg Muscle path: Via points and wrapping surfaces Optimisation: Inverse dynamics-based optimisation Objective function: Min-max muscle recruitment Subjects : Mass 78.4 kg, height 167 cm, left knee	Using pervious study: Third edition data of the Grand Challenge Competition to Predict *In-vivo* Knee Loads (Fregly et al., 2012)	Conclusion: Alterations slightly impacted TF contact force Total contact forces was reported Approximately: 2600 N 3.3 x BW
DeMers et al., (2014)	TF	Software: OpenSim Model: Variant of the Delp (1990) model DoFs: 6 pelvis, 3 hip, 1 TF, 1 ankle Muscular lines of action: 46 per leg Muscle path: Via points Optimisation: Inverse dynamics-based optimisation Objective function: Sum of squared muscle activations and joint loads Joint contact model: One-point rigid contact model (Steele et al., 2012) Subject: 83-year-old male, Mass 64 kg , Height :166 cm	Using pervious study: Third edition data of the Grand Challenge Competition to Predict *In-vivo* Knee Loads (Fregly et al., 2012)	Conclusion: A wide range of TF contact force, and thus model accuracy, can be obtained depending on the objective function Results: 2.3 x BW

Dumas et al, (2012)	TF & Hip	Software: Matlab Model: Variant of the Delp (1990) model DoFs: 6 pelvis, 3 hip, 1 TF, 1 ankle Muscular lines of action: 43 per leg Muscle path: Via points Optimisation: Inverse dynamics-based optimisation Objective function: Sum of squared muscle stresses Joint contact model: Two-point rigid contact (Feikes et al., 2003). Subject: Male - (67 kg , 172 cm)	Using pervious study: Third edition data of the Grand Challenge Competition to Predict *In-vivo* Knee Loads (Fregly et al., 2012)	Conclusion: The use of hinge joints with coupled DoFs at knee and ankle, and the introduction of passive joint moments, improved model accuracy Results: Averaged across 8 models reported in (Superior – inferior): Hip joint: 4.5 x BW (Approx.) TF joint: 4.3 x BW (Approx.)
Guess et al., (2014)	TF	Software: ADAMS and Simulink/Matlab Model: Variant of the Delp (1990) model DoFs: 6 pelvis, 3 hip, 6 TF, 6 PF, 3 ankle, 1 toe Muscular lines of action: 44 per leg Muscle path: Via points Optimisation: Forward dynamics-based Joint Contact model: Deformable contact with viscous damping (Machado et al., 2012) subject : 166 cm height, Mass: 64.6 kg	Using pervious study: Third edition data of the Grand Challenge Competition to Predict *In-vivo* Knee Loads (Fregly et al., 2012)	Conclusion: A decrease of PID gain improved model accuracy Results: Accelerating gait cycle TF Medial :650 $\pm$ 20 N(Approx.) = 1.02 x BW TF Lateral :880 $\pm$ 20 N (Approx.) = 1.31 x BW
Hast and Piazza, (2013)	TF	Software: SIMM Model: Variant of the Delp (1990) model DoFs: 6 pelvis, 3 hip, 6 TF, 6 PF, 1 ankle Muscular lines of action: 13 per leg Muscle path: Via points and wrapping surfaces Optimisation: Computed muscle control EMGs (inverse dynamics level)	Using pervious study: Third edition data of the Grand Challenge Competition to Predict *In-vivo* Knee Loads	Conclusion: A decrease of maximum isometric forces led to a decrease of TF contact forces and an improvement of model accuracy Results: Averaged across the three trials Magnitude of TF contact forces: 2.9 $\pm$ 0.2 x BW

		Joint contact model: Rigid body spring model (Li et al.,1997) Subject: An adult male age 83 year; mass: 67 kg; height 172 cm.	(Fregly et al., 2012)	
Heller et al., (2001)	Hip	Software: Custom-made software Model: Own model based on VH project (Ackerman, 1991) DoFs: 6 pelvis, 3 hip, 6 TF, 3 ankle Muscular lines of action: 95 per leg Muscle path: Via points Optimisation: Inverse dynamics-based optimisation Objective function: Sum of musculotendon forces Joint contact model: One-point rigid contact model	Using pervious study: HIP98 (Data of subjects HSR, KWR, PFL, IBL) (Bergmann, et al., 2001) HIP98 (Typical patient, averaging procedure based on Fourier analysis) (Bergmann, et al., 2001)	Conclusion: An increase of femoral anteversion led to an increase of hip contact forces and a decrease in model accuracy, while a decrease of femoral anteversion led to little or no change Results: Hip superior-inferior contact force 2.8 - 3.8 ($\pm$ 0.1) x BW
Lerner et al., (2015)	TF	Software: OpenSim Model: Variant of the Delp (1990) model DoFs: 6 pelvis, 3 hip, 1 TF, 1 ankle, 1 subtalar Muscular lines of action: 64 per leg Muscle path: Via points Optimisation: Inverse dynamics-based optimisation Objective function: Sum of squared weighted muscle activations, with subject-specific weights minimizing peaks error in TF contact forces (calibrated with validation data) Subject: Male, Age 83, mass 67 kg, Height 172 cm	Second edition data of the Grand Challenge Competition to Predict *In-vivo* Knee Loads (Fregly et al., 2012)	Conclusion: Improvement of knee alignment and contact points location increased model accuracy Quantitative evidence: For Uniformed model First peak medially = 1234 – 1461 N And laterally = 319 – 502 N Max: 1.8 x BW Second peak medially: 786 –1244 N And laterally : 85–417 N

				Max: 1.52 x BW
Lund et al., (2015)	TF	Software: Anybody Model: Variant of the Klein Horsman et al. (2007) model DoFs: 6 pelvis, 3 hip, 1 TF, 1 PF, 2 ankle Muscular lines of action: 159 per leg Muscle path: Via points and wrapping surfaces Optimisation: Inverse dynamics-based optimisation Objective function: Sum of cubed muscle activations Joint contact model: One-point rigid contact Subject: 68 year-old woman, Height 163 cm, Mass 68 kg.	Third edition data of the Grand Challenge Competition to Predict *In-vivo* Knee Loads (Fregly et al., 2012) (1) Linear scaling (baseline) (2) Anatomical scaling (3) Kinematic scaling	Conclusion: Kinematic scaling (3) provided the most accurate TF total contact force and was the method less affected by marker placements errors Quantitative evidence: Maximum force in different stance phases (1) 2.53-3.79 x BW (2) 3.21 – 4.24 x BW (3) 1.63 – 2.11 x BW
Lundberg et al, (2013)	TF	Software: Matlab Model: Knee model, variant of the Delp (1990) model DoFs: 6 TF Muscular lines of action: 15 (reduced to 3) Muscle path: Via points Optimisation: Not used. A model reduction is applied to cancel muscular redundancy, and equations governing dynamic equilibrium and relationship between medial and lateral contact forces are solved Objective function: Not used Joint contact model: Linear function of the varus-valgus moment Subject: Female, Height 167 cm, weight 78.4 kg.	Third edition data of the Grand Challenge Competition to Predict *In-vivo* Knee Loads (Fregly et al., 2012)	Conclusion: The alterations improved the model accuracy in estimating medial and lateral contact forces, while keeping a similar total contact force Outcome: Maximum force: 2186 N 2.8 x BW

Manal and Buchanan, (2013)	TF	Software: SIMM Model: Variant of the Delp (1990) model DoFs: 6 pelvis, 3 hip, 3 TF, 3 ankle Muscular lines of action: 12 Muscle path: Via points Optimisation: EMG-driven Objective function: Sum of squared differences between estimated and inverse dynamic-based joint moments Joint contact model: Two-point rigid contact Subject: female – mass : 78.4 kg, Height: 167 cm	Third edition data of the Grand Challenge Competition to Predict *In-vivo* Knee Loads (Fregly et al., 2012)	Conclusion: An iterative process of parameters' variations allowed to improve the model accuracy Quantitative evidence: Medial and lateral Contact forces was Medial :1.78 BW Lateral : 0.5 BW
Modenese et al. (2011)	Hip	Software: OpenSim Model: Variant of the Klein Horsman et al. (2007) model DoFs: 6 pelvis, 3 hip, 1 TF, 1 ankle Muscular lines of action: 163 per leg Muscle path: Via points and wrapping surfaces Optimisation: Inverse dynamics-based optimisation Joint contact model: One-point rigid contact HSR - Male Age: 55- Mass: 860- Height : 174 cm KWR -Male Age: 61- Mass: 702- Height : 165 cm PFL-Male Age: 51- Mass: 980- Height : 175 cm IBL-Female Age: 76- Mass: 800- Height : 170 cm	HIP98 (Data of subjects HSR, KWR, PFL, IBL) (Bergmann, et al., 2001)	Conclusion: A quadratic objective function provided a better model accuracy than other powers in terms of hip contact force and muscular-tendon forces estimation Quantitative evidence: RMSE averaged range across subjects Averaged cross all subjects 2.8 - 4.2 x BW
Serrancoli et al., (2016)	TF	Software: OpenSim Model: Variant of the Arnold et al. (2010) model DoFs: 6 pelvis, 3 hip, 6 TF, 6 PF, 2 ankle Muscular lines of action: 44 per leg Muscle path: Via points and wrapping surfaces	Fourth edition data of the Grand Challenge Competition	Conclusion: Tracking validation data improved model accuracy Quantitative Results: Total Knee contact force: 1570 N 2.45 x BW

		Optimisation: Inverse dynamics-based optimisation Objective function: Sum of squared muscle activations plus sum of six squared reserve activations Joint contact model: Validated regression equation converting superior-inferior force and varus-valgus moment to medial and lateral contact forces (Fregly et al., 2012) subject: male, age: 88 yrs, Mass: 65 kg, Height: 166 cm	to Predict *In-vivo* Knee Loads (Fregly et al., 2012)	

Appendix B: The local origins and insertion of bony-muscles landmarks of the musculoskeletal

The local origins and bony-muscles landmarks of the musculoskeletal. All magnitudes are estimated as mean points from their local origins (cm) (White, et al., 1989).				
Bone & muscle segments	LASs (Local origins)	Mean position (cm)		
		X	Y	Z
Pelvis (RASIS)	Point a	0.0	0.0	0.0
LASIS (Bony segment)	From point a	-2.1	0.0	-23.3
RPT (Bony segment)	From point a	-1.1	-7.9	-9.5
Femur (GTROCH)	Point b	0.0	0.0	0.0
MEDEP (Bony segment)	From point b	-3.1	-40.3	-12.5
LATEP (Bony segment)	From point b	-2.0	-40.9	-2.8
TIBITUB	Point c	0.0	0.0	0.0
MEDMAL	From point c	-4.8	-32.2	-5.2
LATMAL	From point c	-6.1	-34.3	0.1
HEEL	Point d	0	0	0
Muscles origin and incretion		X	Y	Z
SOL	Origin (From point c)	-4.2	-3.2	0.1
	Insertion (From point d)	1.0	0.0	0.2
GAS (LAT , MED)	Origin (From point b)	-2.6 , -2.0	-39.3 / -38.0	-4.9 / -7.9
	Insertion (From point c)	0.5 , 0.5	0.0 , 0.0	0.2 , 0.2
GRA	Origin (From point a)	-5.3	-10.8	-10.4
	Insertion (From point b)	-1.9	0.0	-1.4
ST	Origin (From point a)	-12.2	-10.0	-4.9
	Insertion (From point b)	-2.3	-0.5	-1.1
SM	Origin (From point a)	-11.0	-9.9	-4.4
	Insertion (From point b)	-4.6	1.4	-1.5
VIM	Origin (From point b)	1.7	-14.7	-4.0
	Insertion (From point c)	0.0	0.0	0.0
SAR	Origin (From point a)	-1.2	-1.1	-0.2
	Insertion (From point b)	-1.6	-0.5	-1.1
IPSOAS (muscle)	Origin (From point a)	-3.1	-4.5	-3.8
	Insertion (From point b)	-2.3	-3.4	-7.2
GMAX	Origin (From point a)	-15.1	-1.4	-6.8
	Insertion (From point b)	-1.5	-7.5	-4.2
ADM	Origin (From point a)	-9.2	-11.9	-7.3
	Insertion (From point b)	-1.0	-21.1	-6.7
ADLB	Origin (From point a)	-4.7	-10.0	-10.2
	Insertion (From point b)	-1.2	-10.1	-5.4
GMEDA	Origin (From point a)	-2.6	1.9	1.1
	Insertion (From point b)	-0.9	1.3	-2.0
BF	Origin (From point b)	-0.4	-18.3	-4.1
	Insertion (From point c)	-3.9	1.2	3.1
RF	Origin (From point b)	-2.4	-4.0	-1.7
	Insertion (From point c)	0.0	0.0	0.0.
VL	Origin (From point b)	-0.3	-3.0	-2.2
	Insertion (From point c)	0.0	0.0	0.0

VM	Origin (From point b)	-0.3	-9.0	-4.4
	Insertion (From point c)	0.0	0.0	0.0

Appendix C: The EMG of hip muscles to obtain muscle contraction adapted from Anderson & Pandy, (2001).

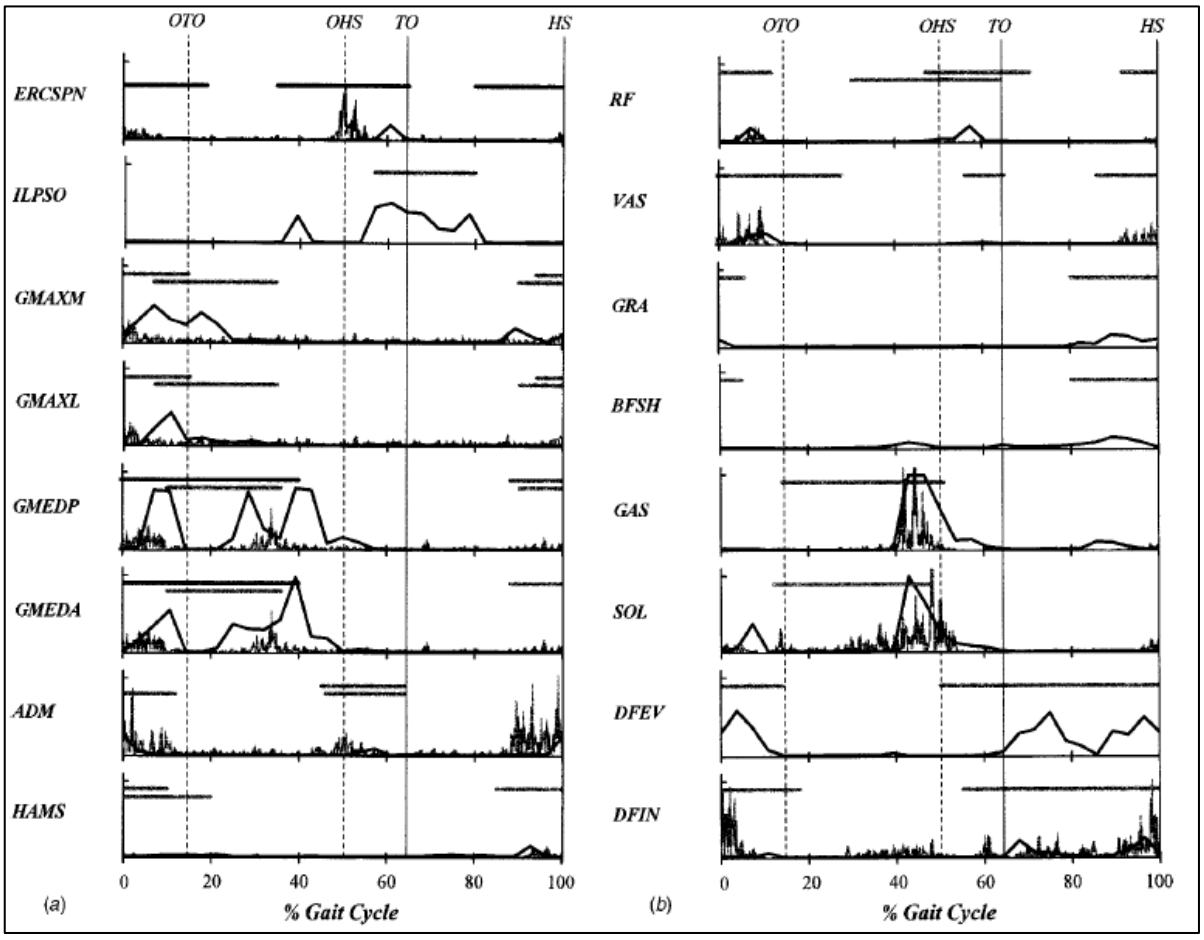

Appendix C: The EMG of hip muscles to predict the muscle contraction. Data was recorded for a subject (grey wavy lines) which normalized. The EMG model for muscle excitation was calibrated from zero to one (Adapted from Anderson & Pandy, 2001).

Appendix D: Method to Find Best-Fitted Graph for the Femoral Region

For the current CAD model, in order to determine the radius-distance function, the datasets used 23 parallel planes to the A-section of the femur. The best-fitted curve demonstrates the radius of any plane at the preferred coordinate from the origin point along with the head-neck axis accurately. Although the R-squared could be aided to select the best curve, nonetheless the residual function is selected to determine the best-fitted curve. The residual function was preferred due to accumulation of positive and negative variances between the actual values and estimated values and showing as positive value. The best fitted-graph shows the lowest residual value. The Eq. () defines the residual function (Hyndman & Koehler, 2006).

$$\mathrm{RS} = \sum_{i=1}^{i=n} (\hat{y}_i - y_i)^2 \qquad (D-1)$$

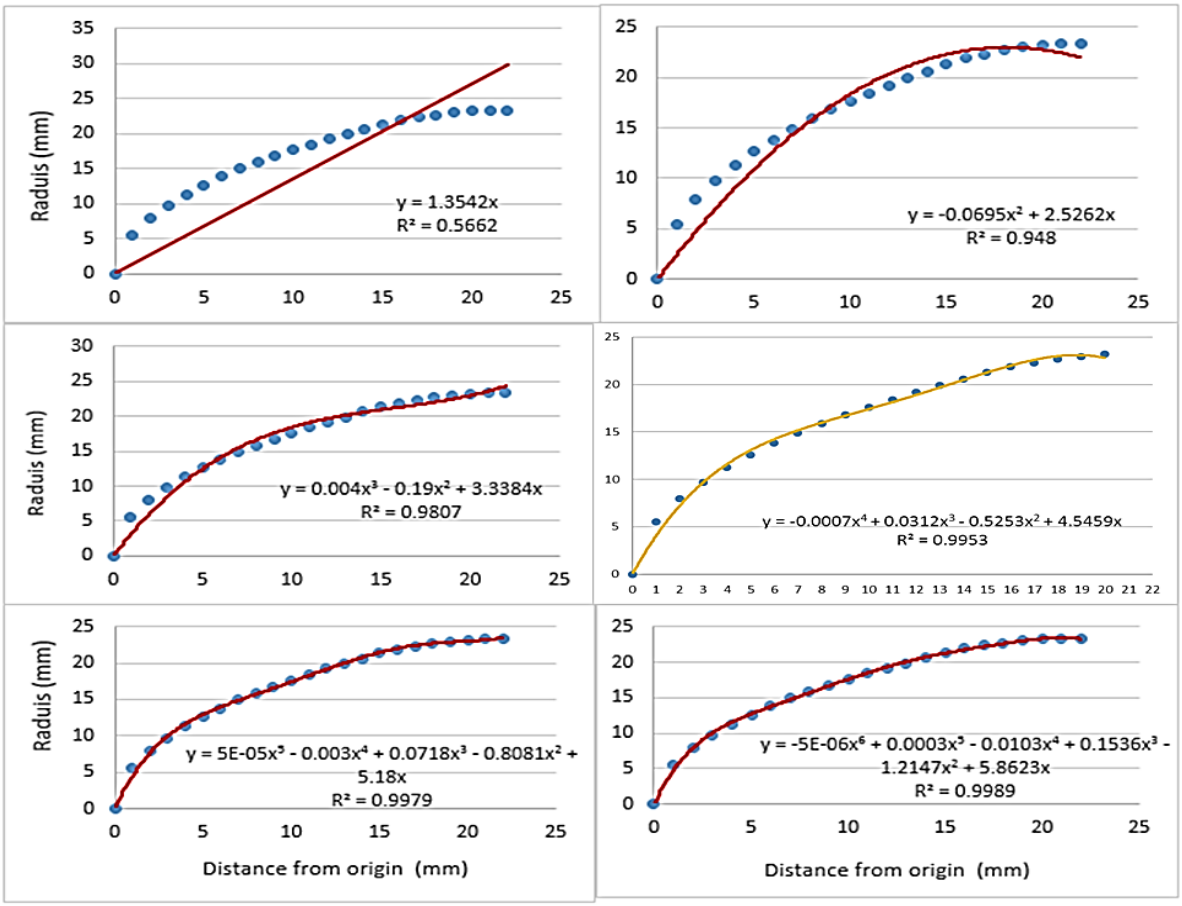

Figure D-1: The fitted-curve process to determine the best polynomial graph (red solid line) to the femoral head profile (blue dots). The best-fitted equations and their regressions are displayed. The yellow solid line selected as a best-fitted graph.

The best-fitted curve to the femoral section A is reported as follows

$$\mathrm{R(z)} = -0.0007\ (\mathrm{z}^4) + 0.0312\ (\mathrm{z}^3) - 0.5253\ (\mathrm{z}^2) + 4.5459\ (\mathrm{z}) \qquad (\mathrm{D}-2)$$

Where n is the number of the observations, $\hat{y}_i$ is the predicted value, and y_i the actual value. Figure D-2 demonstrates logarithmic scale the actual value of the residual values for the obtained graphs. It can be certified that the fourth degree polynomial graph shows the minimum residual value and therefore is selected for the best-fitted graph.

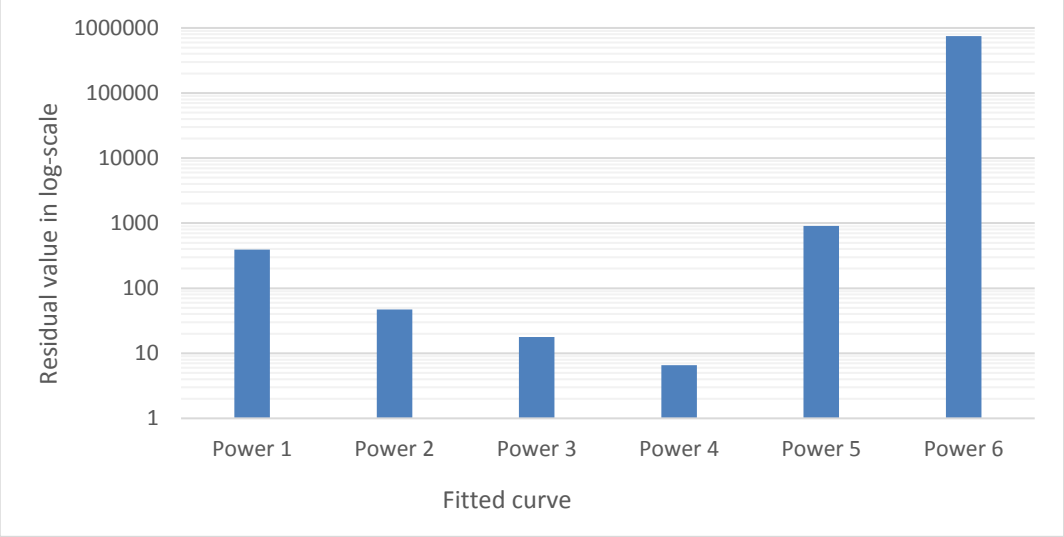

Figure D-2: The logarithmic scale of the residual values for the six nominated fitted-curve. The best-fitted curve has minimum residual value.

The Root Means Squared Error (RMSE) (Eq. D-3) used to obtain the mean error of the estimated value computed from the governed equation (Eq. D-2). The RMSE of the developed equation is the 0.21%, which shows the prediction power of the equation (Hyndman & Koehler, 2006).

$$RMSE = \sqrt{\frac{\sum_{i=1}^{i=n}(\hat{y}_i - y_i)^2}{n}} \qquad (D-3)$$

Where n is the number of observations points, $\hat{y}_i$is the predicted value, and y_i the actual value. Figure D-3 shows the RMSE for the point-to-point analysis between the actual values and estimated values for the femoral head. It can be seen that the 90% of given radius by the governed equation have RMSE less or equal 0.22. While the maximum variety of the given radius can be realised at the second superior plane of the femur towards the superior-inferior plan on the femoral head-neck axis. The points of interest for the femoral head study are located the mid-plane (9 and 10 mm) and at the end plane (18, 19, or 20 mm) where the mean error presented zero variance. Hence, it can be acknowledged that the governed equation can determine the radius and subsequently area of any planes along with the femoral head-neck axis accurately.

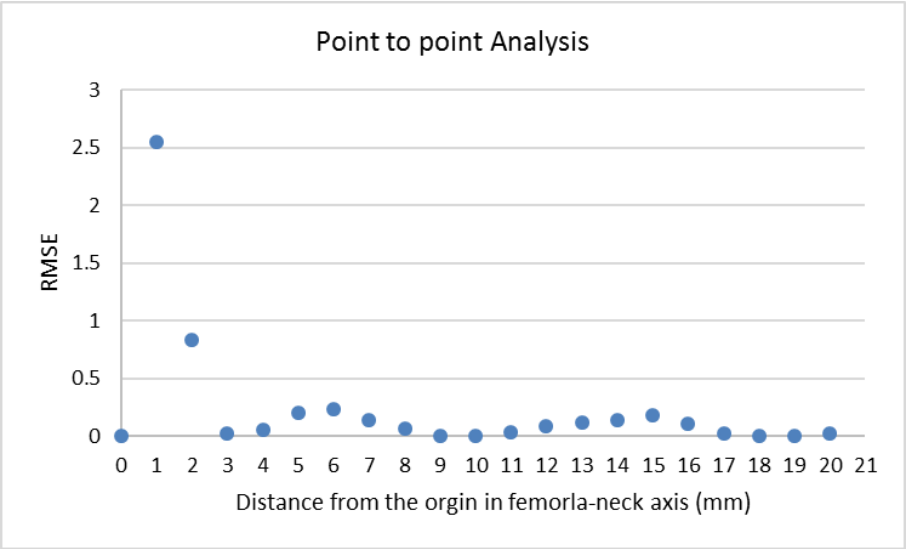

Figure D-3: The Point to point analysis of RMSE between the observed values and the predicted values.

Appendix E: Review Mesh Generation Studies

Recently, the study and evaluation of 3D geometry becomes possible and practical due to the increased resolution meshes created by PCs. Dalstra et al., (1995) generated the primary high-resolution hexahedral meshes for the pelvis by using an extensive layer of shell elements (shell; shell) for the cortical bone, which just convey in plane stress. This technique is a questionable approach for dense cortical bone. Many investigations (Russell et al., 2006; Silvestri & Ray, 2009; Anderson, et al., 2010) adopted the sandwich model method for meshing cancellous and cortical bone, which has recently, becomes a more fashionable technique.

Bachtar et al., (2006) produced a hexahedral mesh of the hip joint and cortical bone, which was demonstrated by 3D continuum elements. Nevertheless, the mesh had numerous unphysical-toothed edges with low resolution and quality. Several researchers conducted FEA studies using hexahedral meshes for the femur and hip joint region with various˚ of resolution (Russell et al., 2006; Silvestri, 2008; Pustoc'h, & Cheze, 2009). It is very difficult to generate the quality of hexahedral meshing for the complex shape such as femur. Hence, application of the smoothing technique to simplify the surfaces of the femur is required which could damage the primary geometry. Due to the significance of making great quality hexahedral meshes of bones, Grosland et al. (2009) developed an open-source meshing software, IA-FEMesh, which used the the multi-block strategy. On the other hand, the unstructured tetrahedral meshes were most widely used to mesh the femur. Despite the fact that it is a generally automated procedure, generation of a decent

quality tetrahedral mesh is not generally an insignificant issue (Cilingir, et al., 2007; Piszczatowski. 2008; Anderson, et al., 2009; Anderson, et al., 2010). Anderson et al., (2010) conducted a study to determine the maximum pressure on the hip joint compartments using hexahedral volumetric mesh for the femur. However, for the other parts of their system tetrahedral meshing system were applied. There is another technique to determine the mesh for the lower limb for the CT-Based models using bone specifications which allocated in CT Hounsfield intensities (Ota et al.,1999; Yosibash et al., 2007; Orwoll, et al., 2009). This method indicates a progression on the more customary biomaterial Sandwich Model method. However, the correct exact connection between Hounsfield stiffness and the intensity can be hard to define and can rely upon the subject and scanner (Taddei, at al., 2006; Yosibash et al., 2007). Table E-1 summarised the statics of the provided mesh for eight activated bodies as well as the value of skewness as a quality criterion to check metric of the provided mesh reported. according to SHARCNet, (2018) the Skewness criterion is one of the primary quality measures for the complex geometries which shows how the provided mesh by software is closed to the ideal situation of a face or cell.

Table E-1: The statistic of the provided mesh and the skewness criterion.

Active Bodies	8	Value of Skewness	Cell Quality
Nodes	572440	1	Degenerate
Elements	380112	0.9 — <1	Bad (sliver)
Mesh Metric	**Skewness**	0.75 — 0.9	Poor
Min	5.9096268E-04	0.5 — 0.75	Fair
Max	0.9999629	0.25 — 0.5	Good
Average	0.2390007	> 0.25	Excellent
Standard Deviation	0.130059	0	Equilateral

Figure E-2 shows that most of the mesh cells are tetrahedral and hexahedron which created the maximum numbers of elements in less than 0.25 which was interpreted as an excellent type of mesh. The second part of the graph shows that the mesh metric was placed between 0.25 to 0.5, which interpreted as good quality of mesh according to the skewness criterion.

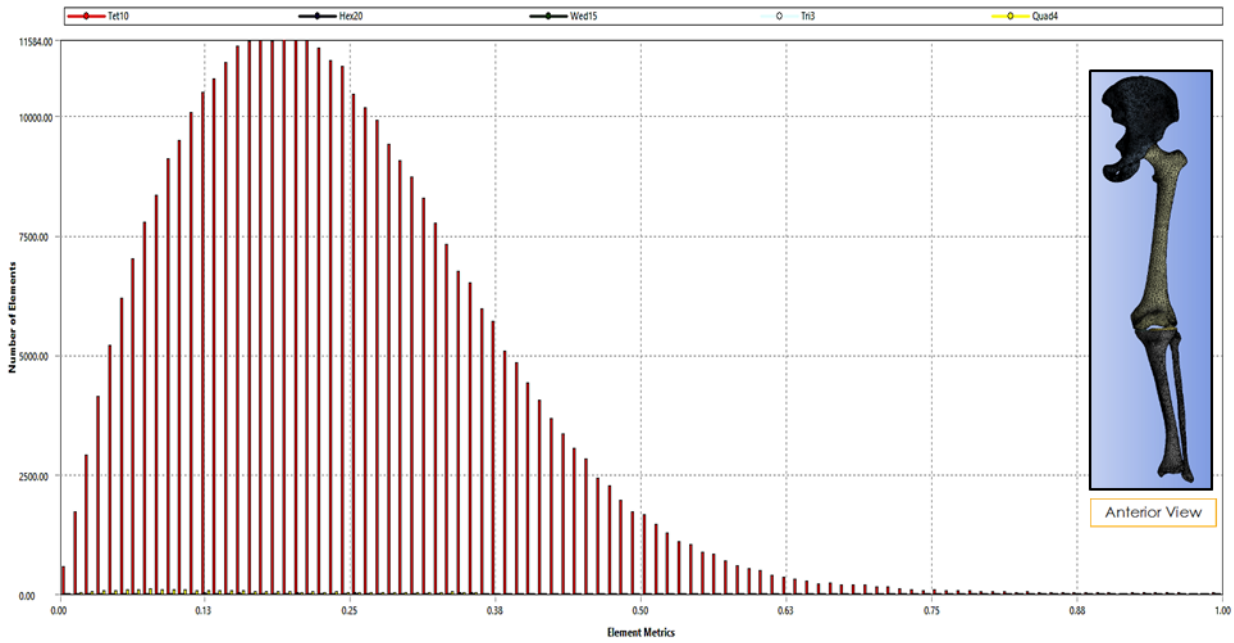

Figure E-2: Illustration of the skewness as a quality criterion of the created mesh for the numerical approach (Ansys R1. 2018).

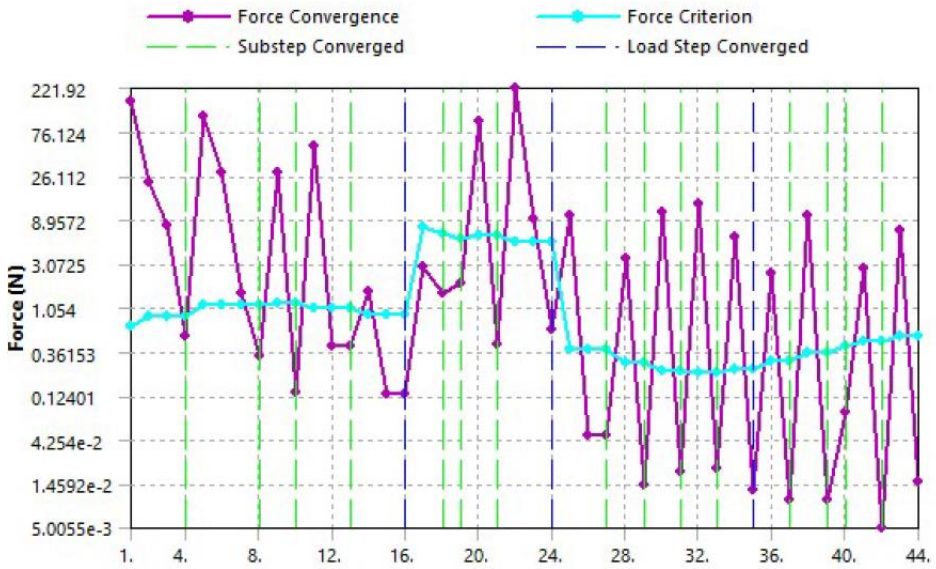

Figure 10-3: Graphical representation of force convergence and time of the gait vs. cumulative iterations of the 3D-Mus. obtained from the solver information of Ansys (R.18.1).

Appendix F: The list of all applied forces including muscles contact force

The list of all applied forces including muscles contraction for 3D-Mus. FEA and their maximum contact forces during the gait cycle.			
Abbreviation	Muscle Location	Explanation (Max Peak × BW)	Reference
HCF- BW		Hip Contact Force - Body Weight	Bergmann et al., (2016)
ACL, LCL, and MCL		Ligaments around Knee joint Lateral collateral (LCL) $(0\hat{\imath} + 0\hat{\jmath} + 0.05\ \hat{k})$ Medial collateral (MCL) $(0\hat{\imath} + 0\hat{\jmath} + 0.08\ \hat{k})$ Anterior cruciate (ACL) $(0\hat{\imath} + 0\hat{\jmath} + 0.29\ \hat{k})$	Adouni et al., (2012)
$M_F + M_T$		Mass of Femur + Mass of tibia =0.16 BW	Applied Density (Clauser, et al., 1969).
ILPSO	Hip Muscle	Iliopsoas $(-0.03\hat{\imath} + 0.01\hat{\jmath} + 0.02\ \hat{k})$	Correa et al., (2010)
ADLB	Hip Muscle	Adductor longus brevis + Adductor magnus $(-0.22\hat{\imath} + 0.03\hat{\jmath} + 0.06\ \hat{k})$	Correa et al., (2010)
ADM	Hip Muscle		
GMED - A	Hip Muscle	Anterior gluteus medius and anterior gluteus minimus + Posterior gluteus medius and posterior gluteus minimus $(-0.22\hat{\imath} + 0\hat{\jmath} + 0.22\ \hat{k})$	Correa et al., (2010)
GMED - P	Hip Muscle		
GMAX - M	Hip Muscle	Medial gluteus maximus + Lateral gluteus maximus $(1.1\hat{\imath} + 0.89\hat{\jmath} + 1.87\ \hat{k})$	Correa et al., (2010)
GMAX - L	Hip Muscle		
SAR	Hip Muscle	Sartorius $(0.0\hat{\imath} + 0.0\hat{\jmath} + 0.60\ \hat{k})$	Adouni et al., (2012)
GRA	Knee-Hip	Gracilis $(0.0\hat{\imath} + 0.0\hat{\jmath} + 0.65\ \hat{k})$	Adouni et al., (2012)
HAMS (ST, SM and BFSL and FSH)	Knee Muscle	Semimembranosus, Semitendinosus, Biceps femoris long-short head $(-0.02\hat{\imath} + 0.01\hat{\jmath} + 0.27\ \hat{k})$	Correa et al., (2010)
RF	Knee-Hip	Rectus femoris $(0.01\hat{\imath} + 0.01\hat{\jmath} + 0.04\ \hat{k})$	Correa et al., (2010)
VAS (VM, VL and VIM)	Knee muscle	Vastus medialis, Vastus intermedius, and Vastus lateralis $(0.18\hat{\imath} + 0.09\hat{\jmath} + 0.32\ \hat{k})$	Correa et al., (2010)
SOL	Knee Muscle	Soleus $(0.01\hat{\imath} + 0.01\hat{\jmath} + 0.01\ \hat{k})$	Correa et al., (2010)
PT		Patellar tendon force $(0.00\hat{\imath} + 0.0\hat{\jmath} + 0.30\ \hat{k})$	Adouni et al., (2012)